Effects of Thermal Annealing and Ion Irradiation on the Microstructures of HT-9 Ferritic Steel

Ji-Jung Kai

May 1986

UWFDM-688

Ph.D. thesis.

FUSION TECHNOLOGY INSTITUTE

UNIVERSITY OF WISCONSIN

MADISON WISCONSIN

Effects of Thermal Annealing and Ion Irradiation on the Microstructures of HT-9 Ferritic Steel

Ji-Jung Kai

Fusion Technology Institute
University of Wisconsin
1500 Engineering Drive
Madison, WI 53706

http://fti.neep.wisc.edu

May 1986

UWFDM-688

Ph.D. thesis.

EFFECTS OF THERMAL ANNEALING AND ION IRRADIATION ON THE MICROSTRUCTURES OF HT-9 FERRITIC STEEL

by

Ji-Jung Kai

A thesis submitted in partial fulfillment of
the requirements for the degree of

DOCTOR OF PHILOSOPHY
(Nuclear Engineering)

at the

UNIVERSITY OF WISCONSIN-MADISON

1986

EFFECTS OF THERMAL ANNEALING AND ION IRRADIATION

ON THE MICROSTRUCTURES OF HT-9 FERRITIC STEEL

Ji-Jung Kai

Under the Supervision of Professor Gerald L. Kulcinski

Ferritic steels have now become the leading candidates for the cladding and structural materials of fast breeder reactors and the first walls and blankets in conceptual fusion reactor designs. The purpose of this thesis research is to examine the effects of high temperatures and radiation levels on the microstructural stability of the HT-9 ferritic steel (12Cr-1MoVW).

The microstructures of as-received HT-9 consisted of tempered martensite laths, carbides and a small amount of ferrite. There were four types of carbides identified in the as-received alloy; namely, equiaxed $M_{23}C_6$, needle-like M_2X, platelet MX, and elongated $M_{23}C_6$. Most of these precipitates were Cr-enriched. The dislocation density in this alloy is very high (greater than 1×10^{11} cm^{-2}).

Thermal annealing studies showed that some major microstructural changes occured after annealing above 600° C which indicates that it is not practical to use this material at 600° C or above. The stability of carbide phases during thermal annealing in increasing in the following order: M_2X, elongated $M_{23}C_6$, MX, and equiaxed $M_{23}C_6$.

No cavity formation was observed in HT-9 following ion

irradiation without helium preimplantation at temperatures of 300 to 600° C (0.3 to 0.5 T_m) to a peak damage level of 200 dpa. However, with 100 appm He preimplantation, there were cavities formed in the specimens irradiated at 500 and 600° C to a damage level as low as 10 dpa. This result indicates that free gas atoms are essential in cavity formation and growth in ion-irradiates HT-9. Radiation-induced phases were observed, chi phase at 500° C and α' phase at 400° C, which may cause embrittlement of this alloy during irradiation. Interstitial dislocation loops are the major microstructure in HT-9 following ion irradiation at 300 and 400° C which may be the major cause of the irradiation hardening.

It is concluded from this study that void swelling may not be a major concern for the use of HT-9 in future reactor systems because of the superior swelling resistance of this alloy. In contrast, the irradiation embrittlement produced by the radiation-induced second phases and the high density of small dislocation loops might be a critical factor and needs further study.

APPROVED:

May 12, 1986

Date

Professor Gerald L. Kulcinski
Nuclear Engineering Department

ACKNOWLEDGEMENTS

There are a number of people who are provided encouragement and asistance during the course of this thesis study. This work is dedicated to my parents, Mr. and Mrs. T. H. Kai, and to my brother and sisters for their steadfast support of my studies.

The encourgement and advice of my advisor, Professor G. L. Kulcinski, served as a mold for my scientific development. Special thanks are also due to Professor R. A. Dodd and Professor W. G. Wolfer for their many enlightening discussions and guidance. I would like to thank Professor T. F. Kelly for his helpful discussions in the area of electron microscopy.

I would like to thank Mr. R. Casper for his training on the proper way to utilize the electron microscope and constantly keeping the microscopes in perfect operating condition. Excellent technical support with the heavy ion irradiations was provided by R. C. Schmidt, Dr. J. H. Billen and the Nuclear Physics group. I would also like to thank D. J. Pertzborn for the technical asistance in the helium preimplantation of this research.

I would like to express my appreciation to the past and present members of the Radiation Effects group for their valuable discussions, suggestions, and asistance. These include Dr. S. J. Zinkle, Dr. R. L. Sindelar, Dr. D. L. Plumton, Dr. S. K. McLaurin and Dr. D. B. Bullen for their experimental asistance and comments. J. H. Liang and Dr. C. D. Croessmann provided computer calculations and graphics on several occasions. I would also like to acknowledge L. E. Seitzman, D. H. Plantz, L. M. Wang and S. H. Han for their asistance.

I would also like to thank Mr. D. Bruggink for his asistance in preparing the graphics and Ms. Pat Caliva and Beth Brown for typing the many reports that were generated during my graduate studies.

This work was supported by the United States Department of Energy.

TABLE OF CONTENTS

	PAGE
ABSTRACT	ii
ACKNOWLEDGEMENTS	iv
TABLE OF CONTENTS	vi
LIST OF FIGURES	x
LIST OF TABLES	xv
I. INTRODUCTION	1
REFERENCES FOR CHAPTER I	8
II. THEORY REVIEW IN RADIATION DAMAGE	10
A. Basic Idea of Radiation Damage	10
B. Point Defects Production and dpa Calculation	12
C. Void Nucleation	17
D. Void Growth	24
1. Gas Effects	26
E. Heavy-Ion Simulation	30
REFERENCES FOR CHAPTER II	34
III. SOLUTE SEGREGATION AND PHASE STABILITY DURING IRRADIATION	39
A. Solute Segregation	39
1. Size Factor	42
2. Solute-Defect Complexes	43

PAGE

3. Inverse Kirkendall Effect..... 46

B. Phase Stability during Irradiation..... 52

1. Radiation-Enhanced Diffusion..... 54

2. Thermodynamics under Irradiation..... 57

3. Alteration of the Nucleation and Growth of Particles..... 60

4. Spinodal Decomposition..... 66

5. Recoil and Disordering Resolution..... 67

6. Particle Coarsening..... 73

7. Ordering-Disordering..... 76

REFERENCES FOR CHAPTER III..... 82

IV. REVIEW OF PREVIOUS STUDIES OF IRRADIATION EFFECTS IN FERRITIC STEELS..... 87

A. Thermodynamics of Iron and Ferritic Steels.. 90

B. The Physical Metallurgy of Ferritic Steels.. 95

C. Radiation Effects in Ferritic Steels..... 107

1. Void Swelling Studies..... 107

2. Dislocation Loop Studies..... 119

3. Solute Segregation and Phase Stability Experiments..... 126

4. Mechanical Property Studies..... 132

D. Swelling Suppression Mechanisms..... 134

E. Recently Developed Ferritic Steels for

PAGE

Breeder and Fusion Reactor Applications..... 141

REFERENCES FOR CHAPTER IV..... 144

V. EXPERIMENTAL FACILITIES AND PROCEDURES..... 159

A. Metallurgy of HT-9 ferritic steel studied... 159

B. Heavy Ion Irradiation Facility..... 162

C. Light Ion Irradiation Facility..... 169

D. Specimen Preparation..... 171

1. Thermal Annealing Study..... 171

2. Ion Irradiation Study..... 173

E. Analysis Procedures..... 182

REFERENCES FOR CHAPTER V..... 186

VI. MICROSTRUCTURAL CHARACTERISTICS OF AS-RECEIVED AND THERMAL ANNEALED HT-9..... 188

A. Microsturctures of As-Received HT-9 Ferritic Steels..... 188

B. Thermal Annealing Effects..... 202

C. Discussion..... 217

1. As-Received Microstructures..... 217

2. Thermal Annealing Effects..... 219

D. Summary..... 224

REFERENCES FOR CHAPTER VI..... 226

VII. MICROSTRUCTURAL EVOLUTION OF HEAVY-ION IRRADIATED HT-9 FERRITIC STEEL..... 227

PAGE

A. HT-9 Irradiated with 14 MeV Ni Ions..... 227

1. Dislocation Loop Evolution..... 228

2. Precipitation Response..... 233

B. Irradiation Effects of HT-9 Specimens Preimplantated with 100 appm He..... 245

C. Discussion..... 255

1. Cavity Formation and Growth..... 256

2. Dislocation Loop Evolution..... 261

3. Phase Stability during Irradiation..... 263

D. Summary..... 267

REFERENCES FOR CHAPTER VII..... 269

VIII. CONCLUSIONS..... 273

A. As-Received and Thermal Annealed HT-9 Ferritic Steel..... 273

B. Ion-Irradiated HT-9 Ferritic Steel..... 274

C. Suggestions for Future Work..... 276

LIST OF FIGURES

		PAGE
Fig.II-1	Schematic of the collision cascade.....	11
Fig.II-2	Calculated 14 MeV ion damage profile and ion deposition in HT-9.....	14
Fig.II-3	General form of swelling vs. dose level....	29
Fig.III-1	Inverse Kirkendall effects in a binary alloy	47
Fig.III-2	Effects of Partial diffusion coefficients on element concentration near a defect sink of a binary alloy.....	51
Fig.III-3	Schematic activation plot for diffusion in an irradiated metal.....	56
Fig.III-4	The critical point of nodal lines for a particle subject and the praticle trajectories	62
Fig.III-5	Schematic of the irradiation effect on precipitate stability.....	63
Fig.III-6	Schematic of concentration variations in a precipitate cell.....	71
Fig.III-7	Schematic of the evolution of a particle under going recoil resolution.....	74
Fig.III-8	The mean particle radius as a function of aging time.....	77
Fig.III-9	Schematic free energy diagram for alteration of particle solubility and stability by irradiation disordering.....	79
Fig.III-10	The Ti-Ru phase diagram as a function of temperature.....	81

		PAGE
Fig.IV-1	A comparison of the swelling behavior of several commercial steels.....	89
Fig.IV-2	The iron-carbon phase diagram.....	91
Fig.IV-3	Schaeffler diagram indicating the effect of Ni and Cr equivalents on the constitution of stainless steels.....	92
Fig.IV-4	TTT diagram of several ferritic steels.....	94
Fig.IV-5	Precipitate evolution of ferritic steels following thermal annealing.....	98
Fig.IV-6	Equivalent carbides in 0.2%C, 1.0%Mo, Cr-V steels at 700° C for 2000 h.....	100
Fig.IV-7	Comparison of swelling measurements as a function of alloy Cr content in Fe-Cr....	111
Fig.IV-8	The summary of the void swelling of ferritic steels.....	116
Fig.V-1	Schematic of heavy-ion irradiation facility	163
Fig.V-2	Schematic of the target section of the heavy-ion irradiation facility.....	166
Fig.V-3	Schematic of light-ion irradiation facility	170
Fig.V-4	Schematic of the carbon extraction replica method.....	174
Fig.V-5	Schematic of the cross-section technique...	177
Fig.V-6	Schematic of sample holder and gas bubbler	179
Fig.V-7	Schematic of the whole plating assembly....	180
Fig.VI-1	Optical micrographes of as-received HT-9...	189
Fig.VI-2	TEM microstructures of as-received HT-9....	191

PAGE

Fig.VI-3 Dislocation density measurement in HT-9.... 193

Fig.VI-4 Carbon extraction replica of as-received HT-9..... 194

Fig.VI-5 $M_{23}C_6$ precipitates in as-received HT-9..... 196

Fig.VI-6 Lattice interference fringes of an $M_{23}C_6$ particle..... 197

Fig.VI-7 Elongated $M_{23}C_6$ precipitates in as-received HT-9..... 199

Fig.VI-8 M_2X needle-like precipitates in as-received HT-9..... 201

Fig.VI-9 MX platelet precipitates in as-received HT-9..... 203

Fig.VI-10 Optical micrographs of HT-9 following thermal annealing for 2 hours..... 205

Fig.VI-11 Optical micrographs of HT-9 following thermal annealing for 24 hours..... 206

Fig.VI-12 Vickers microhardness of thermal annealed HT-9..... 208

Fig.VI-13 Vickers microhardness of thermal annealed HT-9..... 209

Fig.VI-14 TEM microstructures of HT-9 after thermal annealing for 2 hours..... 211

Fig.VI-15 TEM microstructures of HT-9 after thermal annealing for 24 hours..... 212

Fig.VI-16 Carbon extraction replica of HT-9 after thermal annealing for 2 hours..... 214

Fig.VI-17 Carbon extraction replica of HT-9 after thermal annealing for 24 hours..... 215

PAGE

Fig.VI-18 The continuous cooling temperature (CCT) diagram of a material that is very similar to HT-9..... 221

Fig.VII-1 TEM cross-section of HT-9 following ion irradiation to a peak damage of 40 dpa..... 229

Fig.VII-2 TEM microstructures in the peak damage region of HT-9 irradiated to 40 dpa..... 231

Fig.VII-3 Loops and subgrains contrast series of HT-9 irradiated to 30 dpa at 400° C..... 232

Fig.VII-4 TEM cross-section of HT-9 following ion irradiation to a peak damage of 100 dpa.... 234

Fig.VII-5 TEM microstructures in the peak damage region of HT-9 irradiated to 100 dpa..... 235

Fig.VII-6 Plot of dislocation loop density and average diameter vs. irradiation temperature in ion-irradiated HT-9..... 236

Fig.VII-7 carbon extraction replica of HT-9 following ion irradiation at 500° C to a peak damage level of 40 dpa..... 238

Fig.VII-8 TEM cross-section of HT-9 irradiated at 500° C to a peak damage dose of 200 dpa.... 240

Fig.VII-9 The chi phase particles in HT-9 following ion irradiation at 500° C..... 241

Fig.VII-10 The chi phase precipitates in Moire fringe contrast in HT-9 following ion irradiation at 500° C..... 242

Fig.VII-11 Plot of the number density and average diameter of the chi phase particles versus dose level..... 243

Fig.VII-12 Small precipitates associated with

PAGE

dislocation loops in HT-9 following ion irradiation at 400° C to 40 dpa..... 244

Fig.VII-13 Relationship between the calculated damage profile and helium implantation region in ion irradiated HT-9..... 246

Fig.VII-14 Helium bubbles in helium doped HT-9 irradiated at 600° C to 10 dpa..... 248

Fig.VII-15 Voids observed in helium doped HT-9 irradiated at 500° C to 30 and 60 dpa..... 249

Fig.VII-16 Swelling vs. dose level in helium doped HT-9 irradiated at 500° C..... 251

Fig.VII-17 TEM microstructures of He doped HT-9 following ion irradiation to 10 dpa..... 253

Fig.VII-18 TEM microstructures of He dopped HT-9 following ion irradiation to 30 dpa..... 253

Fig.VII-19 Critical cavity size determination in He doped HT-9 following ion irradiation at 500 and 600° C..... 254

LIST OF TABLES

		PAGE
Table IV-1	Summary of precipitate response in various alloy steels following thermal annealing..	99
Table IV-2	Summary of precipitate evolution in 12Cr-1MoV steels under irradiation.....	131
Table V-1	Chemical composition of various 12Cr-1MoV ferritic steels.....	160
Table V-2	Temperature and dose matrix for ion irradiation studies.....	176
Table VI-1	Precipitation phases in as-received HT-9..	204
Table VII-1	Cavity characteristics of He doped HT-9 following ion irradiation.....	250

CHAPTER I

INTRODUCTION

The environment in fast breeder reactors and in proposed designs of fusion reactors can have a strong impact on the surrounding structural material. For example, neutrons produced in the reactors can cause substantial structural damage of the material as a result of the formation of point defects; gas particles produced by transmutations in the reactors can cause the embrittlement of the material and also promote the formation of voids; and the reactive environment in the reactors can cause surface corrosion which will reduce the lifetime of the material. Microstructural phase changes in alloys can also be enhanced or induced by irradiation. These effects in turn change the mechanical properties of the material, usually in an undesirable way. The service lifetime and reliability of the structural material of fast breeder reactors and of fusion reactors should be considered as one of the principal factors governing the commercial development of nuclear energy.[1] For this

reason, the thermal annealing and the radiation damage effects on the properties of the structural material is a very important subject to study before the actual fusion reactors are built.

The effects of high energy neutron (14MeV) irradiation on candidate materials for the first wall in a fusion reactor are hard to assess because of the relatively low flux of such neutrons in existing 14 MeV neutron facilities or the low energy of the neutrons (1 to 2 MeV) of the operating fission irradiation facilities.[2]

High dose neutron irradiation effects must be studied by using fission neutrons, high-energy electrons, or heavy ions.

Heavy ion irradiation can be utilized to partially simulate the displacement damage and the lifetime fluence of a fusion neutron environment in a reasonably shorter time scale. Such irradiation studies can also tell us a great deal about the fundamental processes associated with radiation damage. Since the damage rate of heavy ion irradiation is about 1000 to 10,000 times higher than that of neutron irradiation, one can do the same damage experiment in hours instead of years as required in

presently existing neutron devices. Therefore, the heavy ion experiments are useful for performing scoping studies on fusion reactor structural materials and understanding the mechanisms by which the microstructure is changed during irradiation.

Unfortunately, ion irradiation does not produce helium and hydrogen atoms during irradiation, while neutron irradiation produces these gas atoms via transmutation reactions. It is known that these gases have a considerable effect on void nucleation and growth. This shortcoming can be overcome to a certain degree through the use of gas preimplantation or by dual-ion or triple-ion irradiation. The preimplantation method was used in this thesis research.

Ferritic steels have recently become of interest as a candidate for the first wall structure material for fusion reactors.[2-4] The evidence from irradiation experiments in fission reactors and from heavy ion accelerator irradiations suggests that ferritic steels have very good resistance to swelling.[5-9] Other studies showed that the mechanical properties (e.g., strength, thermal and irradiation creep, embrittlement) are comparable to those

of austenitic steels at reasonable operating temperatures.[4,10,11]

The alloy, HT-9, is a typical ferritic/martensitic stainless steel (12Cr-1MoVW) which has been chosen by the Department of Energy Alloy Development Program as a candidate for the first wall material. It is a commercial alloy with a demonstrated superior resistance to swelling and adequate mechanical properties at elevated temperatures (around 500^{o} C).

The purpose of this thesis research is to examine microstructure stability of HT-9 following thermal annealing alone and also under heavy ion irradiation. Steels have found widespread uses in industrial applications due to relatively high strength and availability. In the past, many hundreds of different alloy steels have been developed. However, due to their complexity, not all alloys have a sufficient level of research data available to completely understand their behavior. Since HT-9 is a newly developed ferritic/martensitic steel, the available data base is weaker, especially in the area of the microstructural evolution during thermal annealing and irradiation.

Therefore, part of this thesis has centered on the microsturctural evolution under thermal annealing alone in order to understand the thermal effects on the microsturcture of HT-9. Following this analysis of the unirradiated response, a major portion of this thesis is concentrated on the microsturctural evolution following heavy ion irradiations, with and without 100 appm helium preimplantation.

When this research was first started, only a few ion irradiation studies had been reported.[6,12,13] Even though the ferritic steels have been considered by researchers in this field for several years now, the results of the irradiation effects on HT-9 are rather sparse, particularly compared to the considerable amount of data available from austenitic steel studies. Therefore, other ferritic steels and pure iron are also included in the literture survey part of this work.

This thesis is organized as follows: first a brief literature review of the theory of radiation damage and a review of previous experiments that pertain to this thesis research are given; the experimental methods and facilities which are used in this study will be outlined

next; then the results of this study are presented; finally, the discussion of the results and the conclusion of this research are outlined. Chapter II summarizes the theories of point defect formation under irradiation, the displacement per atom (dpa) calculation under heavy ion irradiation, and the agglomeration of point defect clusters. Phase stability and solute segregation under irradiation are reviewed in Chapter III. The purpose of these two chapters is to give a fundamental understanding of the origins and inter-relationships among the various types of microstructure changes and localized compositional changes that are related to the experiments. In Chapter IV, a literature survey of the specific radiation effects on ferritic steels including several studies in pure iron is presented. This chapter gives a clear idea of what has been done and what the results were. The experimental methods and facilities are described in detail in Chapter V. In Chapter VI, the results of characterizing the microstructures of as-received and the thermal annealed HT-9 ferritic steel are presented. The irradiation effects on the microstructural evolution in HT-9 with and without helium preimplantation

are presented in Chapter VII. In the latter chapter, it is clearly indicated that the inert gas atoms are necessary for forming cavities in heavy ion irradiated HT-9 ferritic steel. The discussion of the results and the explanations are given in the last section of Chapter VI and VII. The final conclusions and the suggestions for future work are presented in Chapter VIII.

REFERENCES FOR CHAPTER I

1. G. L. Kulcinski, Contemp. Phys. 20(1979) 417-447.

2. The Blanket Composition and Selection Study (BCSS), Argone National Laboratory, March 19, 1984.

3. R. L. Klueh, "Cr-Mo Steels for Fusion Reactor First Walls - A Review", Oak Ridge National Laboratory (ORNL) internal memo.

4. G. J. Butterworth, "Some Initial Considerations of The Suitability of Ferritic/Martensitic Stainless Steels as First Wall and Blanket Materials in Fusion Reactors", UKAEA-CLM-R217 Fusion Association.

5. E. A. Little and D. A. Stow, J. of Nucl. Mat. 87 (1979) 25-29.

6. F. A. Smidt, Jr., P. R. Malmberg, J. A. Sprauge, and J. E. Westmoreland, in Irradiation Effects on The Microstructure and Properties of Metals, ASTM-STP-611(1976) 227-241.

7. D. S. Gelles, J. of Nucl. Mat. 108&109 (1982) 515-526.

8. L. L. Horton, J. Bentley, and W. A. Jessen, J. of Nucl. Mat. 103&104 (1981) 1085-1090.

9. J. M. Vitek and R. L. Klueh, in the Proc. of the Topical Conf. on Ferritic Alloys for Use in Nuclear Energy Technologies, Snowbird, Utah, June 1983.

10. E. A. Little, International Metals Rev. (1976) p.25

11. J. A. Hawthone, in Alloy Development for Irradiations Performance (ADIP) Quarterly Progress Report Dec. 1980, DOE/ER-0045/5, 127-142.

12. G. Ayrault, "Cavity Formation in Single- and Dual-Ion Irradiated HT-9 and HT-9 + 2Ni Ferritic Steels" DAFS Quarterly Report DOE/ER-0046/8 (1982) 182-190.

13. J. L. Brimhall, D. R. Jones, J. of Nucl. Mat. 103&104 (1981) 1379-1384.

CHAPTER II

THEORY REVIEW IN RADIATION DAMAGE

A. Basic Idea of Radiation Damage

High energy particles (e.g., neutrons, heavy ions, and electrons) injected into materials will collide and transfer sufficient energy to lattice atoms to displace them. These displaced atoms are called primary knock-on atoms (PKAs). These PKAs will then become energetic and collide with other lattice atoms to initiate a sequence of displacements of lattice atoms. Fig.II-1 shows the sequence of collision cascades. These cascades will produce many Frenkel pairs (vacancy-interstitial pairs). These point defects (interstitials and vacancies) will then migrate to recombine, form clusters, or move with impurity atoms (solute segregation). In addition, there are different sinks in material (e.g., dislocations, grain boundaries, etc.) that will absorb or emit point defects with different preference. The combination of these mechanisms produces the complex radiation damage effects in the structural material. A detailed description of the

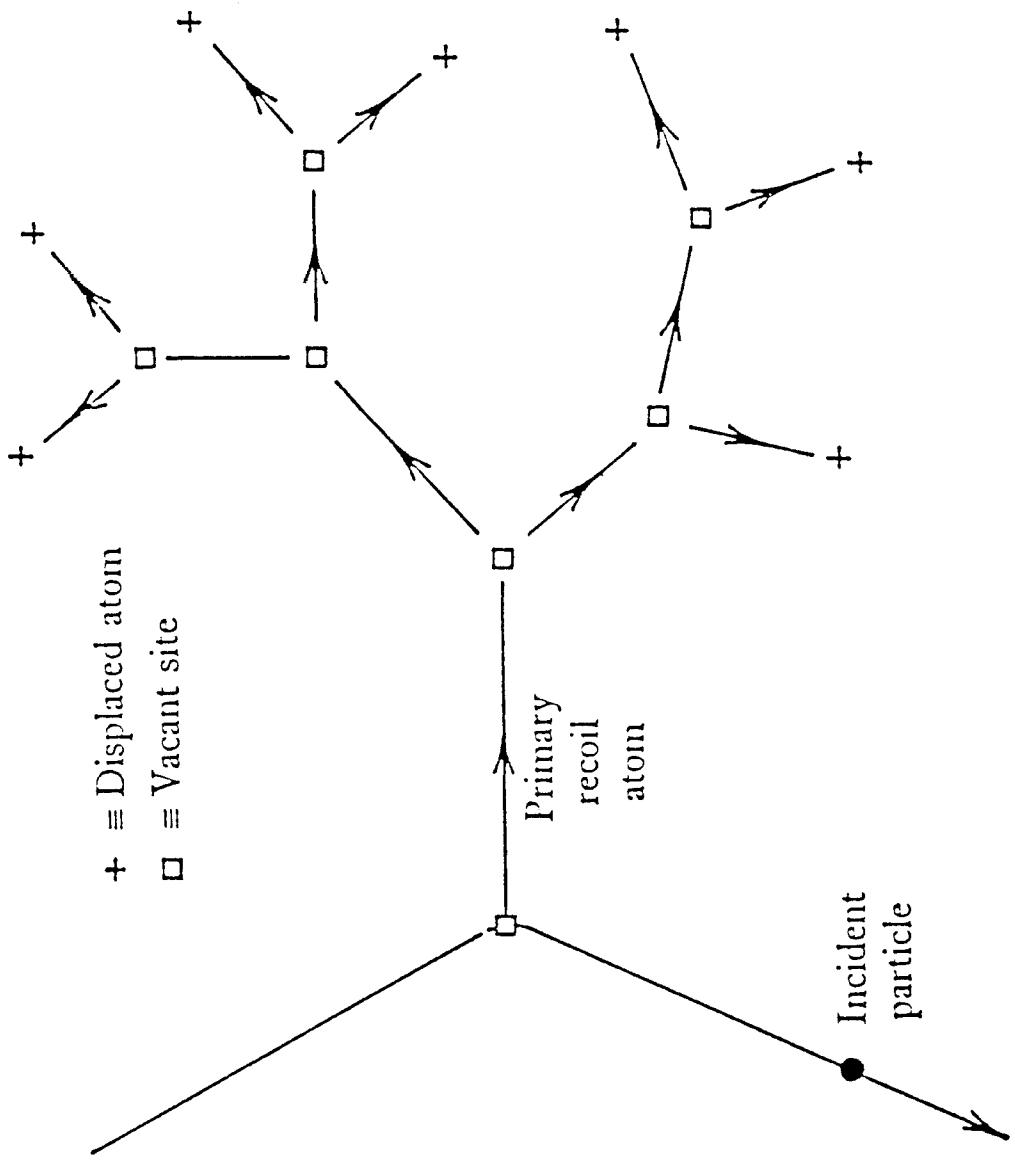

Fig.II-1 Schematic of the collision cascades. (1)

phenomena which occur during irradiation may be found in the literature.[1-3]

B. Point Defects Production and dpa Calculation

An energetic particle penetrates into a material and transfers its energy in two ways; (a) it transfers the energy to the electrons of material through excitation, and (b) it transfers the energy to the atoms by elastic collisions. Because of the different properties of different particles, they have different characteristics. Fast neutrons have no charge so that they transfer energy to the material only by elastic collision and have a relatively small collision cross-section. Therefore, they will travel a relatively longer distance in the material and cause a more homogeneous distribution of point defects. Charged particles (such as heavy ions, electrons and the PKAs produced by fast neutron collisions) transfer energy in both ways and the energy transfer rate is a function of the energy of the charged particles. For higher energy, the transfer rate is smaller and vice versa.

Ion irradiation produces a more dense cluster of

displacement cascades than that found for neutron irradiation due to the large Rutherford collision cross-section between the incident ion and the lattice atoms. The displacement rate of ion irradiation is dependent on depth which is limited to a few microns. Fig.II-2 shows a typical ion irradiation damage profile versus depth. It is clearly seen that the displacement rate varies by a factor of four from the 1 micron depth region to the peak damage region.

In order to compare the different irradiation situations, a measure of damage level known as the dpa (displacement per atom) has been established. A dose level of 1 dpa means that, on the average, each atom in the crystal has been displaced from its original lattice site once during an irradiation. The unit of dpa does not account for point defect recombination, dose rate effects of spatial rearrangement due to thermal-assisted migration. However, it is a useful unit for calculating first-order effects that will be expected under various irradiation conditions.

The mathmetical calcutations of the dpa profile of neutron and heavy ion irradiations are briefly described

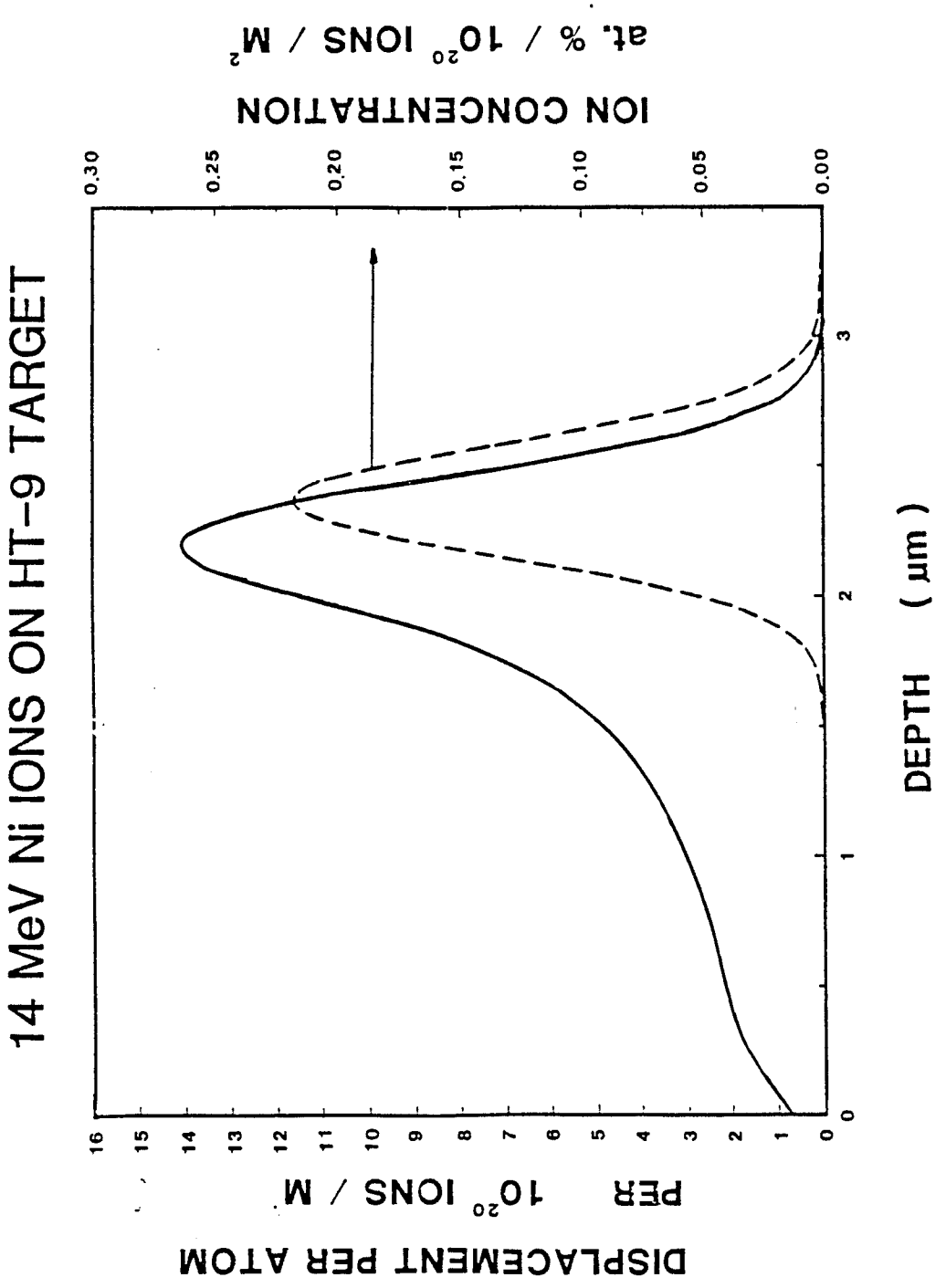

Fig.II-2 Calculated 14 MeV Ni ion damage profile and ion deposition in HT-9.

as follows. For neutron irradiation, one can calculate the dpa by the following general formula:[4]

$$dpa = N_{dn}/N = \Phi_n \iint N_n(E)\,\sigma(E,T)\,\nu(T)\,dE\,dT \qquad (II-1)$$

where N_{dn} is the average number of atoms displaced per unit volume per neutron, N is the atomic number density of the crystal, N_n is the fraction of neutrons with energy E, $\sigma(E,T)$ is the cross section for a neutron of energy E to produce a PKA of energy T, $\nu(T)$ is the total number of atoms displaced by the PKA of energy T, and Φ_n is the total neutron fluence (E > 0.1 MeV).

In the case of heavy ion irradiation, one must know the fraction of the energy lost in nuclear collisions results in displaced atoms. The commonly used model for calculating energy loss of an ion is the theory generated by Linhard and co-workers,[5-8] and is knows as LSS theory. The LSS theory assumes that the electronic energy loss and the nuclear energy loss can be treated separately and the atoms are randomly distributed. In the theory, by using a Thomas-Fermi model for the interactions between heavy ions and atoms, Linhard et al. developed a good

approximation of total range of penetration of charge particles into material. However, it should be emphasized that at moderately low energy the nuclear scattering and stopping power becomes somewhat uncertain because the Thomas-Fermi treatment is a crude approximation when the ion and the atom do not come close to each other.

Once the nuclear energy loss $S_D(x)$ at the projected depth x is obtained (more detail reviews are contained else where),[4,9] the number of displacements per atom (dpa) can be estimated by using a modified Kinchin-Pease model.[10] Torrens and Robinson[11] found the number of dpa is;

$$dpa = \Phi_i \kappa S_D(x)/2E_D N \qquad \text{(II-2)}$$

where Φ_i is the fluence of heavy ions (#/cm^2), N is the atomic density of the target material, E_d is the displacement energy, and κ=0.8 (for the convinence of comparing results). The displacement energy (E_d) varies with the orientation of crystallograph, so the displacement energy of a polycrystal should be average over all orientations. A value of E_d = 25 eV was used in

all dpa calculations, in accordance with the value commonly used for iron in the literature.[12]

Manning and Mueller[13] have developed a computer code, EDEP-1, which uses LSS theory to calculate energy deposition and the injected ion distribution as a function of depth for ion irradiation. Brice[14] has extended the LSS theory to account for energy transport by recoiling target atoms and he has obtained good agreement between experiment and theory. The displacement damage and implanted ion deposition vs. depth curve shown in Fig.II-2 was calculated by the code developed by Brice. Attaya[15] has formulated a three dimensional Monte Carlo code (HERAD) to calculate the ranges and damage of ions in material. HERAD produces better agreement between experiment and theory than the Brice code.

C. Void Nucleation

The point defects which are produced by energetic particles will diffuse through the lattice of crystal and form point defect clusters. Because of relatively low migration energy of interstitials, the thermally activated diffusion of the interstitials is possible at low

temperatures, but the vacancy diffusion needs higher energy. Therefore, at low temperatures, vacancies are immobile and may be annihilated by diffusing interstitials. At very high temperatures, the thermal vacancy concentration is very high, so that the vacancy supersaturation situation will not be significant any more and void embryos become unstable due to vacancy reemission and void nuclei dissolution. The temperature range in which voids will normally nucleate is roughly between 0.3 T_m and 0.6 T_m, where T_m is the absolute melting temperature for the material which of interest.

Cawthorne and Fulton[16] first found voids in austenitic stainless steel irradiated by neutrons. The first step approach for void nucleation theory was made by Harkness et al.[17,18] They utilized an equation applicable to nucleation of voids only in the presence of a vacancy supersaturation and did not consider the interstitials which produced simultaneously. The theory of homogeneous nucleation of voids in the absence of gas or impurity atoms was developed independently by Katz and Wiedersich[19] and Russell.[20] They extended the nucleation theory by considering void formation in the

presence of both supersaturations of vacancy and interstitial during irradiation. This is the basic theory that is used today. Void nucleation is possible only when the rate of arrival of vacancies is larger than that of interstitials. The arrival rates of point defects are proportional to the product of their mobility and concentration. Since interstitials have higher mobility and the concentrations of interstitial and of vacancy are equal, there must be some other sinks that prefer to attract interstitials to form vacancy supersaturation to let voids grow. The only other type of sinks in metal which have long range interactions with point defects are dislocations. This led to the statement by Bullough[21] and Heald and Speight[22] that dislocations preferentially attract interstitials and the preference was a strong function of irradiation temperature.

In the fusion reactor environment, helium gas atoms will be produced by transmutations, so that the effects of inert gas atoms on void nucleation must also be considered. Bullough and Perrin[23] first compared the stability of small gas bubbles and voids (diameter less than 5 nm) under conditions of very low vacancy

supersaturation and concluded that the presence of gas is necessary to the nucleation and growth of voids. Russell[24] has attempted to calculate the co-precipitation of vacancies, interstitials and gas atoms into voids. Using a nodal line and critical point formalism, Russell[25] determined that spontaneous void nucleation may occur during neutron irradiation if sufficient helium is present. Katz and Wiedersich[25] developed a "binary" model for void nucleation with insoluable gas atoms by assuming the atoms are immobile. They considered two parallel nucleation processes, i.e., homogeneous nucleation without gas effects and heterogeneous nucleation of pre-existing immobile helium atoms and helium atom clusters. By changing the activation barrier to nucleation, they expected a much higher void nucleation rate with a small amount insoluable gas atoms. However, the assumption of immobile helium is not consistent with the need for some mobility to form the helium clusters. Russell[27,28] and Wiedersich et al.[29] came up the theory of void nucleation for irradiated materials containing mobile helium. Recently, Parker and Russell[30] modified the theory even further to include

three important effects; (a) non-ideality of the inert gas in bubbles, (b) a helium concentration increasing linearly with dose, and (c) nucleation of cavities on approximate equilibrium bubbles of any size.

Non-gaseous impurity atoms also have a strong effect on void nucleation. There are two general ways that solute of impurity atoms can influence the nucleation of voids. First, impurities can interact directly with point defect clusters to change their nucleation and growth characteristics. They also can interact with point defects to change their free energy of migration. Smidt and Sprague[31] and Mansur[32] predicted that the vacancy trapping at solute atoms will increase the probability of recombination which will lower the vacancy concentration and hence lower the void nucleation rate. This postulate requires immobile or slow moving solute atoms. Venker and Ehrlich[33], on the other hand, investigated the correlation between fast diffusion solutes and nucleation suppression which was explained by Garner and Wolfer.[34] The concept is that when fast-diffusing solute atoms enhance the vacancy mobility, the vacancy supersaturation is reduced, and the void nucleation rate reduced.

Conversely, slow-diffusing solute elements reduce the vacancy mobility, increase the vacancy concentration and thereby enhance void nucleation. The difference between the two results is due to different assumptions concerning the role of trapped vacancies as void nucleation sites. Whereas Mansur[32] considered the traps to be saturable and therefore assumed that bound vacancies cannot be sites for void nucleation, Garner and Wolfer[34] allowed both free and bound vacancies to function not only as nucleation sites but also as defects capable of incorporation into other vacancy clusters.

Anthony[35] was the first to hypothesize that the presence of an enriched solute shell which came from the solute segregation on the void surface could alter the growth rate of a void by changing the vacancy diffusion coefficient and the vacancy chemical potential in the zone around the void. Alteration of the surface energy of the growing void could change the vacancy concentration so that it is in equilibrium with the void, thereby inhibiting void growth. Brailsford[36] treated the problem by assuming that the solute segregating to a void surface will lower the surface free energy and

simultaneously reduce the diffusion of vacancies relative to self-interstitials. Wolfer and Mansur[37-39] made a different approach by considering the mechanical interactions between point defects and voids coated with a shell of impurity atoms to determine the capture efficiency for interstitials and vacancies. They found that shells with a shear modulus only a small percentage larger than in the matrix made voids strongly biased againist interstitials. This strong effect is due mainly to the change in relaxation energy.

The non-gaseous impurity effect on the nucleation theory has been treated by Russell.[25] He modeled the impurity effect by a change of void surface free energy. Si-Ahmed and Wolfer[40] calculated the quantitative results of the effect of segregation on void nucleation by utilizing capture efficiencies of coated voids. Another theoretical approach to void nucleation has been developed recently by Wolfer and Wehner.[41,42] A Fokker-Planck equation is used to provide the continuous and concise description of void nucleation and loop growth. They obtained a close agreement results with experimental values when appropriate bias factor parameters were used.

D. Void Growth

As long as a void nucleates and grows over the critical size, it will continue to grow under the same irradiation conditions. As mentioned before, the void growth generally occurs at irradiation temperatures between 0.3 T_m and 0.6 T_m. The model used for void growth is the chemical reaction rate theory with a steady state defect production. The basic idea and rate equations for void growth will be discussed below.

Harkness and Li[43] first applied the rate theory to void growth modeling. In order for void growth to occur, the authors theorized some kind of preferential attraction between one type of sink and one type of point defect is necessary (i.e., the attraction between the stress field of a dislocation or dislocation loop and the misfit strain of an interstitial). A further improvement was made by Wiedersich[44] and by Brailsford and Bullough.[45] Wiedersich[44] used the chemical reaction rate equations as a basis and assumed all point defects are produced random walk through the material until they recombine or are incorporated into a sink. The defect annihilation

probabilities at void, precipitate, dislocation and grain boundary sinks were estimated by using a cellular model and solving the diffusion equation for geometries approximating that of the cells. Three types of different sinks were considered: voids, sinks with a bias (such as dislocations to interstitials), and sinks with no bias (such as grain boundaries). Brailsford and Bullough[45] derived the rate theory equations for the spatially averaged interstitial and vacancy concentrations in irradiated material containing sessile dislocation loops, deformation dislocations, voids and precipitates (coherent or incoherent) and solved these equations to obtain a general expression for the volume swelling rate.

Brailsford et al.[46,47] have included the sink strength of various sinks into the rate theory equations. Once the point defect concentrations are obtained from the rate equations, the void growth rate can then be given by Mansur[48] (assuming no divacancy contribution);

$$dr_v/dt = \Omega\{Z_V^V(r_v)d_V[C_V-C^e(r_v)] - Z_I^V(r_v)D_IC_I\}/r_v \quad \text{(II-3)}$$

where C_V is the bulk thermal vacancy concentration, $C^e(r_v)$

is the thermal vacancy concentration at a void of radius r_v, and can be expressed as following;

$$C^e(r_v) = C^o \exp[-(P_g - 2\gamma/r_v)\Omega/kT] \qquad \text{(II-4)}$$

where P_g is the gas pressure in the void, γ is its surface tension, and Ω is the atomic volume, C^o is the equilibrium vacancy concentration. The parameters D, C, and Z are the diffusion coefficients, the concentrations and the capture efficiencies of the vacancy and interstitial, respectively. Mansur and Yoo[49] and Wolfer and Si-Ahmed[50] have investigated the effect of incorporating mobile divacancies into the void nucleation and growth equations. They found that divacancies affect the void growth, decreasing the swelling at peak swelling temperature and increasing the swelling at low temperature irradiations.

D.1. Gas Effects

Free gas atoms are known to play a major role in the void nucleation and growth in irradiated materials. Helium[51] and hydrogen are continuously produced in

fusion reactor environment. Oxygen and other reactive gases are introduced into metals during fabrication. Wolfer[52] has pointed out that some reactive gases such as oxygen and hydrogen can be absorbed on subcritical size void surfaces, thereby reducing the surface energy and the activation barrier for void nucleation and promoting void growth.

Farrell[53] has recently reviewed the observed helium effects on void swelling. Helium is the most important inert gas and is primarily active as a cavity nucleant. The internal pressure of gas of a cavity minimizes the thermal emission of vacancies and allows earlier attainment of a critical size and therefore enhances the void nucleation process. There is no evidence of any direct effects of helium on cavity growth. However, an increasing nucleation rate may subsequently cause an increase or decrease in the swelling as compared to the no-helium condition, depending on the experimental conditions and the microstructure of materials. In heavy ion irradiation studies, helium is purposely introduced into the material to study the effects of helium. The method by which helium is introduced strongly influences

swelling. Swelling increases in the following order: cold preimplantation, hot preimplantation, and co-implantation.[53]

Wolfer[52] recently reviewed the void nucleation and growth models and showed that they were in good qualitative agreement with experimental data. Void swelling as a function of dose can be divided into two regimes, an initial transient regime of low-swelling rate followed by a steady-state, higher-swelling rate regime. Brager and Garner[54] found that in austenitic stainless steels, the steady-state swelling rate is about 1%/dpa, regardless of the preirradiation condition of the alloy. However, the transient regime depends strongly on microstructure, temperature and composition. As indicated in Fig.II-3, the transient period is composed of several periods of increasing length: first, a short period for the point defects to reach their stationary values; next, a timelag before void nucleation to start; finally, the void nucleation period which is terminated when the void number density reaches its saturation value. Before the "steady state" swelling rate can be reached, it is necessary for the microstructure to approach the

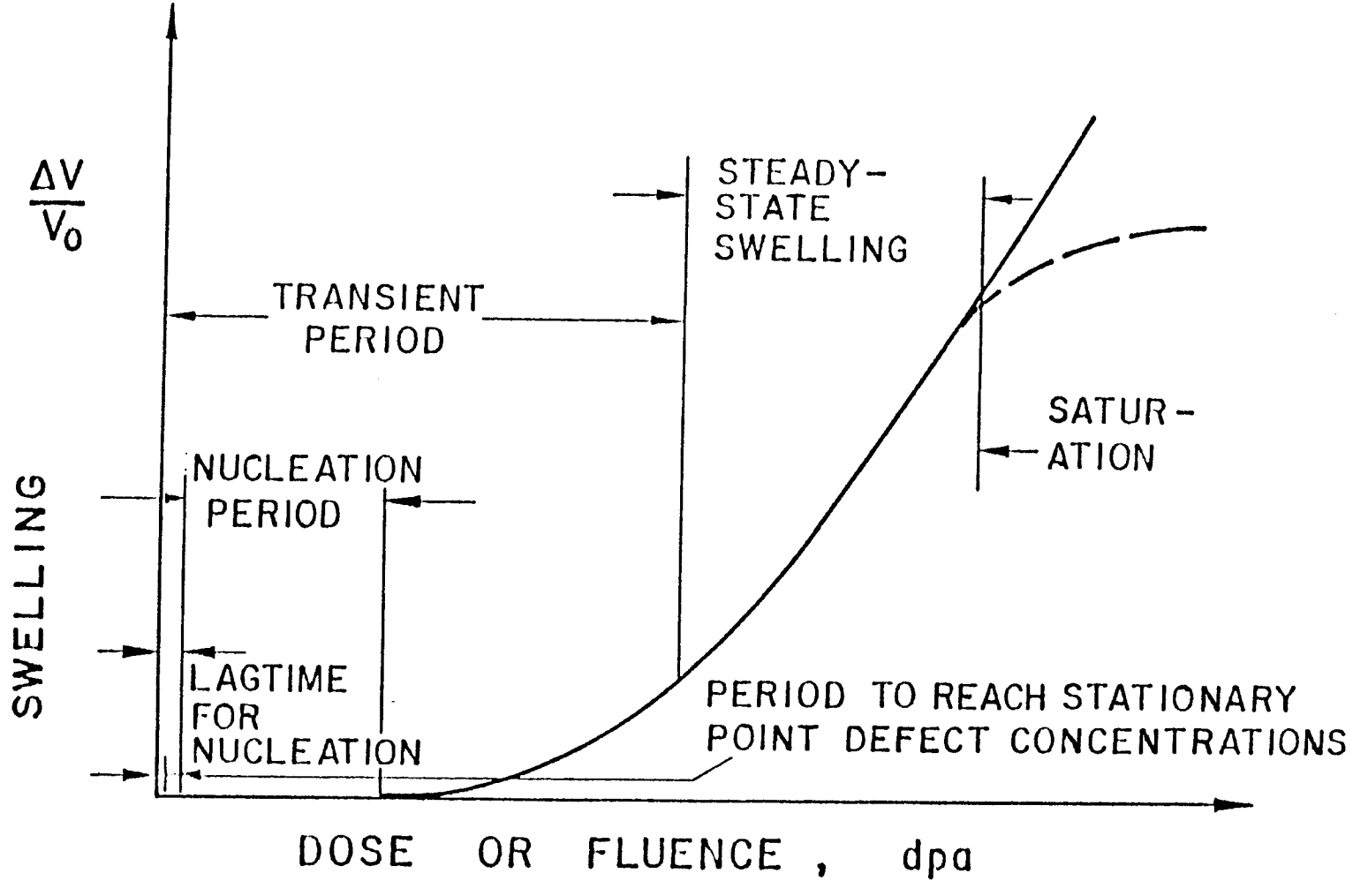

Fig.II-3 General form of swelling vs. dose with various stages indicated. (52)

equalization of the dislocation and void sink strength. At very high doses, when the dislocation sink strength drops below the void sink strength, the saturation of swelling is often observed, especially in ion-bombardment studies.

E. Heavy-Ion Simulation

Nelson and Mazey[55] first proposed using high energy heavy ions to simulate fast neutron irradiation damage because of the higher dose rate (10^{-3} to 10^{-2} dpa/sec for heavy ions verses 10^{-6} dpa/sec for fast neutrons). Another important advantage is the temperature control which is much more precise in accelerators than that in reactors, and therefore allows study of the temperature effect on the irradiation.

However, there are some problems combined with the heavy ion simulation which require correlating the heavy ion irradiation studies to the neutron irradiation. They are; the effective temperature shift, the excess injected interstitials and the surface effects. Kulcinski et al.[4] proposed that the basic damage measurement of dpa should be used to correlate ion damage to neutron damage.

Bullough and Perrin[23], by using rate theory, showed that the peak swelling temperature shifted to higher temperatures with an increasing displacement rate. This means that the peak swelling temperature in heavy ion irradiation should be higher than that in a neutron irradiation. The reason for this is that for the same type of displacement event and constant microsturcture, the point defect arrival ratios at sinks will be remained constant for the different defect production rates only at different temperatures.

Brailsford and Mansur[56] first theoretically examined the effect of self ion injection on void swelling. The effect of the injected ions (also called injected interstitials) is to suppress the void growth at lower irradiation temperatures. But at high temperature swelling, the effect was predicted to be small unless voids were much more important point defect sinks than dislocations. The suppression of void growth varies with the injected interstitial fraction and also depends on the vacancy migration energy. Mansur and Yoo[57] showed that a fair amount of suppression could occur for ion-irradiated materials with a high vacancy migration energy,

low bias or low sink strength. Garner[58] has recently reviewed the ion irradiation experiments which indicated that the injected interstitials can play a significant role in suppressing void growth. Plumton and Wolfer[59,60] investigated the influence of the injected interstitials on void nucleation. They found a dramatic decrease in the void nucleation rate at lower temperatures (i.e., recombination dominant regime). It appears that the suppression of void nucleation by injected interstitials may be the source of the observed discrepancy between low temperature neutron- and low temperature ion-irradiated swellings.

As shown in Fig.II-2, the typical ion irradiated damage zone is concentrated in a few microns depth. Yoo and Mansur[61], studying the effect of free surfaces on void nucleation, calculated the steady state diffusion profiles of vacancies and interstitials in the Ni foil under irradiation at elevated temperatures (450^{o} C or higher) by solving the general rate equations. Their studies showed that after a depth of about 0.4 um, the depletion effect of free surface becomes negligible. Therefore, the surface effects will not be an important

matter in correlating heavy ion irradiation to neutron irradiation in this study because most of the experimental information is taken from the region of 0.5 to 3 microns.

REFERENCES FOR CHAPTER II

1. M. W. Thompson, Defects and Radiation Damage in Metals, Cambridge Univ. Press (1969).

2. Radiation-Induced Voids in Metals, J. W. Corbett and L. C. Ianniello (Eds.), USAEC Technical Information Center (1972) CONF-710601.

3. D. R. Olander, Fundamental Aspect of Nuclear Reactor Fuel Elements, ERDA Technical Information Center Document (1976) TID-26711-P1, Chap. 17.

4. G. L. Kulcinski, J. J. Laidler, and D. G. Doran, Radiation Effects 7 (1971) 195-202.

5. J. Lindhard and M. Scharff, Phys. Rev. 124 (1961) No.1, 128-130.

6. J. Lindhard, M. Scharff, and H. E. Schiott, Mat. Fys. Medd. Dan. Vid. Slesk. 33, No.14 (1963).

7. J. Lindhard, V. Nielsen, and M. Scharff, Mat. Fys. Medd. Dan. Vid. Slesk. 36, No.10 (1968).

8. H. E. Schiott, Mat. Fys. Medd. Dan. Vid. Slesk. 35, No.9 (1966).

9. M. T. Robinson, in Ref. 2, p.397.

10. G. H. Kinchin and R. S. Pease, Reports on Progress in Phys. 18 (1955) 1-51.

11. I. M. Torrens and M. T. Robinson, in Ref. 2, p.739.

12. J. Takamura, K. Furukawa, S. Miura, and P. H. Shingu, J. Phys. Soc. Japan 18, Suppl. III (Intern. Conf. on Crystal Lattice Defects) (1963) p.7.

13. I. Manning and G. P. Mueller, Computer Phys. Communication 7 (1974) 85-94.

14. D. K. Brice, "Ion Implantation Range and Energy Deposition Codes COREL, RASEA and DAMG2", SAND-7500622, Sandia National Lab. (1977).

15. H. M. Attaya, Ph.D. thesis at the Univ. of Wisconsin-Madison (1981), also UWFDM-420.

16. C. Cawthorne and E. J. Fulton, Nature 216 (1967) 575-576.

17. S. D. Harkness and Che-Yu Li, in Radiation Damage in Reactor Material: Vol. II, IAEA 230 (1969) 189-214.

18. S. D. Harkness, J. A. Tesk, and Che-Yu Li, Nuclear Appli. and Tech. 9 (1970) 24-30.

19. J. L. Katz and H. Wiedersich, J. of Chemical Phys. 55, No.3 (1971) 1414-1425.

20. K. C. Russell, Acta Metall. 19 (1971) 753-758.

21. R. Bullough, in "General Discussion on Voids" in Ref. 17, pp.253-257.

22. P. T. Heald and M. V. Speight, Acta Metall. 23 (1975) 1389-1399.

23. R. Bullough and R. C. Perrin, in Ref. 17, p.233.

24. K. C. Russell, Scripta Metall. 6 (1972) 209-214.

25. K. C. Russell, Acta Metall. 26 (1978) 1615-1630.

26. J. L. Katz and H. Wiedersich, J. of Nucl. Mat. 46 (1973) 41-45.

27. K. C. Russell, Scripta Metall. 7 (1973) 755-760.

28. K. C. Russell, J. of Nucl. Mat. 61 (1976) 330-333.

29. H. Wiedersich, J. J. Burton, and J. L. Katz, J. of Nucl. Mat. 51 (1974) 287-301.

30. C. A. Parker and K. C. Russell, in Effects of Radiation on Materials: 11th Conf., H. R. Brager and J. S. Perrin (Eds.), ASTM-STP-782 (1982) 1042-1053.

31. F. A. Smidt, Jr. and J. A. Sprague, Scripta Met. 7 (1973) 495-502.

32. L. K. Mansur, J. of Nucl. Mat. 83 (1979) 109-121.

33. H. Venker and K. Ehrlich, J. of Nucl. Mat. 60 (1976) 347-349.

34. F. A. Garner and W. G. Wolfer, J. of Nucl. Mat. 102 (1981) 143-150.

35. T. R. Anthony, in Ref. 2, pp.631-646.

36. A. D. Brailsford, J. of Nucl. Mat. 56 (1975) 7-17.

37. W. G. Wolfer and L. K. Mansur, Phys. Stat. Solidi 37A (1976) 211-222.

38. L. K. Mansur and W. G. Wolfer, J. of Nucl. Mat. 69&70 (1978) 825-829.

39. W. G. Wolfer and L. K. Mansur, J. of Nucl. Mat. 91 (1980) 265-276.

40. A. Si-Ahmed and W. G. Wolfer, in Ref. 30, p.1008.

41. W. G. Wolfer, L. K. Mansur, and J. A. Sprague, in Intern. Conf. on Radiation Effects in Breeder Reactor Structural Materials, M. L. Bleiburg and J. W. Bennett (Eds.), (1977) 841-863.

42. M. F. Wehner and W. G. Wolfer, "Vacancy Cluster Evolution in Metals Under Irradiation", to be published in Phil. Mag. (1985); also UWFDM-590.

43. S. D. Harkness and Che-Yu Li, Metall. Trans. 2 (1971) 1457-1470.

44. H. Wiedersich, Rad. Eff. 12 (1972) 111-125.

45. A. D. Brailsford and R. Bullough, J. of Nucl. Mat. 44 (1972) 121-135.

46. A. D. Brailsford, R. Bullough, and M. R. Hayns, J. of Nucl. Mat. 60 (1976) p.246.

47. A. D. Brailsford and R. Bullough, J. of Nucl. Mat. 69&70 (1978) 434-450.

48. L. K. Mansur, Nucl. Tech. 40 (1978) 5-34.

49. L. K. Mansur and M. H. Yoo, in the Proc. of the Intern. Conf. on Irradiation Behavior of Metallic Materials for Fast Reactor Core Components, Corsica, France (1979) 9-16.

50. W. G. Wolfer and A. Si-Ahmed, Phil. Mag. 46A (1982) 723-736.

51. H. Ullmaier, Rad. Eff. 78 (1983) 1-10.

52. W. G. Wolfer, J. of Nucl. Mater. 122&123 (1984) 367-378.

53. K. Farrell, Rad. Effects 53 (1980) 175-194.

54. H. R. Brager and F. A. Garner, in Ref. 30, P.152.

55. R. S. Nelson and D. J. Mazey, In Ref. 17, p.157.

56. A. D. Brailsford and L. K. Mansur, J. of Nucl. Mater. 71 (1977) 110-116.

57. L. K. Mansur and M. H. Yoo, J. of Nucl. Mater. 85&86 (1979) 523-532.

58. F. A. Garner, J. of Nucl. Mater. 117 (1983) 177-197.

59. D. L. Plumton and W. G. Wolfer, J. of Nucl. Mater. 120 (1984) p.245.

60. B. Bager, Jr., D. L. Plumton, S. J. Zinkle, R. L. Sindelar, G. L. Kulcinski, R. A. Dodd, and W. G. Wolfer, 12th Intern. Symp. on the Effects of Radiation on Materials, Williamsburg, VA, (1984) ASTM-STP-870, pp.297-316; also UWFDM-582.

61. M. H. Yoo and L. K. Mansur, J. of Nucl. Mater. 62 (1976) 282-292.

CHAPTER III

SOLUTE SEGREGATION AND PHASE STABILITY DURING IRRADIATION

The ferritic steel, HT-9, has a superior void swelling resistance compared to other materials (such as austenitic stainless steels) under irradiation. Some recent experiments showed solute segregation under irradiation, and others showed radiation-induced or -enhanced phase instabilities in ferritic steels.[1-4] Also, as described in Section II.C, the solute segregation around a subcritical void can affect both void nucleation and growth by modifying the void bias factors.[5,6] Precipitation of second-phase particles can also alter the alloy composition of the matrix, which may affect the swelling. Therefore, it is important to understand the phenomena of solute segregation and phase transformation under irradiation.

A. Solute Segregation

As energetic particles penetrate into a material,

they produce displaced atoms throughout the entire injection range. At elevated temperatures, point defects are mobile and are annihilated by mutual recombination or attracted by different sinks (such as dislocations, grain boundaries, and voids). If either one of these mechanisms is inhomogeneous, a net flux of point defect will be induced. In order to complete the motion of point defects, it is necessary to move atoms along the path of moving defects. Several mechanisms can be envisaged, such as: (a) a vacancy exchanges site with a neighboring atom, (b) interstitial jumps to a neighboring interstice, or (c) interstitial motion forces an atom into a interstice while returning a different atom. This is the phenomenon of radiation-induced solute segregation (RIS). Okamoto and Rehn[7] have reviewed the results obtained on RIS from surface segregation experiments.

In an alloy, more than one element exists; therefore, point defects migrate by preferential motion of one or more elements. A coupling between point defect fluxes and atom fluxes is required for the segregation to occur. There are several important effects of solute segregation: (a) precipitates which are stable at the average matrix

compositions may dissolve in depleted zones, (b) precipitates may form in locally enriched areas even though the phase is unstable at the average matrix composition, (c) the surface composition of voids may be altered which will cause significant changes in the rates of void nucleation and growth, (d) these changes may also affect the mechanical properties of the irradiated material.

Anthony[8] first proposed the possibility of radiation-induced solute segregation in 1972. Since then, extensive efforts of experimental and theoretical research have been directed toward a basic understanding of radiation-induced solute segregation (RIS). Most studies have concentrated on simple binary alloy systems, but recent investigations have been carried out on more complicated alloy systems (e.g., ternary and commercial alloys).[9,10] Because it is a complex physical phenomenon, there is no complete physical model at the present time. Three kinetic models have been developed which are discussed below. These are based on (1) size factor, (2) dilute solution, solute-defect complexes binding, and (3) concentrated solution, inverse Kirkendall effect.

A.1 Size Factor

The size factor model can be explained by the fact that any solute which is preferentially present as an interstitial will tend to be segregated toward point defect sinks.[11] According to Haubold and Martinson[12] self-interstitials in bcc and fcc metals are believed to exist in a "dumbbell" configuration where two atoms share a single lattice site. Incorporation of an undersized solute atom into the dumbbell can reduce the strain energy of the configuration and will be preferred. This mixed dumbell can then migrate by interchanging solvent atoms. During irradiation, the dumbbell will tend to migrate toward point defect sinks which leads to a preferential segregation of the undersized solute atoms around sinks. At the same time, oversized solutes will have a preference for substitutional sites and tend to be depleted from sinks by vacancy migration. The size factor, δ_{SF}, is defined as;

$$\delta_{SF} = (\Omega_B - \Omega_A)/\Omega_A \qquad \text{(III-1)}$$

where Ω_B is the atomic volume of the solute and Ω_A is the

atomic volume of solvent. Undersized atoms have a negative size factor ($\delta_{SF}<0$), and should be segregated toward point defect sinks. This result has been observed in 316 stainless steel during irradiation.[11]

A.2 Solute-Defect Complexes

For a dilute solution system, Anthony[8] first proposed that a solute could be dragged toward a sink along with a point defect where there was a strong binding energy between the vacancy and solute. Johnson and Lam[13] further developed a kinetic model for dilute binary alloys which takes into account the effects of both radiation-induced vacancies and interstitials. Rate equations were set up for free vacancies, interstitials, solute atoms, and solute-defect complexes. The resultant rate equations have been solved numerically for a thin-foil geometry as a function of time for different temperatures, defect production rates, internal sink concentrations, foil thicknesses, defect-impurity binding energies, and initial impurity concentrations. They also extended
the theory[14] to study solute segregation to a void

surface during irradiation. The results are qualitatively similar to those for the foils but vary in magnitude with void size and number density. The solute segregation occurs within the temperature range from 0.2 T_m to 0.6 T_m, and the maximum segregation temperature depends on the displacement rate. It is found that interstitials make a major contribution in the transport of solute during irradiation.

The effect of temperature on solute segregation at a given displacement rate can be summarized as followings: (a) At very low temperatures, vacancies are immobile and the recombination mechanism is dominant; therefore, no segregation will occur. However, there is an initial transient period (i.e., before the vacancy concentration builds up) which interstitials can migrate to sinks and produce a transient form of segregation. (b) At intermediate temperautres, vacancies become mobile and are lost to sinks; therefore, interstitials can migrate to different sinks and segregation occurs. (c) At high temperatures, the solute concentration gradient induces a diffusion of solute atoms away from the high concentrated region and reduces segregation; also, the high thermal

vacancy concentration increases the recombination and decreases segregation. For low displacement rate irradiations (e.g., neutron irradiation), the mechanisms discussed above are shifted toward lower temperatures. Therefore, the peak segregation temperature is reduced which means that lower displacement rate irradiations give more segregation than higher rate ones conducted at lower temperatures. Segregation is also found to be maximum where the interstitial-solute binding energy is high enough so that the migration energies of vacancy and interstitial-solute complex become comparable.[15]

Okamoto et al.[16,17] applied this mechanism to ion bombardment studies. They extended the model to include the effects of spatially dependent damage rates on solute segregation in a semi-infinite medium under heavy ion irradiation and found that the peak damage region is enriched of solutes at the expense of solute depletion at both the surface and far into the bulk (up to twice the range of the incident ions). It is also found that both the type and amount of segregation are affected not only by the target material and irradiation conditions, but also by the mass and energy of the incident ion.

A.3 Inverse Kirkendall Effect

In concentrated alloy systems, a point defect will be generally surrounded by several solute atoms, so the concept of binding between distinct vacancy-solute or interstitial-solute complexes becomes meaningless. Since the Johnson-Lam model is restricted to dilute solution systems, it cannot be applied to concentrated alloys. Therefore, the so called "inverse Kirkendall effect" is used for modeling the solute segregation in concentrated systems.

In the normal Kirkendall effect, various components of an alloy diffuse via vacancies at different rates, a composition gradient can induce a net flux of vacancies across a lattice plane even though the vacancy distribution is initially uniform. However, during irradiation, the inverse situation arises near sinks where gradients in the vacancy and interstitial concentrations can induce a net flux of solute and solvent atoms in an initially homogeneous alloy to produce segregation of the alloy components. Fig.III-1[7] illustrates the inverse Kirkendall effect near a sink in a binary alloy system.

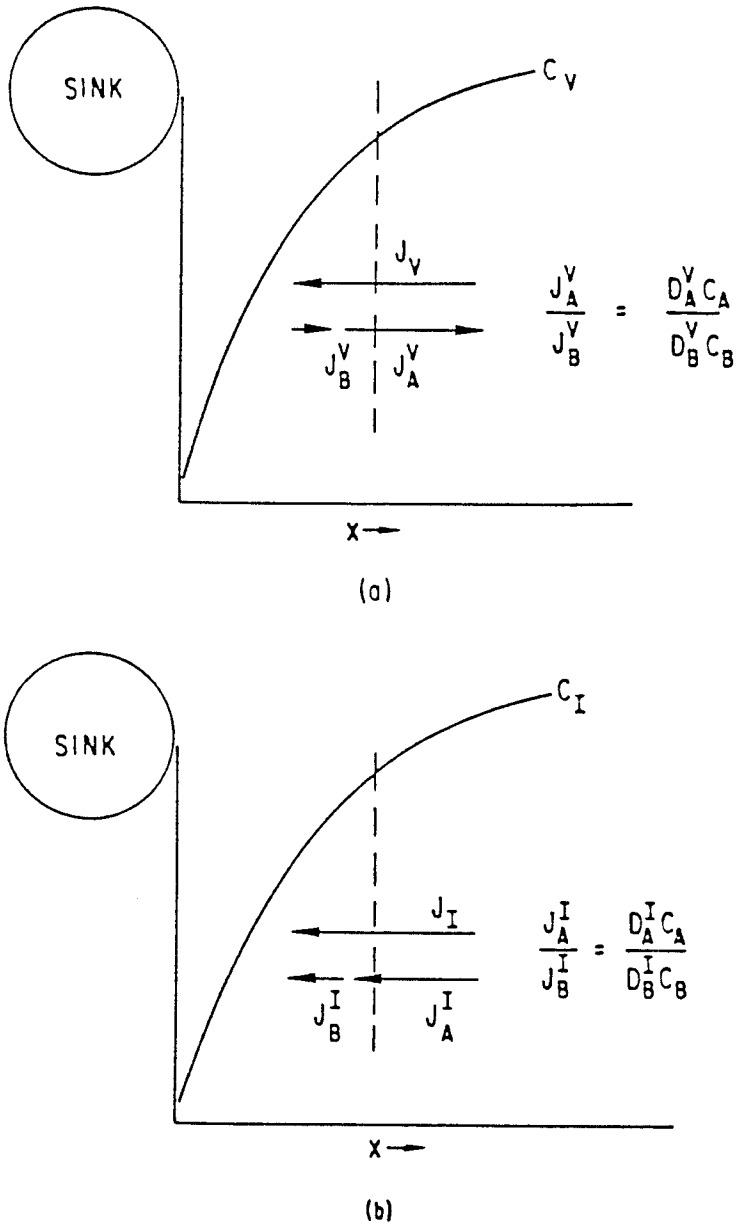

Fig.III-1 Inverse Kirkendall effects induced near a defect sink in a binary alloy of elements A and B by (a) a vacancy flux; (b) an interstitial flux. (7)

Since the vacancy flux is reversal of the direction of the associated atom fluxes, the inverse Kirkendall effect induced by vacancy flux will always cause depletion at the sink of the faster diffusing components. However, because the interstitial flux and the associated atom fluxes move in the same direction, the interstitial flux will preferentially transport the faster diffusing component toward the sink.

Marwick[18] and Wiedersich et al.[19] presented analysis of the inverse Kirkendall effect which is applicable to concentrated systems. Marwick's work was based on Manning's[20] assumption that for concentrated systems, only vacancies contributed to the inverse Kirkendall effect and interstitials can be considered as neutral in its effects. This model predicts that the slower moving solute atoms will diffuse down the vacancy gradient and be segregated to the point defect sinks. Conversely, the faster moving solute atoms diffuse away from sinks. The result of the solute segregation toward sinks induces a vacancy flux which opposes the vacancy flux to the sink. Therefore, the mechanism of vacancies flowing into sinks is reduced, the mutual recombination is

increased and the nucleation and growth rates are reduced.

Wiedersich et al.[19] extended the model of Marwick for radiation-induced solute segregation in concentrated alloys. They included the interstitial contribution to the inverse Kirkendall effect. Their analysis, which generally parallels that of Marwick arrives at an expression for the steady-state solute concentration gradient near a sink. The coupling between defect fluxes and atom fluxes is accounted for by the concept of preferential migration of vacancies and interstitials via A atoms and B atoms in a binary A-B alloy. Similarly, atom fluxes are partitioned into those occuring via vacancies and interstitials. In the steady-state segregation, the solute concentration gradient for element A can be expressed as:

$$\nabla C_A = F(D_A, D_B)\left(\frac{d_A^v}{d_B^v} - \frac{d_A^i}{d_B^i}\right)\nabla C_v \qquad \text{(III-2)}$$

where $F(D_A, D_B)$ is a function of diffusion coefficient of element A and B, ∇C_v is the vacancy concentration gradient which is negative near a sink, and d_A/d_B are essentially the ratio of the effective jump frequencies of A and B

atoms into neighboring vacancies and interstitials. Therefore, the element A becomes enriched at sinks if preferential transport of A atoms via interstitials outweighs that via vacancies (e.g., $R^i > R^v$, $R=d_A/d_B$), and vice versa. Fig.III-2[7] illustrates this effect. Due to the elimination of migrating vacancy-solute complexes, this model is not suitable for dilute alloy systems in which solute transport by tightly bound vacancy-solute complexes is important.

Recently, Lam et al.[21] have extended the concentrated binary alloy model to the case of ternary alloys. It basically followed the work that was done by Wiedersich et al.[19] The segregation problem can be cast into a system of four coupled partial differential equations, which can be solved numerically for appropriate initial and boundary conditions. Model calculations have been performed for Fe-Cr-Ni and Ni-Al-Si alloys under various irradiation conditions. In general, the simple calculations were in good qualitative agreement with the experimental results.[22,23] However, the predictive ability of this model is rather limited due to the limited information of the physical parameters required for these calculations.

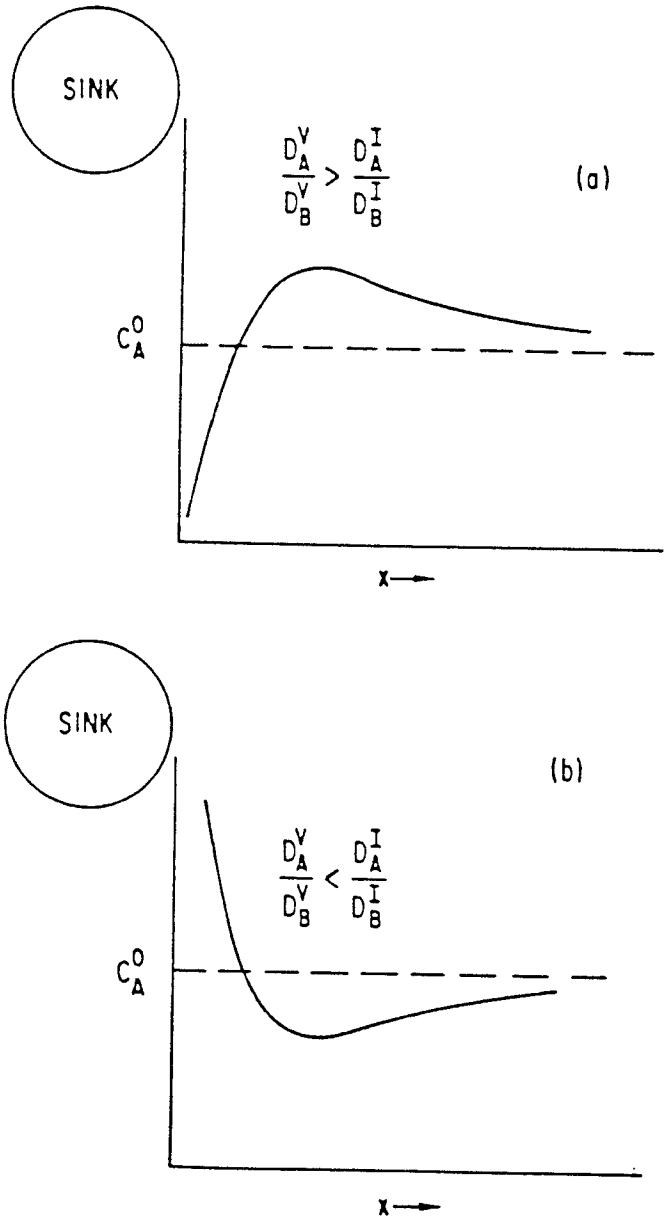

Fig.III-2 Effects of Partial diffusion coefficients on element concentration near a defect sink of a binary alloy of A and B atoms. (7)

B. Phase Stability During Irradiation

Phase stability during irradiation is a metallurgical phenomenon of general interest for studies of material subject to fast fission and fusion neutron irradiations. Several recent review papers discussed this effect and summarized the present theory.[24-29] The following mechanisms have been found to have related to irradiation phase stability: radiation-enhanced diffusion, solute segregation, radiation-enhanced precipitation, metastable precipitate sequence alteration, radiation-induced precipitation, phase diagram modification, and precipitate dissolution. Following the terminology used by Wilkes,[25] phase transformations may be classified as either radiation-enhanced or radiation-induced. The term "radiation-enhanced" is used for transformations in which equilibrium is attained at an enhanced rate. The phrase "radiation-induced" should be used for phase changes which revert when the irradiation is removed. In addition, Lee et al.[30] have mentioned that the radiation-modified phases may also occur (phases develop with composition that are significantly different from the normal

equilibrium phases).

A complication that arises with predicting irradiation phase stability for steels is the wide range of microstructures and constituents that are possible (e.g., ferrite, martensite, bainite, austenite, carbides, and intermatallic phases). Some of these phases appear to be stable under thermal equilibrium conditions may become unstable or metastable during irradiation, and vice versa. Therefore, for the completeness of theory review, Wolfenden et al.[27] discussed those mechanisms of irradiation phase stability which are important for irradiated materials. There is no general theory regarding the phase stability during irradiation. However, there are various independent models which can be applied to describe various situations. Although there is a general lack of predictive capability for these various models of phase evolution, the examination has served the purposes of identifying and defining the pertinent irradiation phase stability phenomenon. These models are briefly reviewed as follows.

B.1 Radiation-Enhanced Diffusion

The diffusion coefficient of atom moving in substitutional alloys is given by: $D=\Gamma d^2/6$, where d is the atomic jump distance, and Γ is the atomic jump frequency for uncorrelated jumps. Diffusion by the vacancy mechanism is simply the product of the vacancy concentration, C_v, the vacancy jump frequency, Γ_v, and a correlation factor, f_v. The diffusion coefficient for vacancy, $D_v=\Gamma_v d^2/6$, can be used to express the atomic diffusion coefficient as; $D=f_v D_v C_v$. Diffusion during irradiation may also take place by the motion of interstitials, divacancies and/or other defect aggregates. In general, the diffusion coefficient can be expressed as;

$$D = f_v C_v D_v + f_i C_i D_i + f_{2v} C_{2v} D_{2v} + - - - \qquad \text{(III-3)}$$

The increased concentrations of vacancy, interstitial, or divacancy will then give a corresponding increase in diffusion coefficient.[31] During irradiation, many more Frenkel pairs will be produced in the material compared to the thermal equilibrium concentration. Therefore, the diffusion mechanism should be largely enhanced. However,

another consideration is needed to be thought.

Temperature has a major effect on diffusion coefficient. Fig.III-3 shows the schematic activation plot for diffusion in an irradiated metal.[29] At high temperatures, point defects have high mobilities and the thermal equilibrium vacancy concentration is very high and it dominates over any irradiation produced concentration. Therefore, in this temperature range, the diffusion coefficient is relatively unaltered by irradiation and the activation energy equals to the vacancy self-diffusion energy (i.e., $Q=E_f^V+E_m^V$, and E_f^V is the vacancy formation energy, E_m^V is the vacancy migration energy). At intermediate temperatures, most point defects are lost to fixed sinks (i.e., dislocations), and the diffusion coefficient is expected nearly independent to temperature (varying only with the dislocation density). At low temperatures, recombination mechanisms become dominant and most point defects produced by irradiation are directly annihilated. Therefore, the diffusion coefficient is proportional to $(\Gamma_v K)^{1/2}$ and the activation energy is $E_m^V/2$, where K is the atomic displacement rate.

Adda et al.[31] found that when the diffusion

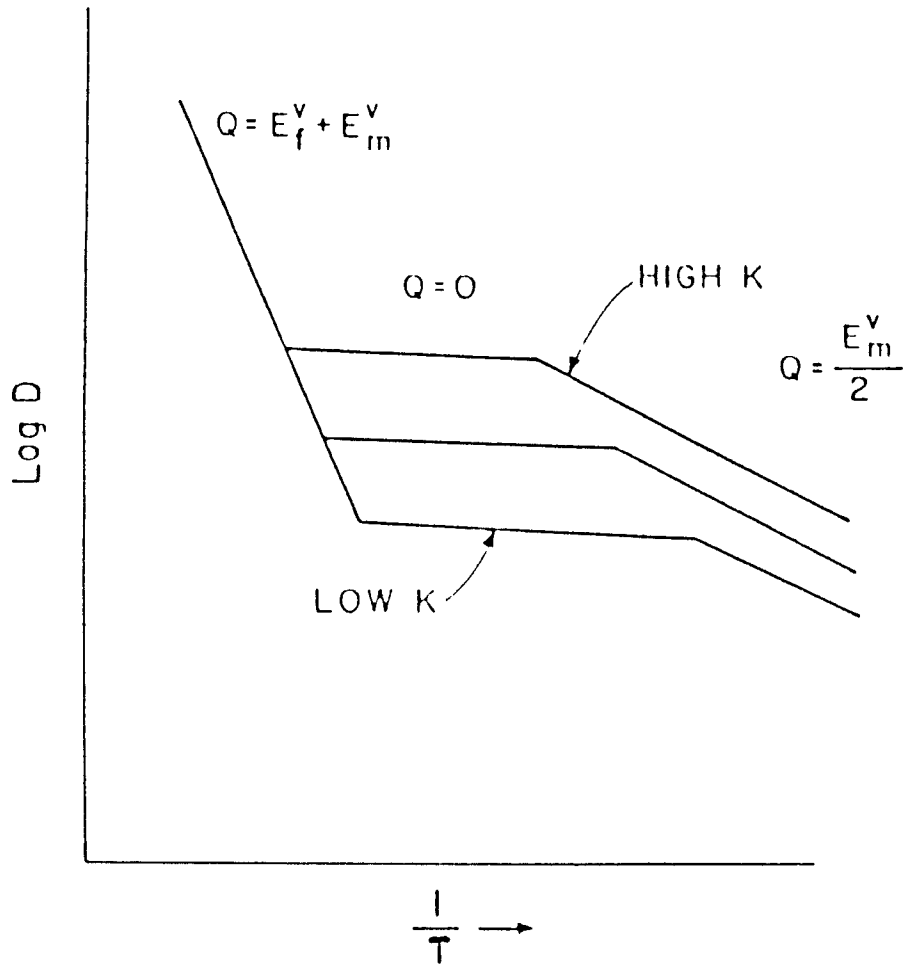

Fig.III-3 Schematic activation plot for diffusion in an irradiated metal. (29)

coefficient is higher than 10^{-16} cm^2/sec, there will be no irradiation enhancement. Conversely, the diffusivity will not drop below the 10^{-16} cm^2/sec range during irradiation due to the production of defects. This result indicates that the recovery process may be enhanced by irradiation at lower temperatures, but not at high temperatures.

B.2 Thermodynamics under Irradiation

Russell[26] has pointed out that although a large solute segregation could cause precipitation at sinks, it could shift only the phase diagram laterally (i.e., locally, it would be the same as if the material was at a different composition). Solute segregation cannot produce a phase which would not normally appear at that temperature without irradiation. Martin[32] has analyzed solute segregation in terms of the energetics of the various defect interactions and derived a restriction on possible phase instabilities. He found that solute segregation could widen but not diminish a two-phase region. That is, this process can produce precipitation in a single phase region but cannot dissolve precipitates to transform a two-phase alloy to a single phase.

Therefore, the solute segregation cannot account for the production of new phases which are not stable at that temperature or dissolve existing precipitates during irradiation. These conclusions mean that there must be other mechanisms which need to be studied to understand the radiation-induced precipitation phenomenon.

Materials under irradiation fall in the regime of irreversible thermodynamics and may reach a stable steady state but not equilibrium.[28] Such systems may be approached by one of two methods. The first is the continuum approach, which optimizes a minimum entropy production to dictate the steady-state configuration of the system. The second approach is atomistic, whereby one considers the kinetics of the various processes involving irradiation-induced defects and rate theory, and determines the final state of the system along with the rate and path to this state. The second approach is often used in radiation damage work.

Various authors have attempted to find a thermodynamic-based cause of radiation-induced precipitates. Hudson[24] reviewed several experimental results to discuss the so called new phases produced under

irradiation (e.g., γ' in PE-16, rod-type precipitate in 316 stainless steel, etc.) but did not present the reasons for the formation of precipitates. Wilkes et al.[33] intended to explain this phenomenon by the free energy changes of various phases due to the additional free energy which comes from excess point defects. Therefore, the most possible combination of phases is the one which gives the lowest total free energy. Also, the free energy of phases in the steady-state includes an extra contribution from defects which shifts the free energy curve upwards and then changes the composition of phases. However, the contribution of excess vacancies was found to be around 10 J/mole which is small compared to the free energy difference (on the order of 100-10,000 J/mole) which is required to significantly modify the phase diagram.

Yamauchi et al.[34] developed a "constrained phase equilibrium" scheme for the study of phase equilibrium in binary alloys under irradiation. In this scheme, as long as the vacancy concentration in the matrix phase is higher than that in the precipitate phase, phase boundaries shift toward the inside of the matrix phase, as the difference

in vacnacy concentrations between the two phases is increased. There exists a limit to the maximum phase boundary shift when the vacancy concentration in the precipitate phase is fixed. The authors emphasized that the model is only good for the homogeneous, coherent radiation-induced precipitate. They also found substantial shifts in the phase boundary for an ordering system which are consistent with the shifts observed by Cauvin and Martin[35] in Al-Zn alloys.

B.3 Alteration of the Nucleation and Growth of Particles

Maydet and Russell[36] first proposed a kinetic theory for the stability of incoherent precipitates under irradiation. A precititate was characterized by two variables; namely, the number of solute atoms x and the number of excess vacancies n. Therefore, a precipitate with a greater atomic volume than the matrix would thus have n>0 to relieve the strain energy, and vice versa for an undersized precipitate. The rate equations for excess vacancy and solute atom can be set up by using the same method that discussed in Section II.C. Nodal lines which are shown in Fig.III-4[36] are obtained by setting rate

equations to zero. The point of intersection is known as a critical point. A critical point exists only if the irradiation modified free energy, which determines phase stability under irradiation, is negative ($\Delta\phi<0$). This also means if $\Delta\phi>0$, all particles will decay. In general, particles, which are between lines (x=0 and n=0 lines), with $x>x^*$ will grow and those with $x<x^*$ will decay. Particles not between the lines will approach the curve to the crosses (in Fig. III-4) in the appropriate direction. Maydet and Russell[36] suggested that, by considering excess vacancies produced by irradiation and neglecting excess interstitials, the precipitates with a greater atomic volume than the matrix ($\delta>0$) would enhance their stability and vice versa for undersized ($\delta<0$) precipitates.

Figure III-5 shows, schematically, the effect of irradiation on the the stability of two phases in a matrix of α phase. The θ phase is thermally stable, but is destablized by irradiation due to its negative volumentric misfit. The ψ phase is stablized by irradiation since it has a positive volumentric misfit, and it should precipitate in favor of θ phase. This model is applicable

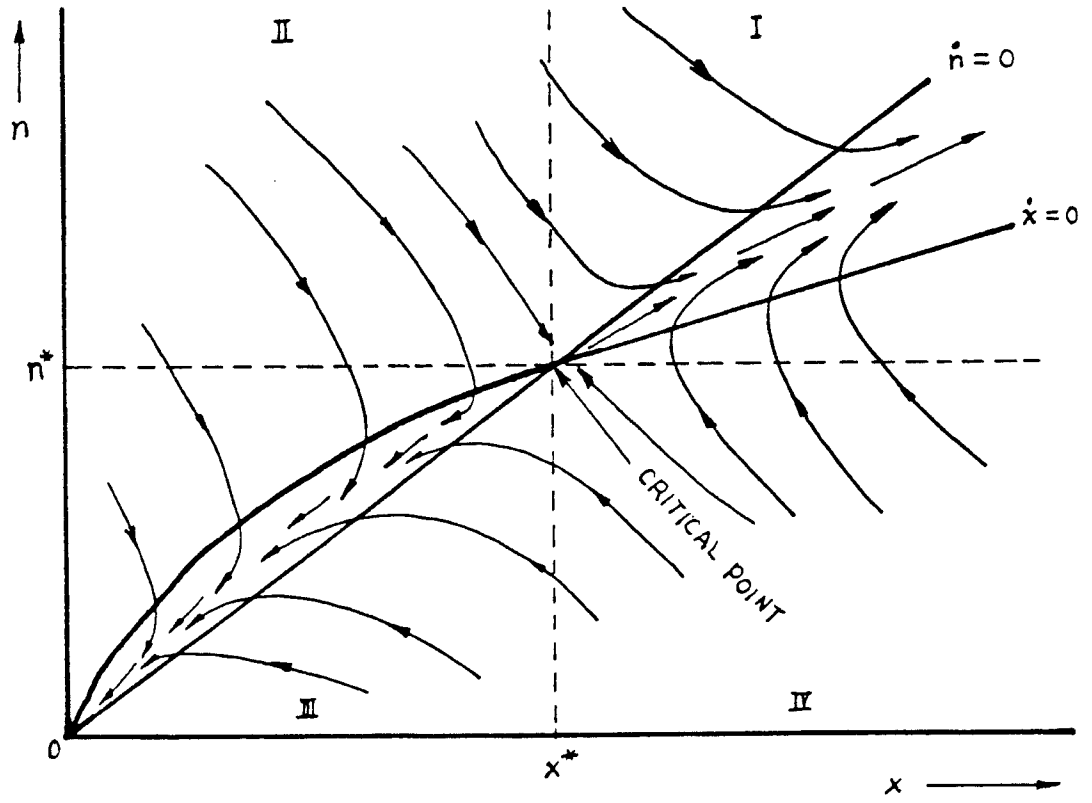

Fig.III-4 The critical point of nodal lines for a particle subject and the praticle trajectories. (36)

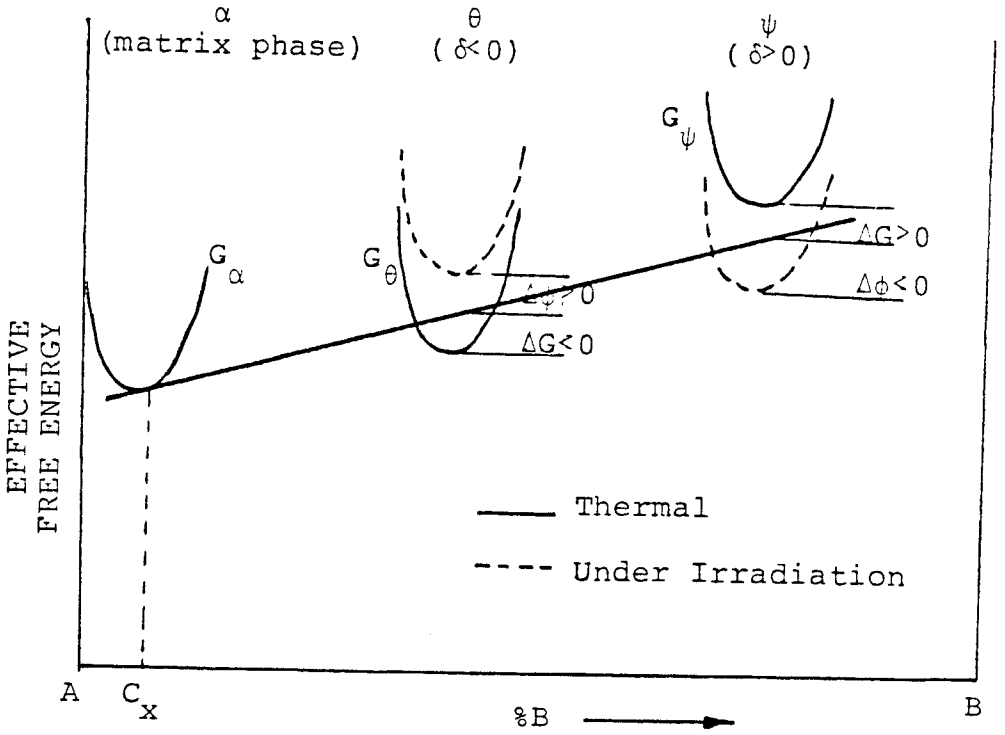

Fig.III-5 Schematic of the irradiation-induced defects on precipitate stability. (36)

only for incoherent, small disordered precipitates under neutron and heavy ion bombardment. Martin et al.[37] reported a systematic experimental study of dose rate effects for radiation-induced precipitation of Ni-Si alloys. They found that the radiation-induced precipitation in undersaturated solid solution occurs only for undersized solute atoms. The contradictions between the experimental results and the Maydet and Russell model, indicate that the model is not realistic for the systems examined. Cauvin and Martin[35] examined a Al-Zn alloy under irradiation and also found an undersized radiation-induced precipitate. Therefore, they reanalyzed Maydet and Russell's model for the growth of incoherent precipitates and showed that it may qualitatively account for the observed behavior of undersized precipitation.

Cauvin and Martin[38,39] recently developed a model for coherent precipitates in undersaturated solid solutions which is similar to the Maydet and Russell's model. It is assumed that the interfaces are the trapping centers for the point defects and the defect-defect interactions are sufficiently weak compared to solute-solute and solute-defect interactions. The model

suggested that the dominant mechanism for radiation-induced homogeneous precipitation was the irreversible recombination of mixed interstitials with vacancy-solute complexes, and that the coherency or incoherency at the precipitate matrix interface played only a minor role. Several features are important in this model: (a) at high temperature, the solubility limit decreases when the irradiation flux is increased (i.e., enhances precipitation), (b) at low temperature, the solubility limit is a function of temperature only, and (c) the precipitation may saturate before the solute content in the matrix between the precipitates has reached the solubility limit. It also neglects the details of the trajectories of the clusters in the solute defect phase space. Therefore, the model does not give information on the nucleation rate, nor on the role of solute atoms in catalyzing defect clustering. Similarly, the model does not predict radiation-induced precipitate resolution. They also studied radiation-induced Zn precipitation in undersaturated Al-Zn alloys.[39] The experimental results were in good agreement with the calculated data.

B.4 Spinodal Decomposition

In the discussion of radiation-induced solute segregation so far, all theories have assumed that the solid solution is stable under irradiation condition, that concentration fluctuations do not spontaneously increase or decrease as occurs during spinodal decomposition. Martin[40,41] has considered this assumption of stability and found to be unjustefied under certain experimental conditions. Garner and co-workers[42,43] have also reported the spinodal decomposition phenomena in a Fe-Ni-Cr ternary alloy under irradiation.

The basic physical idea of the spinodal decomposition is that a local increase in solute concentration during irradiation attracts vacancies. Therefore, more interstitials are annihilated in the vacancy rich region, which in turn increases the local solute concentration yet more. Martin has noted that just as irradiation may destabilize a stable solid solution, the reverse effect is also possible.

Irradiation could very well stabilize a solid solution which would otherwise decompose through radiation-induced solute segregation.

Recently, Kirshman and Abromeit[44] presented a theory for radiation-induced spinodal type instability in concentrated alloys. The physical basis of their theory is a composition-induced bias in A or B interstitial:vacancy recombination. In this way, the bias could give fewer A interstitials in A-rich regions than elsewhere in the alloy. Then, A interstitials would diffuse down the concentration gradient into the A-rich region, and enrich it further. It will eventually build up a spatially periodic structure which is the phenomenon of spinodal decomposition. Although Kirshman and Abromeit used a similar formalism to that of Martin, the physical bases of the two theories are quite different.

B.5 Recoil and Disordering Resolution

In studying recoil resolution of precipitate under irradiation, ther are basically two types of analyses that have been made. In one case, it is assumed that particles are infinitely spaced; therefore, the diffusion field around a spherical particle is in an infinite medium. In the other case, a cellular model is employed and the diffusion fields around the particles depend on the inter-

particle spacing.

The first analysis of recoil resolution of precipitates was proposed by Nelson, Hudson and Mazey[45] and known as NHM model. They suggested that the stability of precipitates under irradiation depended on the balance between the radiation dissolution of precipitates and their growth by both irradiation-enhanced diffusion and thermal diffusion. Precipitate dissolution can occur via two mechanisms. (a) Recoil dissolution, which is due to the dynamic collision events which occur as a result of atomic displacement within collision cascades. This causes atoms within the precipitates to recoil into the surrounding matrix at a rate proportional to the precipitate surface area and the irradiation flux. (b) Disordering dissolution, particularly pertinent to ordered precipitates, occurs when the disordering effect of the displacement cascades essentially destroys the ordered lattice of the precipitate so that localized regions of high solute concentration are created. When diffusion occurs, the small disordered regions created within the precipitate will reorder while those near the surface will result in the loss of solute, by diffusion, to the

surrounding matrix. The authors concluded that during irradiation some coarsening of small precipitates could occur, but only to the extent defined by the equilibrium conditions, and large precipitates would shrink to the equilibrium size.

Brailsford[46] modified the NHM model by considering that the resolved solute atoms had only a finite distance instead of infinite range and the precipitates themselves might influnce the point defect concentration, thereby modifying the irradiation enhancement of the solute transport. The author did some initial calculations and suggested two conclusions: (a) in order for a fine distribution to coarsen and vice versa, it is necessary that thicker concentric shell forms, surrounding the precipitates; (b) it is necessary for there to be no intrinsic point defect trapping at the precipitate-matrix interface.

Wilkes[25] concluded that the analysis of NHM model simply showed that under irradiation, a non-equilibrium, steady-state solute concentration was reached in the matrix and the degree of supersaturation was dependent on the irradiation rate. All equilibrium precipitates would

shrink under irradiation until the steady-state solute concentration level was reached. No conclusion on size distribution could be obtained from the analysis. Therefore, Wilkes modified the theory with a cellular model in which all precipitates were of the same size and uniformly distributed throughout the matrix. The boundary conditions used in the calculations were that the solute concentration gradient was zero at the cell boundary and the equilibrium concentration occurs at the particle surface. A schematic diagram of concentration variations in a precipitate cell is given in Fig.III-6. In the figures, (a) shows the concentration before irradiation, (b) the irradiation promotes surface dissolution which causes a local supersaturation, (c) at steady-state, the matrix is uniformly supersaturated, (d) the local supersaturation around precipitate exceeds that required for nucleation and new precipitates may form, (e) if the precipitates are widely spaced, the matrix may not reach the steady-state value and all precipitates will then be dissolved.

Frost and Russell[47,48] expanded Wilkes' cellular model to include a time dependent effect of the solute

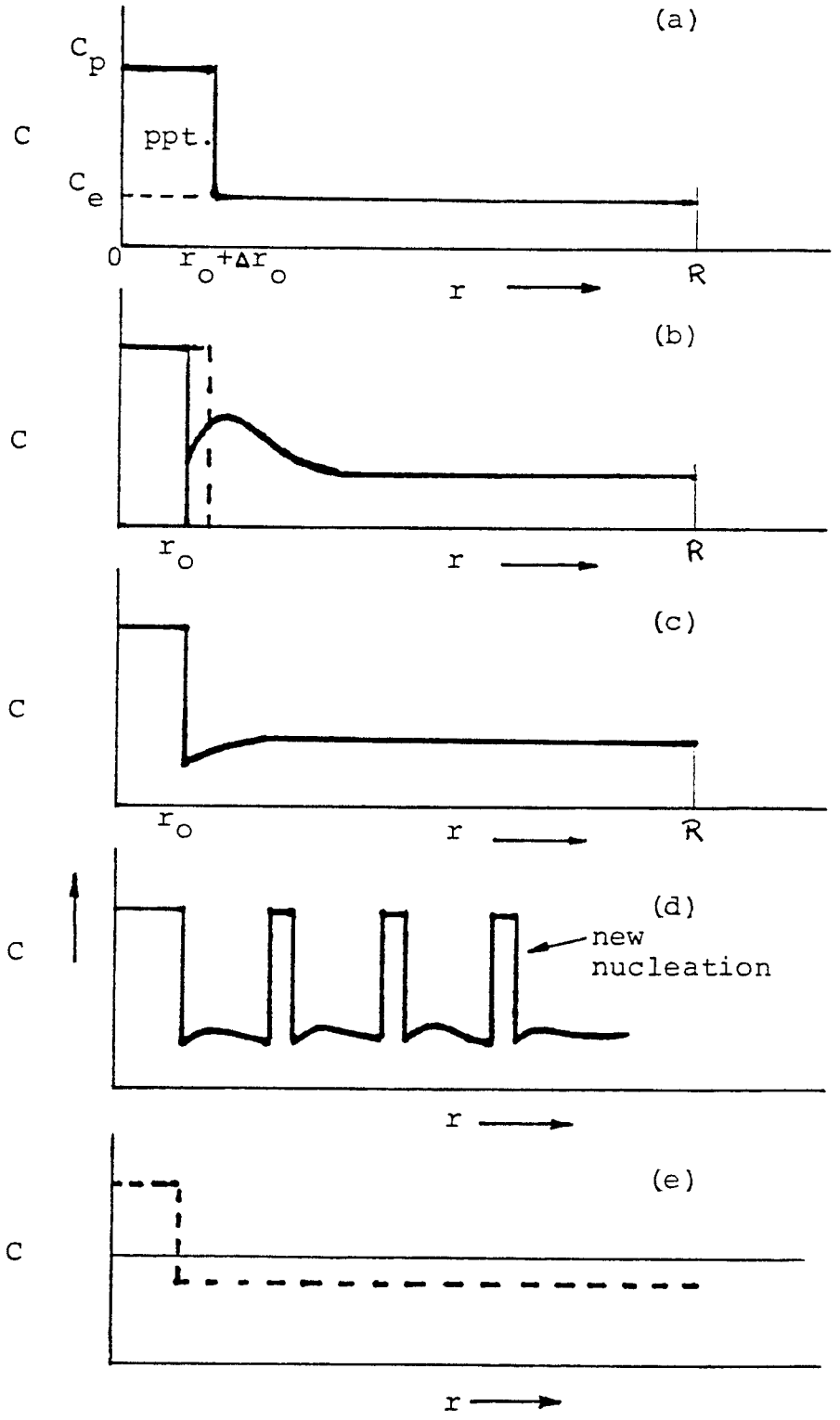

Fig.III-6 Schematic of concentration variations in a precipitate cell. (25)

concentration in the matrix. That means there is an incubation time before the steady-state solute concentration can be reached. They found that the rate of growth or shrinkage of the precipitates is dependent directly on the recoil rate and the recoil distance cube. The rate of growth or shrinkage depended only weakly on the particle spacing and not at all on the diffusion coefficient. The authors pointed out that the time for completion of the recoil resolution process is much longer than is usually experimentally available which means that other physical processes, such as solute segregation and re-precipitation of new particles, are likely to be important for observed evolution of the change of particle size. They also concluded that at high temperatures and low damage rate, the steady-state solute concentration in matrix (C_{ss}) will be close to the thermal value; therefore, the recoil resolution will not be important and thermal coarsening will proceed normally. However, if the C_{ss} value is large compared to the equilibrium solute concentration, but not high enough to start new precipitates, then the recoil resolution will produce inverse coarsening in which all particles tend toward the

same size (i.e., large particles shrink and small particles grow).

Unless the equilibrium matrix concentration is very high, there will be a temperature range in which the recoil resolution induced concentration exceeds the equilibrium concentration by several orders of magnitude. This high supersaturation of solute will promote the nucleation of a new phase. This reprecipitation will start near the particles as the solute builds towards the steady state profile. Each original particle will become surrounded by a tight halo of subparticles, as appears to be the case of the ThO_2 particles observed by Jones.[49] Fig.III-7 shows this mechanism continued until the entire area is filled with an even distributed fine particles.

B.6 Particle Coarsening

Bilsby[50] first presented the model which included a irradiation-enhanced dissolution effect into the diffusion-controlled thermal coarsening equation. The model used a dispersion of spherical particles developed by Wagner[51] and Lifshitz and Shyozov[52] (WLS). Bilsby defined a dissolution parameter which was the ratio of the

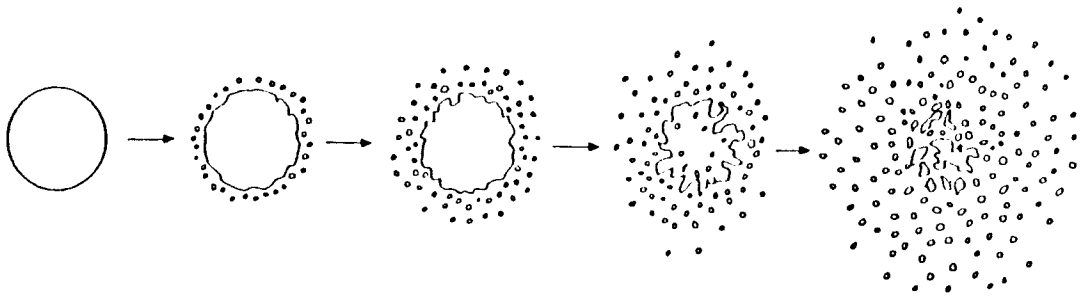

Fig.III-7 Schematic of the evolution of a particle under going recoil resolution. (49)

rate of irradiation-enhanced dissolution to that of thermal coarsening. Unfortunately, the model is valid for only a small value of this parameter which means only for small dissolution rates that the matrix solute concentration is nearly unchanged from the thermal value. Baron et al.[53,54] developed an independent formulation by using a coarsening concept similar to that of Bilsby's model except allowed the matrix concentration to rise above the thermal value. They considered two kinetic mechanisms for irradiation-induced precipitate instability: first, assuming precipitates act as vacancy sources with respect to the solution; second, considering the effects of an efficient solute sink on precipitates coarsening. It is found that regardless of the initial starting condition a steady-state is approached at high doses which is characterized by a maximum particle size and an excess solute concentration. Therefore, it was shown that both particle growth as well as dissolution are possible in an irradiation environment.

Urban and Martin[55,56] have recently extended Cauvin and Martin's[38,39] model which described point defect recombination at the precipitate-matrix interface. Urban

and Martin showed that this leads to a reduction of the solute solubility and to a novel driving force for particle coarsening under irradiation. They neglected radiation-induced precipitate dissolution and solute segregation to or away from point defect sinks other than the precipitates themselves. On the other hand, they took full account of radiation-enhanced diffusion and found that under a coarsening condition, the precipitate growth rate was proportional to the solute diffusion coefficient by vacancy mechanism only rather than the sum of both vacancy and interstitial mechanisms. Irradiation was observed to substantially increase the coarsening rate of small particles ($r < 10$ nm). But for particles above 15 nm in radius, irradiation affected coarsening only through an enhanced diffusion coefficient. Fig.III-8 illustrates the comparison between Urban and Martin's result and the predicted result of WLS theory.

B.7 Ordering-Disordering

The effect of radiation on ordered alloy phases can be described as a balance between two conflicting processes: (a) the disordering produced by the atomic

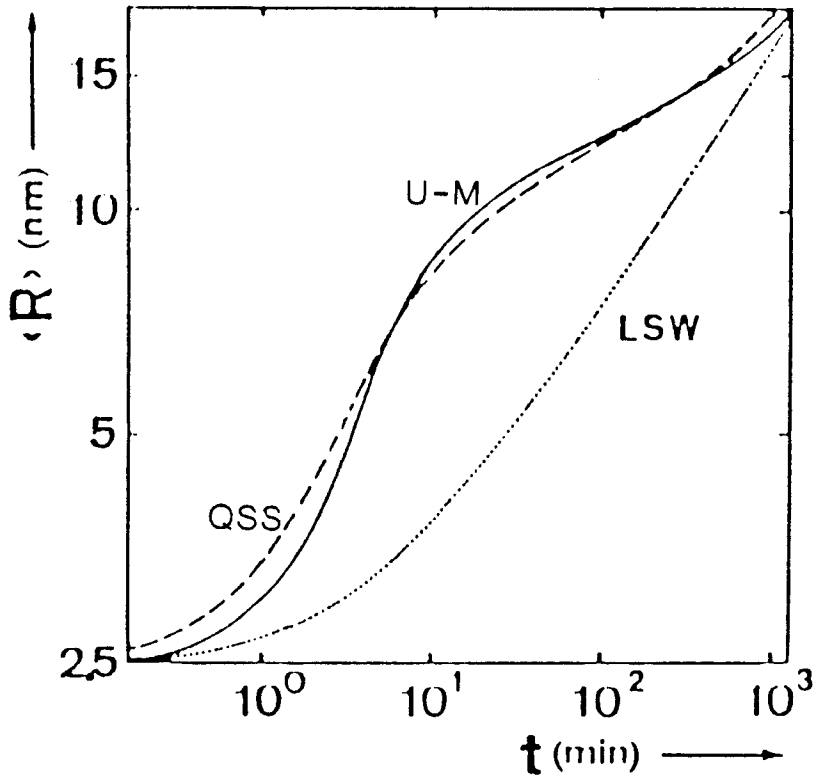

Fig.III-8 The mean particle radius as a function of aging time. (29)

replacements during cascade and point defect production, and (b) the ordering facilitated by the migration of vacancies and interstitials. Schulson[57] has reviewed the experimental observation of both these precesses.

The detailed kinetics of the processes have been modeled by Liou and Wilkes.[58] The rate of change of the order parameter, S, is the sum of the irradiation disordering and radiation-enhanced thermal ordering rates. Under constant flux and temperature, S will approach a steady state value which will not exceed the equilibrium value for that temperature. The effect of decreased order in ordered precipitate phase will be to raise the free energy over the equilibrium value. The free energy increase will change the compositions that result from the local approach to equilibrium at the particle:matrix interface, as shown in Fig.III-9. The ordered β phase is in equilibrium with α phase of composition C_A. If β is partially disordered to a state of higher free energy, β', local approach to equilibrium will tend toward a matrix composition of C_A'. If the alloy composition is between C_A and C_A', the precipitate will be dissolved. In the extreme case, the disordered state (e.g., β''phase) may have such

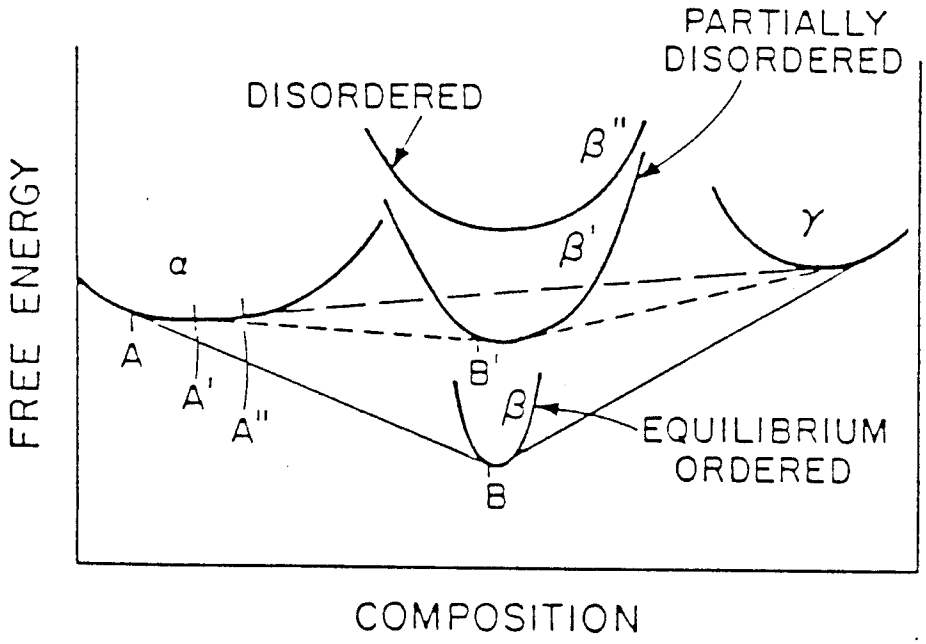

Fig.III-9 Schematic free energy diagram for alteration of particle solubility and stability by irradiation disordering. (58)

a high free energy that the phase does not form at all (or completely dissolves) and the next phase (γ) may appear and the solute concentration in the matrix would approach C_A''.

The effect of irradiation on the stability of ordered phases may also be illustrated by Fig.III-10. It shows the Ti-Ru phase diagram under thermal equilibrium condition and irradiation. Irradiation destabilizes the ordered TiRu phase; at low temperatures, it disappears and is replaced by the other phases (i.e., ε, ε', β).

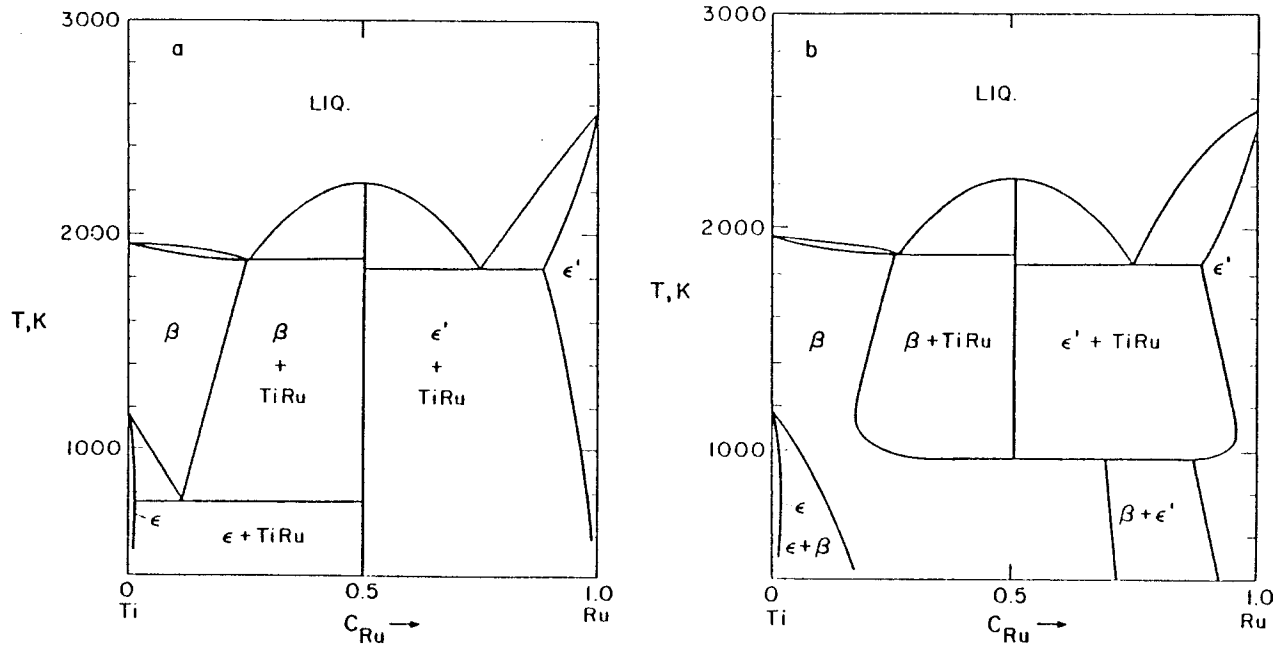

Fig.III-10 The Ti-Ru phase diagram as a function of temperature: (a) as calculated at equilibrium; (b) as modified by a dose rate of 10^{-7} dpa/s, using a dislocation of 10^{11} cm^{-2} as the only sinks. (58)

REFERENCES FOR CHAPTER III

1. J. L. Brimhall, D. R. Baer, and R. H. Jones, J. of Nucl. Mater. 103&104 (1981) 1379-1384.

2. J. L. Brimhall, D. R. Baer, and R. H. Jones, "Radiation Induced Phosphorus Segregation in Austenitic and Ferritic Alloys", PNL Report.

3. E. A. Little and L, P. Stoter, in Effects of Radiation on Materials: 11th Conf., H. R. Brager and J. S. Perrin (Eds.) ASTM-STP-782 (1982) 207-233.

4. D. S. Gelles and L. E. Thomas, "Microstructural Examination of HT-9 and 9Cr-1Mo Contained in the AD-2 Experiment", ADIP report DOE/ER-0045/8 (1982) 343-362.

5. W. G. Wolfer and L. K. Mansur, Phys. Status Solid. 37A (1976) 211-222.

6. L. K. Mansur and W. G. Wolfer, J. of Nucl. Mater. 69&70 (1978) 825-829.

7. P. R. Okamoto and L. E. Rehn, J. of Nucl. Mater. 83 (1979) 2-23.

8. T. R. Anthony, in Radiation-induced Voids in Metals, USAEC (1972) 631-646.

9. V. K. Sethi and P. R. Okamoto, in Phase Stability During Irradiation, J. R. Holland, L. K. Mansur, and D. I. Potter (Eds.), TMS-AIME (1981) p.109.

10. W. G. Wolfer, F. A. Garner, and L. E. Thomas, in Effects of Radiation on Materials: 11th Conf., ASTM-STP-782 (1982) p.1023.

11. P. R. Okamoto and H. Wiedersich, J. of Nucl. Mat. 53 (1974) 336-345.

12. H. G. Haubold and D. Martinsen, J. of Nucl. Mater.

69&70 (1978) 644-649.

13. R. A. Johnson and N. Q. Lam, Phys. Review 13B, No.10 (1976) 4364-4375.

14. R. A. Johnson and N. Q. Lam, Phys. Review 15B, No.4 (1977) 1794-1800.

15. R. A. Johnson and N. Q. Lam, J. of Nucl. Mater. 69&70 (1978) 424-433.

16. P. R. Okamoto, L. E. Rehn, and R. S. Averback, J. of Nucl. Mater. 108&109 (1982) 319-330.

17. N. Q. Lam, P. R. Okamoto, and R. A. Johnson, J. of Nucl. Mater. 78 (1978) 408-418.

18. A. D. Marwick, J. of Phys. F; Metal Phys. 8 (1978) 1849-1861.

19. H. Wiedersich, P. R. Okamoto, and N. Q. Lam, J. of Nucl. Mater. 83 (1979) 98-108.

20. J. R. Manning, Diffusion Kinetics for Atoms in Crystals, J. Van Nostrand, Princeton (1968).

21. N. Q. Lam, A. Kumar, and H. Wiedersich, in Effects of Radiation on Materials: 11th Conf., ASTM-STP-782 (1982) 985-1007.

22. L. E. Rehn, P. R. Okamoto, D. I. Potter, and H. Wiedersich, in Effects of Radiation on Structural Materials, ASTM-STP-683 (1979) 184-193.

23. P. R. Okamoto, S. D. Harkness, and J. J. Laidler, American Nucl. Soc. Trans. 16 (1973) p.70.

24. J. A. Hudson, J. of British Nucl. Energy Soc. 14, No.2 (1975) 127-136.

25. P. Wilkes, J. of Nucl. Mater. 83 (1979) 166-175.

26. K. C. Russell, J. of Nucl. Mat. 83 (1979) 176-185.

27. A. Wolfenden, J. R. Holland, R. G. Lott, and J. A. Spitznagel, in Phase Stability During Irradiation, TMS-AIME (1981) P.383.

28. K. C. Russell, Progress in Material Science 28 (1984) 229-434.

29. H. J. Frost and K. C. Russell, in Phase Transformations and Solute Redistribution in Alloys During Irradiation, F. V. Nolfi, Jr, (Ed.) Applied Sci. Pub., England (1983) 75-113.

30. E. H. Lee, P. J. Maziasz, and A. F. Rowcliffe, in Phase Stability During Irradiation (1981) p.191.

31. Y. Adda, M. Beyeler, and G. Brebec, Thin Solid Films 25 (1975) 107-156.

32. G. Martin, Phil. Mag. 38A (1978) 131-140.

33. P. Wilkes, K. Y. Liou, and R. G. Lott, Rad. Eff. 29 (1976) 249-251.

34. H. Yamauchi and D. de Fontaine, In Phase Stability During Irradiation, TMS-AIME (1981) 73-85.

35. R. Cauvin and G. Martin, J. of Nucl. Mater. 83 (1979) 67-78.

36. S. I. Maydet and K. C. Russell, J. of Nucl. Mater. 64 (1977) 101-114.

37. G. Martin, J. L. Bocquet, A. Barbu, and Y. Adda, in Radiation Effects in Breeder Reactor Structural Materials, AIME (1977) 899-915.

38. R. Cauvin and G. Martin, Phys. Rev. 23B, No.7 (1981) 3322-3332.

39. R. Cauvin and G. Martin, Phys. Rev. 23B, No.7 (1981) 3333-3348.

40. G. Martin, Phil. Mag. 32 (1975) 615-627.

41. G. Martin, Phys. Rev. 21B (1980) 2122-2130.

42. F. A. Garner, H. R. Brager, R. A. Dodd, and T. Lauritzen, "Ion-Induced Spinodal Decomposition in Fe-Ni-Cr Invar Alloys", presented at the 1985 TMS-AIME Fall Meeting Irradiation Effects Associated with Ion Implantation, Toronto, Canada (1985).

43. R. A. Dodd and F. A. Garner, "Spinodal-like Decomposition Induced by Ion Irradiation in Simple Fe-Ni and Fe-Ni-Cr Alloys", to be presented at the 13th Intern. Symps. on the Effects of Radiation on Materials, Seattle, WA (1986) ASTM.

44. K. Krishman and C. Abromeit, J. of Phys. F; Metal Phys. 14 (1984) 1103-1116.

45. R. S. Nelson, J. A. Hudson, and D. J. Mazey, J. of Nucl. Mater. 44 (1972) 318-330.

46. A. D. Brailsford, J. of Nucl. Mat. 91 (1980) p.221.

47. H. J. Frost and K. C. Russell, J. of Nucl. Mater. 103&104 (1981) 1427-1432.

48. H. J. Frost and K. C. Russell, Acta Metall. 30 (1982) 953-960.

49. R. H. Jones, J. of Nucl. Mater. 74 (1978) 163-166.

50. C. F. Bilsby, J. of Nucl. Mat. 55 (1975) 125-133.

51. C. Wagner, Z. Elektrochem 65 (1961) p.581.

52. I. M. Lifshitz and V. V. Slyozov, Phys. Chem. Solids 19 (1961) 35-50.

53. M. Baron, A. Chang, and M. L. Bleiberg, in Radiation Effects in Breeder Reactor Structural Materials, AIME (1977) 395-404.

54. M. Baron, in Phase Stability During Irradiation, TMS-AIME (1981) 63-72.

55. K. Urban and G. Martin, Acta Metall. 30 (1982) 1209-1218.

56. K. Urban and G. Martin, in Proc. of an Inter. Conf. on Solid-Solid Phase Transformation H. I. Aaronson, D. E. Laughlin, R. F. Sekerka and C. M. Wayman (Eds.) TMS-AIME (1983) 317-322.

57. E. M. Schulson, J. of Nucl. Mater. 83 (1979) 239-264.

58. K. Y. Liou and P. Wilkes, J. of Nucl. Mater. 87 (1979) 317-330.

CHAPTER IV

REVIEW OF PREVIOUS STUDIES OF IRRADIATION EFFECTS IN FERRITIC STEELS

Ferritic steels are of interest in the nuclear community for use in pressure vessels and steam generators, piping, core structures in light water reactors and breeder reactors, and first walls and blankets material in fusion reactors. As a result, a number of research programs and design studies are currently in progress to evaluate these materials. Recently, two conferences related to the application of ferritic steels in nuclear power systems have been held.[1,2] A great deal of research was presented in the conferences. In the past few years, several review papers were also published discussing the thermal properties and irradiation effects and applications of ferritic steels in fusion,[3-7] fast breeder,[8,9] and thermal reactors.[10-12]

A major concern for any nuclear structural design is the potentially high irradiation induced swelling that can

lead to large dimensional changes, high stress levels, and eventually even to failure. The swelling resistance of ferritic steel is the one major reasons that researchers have switched from austenitic steels to ferritic steels. Fig.IV-1 illustrates the swelling versus dpa curves of several commercial alloys.[3] It is clearly seen that ferritic steels have the best swelling resistance among these alloys up to 100 dpa and have more than an order of magnitude better swelling resistance than austenitic steels.

There are many other things that need to be investigated before the applications of ferritic steels in various reactors can actually proceed. For example, the irradiation-induced mechanical property changes, creep resistance, microstructural evolution, gas effects (especially hydrogen and helium), corrosion (both liquid metal and aqueous corrosion), and weldability. A detail review of microstructural evolution (including void swelling, precipate evolution, and loop analysis) will be discussed later in this chapter. Before the review of microstructures is given, the basic thermodynamics of iron and ferritic steels and the physical metallurgy of various

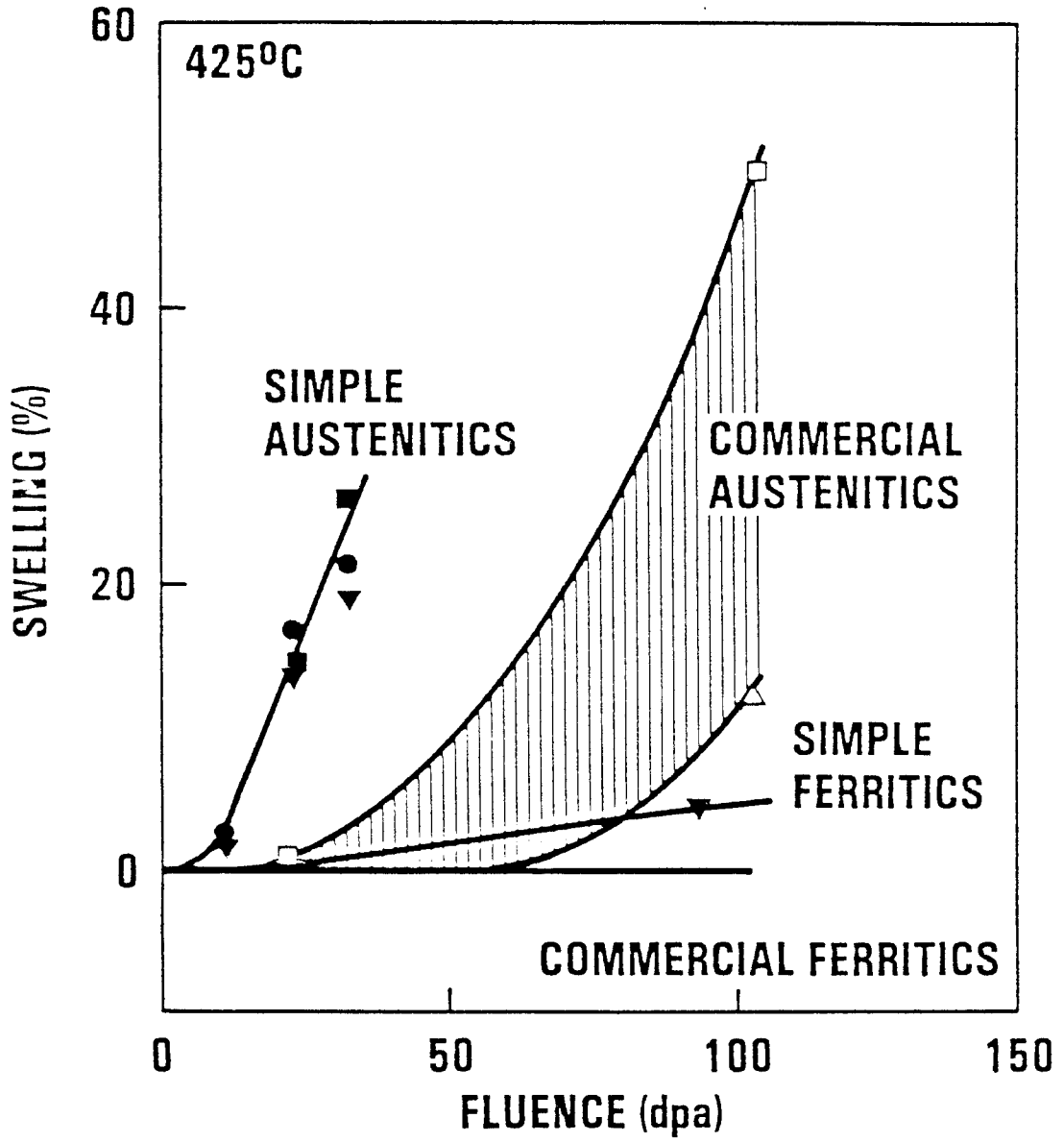

Fig.IV-1 A comparison of the swelling behavior of several commercial and simple ferritic steels to austenitic steels. (3)

steels will be presented.

IV.A Thermodynamics of Iron and Ferritic Steels

A study of the constitution and structure of all steels must first start with the iron-carbon equilibrium phase diagram. Fig.IV-2 gives the iron-carbon diagram after Hansen.[14] Many of the basic features of this system influence the behaviour of even the most complex alloy steels. For example, the phases found in the simple binary Fe-C system persist in complex steels, but it is necessary to examine the effects that alloying elements have on the formation and properties of these phases (i.e., austenite, ferrite, cementite, etc.) The constitution of steels with the effects of nickel and chromium and their equivalent elements is shown in Fig.IV-3,[15] which is known as Schaeffler diagram and modified by Schneider. The chromium and nickel equivalents are:

$$\begin{aligned} Cr &= [Cr] + 2[Si] + 1.5[Mo] + 5[V] + 5.5[Al] \\ &\quad + 1.75[Nb] + 1.5[Ti] + 0.75[W] \\ Ni &= [Ni] + [Co] + 0.5[Mn] + 0.3[Cu] \\ &\quad + 25[N] + 30[C] \end{aligned} \qquad \text{(IV-1)}$$

where the brackets indicate the wt% of the alloy elements.

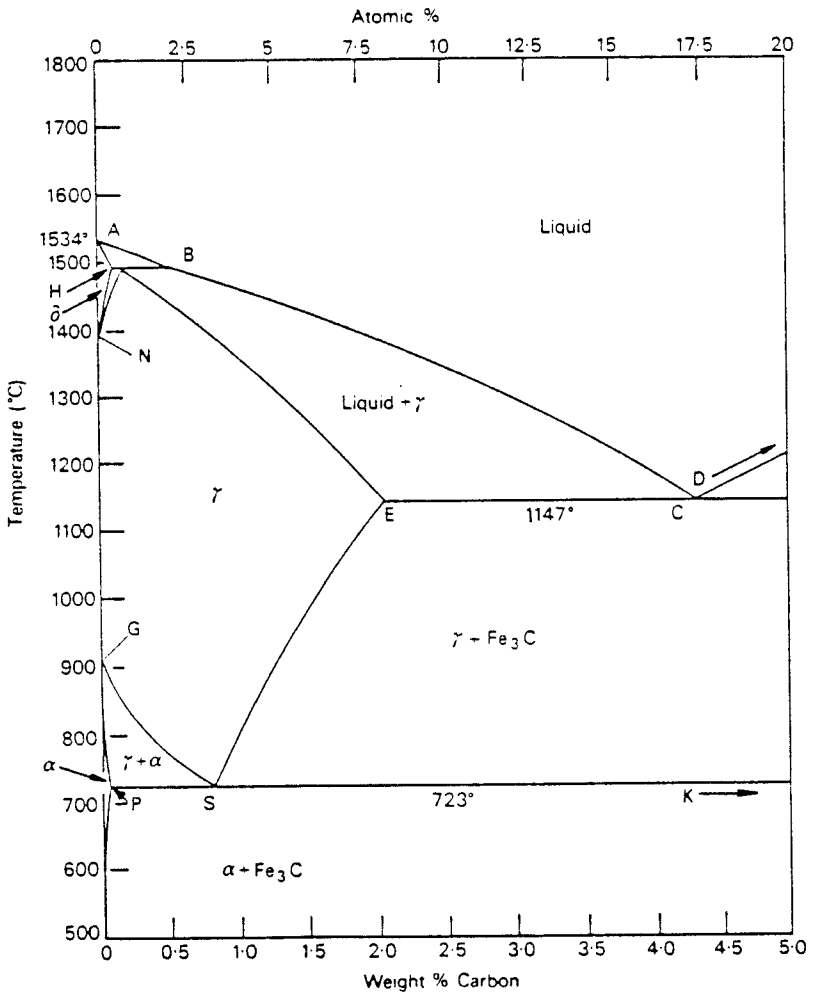

Fig.IV-2 The iron-carbon phase diagram. (14)

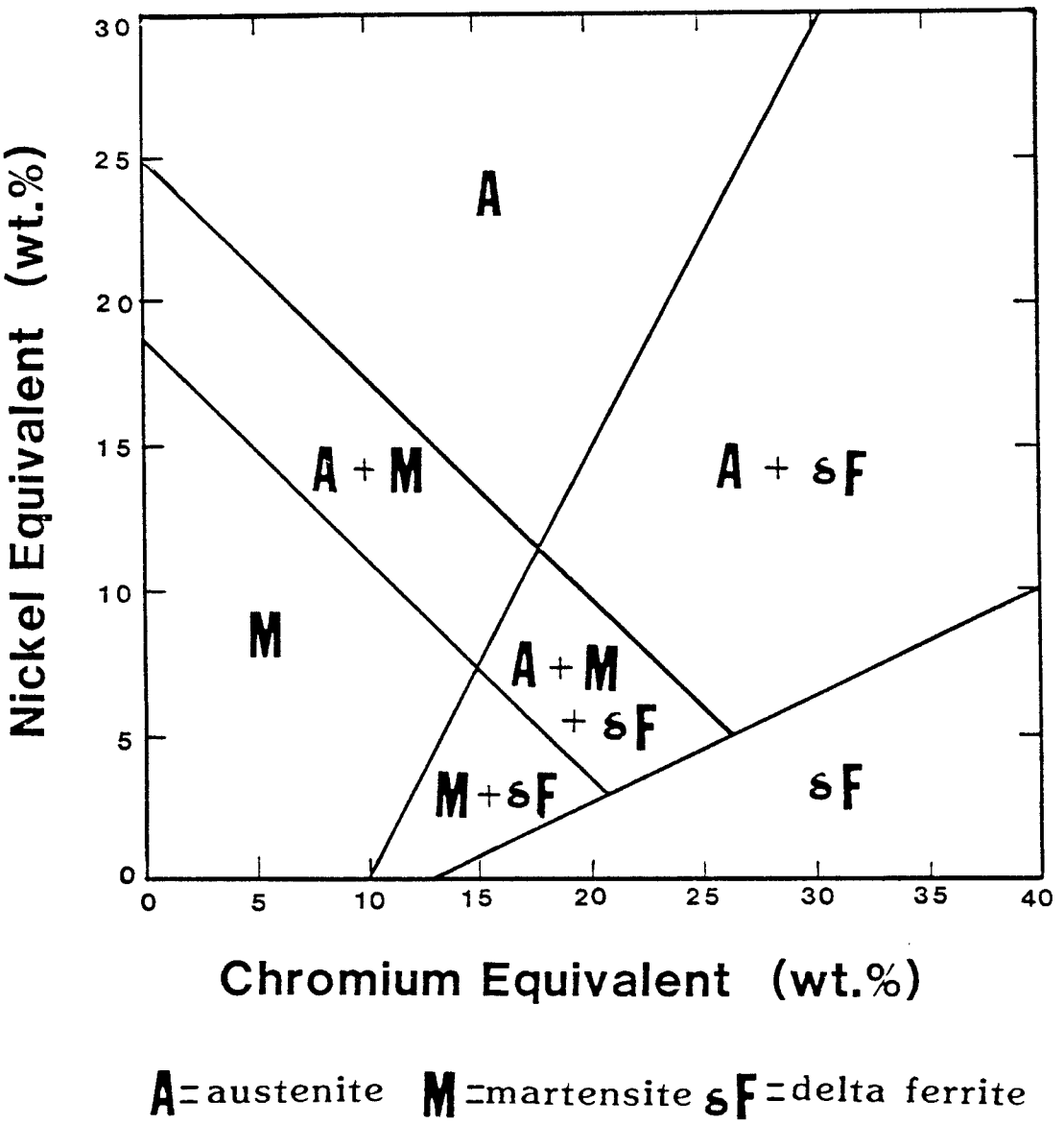

Fig.IV-3 Schaeffler diagram indicating the effect of Ni and Cr equivalents on the constitution of stainless steels. (15)

The chromium-molybdenum alloy steels are sometimes called by the generic title -- ferritic creep resisting steels (ferritic steels), but few contain recognizable ferrite in the optical microstructures.[11] This term derives from the fact that, on cooling from austenite, transformation can occur over a range of temperatures to structures which have essentially a body centered cubic lattice. The various structures which may appear individually, or more often, in combination are polygonal ferrite, bainite, and martensite. Since this research is concentrated in HT-9 ferritic steel, it is important to understand the transformation from austenite to other phases.

The transformation from austenite to other phases is very sensitive to the continuous cooling rate and the chemical composition. Davenport and Bain[16] first introduced the isothermal transformation approach, and showed that by studying the reaction isothermally at a series of temperatures below the Ae_1, a characteristic time-temperature-transformation (TTT) curve can be obtained for each particular steel. Fig.IV-4 shows a group of typical TTT diagrams of several steels.[17,18] It is clearly seen that the alloy elements affect the nose of

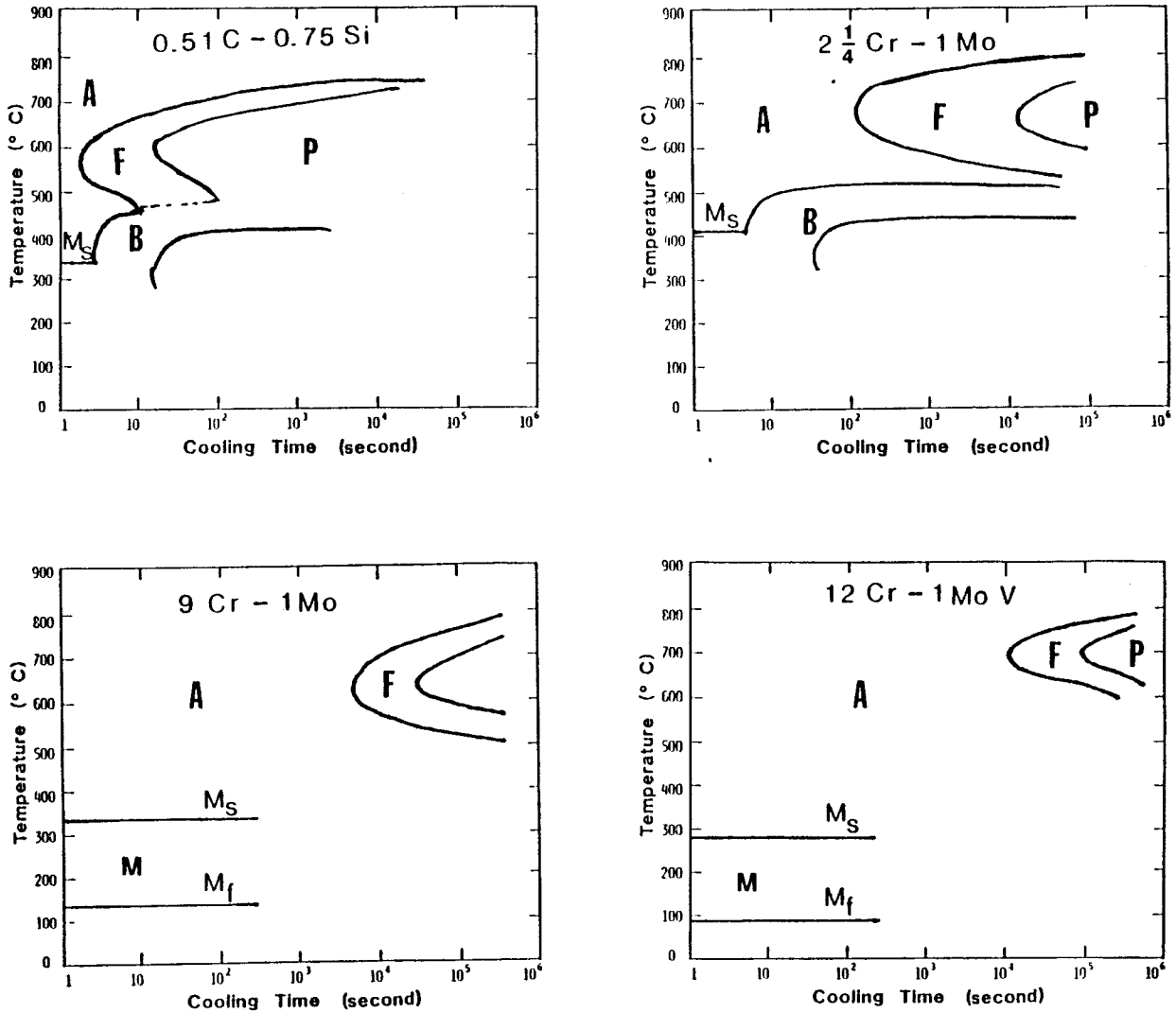

Fig.IV-4 The time-temperature-transformation (TTT) diagram of several ferritic steels. (17,18)

the C-curve and push the nose farther back with higher concentration of alloy elements. Therefore, in high alloy steels (e.g., HT-9), the cooling rate to form martensite is not as critical as in low alloy steels (e.g., 2 1/4 Cr-1 Mo).

B. The Physical Metallurgy of Ferritic Steels

There have been many investigations of the microstructure and physical properties of ferritic steels during past 30 years. Several review papers [11,12,13,19-23] have discussed the strengthening mechanisms, precipitation reactions, and alloy elements effects in microstructure and physical properties.

The strengthening mechanisms described by Kelly and Nutting[20] included work hardening, precipitate and dispersion hardening, grain-size hardening, solution hardening, martensitic hardening, and radiation hardening. However, with respect to reactor design, the precipitate and dispersion hardening is the most important mechanism due to the elevated temperature creep resistance requirement. The structure, composition, and morphology of many precipitates in ferritic steels are very

complicated and although they have been extensively studied, many problems still remain. Goldschmidt[24] found that, in general, the binary carbides could be divided into three classes of structure: (a) cubic system, e.g., $Cr_{23}C_6$, VC; (b) close packed hexagonal, e.g., Mo_2C; (c) orthorhombic, e.g., Fe_3C, Cr_7C_3. However, in steels, the pure binary carbides do not generally occur as there is always some solubility of most of the alloying elements in the various carbide phases; in some cases these solubilities may be very extensive. It is usual to refer to the carbides by general formulae, e.g., $M_{23}C_6$, MC, where M indicates a mixture of metal atoms. Often the carbides are stable over an appreciable composition reange, i.e., they are not stoichiometric, and the general formulae should be regarded as represnting certain structural types rather than specific chemical species. In addition, there is sometimes an appreciable solubility for nitrogen; this is particularly true of the cubic carbides with formula of MC and the hexagonal carbides of formula M_2C, for which there are usually isomorphous nitrides and where the carbides and nitrides show complete intersolubility. In such cases, it is better to refer to

compounds as MX and M_2X, respectively.

In summary of the work performed by several research groups, [11,21,22,140] the general carbide sequences formed in ferritic steels during tempering are shown in Fig.IV-5. There are also other researchers[26-31] who have discussed the transformation of carbides in chromium, vanadium, molybdeium, and tungsten steels. The results are presented in the Table IV-1 and they fall into the same category of the Fig.IV-5.

In studying the precipitation reactions of 12% Cr steels, Irvine et al.[32] examined the effects of alloy elements on various properties of these steels. Koutsky and Jezek[33] found Laves phase in addition to carbides and stated that the precipitation of the Laves phase was of decisive importance for increased heat resistance of these steels. Vitek and Klueh[34] studied the effects of heat treatments on HT-9 ferritic steel with an analytical electron microscope and a EDS system. Their work revealed the qualitative chemical composition of various carbides.

Smith[35] studied the chromium-vanadium steels with molybdenum added and derived the equilibrium carbide diagrams. Fig.IV-6 shows the equilibrium carbides in

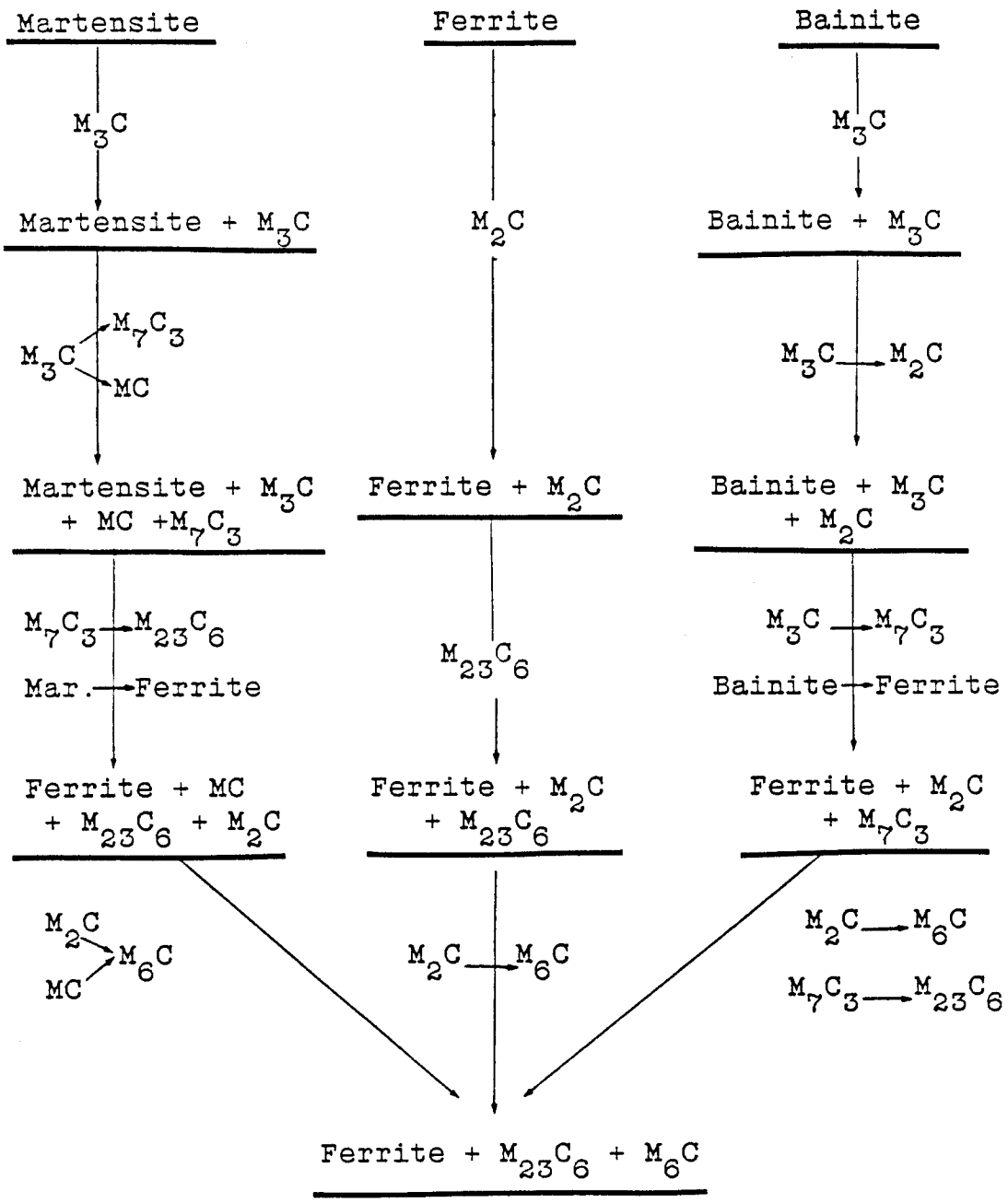

Fig.IV-5 Precipitate evolution of ferritic steels following thermal annealing. (11,21,22,140)

Table IV-1 Summarization of precipitate response in various alloy steels

(a) Chromium steels

$$Fe_2C \longrightarrow Fe_3C \longrightarrow Cr_7C_3 \longrightarrow Cr_{23}C_6$$

in the presence of nitrogen the sequence may become

$$Fe_2C \longrightarrow Fe_3C \longrightarrow Cr_7C_3 \longrightarrow Cr_2X \longrightarrow Cr_{23}C_6$$

(b) Molybdenum or tungsten steels

$$Fe_2C \longrightarrow Fe_3C \longrightarrow Mo_2C \text{ or } W_2C \longrightarrow M_6C$$

(c) Vanadium steels

$$Fe_2C \longrightarrow Fe_3C \longrightarrow V_4C_3 \longrightarrow M_6C$$

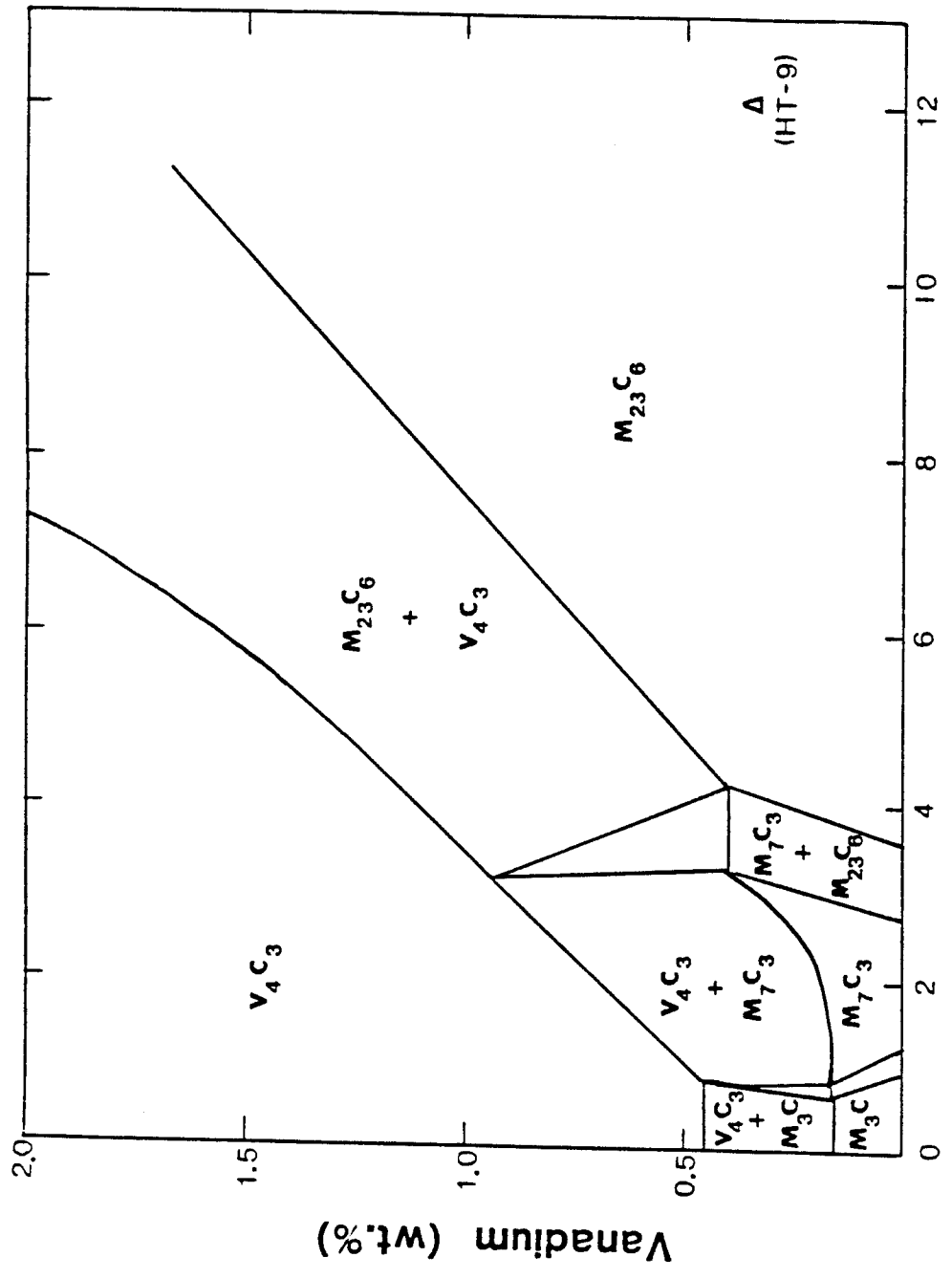

Fig.IV-6 Equivalent carbides in 0.2%C, 1.0%Mo, Cr-V steels after thermal annealed at 700° C for 2000 h. (35)

0.2C-1.0Mo Cr-V steels at 700° C. As pointed out by Smith[35] in Cr-V steels the sequence of carbides formed during tempering is simply that found along a line drawn from the origin to the steel composition on the equilibrium diagram. Therefore, a steel such as HT-9 (containing 12Cr-0.3V-1.0Mo-0.2C), during tempering, would form M_3C, VC, M_2X, M_7C_3, and $M_{23}C_6$ carbides in sequence or a combination of these phases. Maziasz et al.[187] examined the microstructures of 2% Ni-doped HT-9 after similar heat treatment and found that the additional nickel had no major effect on the phase identity or chemical composition of precipitates compared to that of 'normal' HT-9.

The evolution of precipitates in several other ferritic and martensitic steels has also been studied in detail (such as 9Cr-1Mo steel[34,187] and 2 1/4Cr-1Mo steel[36,37]). A similar precipitate sequence as stated in Fig.IV-5 was found in both of these steels.

Irvine[38] studied the precipitation hardening in commercial steels in order to provide a background for practical heat treatments. Tekin et al.[39] and Irvine[38] also investigated the secondary hardening of

vanadium steels and molybdenum steels. Grobner[40] and Jacobsson et al.[41] studied the 475° C embrittlement in ferritic steels and found that was caused by precipitation of a chromium-rich ' phase on dislocations.

There are also many studies centered on microstructure-property correlations, weldability and properties of the heat affected region, corrosion and compatibility, and creep strength of ferritic steels. Because the interest of this research is HT-9, the review on these topics will be concentrated in 12% Cr steels rather than other ferritic steels.

In general, ferritic steels have a good stress corrosion resistance[42] in sodium or water compared to austenitic steels. However, they do corrode when in contact with water or steam at high temperatures.[43] In a flowing lithium environment, the results of fatigue life of HT-9 decreases with an increase in nitrogen content in lithium.[44] The reduction in fatigue life in high-nitrogen lithium is attributed to an internal corrosion attack of the HT-9 ferritic steel.

The mechanical strength of 12Cr-1Mo ferritic and martensitic steels is comparable to austenitic steels at a

temperature up to 500° C.[45] Several studies have measured the effects of heat treatment on the microstructures and properties of 12Cr-1Mo ferritic steels.[45-51] Little et al.[45,46] concluded that the minor elements in commercial 12Cr ferritic steels, such as V, W, Nb, accentuate secondary hardening and retard overaging primarily by inhibiting the annealing of dislocations. Lechtenberg[47] stated that the tempered martensite embrittlement (HT-9 tempered at 350° C) is due to retained austenite films arround martensite laths decomposing to carbides which act as crack nucleators. However, Edward and Little[48] found that the peak DBTT (ductile-brittle transition temperature) of 12Cr steels occured at a tempering temperature of 500° C which is the temperature for the M_7C_3 and M_2X to $M_{23}C_6$ carbide transformation. Therefore, the authors suggested that the precipitation reaction was responsible for the embrittlement. Chin and Wilcox[49] found that the DBTT of 12Cr-1MoVW steels (HT-9) could be improved be as much as 50° C through heat treatment (i.e., combining a high temperature austenitization with a moderate temperature age). The heat treatment dissolves both the interfacial

carbide particles and the δ-ferrite yielding the highest strength. However, other works showed that the formation of δ-ferrite decreased the creep resistance at elevated temperature applications, and the best heat treatment for fatigue crack growth resistance is a moderate temperature austenitization with a high temperature age (1038° C for 5 min. + AC, and 780° C for 2.5 hours + AC).[50] The discrepancy between studies shows that more work is needed in this area.

In studying the thermal creep strength of 12% Cr steels, Hede and Aronsson[52] found that the creep strength improved dramatically at higher temperature (500 to 600° C) by adding strong carbide formation elements (such as Mo, V, W, Nb). They also found the evidence of fine carbides interacting with dislocations and attributed the loss of creep strength due to the coalescence of fine carbides at higher temperatures. Egnell and Persson[53] reported that a small amount of tungsten can make a great deal of difference in creep strength of 12% Cr steels. Oakes et al.[54] proved that additions of 0.5% W into 12% Cr steel greatly increases the creep rupture strength at temperatures up to 650° C. Other studies[55,56] showed

that, by adding more nickel into 12% Cr steels, the impact properties at room temperature can be improved and the DBTT can be reduced. However, the disadvantage of adding more nickel can be a decrease of strain at failure and the creep rupture strength at high temperatures.

Hydrogen embrittlement is also a major concern for the application of 12% Cr steels in fusion reactor environment. Garrison et al.[57-59] found that brittle intergranular fracture was the primary fracture mode in hydrogen charged HT-9. This hydrogen embrittlement effect could be reduced significantly by cold-working and re-tempering the original quenched-and-tempered microstructure.[59] Jones and Thomas[60], in addition, pointed out that the decrease in the intergranular fracture toughness in hydrogen charged HT-9 could be correlated with the phosphorus and sulfur concentrations in the grain boundary.

In industry applications, workability of a material is very important in determining the usefulness of the material. For ferritic steels, it is noted that the higher the chromium content, the more difficult are the problems of weldability of the steels.[61]

A substantial amount of research in studying the weldability of HT-9 is being conducted.[62-65] An untempered martensite has been usually found in weld heat affected zones (HAZ) which limits the service usefulness of the material; as a result, a postweld heat treatment must be normally employed to restore the properties of HAZ. Foulds et al. [63,64] reported the thermal histories of the various HAZs during gas tungsten arc (GTA) welding of HT-9 and also examined the microstructures of the weld metal, the HAZs, and the base metal. Lippold[65,66] found that with a proper postweld heat treatment (such as, at 760° C for 1 hour) the toughness of the individual HAZ was superior to that of the original base metal. However, Huang and Gelles[67] reported that even after postweld heat treatment (at 780° C for 1 hour), the tearing modulus of welds was still lower than that of base metal (HT-9) indicating that the alloy has less resistance to crack propagation as a result of welding. Odette et al.[68], on the basis of a Ritchie-Knott-Rice [69] cleavage fracture model, have determined the fundamental micromechanism of fracture is a critical tensile stress operating over a critical microstructural distance and found that the

critical microcleavage fracture stress was controlled by the martensite lath size and the critical distance appeared to be controlled by the prior austenite grain size. These observations pointed to the important role of microstructure in the fracture behaviour.

C. Radiation Effects in Ferritic Steels

In this section, a review of previous experimental radiation damage studies on ferritic steels is presented. Because of the specific interest of this research, the review will emphasize the studies of 12% Cr steels and the studies of other steels which contain detailed microstructural analysis. For convenience, the section will be divided into several subsections including void swelling studies, dislocation loop studies, solute segregation and phase stability experiments, and post-irradiation mechanical property studies.

C.1. Void Swelling Studies

In 1969, Kulcinski et al.[70] reported the first observation of voids in neutron-irradiated pure iron (99.999%). They concluded that voids might form in high

purity iron at fluences less than $3X10^{25}$ n/m^2 ($E>0.1$ MeV) at proper temperatures ($0.3T_m<T<0.5T_m$). The reported void morphology was a truncated octahedron with {110} planes as both the facets and truncations. The 0.12% swelling was relatively low compared to other metals.[70] The void distribution was homogeneous within the grains with a wide denuded zone (about 1 um) at grain boundary. However, Farrell and Houston[71] found a heterogeneous void distribution along the sites of the original grain boundaries in the same pure iron irradiated with neutrons. The discrepancy of these two experiments might come from the irradiations were conducted at different reactors (EBR-II vs. HFIR) or the pre-irradiation heat treatment (Kulcinski et al. pre-annealed the iron at 800^{o} C for 2 hours).

Since these initial investigations, a considerable amount of effort has been devoted to study the void formation in iron and ferritic steels following neutron[72-96], ion[73,97-100,104-115], or electron[100-103,115,116] irradiation.

The damage levels of the void formation studies of pure iron[72-74,78,103-105,109] have ranged from less than

1 dpa up to 50 dpa in the temperature range between 275 and 615^{o} C (usually, in neutron irradiation, 1 dpa roughly equals to 2X10^{25} n/m^{2} with E>0.1MeV). The peak swelling that was found in all studies was equal to or less than 1%. The swelling rate is estimated less than 0.1%/dpa which is an order of magnitude lower than that of austenitic steels.[3] The peak swelling temperature is around 400^{o} C for neutron irradiations [74,78] and about 500^{o} C for ion irradiations.[104] Although the total swelling might not have linear relationship with dose levels in different studies, the overall low swelling characteristics showed a superior swelling resistance of pure iron.

Smidt et al.[73] studied the effect of minor elements on void swelling in pure iron and showed that small solute additions could greatly influence the damage produced. With a 0.3% V addition to pure iron, the void nucleation was completely suppressed at damage level up to 32 dpa in ion irradiations and up to 5.5 dpa in neutron irradiations. In contrast, the addition of 0.3% Ni in Fe can increase the swelling during neutron irradiation by a factor of two or more.

Several studies[77-80,108-112,115] of the swelling behaviour in irradiated simple Fe-Cr binary alloys were published recently (both in neutron and ion irradiations) in order to obtain the fundamental information on the factors responsible for the swelling resistance of ferritic alloys. Little and Stow[77,78] examined a series of Fe-Cr binary alloys irradiated in the temperature range between 380 and 615° C to a fluence of about 30 dpa. The peak swelling temperature was 420° C with a peak swelling less than 1% at 30 dpa. The lowest swelling was observed for Fe-5%Cr alloy. Gelles and co-workers[79,80] investigated a different series of Fe-Cr alloys which were irradiated in EBR-II over the temperature range 400 to 650° C and up to a fluence of 100 dpa. The peak swelling temperature was about 425° C and the peak swelling rate was about 0.06%/dpa. The lowest swelling was observed for Fe-3%Cr alloy at lower damage level (about 20 dpa). Fig.IV-7 shows the swelling measurements as a function of alloy chromium content in neutron irradiations.[79]

Johnston et al.[108] examined Fe-15%Cr alloy irradiated with 5 MeV nickel ions to a fluence of 116 dpa. The peak swelling temperature was centered at about 550° C

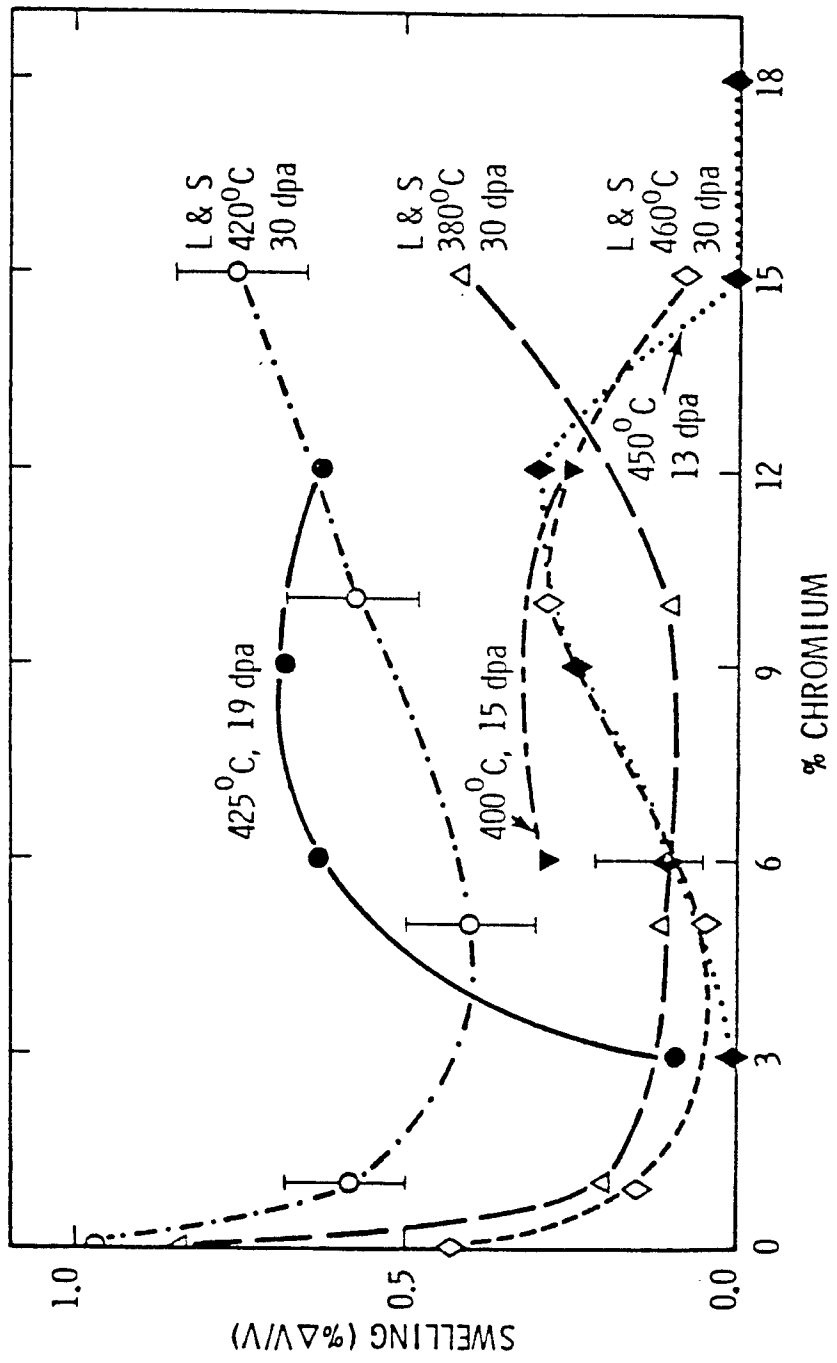

Fig. IV-7 Comparison of swelling measurements as a function of alloy Cr content in Fe-Cr simple ferritic steels. (79)

and the swelling rate was about 0.1%/dpa. Horton et al.[109,112] studied triple beam ion irradiated Fe-10%Cr up to a fluence of 10 dpa in order to simulate the fusion reactor environment. The swelling was about 0.03% per dpa at irradiation temperature of 575° C. The cavities observed in the specimen bombarded with only heavy ions were larger and had a lower concentration than the cavities in the specimens bombarded with triple beam ions. Ohnuki et al.[111,115] examined Fe-10%Cr and Fe-13%Cr alloys irradiated by 200 KeV carbon ions up to 114 dpa over the temperature range 475 to 575° C and found that the void swelling in all specimens was less than 1%.

Recently, more detailed investigations of several commercial ferritic and martensitic steels have been studied. These commercial alloys are mainly Cr-Mo steels which include 12Cr-1MoVW (HT-9)[88-102], 2 1/4 Cr-1Mo[85,86,95,106,107], 9Cr-1Mo[84,87,91,93,95,113,114], and other steels (H-11, EM-12, 13Cr-1Mo, etc.)[75,76,81-83,90,95,97,116,117] With few exceptions of these studies,[97,101,102,116] the total swelling in all irradiation conditions of every commercial ferritic and martensitic alloys are very low (usually less than 1%

of total volume).

Huet et al.[75,76] examined 13Cr-Mo-Ti alloys irradiated by fast neutrons up to 25 dpa and found the peak swelling is about 0.5% at 425° C. Gelles[82,83,95] and Powell et al.[81] examined five commercial ferritic alloys: 2 1/4Cr-1Mo, H-11 (5Cr-1Mo), EM-12 (10Cr-2Mo), AISI 416, and AISI 430F, which were irradiated in EBR-II over the temperature range of 400 to 650° C and to a peak fluence of 125 dpa. The maximum swelling observed was about 0.6% in EM-12 at 400° C. Gelles and co-workers[85,86,95] also examined neutron irradiation 2 1/4Cr-1Mo steel irradiated over the temperature range of 390 to 570° C to a peak fluence of 116 dpa. Swelling remained below 0.3% for all conditions examined. A maximum swelling was found at the lowest irradiation temperatures (25 dpa at 390° C and 116 dpa at 400° C). A correlation swelling equation was developed for design purpose. The experimental results suggested that the steady-state swelling rate (0.06%/dpa) obtained from simple Fe-Cr alloys experiments[79] was not reached even after 120 dpa irradiation.

In the investigation of swelling behaviour of 9Cr-1Mo

alloy under irradiation, several research groups found similar results in various irradiation conditions. Gelles and Thomas[91,95] found negligible swelling in the material irradiated to 12 dpa at temperature range of 400 to 550° C. Vitek and Klueh[84,93,95] found a maximum swelling about 0.2% at 400° C in the material irradiated to 36 dpa over the temperature range 300 to 600° C. Ayrault[113] irradiated the material with both single and dual-ion over a temperature range of 450 to 600° C up to 25 dpa and found very low swelling (<0.05%) in all samples. Farrell and Lee[114] examined ion irradiated 9Cr-1Mo steel to 100 dpa over a temperature range of 400 to 600° C and found that the peak swelling was less than 0.4% at the irradiation temperature of 500° C. Although Maziasz et al.[87] claimed that increasing the helium production rate in neutron irradiation by using nickel-dopped 9Cr-1Mo steel would increase the swelling dramatically, the overall swelling of this alloy and other commercial ferritic steels is belived would be still low compared to austenitic steels.

During the late 1970s, HT-9 was being evaluated as a candidate material for the first wall and blanket of the

fusion engineering device (FED). Since then, more and more research groups are working on this material. Fig.IV-8 summarizes the swelling results of 12% Cr steels and other ferritic steels.[203]

Gelles and Thomas[91,92,95] examined HT-9 following irradiations in EBR-II at 400 to 650° C to a peak fluence of 70 dpa and found that the maximum swelling was about 0.2% at the 400° C irradiation. Gelles and Thomas[96] also compared the differences in swelling behaviour following irradiations in EBR-II and HFIR and concluded that helium atoms (produced at a much higher rate in HFIR) promoted void swelling in HT-9. Vitek and Klueh[93,94] examined a similar material irradiated in HFIR to 36 dpa at 300 to 600° C and found a 0.2% peak swelling at 400° C. Other researchers[88-90] also reported the same low swelling characteristics of this type material in numerous irradiation conditions.

Only a few ion irradiation experiments of HT-9[97,98] have been reported. Smidt et al.[97] irradiated HT-9 specimens up to around 250 dpa damage level at the peak swelling temperature of 500° C and evaluated a swelling rate of about 0.02%/dpa. Ayrault [98] reported both

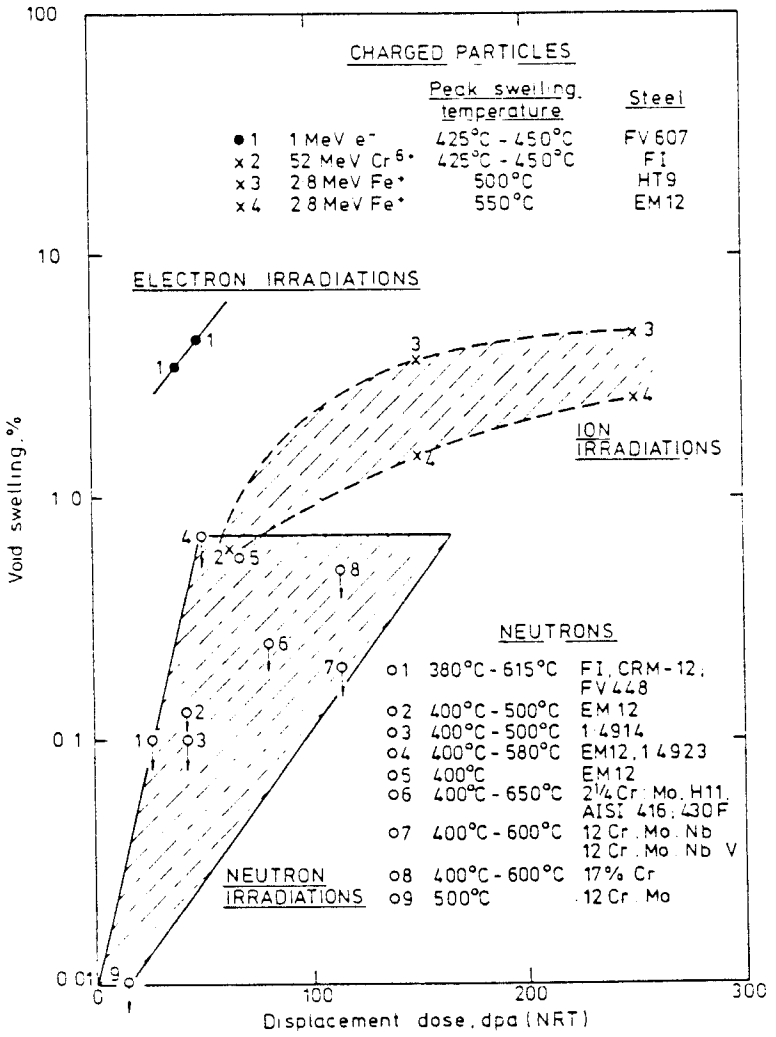

Fig.IV-8 The summary of the void swelling of ferritic steels after irradiation. (203)

single- and dual-ion irradiated HT-9 and HT-9 + 2Ni to 25 dpa and concluded that helium was necessary for promoting void swelling. Ayrault also concluded that excess nickel in HT-9 suppressed the swelling at the peak swelling temperature (470^{o} C) and the total swelling was negligible. Suzuki et al.[100] re-irradiated the dual-ion irradiated HT-9 specimens of Ayrault[98] with 1 MeV high voltage electron microscope (HVEM) and concluded that there was clear evidence of two kinds of cavity growth mechanisms (bias-driven and pressure-driven cavity growth) in ferritic steels. The peak swelling temperature was about 50^{o} C lower than that found in the dual-ion irradiation. This behaviour could be explained by the surface effects of HVEM experiments.

Swelling levels as high as 4% have been observed in HVEM irradiated ferritic steels.[101,102,116] There is apparent no appreciable incubation dose prior to steady-state swelling for 12Cr-1MoVW steels.[101,102] The steady-state swelling rate for electron irradiation was about 0.1%/dpa which was much higher than that found in neutron- or ion-irradiation. The reason for this high swelling of ferritic steels in electron irradiation is not

quite understood. However, Little[102] tried to explain this phenomenon by using his dual loop system arguments[132]. He claimed that electron irradiation resulted in the formation of homogeneous dislocation networks and the rapid nucleation of a high number density of small voids. After the void nucleation process was completed, the dual loop system has occured clearly then failed to suppress swelling. The discrepancy of swelling rate between electron irradiation and ion and neutron irradiations is probably due to the difference of the displacement coefficient factor between them. In general, the displacement coefficient factor, in the Kinchin-Pease model, is assumed equal to a constant of 0.8. However, recent experiments and computer calculations have shown that the factor varies strongly with the PKA energy.[201,202] In these studies, it is calculated that the factor is about 0.9 for electron irradiation and is about 0.3 for ion and neutron irradiations. The ratio of this difference might be able to explain the factor of three difference in swelling rate between electron irradiation and ion and neutron irradiations.

In summary, the measured void swelling in ferritic

steels is very low and should not be the critical problem in their use in nuclear reactors. However, helium atoms may play a major role in promoting void nucleation and growth in ferritic steels. Much more work is needed to clarify the latter condition.

C.2 Dislocation Loop Studies

In 1962, Eyre[118] first reported the observation of "black spot" damage in neutron-irradiated iron. For an irradiation temperature of 60^{o} C, the threshold fluence for the formation of observable damage in this study was between $5X10^{22}$ to $1X10^{23}$ n/m^2 ($E>1MeV$). Eyre and Bartlett[120], later on, proved that these black spots were point defect clusters and most probably interstitial in nature. With post-irradiation annealing above 300^{o} C, they found that these black spots grew into dislocation loops with Burgers vector in a$\langle 111 \rangle$ direction and both vacancy and interstitial loops were detected. Eyre and Bullough[121] discussed how the two types of interstitial loops with Burgers vector $b=a/2\langle 111 \rangle$ and $b=a\langle 100 \rangle$, respectively, could form in irradiated bcc metals which had a common loop nucleus on a {110} plane. The

mechanisms are described as followings:

$$a/2[110] + a/2[001] = a/2[111]$$

$$a/2[110] + a/2[110] = a[010] \qquad \text{(IV.2)}$$

Either one of these two shears would transform the a/2‹110› type loops into a/2‹111› or a‹100› type loop, respectively. Since the ‹110› shear requires higher energy, it only occurs at elevated temperature or under irradiation. Bryner[122] and Milasin[123] investigated neutron-irradiated iron under similar conditions as Eyre[118] and observed the similar results. However, Farrell and Houston[71] examined iron irradiated in HFIR at 415^{o} C to a fluence of 1.5X10^{25} n/m^{2} (E›0.1MeV) and found no readily resolvable loops.

Smidt et al.[73] irradiated a group of iron and dilute iron alloys in ATR at 280^{o} C to a fluence of 5X10^{24} n/m^{2} (E›0.1MeV) and observed a high density of small dislocation loops (about 10^{16} #/cm^{3} and 6 nm in diameter). They also irradiated the same group of alloys in EBR-II at 596^{o} C to a fluence of 7.4X10^{25} n/m^{2} (E›0.1MeV) and found a very high number density of loops in Fe-0.3V steel but only few large loops in other alloys. Kayano et al.[128] observed vacancy type dislocation loops with Burgers

vectors corresponding to a/2‹111› on the {111} plane in Fe-N alloy (150 ppm N) irradiated to $5.5X10^{23}$ n/m^2 at the temperature below 250^{o} C and post-irradiation annealing at 300^{o} C for 100 hours. Recently, Horton and co-workers[74,110] reported the most complete study in loop analysis of neutron-irradiated iron. The iron specimens were irradiated in the ORR (Oak Ridge Research Reactor) at temperatures of 180 to 740^{o} C to 1.0 dpa. The dislocation microstructures could be classified into four groups corresponding to four irradiation-temperature ranges. For the lowest temperature range (180-250^{o} C) the dislocation microstructure was primarily limited to small defect clusters formed near pre-irradiation dislocation segments (about 10^{16} $\#/cm^3$ and less than 6 nm in diameter). In the second temperature group (275-300^{o} C), clusters of small dislocation loops were observed. A higher number density of clusters were observed at low-angle grain boundaries and at preirradiation dislocation segments. The average diameter of each individual loop was about 10 nm and each cluster contained 15 to 20 loops. The number density of loops was about $2X10^{15}$ $\#/cm^3$. It was found that all the loops were interstitial in nature

and were near-edge loops with b=a‹100›. The third temperature range was between 350 and 500° C, for which a fairly homogeneous distribution of loops and network segments was present. The quantitative data for the loop structure were presented in the reference.(74) All the loops analyzed, with only one exception, were of near-edge character with b=a‹100› and were interstitial in nature. In the fourth temperature range (650 to 740° C), there was no observable difference in the dislocation microstructure as compared to that found in unirradiated specimens. Robertson et al.(129) also reported a detailed study of neutron-irradiated iron up to $1.2X10^{24}$ n/m^2 (E›1MeV). The dislocation loops were all interstitial in nature and contained both b=a/2‹111› and b=a‹100› Burgers vectors. The average loop diameter was about 10 nm and the loop number density was about 10^{16} $\#/cm^3$.

Many studies(79,88,91,92,96,132,133) of loops in neutron-irradiated ferritic steels have been reported recently. Little and co-workers(132,133) examined a commercial steel FV448 (12Cr-1MoVNb) irradiated in DFR (Dounreay Fast Reactor) at temperature of 380 to 615° C and to a fluence of 30 dpa. Only interstitial-type loops

were been identified and more than 98% of the loops were lying on {100} planes with b=a‹100›. The unusual feature of this study was that the loop size and number density vary abnormally with irradiation temperature. Little et al.[132,133] proposed that the low swelling behaviour of ferritic steels might be able to explain by the relative rates of nucleation and growth of the two interstitial dislocation loop types, with b=a/2‹111› and b=a‹100›. Gelles[79] examined simple Fe-Cr binary alloys irradiated in EBR-II to a fluence of $4.3X10^{26}$ n/m^2 over the temperature range of 400 to 450^{o} C. Both types of loops (a/2‹111› and a‹100›) were found, however, lower chromium content alloys produced predominantly a‹100› type loops and higher chromium content (above 12% Cr) produced predominantly a/2‹111› loops. Gelles and Thomas[91,92] found dislocation loops in HT-9 irradiated in HFIR and EBR-II, but did not describe them in detail. It was concluded by Gelles[96] that the additional helium in HT-9 had negligible effect on dislocation loop evolution under irradiation.

In 1964, Masters[119] first reported the observation of loops in ion-irradiated iron. The material was

irradiated at 550^{o} C with 150 KeV Fe^{+} ions to a total dose of 1.7X10^{20} ions/m^{2}. The loops were about 100 to 150 nm in diameter along with being pure edge and interstitial in nature. They were normally square, with the sides in the corresponding ‹100› directions with b=a‹100›. Jenkins et al.[127] also examined low energy Fe^{+} ion irradiated iron to a total dose of 5X10^{16} ions/m^{2} but found no observable damage. However, they observed vacancy loops with b=a‹100› and b=a/2‹111› in the specimen irradiated with 80 KeV W^{+} ions to the fluence of 5X10^{16} ions/m^{2}. The two types of loops were produced in approximately equal numbers. Kuramoto et al.[104] studied pure iron irradiated up to 50 dpa over the temperature range of 350 to 500^{o} C by 4 MeV nickel ions with and without simultaneous helium ions injection. A number of vacancy type dislocation loops were observed at 350 and 400^{o} C irradiations, especially along the dislocation lines. Horton et al. [105,109] studied the microstructure of triple beam ion irradiated iron and Fe-Cr alloys. The loops that found in iron and Fe-10Cr alloy were determined to be interstitial in nature with predominantly b=a‹100›. A few loops with b=a/2‹111› were also observed. At low

tempreatures (T‹450^{o} C), the loops varied in shape from round to rectilinear, with the sides aligned in ‹100› directions. For irradiation temperature above 490^{o} C, many of the dislocation loops had an irregular convoluted shape and the loops appeared to have grown preferentially in ‹110› directions.

There have been several studies of dislocation loops in HVEM irradiated iron and steels.[103,115,124,125,131] Most of the loops that found in irradiated specimens were interstitial in nature, pure edge with b=a‹100›, and had sides parallel to ‹100› directions. However, Suganuma and Kayano[131] reported that the morphology and the habit plane of electron-irradiation induced loops in Fe-15Cr varied with irradiation temperatures. They found that in the temperature range of 300 to 400^{o} C, most loops were on the {100} plane with b=a‹100›. But if the irradiation temperature range was between 450 and 550^{o} C, star-like dislocation loops grew, and most of these loops existed on the {111} plane with b=a/2‹111›.

In summary, most dislocation loops that found in previous studies in iron and ferritic steels are interstitial-type loops with b=a‹100› and b=a/2‹111›.

Some experimental results have indicated that vacancy type loops also existed. The number density and average diameter of loops vary with irradiation temperature and dose level and, in general, the number density of loops decreases with increasing temperature and the average diameter of loops increases with increasing temperature.

C.3 Solute Segregation and Phase Stability Experiments

Up to date, only few studies[111,130,184] in irradiation induced solute segregation (RIS) in ferritic steels have been published. Brimhall et al.[184] studied the solute segregation of HT-9 under 5 MeV Ni^{++} ion irradiation up to 2 dpa at the surface in the temperature range from 450 to 600° C. The analysis of solute segregation was done by utilizing an Auger electron spectroscopy (AES). Radiation-enhanced segregation of nitrogen was the only measurable effect of radiation in the HT-9 alloy. In general, the radiation-induced or -enhanced segregation of elements in HT-9 was less than that in the austenitic steels. Ohnuki et al. studied the solute segregation of simple ferritic binary alloys under electron-[130] or ion-irradiation[111]. Irradiation with

electrons in the HVEM at 650 KV and 400^{o} C,[130] showed that the oversize solute in Fe-5Cr, Fe-13Cr, and Fe-1Mn alloys were depleted near the sinks (such as grain boundaries) due to an interaction between vacancies and solutes. This result was in agreement with the conclusion of chromium depletion around voids in neutron irradiated Fe-10Cr alloy reported by Little and Stow.[78] However, in studying alloys irradiated with 200 KeV C^{+} ions at 525^{o} C to 57 dpa, Ohnuki et al.[111] found chromium enriched in grain boundaries both in Fe-13Cr and Fe-31Cr-1Si alloys. To explain this result, the authors considered the effect of chromium-carbon complexes on radiation induced segregation. This explanation was further supported by adding strong carbides formers (such as titanium) into the material. Titanium enrichment and chromium depletion were found in grain boundaries in irradiated Fe-13Cr-1Ti alloy.[111]

A recent thorough review of phase stability during irradiation of iron based binary alloys and ferritic steels was published by Wolfenden et al.[141] The precipitate evolution during irradiation did basically follow the thermal annealing results that discussed in

Section IV.B with some exceptions of intermetallic phases (chi, σ, α', and Laves phases). The studies of Fe-C[126,73,142], Fe-N[126,143], and Fe-Cu[73,138,144] are of no particular concern to the material (HT-9) investigated in this thesis, therefore they will not be discussed here.

The major microstructural effect of irradiation in commercial ferritic steels is second phase precititation. The precipitation takes many forms both as a function of alloy composition and irradiation conditions.[82] It is anticipated that this precipitation will have significant effects on post-irradiation mechanical properties. Smidt and co-workers have already demonstrated a shift of about 100^{o} C of the DBTT in HT-9 and attributed the behaviour to precipitation.[97]

Little and Stow[78] found α'-precipitate in Fe-10 to 15 Cr ferritic alloys irradiated with neutron to 30 dpa. Ohnuki et al.[115] observed $M_{23}C_6$ carbides in Fe-13Cr and Fe-13Cr-1Si and MC (Ti-riched) carbides in Fe-13Cr-1Ti irradiated with 200 KeV C^{+} to 114 dpa. Gelles[82,85,95] studied the microstructural evolution of 2 1/4Cr-1Mo steel after neutron irradiation and found the mean precipitate

size increased with increasing irradiation temperature. Two types of precipitate morphologies were found, namely, equaxied M_6C and rod-shaped Mo_2C. Sindelar et al.[139] examined the same material used by Gelles[85] following irradiation with 14 MeV nickel ions at 500° C up to 400 dpa. Several irradiation-enhanced phases (M_7C_3, M_2C) and -induced phases (G-phase and chi-phase) were found in various irradiated regions.

In studying 9Cr-1MoVNb alloy, several research groups[91,93,84,87] have reported their experimental results. Gelles and Thomas[91] found radiation-induced Cr_2C phase and phosphide in addition to the preexisted $M_{23}C_6$ and MC carbides. Vitek and Klueh[84,93] found a new phase, which was not identified, in addition to preexisted $M_{23}C_6$ and MX (vanadium or niobium enriched) precipitates. Maziasz et al.[87] found that the addition of 2% Ni to the 9Cr-1MoVNb alloy, which was irradiated in HFIR in order to examine the effect of helium, promoted a considerable amount of irradiation-produced precipitation in the grain. Gelles[82,95] also studied precipitate evolution in EM-12, H11, AISI 416, and AISI 430F. He found chi-phase and Laves phase (Fe_2Mo) in EM-12 in addition to preexisting

$M_{23}C_6$ carbides.

Table IV-2 summarizes the precipitate evolution of 12% Cr ferritic and martensitic steels under irradiation. There is no general rule that the precipitate evolution can be predicted and the experimental results vary with each individual specific experimental conditions and chemical composition of the material used. For example, Gelles and Thomas [91,92,95,96] found $M_{23}C_6$, chi phase, G phase and α' phase; Vitek and Klueh[93,94] and Wassilew and Hweschbach[137] reported only $M_{23}C_6$ with some additional V or Nb riched carbides. Little and Stoter[135] published the most detailed precipitation study in 12% Cr ferritic and martensitic steels and found the same precipitates that were reported in other experiments (see Table IV-2).

It seems that this type material is so complicated that it is difficult to thoroughly understand the properties after irradiation. However, it may be noted that because a wide range of precipitate types can form in 12% Cr ferritic and martensitic steels. If an alloy is found to provide unacceptable post-irradiation mechanical properties, minor changes in alloy composition or heat

Table IV-2 The precipitate evolution of 12Cr-1MoV ferritic steels during irradiation.

Materials	Irradiation	Fluence (n/m^2)	Temperature (^oC)	Precipitate Observed		Reference
				before irr.	after irr.	
HT-9* XAA-3587	neutron HFIR	$4.9x10^{26}$ (36 dpa)	300,400 500,600	$M_{23}C_6$, MC	$M_{23}C_6$, MC	(34,93, 94)
HT-9* 91354	neutron EBR-II	up to $1.5x10^{27}$ (75 dpa)	400 to 650	$M_{23}C_6$	Chi, G,	(91,92 95,96)
	HFIR	(39 dpa)	300,400		$M_{23}C_6$	
CRM-12#	neutron DFR	30 dpa (N/2)	380,420 460,615	$M_{23}C_6$, MX, Laves(b)	Laves, MX(a), Chi, M_6X, $M_{23}C_6$,	(135)
FV448#	neutron DFR	30 dpa (N/2)	380,420 460,615	Laves(b), NbC, M_2X, $M_{23}C_6$	Laves, M_2X(a) Sigma, Chi Phopshides, $M_{23}C_6$, M_6X	(135)
FI#	neutron DFR	30 dpa (N/2)	380,420 460,615	$M_{23}C_6$, M_2X	Phosphides M_6X, $M_{23}C_6$(a) M_2X	(135)
HT-9 9607-R2	14 MeV Ni ion	up to 200 dpa	300,400 500,600	MX, M_2X(c) $M_{23}C_6$	MX, Chi, $M_{23}C_6$	present study

* see Table V-1 for the chemical composition of these materials

\# see Reference (135) for the chemical composition of these materials

(a) some dissolution occured after irradiation

(b) phase formed after thermal annealing

(c) phase totally dissolved after irradiation

treatment may eliminate the deleterious phases resulting in improved properties.

C.4 Mechanical Property Studies

Because of the thrust of this thesis, the mechanical properties review is limited to recent studies and mainly to the studies of HT-9 (12Cr-1MoVW) ferritic steel. Since the study of pressure vessel steels (PVS) are limited to simple iron-based alloys and low irradiation temperatures ($t<200^{o}$ C) and low neutron fluences (less than $1X10^{24}$ n/m^{2}, E>1MeV), the detail of studies in PVS will not be discussed here. There are many conference proceedings[1,188-200] which contain the informations of irradiation effects in PVS.

Klueh et al.[145-148] irradiated tensile specimens of 12Cr-1MoVW, 9Cr-1MoVNb, and 2 1/4Cr-1Mo steels in HFIR at approximately 50^{o} C to a damage level of 9 dpa. For all alloys, irradiation caused a significant increase in yield strength and ultimate tensile strength; the increase in strength was accompanied by a decrease in ductility. All indications were that the increased strength and decreased ductility were caused by irradiation-induced dislocation

loops. At this low temperature, no precipitation was expected and no irradiation-aided tempering was possible.[148] Gelles and Thomas[91,91,95] examined 12Cr-1MoVW steel irradiated in EBR-II at 390° C and concluded that much of the strengthening observed was caused by radiation-induced G-phase, and the hardening caused by G-phase could also lead to an radiation-induced increase in the DBTT. Several studies[149-151] proved that HT-9 had superior in-reactor creep resistance when compared to 20% CW 316 austenitic steel for irradiation temperatures up to 570° C. Hawthorne and co-workers[152-155] examined the fracture resistance of HT-9 and 9Cr-1Mo ferritic steels after neutron irradiation. A 36° C shift in DBTT after irradiation at intermediate temperature (288° C) and up to a 117° C shift in DBTT at lower irradiation temperatures (93-149° C) was found. Many other studies examing the effect of irradiation on the mechanical properties in iron[156-159] and other ferritic steels [75,86,161-168,186] were also reported. Mancuso et al.[169] developed a correlation between microhardness, tensile properties and notch-ductility of irradiated ferritic steels.

D. Swelling Suppression Mechanisms

As discussed in Section IV.C.1, ferritic steels showed very high resistance to void swelling after irradiation by either neutrons, ions or electrons. Currently, several mechanisms have been presented to explain the low swelling behaviour exhibited by ferritic alloys. In this section, some models and ideas are discussed.

Singh[170] discussed the effect of fine grain size on void formation. Although his study was done for austenitic stainless steels, the idea could be used for ferritic steels as well. He found that in fine-grained stainless steel, void nucleation and void swelling were grain size dependent. During irradiation, in both undoped and helium doped samples, void nucleation (as observed in the HVEM) was delayed, void concentration was lowered, and void swelling was reduced by decreasing the grain size. This grain size effect was explained by the author in terms of "defect depletion" model. Singh suggested that void nucleation was very sensitive to vacancy supersaturation and that a critical level of vacancy

supersaturation was necessary to produce critically sized void nuclei which could grow into observable voids. He concluded that the presence of stable and small grains improved the damage resistance of the material tremendously. Since the grain size in ferritic and martensitic steels is usually small (less than 1 um) and stablized by carbides, this effect may account for the lower swelling rate of commercial ferritic steels compared to that of iron and simple ferritic alloys.

Hayns and Williams[171] presented a model based on point defect trapping to explain the void swelling characteristics of electron-irradiated FV607 ferritic steel. This is the only available model which utilizes rate theory calculations to provide semiquantitative support for the conclusions. By incorporating point defect trapping into a rate theory model, the qualitative features of the void swelling behaviour in FV607 steel could be consistently interpreted. The model yielded low peak swelling temperature, overall low swelling and a rapid drop in swelling at temperatures above the peak swelling temperature as observed in experiments by Arkell and Williams.[101] The authors suggested that, if their

model is correct, they would expect much less importance of vacancy loop formation and a weaker dose rate dependence for ferritic steels than usually observed in austenitic alloys. Thus, a shift in the peak swelling temperature of about 55° C for ion irradiation was suggested for FV607 steel by the rate theory calculations instead of a 150 to 200° C shift for austenitic steels.

Little[172] suggested that both point defect trapping and dislocation-solute interactions played key roles in determining the void swelling behaviour of ferritic steels. He mentioned that three mechanisms for suppression of void swelling were considered to operate strongly in ferritic steels. These are (a) the effect of point defect trapping by solute atoms in enhancing mutual point defect recombination, (b) the effect of dislocation and solute atom interactions in reducing the dislocation bias for preferential self-interstitial capture, and (c) the effect of the interactions between solute atoms and dislocations in inhibiting the climb rate of the dislocations.

Little concluded that for mechanism (a) the most likely combination is the trapping of the radiation-

induced vacancies by the interstitial solute carbon and nitrogen atoms. The vacancy-solute atom complexes act as sites for preferred recombination of the incoming interstitials. Consequently, the fraction of point defects available to contribute to the growth of both the voids and the interstitial dislocation loops is reduced. In addition, a reduced vacancy supersaturation should also have the effect of decreasing the rate of void nucleation. Void nucleation and growth can be further influenced by the non-equilibrium segregation of solutes to sinks, because of the change in the composition of the regions near the sinks. For mechanism (b), the solute atoms which are attracted elastically to dislocations will migrate to the dislocations and form a "condensed" atmosphere close to the dislocation cores and therefore decrease their bias for interstitial capture. That will reduce the vacancy supersaturation for void growth. The calculations by Weertman and Green[25] have shown that void growth can be completely eliminated if dislocations are surrounded by a condensed atmosphere of either oversized substitutional atoms or interstitial solutes. In mechanism (c), provided the diffusion rate of the solute atoms in the correct

magnitude, solutes are likely to be effective in impeding the climb (and glide) of dislocations as a consequence of the restraining force imposed on the dislocation in dragging with it the impurity atmosphere. When climb cannot occur, a dislocation acts as a neutral, but saturable, sink for point defects. Therefore, the dislocations can act as recombination centers and reduce void growth. In summary, Little mentioned that the above mechanisms could act together to produce extremely low swelling or total lack of voids such as is often observed in ferritic steels. In addition, the formation of precipitates, as in many 12% Cr steels, could further enhance point defect recombination and reduce swelling if the precipitates behaved in a manner similar to isolated solute atoms.

Little et al.[132,133] presented another model which considered the relationship between swelling resistance and dislocation evolution. This model was developed to explain the observation of interstitial loops with b=a‹100› exclusively and no cavities in regions of FV448 ferritic steel specimens which contained a high network density of dislocations with b=a/2‹111› prior to

irradiation. The mechanism was explained by the authors as follows. The interstitial loops with b=a‹100› and with b=a/2‹111› are formed prior to void nucleation due to the high mobility of interstitials. Although loops with b=a/2‹111› are predominant, a small and finite number of loops with b=a‹100› are also nucleated. The a‹100› loops act as biased sinks for preferential interstitial absorption, while the pre-existing a/2‹111› dislocation network and the irradiation-induced a/2‹111› loops are relatively neutral sinks (due to the higher magnitude of the a‹100› Burgers vector). The vacancy supersaturation resulting from the growth of the a‹100› loops can be absorbed by the surrounding neutral a/2‹111› dislocation sinks, causing void nucleation to be suppressed. Eventually, the a/2‹111› network in the immediate vicinity of the a‹100› loops coupled with annihilation (by vacancy absorption) and renucleation of a/2‹111› loops establishes a steady-state condition in which void nucleation is unlikely. The formation of an array of discrete domains which contains only a‹100› loops is suggested by the above mechanism. Each domain grows around an initial, isolated a‹100› loop. As more a‹100› loops form around the initial

loop, the growth of the initial loop gradually ceases due to the shielding by the outer loops. This produces domains of approximately equal sized loops. Between these domains, regions containing both the dislocation network and small a/2‹111› loops remain. Voids can nucleate in these regions. However, if the network dislocation density is sufficiently high, both loop and void nucleation will be suppressed by point defect recombination at the network.

Sniegowski and Wolfer[173] examined this low swelling behaviour of ferritic alloys from another viewpoint. They supposed that a fundamental difference exists between austenitic and ferritic alloys which originates from the difference in the net bias. Since the net bias depends most critically on the relaxation volume of interstitials and vacancies, the difference of relaxation volume between these two alloys will play a dominant role on the swelling behaviour. They assumed that the relaxation volumes for interstitials and vacancies are 1.8 Ω and -0.1 Ω respectively in austenitic steels, and 1.1 Ω and -0.5 Ω in ferritic steels. By using these values in the equations given for the bias factors of voids and dislocations for

both vacancy and interstitial captures, they showed that the net bias was smaller by a factor of 4 or higher in ferritic steels as compared to austenitic steels. Based on the net bias results from the calculations, they expected therefore that the swelling rate in austenitic alloys was less or equal to about 1.4%/dpa. This value is remarkably close to the experimental value of 1%/dpa found for the steady-state swelling rate in austenitic steels. They also predicted that the maximum steady-state swelling rate for ferritic alloys was about 0.14%/dpa by using a vacancy relaxation volume of -0.5 Ω and an interstitial relaxation volume of 0.9 Ω.

In summary, none of the above models or ideas presents a clear, general picture of the radiation damage processed which occur in ferritic materials. In order to develop a complete understanding of the microstructural evolution, a more complete data base is necessary.

E. Recently Developed Ferritic Steels for Breeder and Fusion Reactor Applications

In general, the Cr-Mo ferritic steels can be divided into two categories: unmodified, basically Cr-Mo-C steels

and Cr-Mo-C steels modified by the addition of carbide forming elements (such as V, Nb, Ti, and W).[174] Recently, much of research effort on the second type alloys has been directed to opitimize the properties for breeder and fusion reactor applications. These alloys include HT-9 (12Cr-1MoVW) and 9Cr-1MoVNb.

There are several crucial problems to the application of 12Cr-1MoVW steels for reactor components. For example, weldability, high temperature creep strength, the upward shift of DBTT, and the activity of spent structural materials are all needed to be improved. Vineberg and Cox[175] developed a readily weldable 12Cr-2Mo steel with excellent creep-rupture characteristics. With lower carbon content (0.075 wt%) and higher Ni content (6%), the excellent properties of this material will be an attractive candidate for use in elevated temperatures. Anderko et al[176] developed a 12Cr-1MoVNb steel and achieved a DBTT at -17^{o} C by limiting the nitrogen content to less than 100 ppm. The low DBTT and high creep structural strength made this material a good candidate for reactor applications.

During the operation of a fusion reactor, the

structural material of the first wall and blanket structure will become highly radioactive from activation by the high-energy (14 MeV) fusion neutrons. A difficult radioactive waste problem will be involved in the disposal of this material after service. Therefore, much of effort is being made to develop a type of materials which the induced radioactive decays rather quickly to levels that allow for simplified disposal technique. Several studies[177-180] showed that some alloying elements (e.g., Nb, Mo, and Ni) in currently used ferritic steels should be substituted by other elements such as V, W, Ti, and Mn. Another way to bypass the activation problem is using isotropic tailoring of the elements that are used in the material.[178] Several research groups have started to examine the recently designed low activation alloys.[181-183] They found that the low activation ferritic alloys were feasible by using vanadium and tungsten instead of Mo and using Mn to substitute Ni. More research efforts are definitely needed in this area in order to solve the waste disposal problem.

REFERENCES FOR CHAPTER IV

1. J. W. Davis and D. J. Michel (Eds.), the Proceedings of Topical Conference on Ferritic Alloys for Use in Nuclear Energy Technologies, Snowbird, Utah (1983).

2. S. F. Pugh and E. A. Little (Eds.), the Proceedings of an international conf. on Ferritic Steels for Fast Reactor Steam Generators, held by BNES, Lodon, UK (1978).

3. T. A. Lechtenberg, in Alloy Development for Irradiation Performance (ADIP) Progress Report, DOE/ER-0045/14 (1985) p.109.

4. J. W. Davis, J. of Nucl. Mater. 122&123 (1984) 3.

5. R. F. Mattas, F. A. Garner, M. L. Grossbeck, P. J. Maziasz, G. R. Odette, and R. E. Stoller, J. of Nucl. Mater. 122&123 (1984) 230-235.

6. G. J. Butterworth, "Some Initial Considerations on the Suitablity of Ferritic/Martensitic Stainless Steels as First Wall and Blanket Materials in Fusion Reactors", UKAEA Fusion Association, CLM-R217 (1981).

7. D. R. Harris, in Ref. 1 (1983) 141-156.

8. P. Patriarca, in Ref. 1 (1983) 107-112.

9. T. U. Marston, in Ref. 1 (1983) 19-26.

10. E. A. Little, D. R. Arkell, D. R. Harries, G. R. Lewthwaite, and T. M. Williams, in the Intern. Conf. of Irradiation Behavior of Metallic Materials for Fast Reactor Core Components, Corse, France (1979) 31-37.

11. J. Orr, F. R. Beckitt, and G. D. Fawkes, in Ref. 2 (1978) 91-109.

12. J. Nutting, in Ref. 1 (1983) 3-16.

13. K. Farrell and E. H. Lee, Scripta Metall. 17 (1983) 791-796.

14. M. Hansen, Constitution of Binary Alloys, 2nd ed. McGraw Hill (1958).

15. H. Schneider, Foundary Trade J. 108 (1960) p.562.

16. E. S. Davenport and E. C. Bain, "Transformation of Austenite at Constant Subcritical Temperature", Trans. AIME 90 (1930) p.117.

17. Isothermal Transformation Diagrams of Austenite in A Wide Variety of Steels, 3rd. Ed. US Steel Co. (1963).

18. M. Atkins, Atlas of Continuous Cooling Transformation Diagrams for Engineering Steels, ASM and BSC (1977).

19. K. J. Irvine, J. D. Murray, and F. B. Pickering, Iron and Steel Institute (ISI) Special Report No.70 (1961) 246-275.

20. P. M. Kelly and J. Nutting, ISI Spec. Rept. No.76 (1962) 7-11.

21. J. H. Woodhead and A. G. Quarrell, Journal of the Iron and Steel Institute (JISI) 203 (1965) 605-620.

22. J. Nutting, JISI 207 (1969) 872-893.

23. F. B. Pickering, Intern. Metals Reviews, Dec. 1976, pp. 227-268.

24. H. J. Goldschmidt, JISI 160 (1948) 345-362.

25. J. Weertman and W. V. Green, in Irradiation Effects on the Microstructure and Properties of Metals, ASTM-STP-611 (1976) 256-269.

26. K. Kuo, JISI 173 (1953) 363-375.

27. S. W. K. Shaw and A. G. Quarrell, JISI 185 (1957) 10-22.

28. R. G. Baker and J. Nutting, ISI Spec. Rept. No.64 (1959) 1-22.

29. K. W. Andrews and H. Hughes, ibid. pp. 57-60.

30. K. A. Ridal and A. G. Quarrell, JISI 200 (1962) 359-365.

31. F. B. Pickering, ISI Spec. Rept. No.64 (1959) 23.

32. K. J. Irvine, D. J. Crowe, and F. B. Pickering, JISI 195 (1960) 386-405.

33. J. Koutsky and J. Jezek, JISI 203 (1965) 707-714.

34. J. M. Vitek and R. L. Klueh, Metall. Trans. 14A (1983) 1047-1055.

35. R. Smith, ISI Spec. Rept. No.64 (1959) 307-311.

36. R. G. Baker and J. Nutting, JISI 192 (1959) p.257.

37. R. L. Klueh, Nucl. Tech. 57 (1982) 114-124.

38. K. J. Irvine, ISI Spec. Rept. No.95 (1966) 37-55.

39. E. Tekin and P. M. Kelly, JISI 203 (1965) 715-720.

40. P. J. Grobner, Metall. Trans. 4 (1973) 251-260.

41. P. Jacobsson, Y. Bergstrom, and B. Aronsson, Metall. Trans. 6A (1975) 1577-1580.

42. M. Aubert, B. Mathieu and P. Peterquin, in Ref. 1 (1983) 245-251.

43. Sessions 3 and 4 in Ref. 2 (1978).

44. O. K. Chopra and D. L. Smith, in Ref. 1 (1983) 481.

45. E. A. Little, D. R. Harries, F. B. Pickering, and

S. R. Keown, Metals Tech., April 1977, pp. 205-217.

46. E. A. Little, D. R. Harries, and F. B. Pickering, in Ref. 2 (1978) 136-144.

47. T. A. Lechtenberg, J. of Nucl. Mater. 103&104 (1981) 1133-1138.

48. B. C. Edwards and E. A. Little, in Ref. 2 (1978) 145-150.

49. B. A. Chin and R. C. Wilcox, in Ref. 1 (1983) 347.

50. D. A. Mervyn, D. T. Peterson, and F. H. Huang, ADIP DOE/ER-0045/2 (1980) 132-155.

51. D. Burton, J. Orr, and J. B. Marriott, in Ref. 2 (1978) 205-211.

52. A. Hede and B. Aronsson, JISI 207 (1969) p.1241.

53. L. Egnell and N. G. Persson, in Ref.2 (1978) 212.

54. G. Oakes, J. Orr, and P. W. Taylor, in Ref. 2 (1978) 222-227.

55. T. Marrison and A. Hogg, in the Proceedings of the Conf. on Creep Strength in Steels and High Temperature Alloys, ISI (1972) 242-268.

56. W. R. Corwin, R. L. Klueh, and J. M. Vitek, J. of Nucl. Mater. 122&123 (1984) 343-348.

57. W. M. Garrison, Jr., J. M. Hyzak, and T. A. Lechtenberg, in Ref. 1 (1983) 379-384.

58. T. A. Lechtenberg, W. M. Garrison, Jr., and J. M. Hyzak, in Ref.1 (1983) 365-370.

59. J. M. Hyzak and W. M. Garrison, Jr., ibid. p.385.

60. R. H. Jones and M. T. Thomas, ibid. p.395.

61. F. Bruhl and H. Musch, in Ref. 1 (1983) 253-260.

62. R. S. Fidler and D. J. Gooch, in Ref. 2 (1978) 128.

63. J. R. Foulds, ADIP DOE/ER-0045/11 (1983) 155-161.

64. J. R. Foulds and T. A. Lechtenberg, ADIP DOE/ER-0045/11 (1983) 163-170.

65. J. C. Lippold, J. of Nucl. Mater. 103&104 (1981) 1127-1132.

66. J. C. Lippold, in Ref. 1 (1983) 497-506.

67. F. H. Huang and D. S. Gelles, in Ref.1 (1983) 337.

68. G. R. Odette, G. E. Lucas, R. Maiti, and J. W. Shecknerd, J. of Nucl. Mater. 122&123 (1984) 442.

69. R. O. Ritchie, J. F. Knott, and J. R. Rice, J. of Mech. Phys. Solids 21 (1973) p.395.

70. G. L. Kulcinski, B. Mastel, and J. L. Brimhall, Rad. Effects 2 (1969) 57-59.

71. K. Farrell and J. T. Houston, J. of Nucl. Mater. 35 (1970) 352-355.

72. J. L. Brimhall, H. E. Kissinger, and G. L. Kulcinski, in the Proceedings of Intern. Conf. on Radiation-Induced Voids in Metals, J. W. Corbett and L. C. Ianniello (Eds.), USAEC (1972) 338-362.

73. F. A. Smidt, Jr., J. A. Sprague, J. E. Westmoreland , and P. R. Malmberg, in Defects and Defect Clusters in BCC Metals and Their Alloys, Nucl. Met. Vol.18, ed. by J. Arsenault (1973) 341-362.

74. L. L. Horton, J. Bentley, and K. Farrell, J. of Nucl. Mater. 108&109 (1982) 222-233.

75. J. J. Huet and V. Leroy, Nucl. Tech. 24 (1974) 216.

76. J. J. Huet, A. Delbrassine, Ph. Van Asbroeck, and W. Vandermeulen, in the Intern. Conf. on Radiation

Effects on Breeder Reactor Structural Materils, M. L. Bleiberg and J. W. Bennett (Eds.), AIME (1977) 357-365.

77. E. A. Little and D. A. Stow, in Irradiation Behavior of Metallic Materials for Fast Reactor Core Components, France (1979) 18-24.

78. E. A. Little and D. A. Stow, Metal Sci., March 1980 89-94.

79. D. S. Gelles, J. of Nucl. Mater. 108&109(1982) 515.

80. D. S. Gelles and R. L. Meinecke, ADIP DOE/ER-0045 /11 (1983) 103-107.

81. R. W. Powell, D. T. Peterson, M. K. Zimmerschied, and J. F. Bates, J. of Nucl. Mater. 103&104 (1981) 969-974.

82. D. S. Gelles, J. of Nucl. Mater. 103&104(1981) 975.

83. D. S. Gelles, J. of Nucl. Mater. 122&123(1984) 207.

84. J. M. Vitek and R. L. Klueh, J. of Nucl. Mater. 122&123 (1984) 254-259.

85. D. S. Gelles, ADIP DOE/ER-0045/12 (1984) 113-137.

86. D. S. Gelles and R. J. Puigh, in Effects of Radiation on Materials: 12th Conf., F. A. Garner and J. S. Perrin (Eds.), ASTM-STP-870 (1985) 19-37.

87. P. J. Maziasz, R. L. Klueh, and J. M. Vitek, ADIP DOE/ER-0045/14 (1985) 81-86.

88. V. I. Scherbak, V. N. Bykov, A. N. Vorobiev, and V. D. Dmitriev, in Radiation Effects in Breeder Reactor Structural Materials, AIME (1977) 773-779.

89. E. A. Little and D. A. Stow, J. of Nucl. Mater. 87 (1979) 25-39.

90. J. J. Huet, A. de Bremaecker, M. Snykers, Ph. Van

Asbroeck, and W. Vanderneulen, in Irradiation Behavior of Metallic Materials for Fast Reactor Core Components, France (1979) 5-9.

91. D. S. Gelles and L. E. Thomas, ADIP DOE/ER-0045/8 (1982) 343-362.

92. D. S. Gelles and L. E. Thomas, ADIP DOE/ER-0045/9 (1982) 162-177.

93. J. M. Vitek and R. L. Klueh, ADIP DOE/ER-0045/11 (1983) 108-114.

94. J. M. Vitek and R. L. Klueh, in Ref. 1 (1983) 551.

95. D. S. Gelles and L. E. Thomas, in Ref.1 (1983) 559.

96. D. S. Gelles, ADIP DOE/ER-0045/14 (1985) 129-136.

97. F. A. Smidt, Jr., P. R. Malmberg, J. A. Sprague, and J. E. Westmoreland, in Irradiation Effects on the Microstructure and Properties of Metals, ASTM-STP-611 (1976) 227-241.

98. G. Ayrault, Damage Analysis and Fundamental Studies (DAFS) Progress Report DOE/ER-0046/8 (1982)182-190.

99. P. Darben, R. P. Wahi and H. Wollenberger, J. of Nucl. Mater. 133&134 (1985) 619-622.

100. K. Suzuki, A Kohyama, G. Ayrault, and N. Igata, J. of Nucl. Mater. 133&134 (1985) 632-635.

101. D. R. Arkell and T. M. Williams, J. of Nucl. Mat. 74 (1978) 144-150.

102. E. A. Little, in Ref. 1 (1983) 587-591.

103. E. A. Little, Rad. Effects 16 (1972) 135-137.

104. E. Kuramoto, N. Yoshida, N. Tsukuda, K. Kitajima, N. H. Packan, M. B. Lewis, and L. K. Mansur, J. of Nucl. Mater. 103&104 (1981) 1091-1096.

105. L. L. Horton, J. Bentley, and W. A. Jesser, J. of Nucl. Mater. 103&104 (1981) 1343-1348.

106. W. G. Johnston, J. H. Rosolowski, and A. M. Turkalo, J. of Nucl. Mater. 54 (1974) 24-40.

107. W. G. Johnston, T. Lauritzen, J. H. Rosolowski, and A. M. Turkalo, GE Tech. Infor. Series 1, Report No. 76CRD019 (1976).

108. W. G. Johnston, T. Lauritzen, J. H. Rosolowski, and A. M. Turkalo, in EFfectsof Radiation on Materials: 11th Conf., H. R. Brager and J. S. Perrin (Eds.), ASTM-STP-782 (1982) 809-823.

109. L. L. Horton, J. Bentley, and W. A. Jesser, J. of Nucl. Mater. 103&104 (1981) 1085-1090.

110. L. L. Horton, Ph.D. Thesis at the University of Virginia (1982), also ORNL/TM-8303.

111. S. Ohnuki, H. Takahashi, and T. Takeyama, J. of Nucl. Mater. 103&104 (1981) 1121-1126.

112. L. L. Horton and J. Bentley, in Ref. 1 (1983) 569.

113. G. Ayrault, J. of Nucl. Mater. 114 (1983) 34-40.

114. K. Farrell and E. H. Lee, in Effects of Radiation on Materials: 12th Conf., ASTM-STP-870 (1985)383.

115. S. Ohnuki, H. Takahashi, and T. Takeyama, J. of Nucl. Mater. 122&123 (1984) 317-321.

116. M. Snykers, F. Biermans, and J. Cornelis, J. of Nucl. Mater. 103&104 (1981) 1079-1084.

117. R. W. K. Honeycome, Steels: microstructure and properties, ASM (1981).

118. B. L. Eyre, Phil. Mag. 7 (1962) 2107-2113.

119. B. C. Masters, Phil. Mag. 11 (1965) 881-893.

120. B. L. Eyre and A. F. Bartlett, Phil. Mag. 12 (1965) 261-272.

121. B. L. Eyre and R. Bullough, Phil. Mag. 12 (1965) 31-39.

122. J. S. Bryner, Acta Metall. 14 (1966) 323-336.

123. N. Milasin, Rad. Effects 15 (1972) 153-165.

124. E. A. Little and B. L. Eyre, J. of Nucl. Metal Sci. 7 (1973) 100-102.

125. M. Kiritani, H. Takata, N. Yoshida, and Y. Maehara, in Fundamental Aspects of Radiation Damage in Metals, M. T. Robinson and F. W. Young (Eds.), CONF-751006-P2, NTIS (1976) 889-895.

126. T. Takeyama and H. Takahashi, ibid pp.1100-1106.

127. M. L. Jenkins, C. A. English, and B. L. Eyre, Phil. Mag. 38A, No.1 (1978) 97-114.

128. H. Kayano, H. Yoshinaga, K. Abe, and S. Morozumi, Nucl. Sci. and Tech. 15 (1978) 200-212.

129. I. M. Robertson, M. L. Jenkins, and C. A. English, J. of Nucl. Mater. 108&109 (1982) 209-211.

130. H. Takahashi, S. Ohnuki, and T. Takeyama, J. of Nucl. Mater. 103&104 (1981) 1415-1420.

131. K. Suganuma and H. Kayano, Rad. Eff. 54 (1981) 81.

132. E. A. Little, R. Bullough, and M. H. Wood, Proc. Roy. Soc. Lond. A372 (1980) 565-579.

133. R. Bullough, M. H. Wood, and E. A. Little, in Effects of Radiation on Materials: 10th Conf., D. Kramer, H. R. Brager, and J. S. Perrin (Eds.), ASTM-STP-725 (1981) 593-609.

134. T. A. Lechtenberg, ADIP DOE/ER-0045/5 (1980) 143.

135. E. A. Little and L. P. Stoter, in Effects of Radiation on Materials: 11th Conf., ASTM-STP-782 (1982) 207-233.

136. J. A. Sprague and J. R. Reed, ADIP DOE/ER-0045/14 (1985) 70-73.

137. C. Wassilew, K. Herschbach, E. Materna-Morris, and K. Ehrilich, in Ref. 1 (1983) 607-614.

138. D. K. Hulett and W. A. Jesser, in Effects of Radiation on Materials: 12th Conf., ASTM-STP-870 (1985) 151-166.

139. R. L. Sindelar, J. J. Kai, D. L. Plumton, R. A. Dodd, and G. L. Kulcinski, in Irradiation Effects Associated with Ion Implantation, TMS-AIME Fall Meeting 1985.

140. M. Pelletier, R. M. Vilar, and G. Cizeron, J. of Nucl. Mater. 105 (1982) 237-247.

141. A. Wolfenden, J. R. Holland, R. G. Lott, and J. A. Spitznagel, in Phase Stability during Irradiation, AIME (1980) 383-413.

142. D. Hull and I. L. Mogford, Phil. Mag. 6 (1961)535.

143. N. Igata, R. R. Hasiguti, E. Yagi, U. Nishiike, and K. Watanabe, in Irradiation Effects on Structural Alloys for Nuclear Reactor Applications, ASTM-STP-484 (1970) p.128.

144. S. S. Brenner, R. Wagner, and J. A. Spitznagel, Metall. Trans. 9A (1978) p.1761.

145. R. L. Klueh, J. M. Vitek, and M. L. Grossbeck, J. of Nucl. Mater. 103&104 (1981) 887-892.

146. R. L. Klueh, J. M. Vitek, and M. L. Grossbech, in Effects of Radiation on Materials: 11th Conf., ASTM-STP-782 (1982) 648-664.

147. R. L. Klueh and J. M. Vitek, in Ref. 1 (1983) 615.

148. R. L. Klueh, P. J. Maziasz, and J. M. Vitek, ADIP DOE/ER-0045/14 (1985) 87-98.

149. M. M. Paxton, B. A. Chin, E. R. Gilbert, and R. E. Nygren, J. of Nucl. Mater. 80 (1979) 144-151.

150. W. Vandermeulew, A. de Bremaecker, S. de Burbure, J. J. Huet, and Ph. Van Asbroeck, in Irradiation Behavior of Metallic Materials for Fast Reactor Core Components, France (1979) 1-4.

151. R. J. Puigh, in Effects of Radiation on Materials: 12th Conf., ASTM-STP-870 (1985) 7-18.

152. J. R. Hawthorne and F. A. Smidt, Jr., J. of Nucl. Mater. 103&104 (1981) 883-886.

153. F. A. Smidt, Jr., J. R. Hawthorne, and V. Provenzano, in Effects of Radiation on Materials: 10th Conf., ASTM-STP-725 (1981) 269-284.

154. J. R. Hawthorne, ADIP DOE/ER-0045/11 (1983) 136.

155. J. R. Hawthorne, J. R. Reed, and J. A. Sprague, in Effects of Radiation on Materials: 12th Conf. ASTM-STP-870 (1985) 580-604.

156. E. A. Little, Intern. Metals Rev., March 1976, 25.

157. E. A. Little and D. R. Harries, in Irradiation Effects in Structural Alloys for Thermal and Fast Reactors, ASTM-STP-457 (1969) 215-240.

158. K. L. Murty and E. O. Hall, in Irradiation Effects on the Microstructure and Properties of Metals, ASTM-STP-611 (1976) 53-71.

159. K. Shinohara, G. E. Lucas, and G. R. Odette. J. of Nucl. Mater. 133&134 (1985) 326-331.

160. Ph. Van Asbroeck, W. Vandermeulen, M. Snyders, and J. J. Huet, in Irradiation Embrittlement and Creep in Fuel Cladding and Core Components, BNES, London

(1972) 179-186.

161. J. J. Huet, L. Coheur, L. De Wilde, J. Gedopt, W. Hendrix, and W. Vandermeulen, in Ref.1 (1983) 329.

162. H. Kayano, K. Suganuma, M. Narui, S. Suzuki, and S. Yajima, J. of Nucl. Mater. 85&86 (1979) p.925.

163. Ph. Van Asbroeck, M. Snykers, and W. Vandermeulen, in Effects of Radiation on Substructure and Mechanical Properties of Metals and Alloys, ASTM-STP-529 (1973) 349-359.

164. R. L. Klueh and J. M. Vitek, ADIP DOE/ER-0045/14 (1985) 99-108.

165. J. A. Shields, Jr. and K. J. Longua, Nucl. Tech. 28 (1976) 471-481.

166. H. Yoshida, K. Miyata, Y. Hayashi, M. Narui, and H. Kayano, J. of Nucl. Mater. 133&134 (1985) 317.

167. N. Igata, J. of Nucl. Mater. 133&134 (1985) 141.

168. H. Kayano, M. Narui, S. Ohta, and S. Morozumi, J. of Nucl. Mater. 133&134 (1985) 649-653.

169. J. F. Mancuso, J. A. Spitznagel, R. P. Shogan, and J. R. Holland, in Effects of Radiation on Materials: 10th Conf., ASTM-STP-725 (1981) 38-48.

170. B. N. Singh, Phil.Mag. 29 (1974) 25-42.

171. M. R. Hayns and T. M. Williams, J. of Nucl. Mater. 74 (1978) 151-162.

172. E. A. Little, J. of Nucl. Mater. 87 (1979) 11-24.

173. J. J. Sniegowski and W. G. Wolfer, in Ref. 1 (1983) 579-586.

174. R. L. Klueh, "Cr-Mo Steels for Fusion Recator First Walls- A Review", Metals and Ceramics Div. ORNL (1981).

175. E. J. Vineberg and T. B. Cox, in Ref. 1 (1983)291.

176. K. Anderko, K. David, W. Ohly, M. Schirra, and C. Wassilew, in Ref. 1 (1983) 299-306.

177. K. Saneyoshi and K. Abe, J. of Nucl. Mater. 133&134 (1985) 902-906.

178. T. Lechtenberg, J. of Nucl. Mater. 122&123 (1984) 777-782.

179. G. J. Butterworth and O. N. Jarvis, J. of Nucl. Mater. 122&123 (1984) 982-988.

180. E. E. Bloom, R. W. Conn, J. W. Davis, R. E. Gold, R. Little, K. R. Schultz, D. L. Smith, and F. W. Wiffen, J. of Nucl. Mater. 122&123 (1984) 17-26.

181. H. R. Brager, F. A. Garner, D. S. Gelles, and M. L. Hamilton, J. of Nucl. Mater. 133&134 (1985)907.

182. D. S. Gelles and M. L. Hamilton, ADIP DOE/ER-0045 /13 (1984) 128-140.

183. R. L. Klueh and J. M. Vitek, ADIP DOE/ER-0045/13 (1984) 141-146.

184. J. L. Brimhall, D. R. Baer, and R. H. Jones, J. of Nucl. Mater. 103&104 (1981) 1379-1384.

185. J. I. Bramman, E. W. Etherington, R. S. Nelson, and M. J. Norgett, in Irradiation Embrittlement and Creep in Fuel Cladding and Core Components, BNES, London (1972) 27-31.

186. T. Misawa, H. Sugawara, R. Miura, and Y. Hamaguchi, J. of Nucl. Mater. 133&134 (1985) 313.

187. P. J. Maziasz and R. L. Klueh, ADIP DOE/ER-0045/14 (1985) 74-80.

188. L. P. Trudeau, Radiation Effects on Thoughness of Ferritic Steels for Reactor Vessels, ASM (1964).

189. Irradiation Effects in Structural Alloys for Thermal and Fast Reactors, ASTM-STP-457 (1969), Sessions II and III, 92-260.

190. L. E. Steele and C. Z. Serpan, Jr., Analysis of Reactor Vessel Radiation Effects Surveillance Programs, ASTM-STP-481 (1970).

191. Irradiation Effects on Structural Alloys for Nuclear Reactor Applications, ASTM-STP-484 (1970) Sessions I and II, 8-95.

192. Effects of Radiation on Substructure and Mechanical Propertiex of Metals and Alloys, ASTM-STP-529 (1973) Sessions I and II, 387-482.

193. J. S. Davis (Ed.), Irradiation Embrittlement and Creep in Fuel Cladding and Core Components, BNES (1972), London, UK.

194. Irradiation Effects on the Microstructure and Properties of Metals, ASTM-STP-611 (1976) Session V, 387-482.

195. M. L. Bleiberg and J. W. Bennett (Eds.), Radiation Effects in Breeder Reactor Structural Materials, (1977).

196. J. A. Sprague and D. Kramer (Eds.), Effects of Radiation on Structural Materials: 9th Conf., ASTM-STP-683 (1979).

197. Radiation Behavior of Metallic Materials for Fast Reactor Core Components, Intern. Conf., Corse, France (1979).

198. D. Kramer, H. R. Brager, and J. S. Perrin (Eds.), Effects of Radiation on Materials: 10th Conf., ASTM-STP-725 (1981).

199. H. R. Brager and J. S. Perrin (Eds.), Effects of Radiation on Materials: 11th Conf., ASTM-STP-782 (1982), Session III, 343-593.

200. F. A. Garner and J. S. Perrin (Eds.), Effects of Radiation on Materials: 12th Conf., ASTM-STP-870 (1985).

201. R. S. Averback et al., Phys. Rev. B18 (1978) 4156.

202. J. H. Kinney, M. W. Guinan, Z. A. Munir, J. of Nucl. Mater. 122&123 (1984) 1028-1032.

203. K. Anderko, J. of Nucl. Mater. 95 (1981) 31-34.

CHAPTER V

EXPERIMENTAL FACILITIES AND PROCEDURES

A. Metallurgy of HT-9 Ferritic Steel Studied

The HT-9 ferritic steel used in this study was obtained from the General Atomic Company (Fusion-Ferritics Electroalloy with heat treatment number 9-607-R2). The chemical composition of this material is given in Table V-1.[1,2] The material, which was a plate with the dimension 254mmX254mmX3.18mm, was received in January 1982.

Since the thickness of the material received was not proper for the TEM study, the material was delivered to Argone National Laboratory (ANL) Material Science Division for rolling and a reheat-treatment. According to the record of ANL engineers,[3] the material used in this research was mechanical treated as follows. A piece of the material with dimension 114.5mmX254mmX3.18mm was ground to about 2.2mm in thickness with an equal amount of material removed from each face. Then it was cold rolled to 1.27 mm, heat treated, vapor blast cleaned, cold rolled

Table V-1. Summary of Chemical Composion (in wt.%) for Various Heats of 12Cr-1MoV Ferritic Steels.

Materials Specifi-cations	Elements													
	Fe	Cr	Mo	V	W	Ni	Mn	C	S	Si	P	N	O	Nb
AISI 422	bal.	11.0 to 13.0	0.75 to 1.25	0.15 to 0.30	0.75 to 1.25	0.5 to 1.0	1.0	0.20 to 0.25	.025	0.75	.025	-	-	-
Sandvik HT-9	bal.	11.5	1.0	0.3	0.5	0.5	0.55	0.20	0.02	0.4	0.02	-	-	-
HEDL/FBR 91353	bal.	12.34	0.99	0.45	0.50	0.46	0.39	0.23	.002	0.23	.006	.005	-	-
HEDL/FBR 91354	bal.	12.39	0.99	0.45	0.50	0.49	0.39	0.20	0.01	0.14	0.02	0.01	-	-
ORNL/FBR XAA-3587	bal.	11.99	0.93	0.27	0.54	0.43	0.50	0.21	.004	0.18	.011	0.02	.005	.02
GA/(AOD) 9607	bal.	11.64	1.01	0.30	0.57	0.52	0.57	0.20	.007	0.24	.018	.044	.013	-
GA/(ESR) 9607-R2*	bal.	12.10	1.04	0.28	0.45	0.51	0.57	0.20	.003	0.17	.016	.027	.002	-

* the material used in this thesis research.

again to 0.76 mm (0.030 in), and heat treated and cleaned again. The heat treatments were conducted in an electrically heated resistance furnace in air, but the sheets were double-wrapped in stainless steel foil. All heat treatments consisted of heating for 35 minutes at 1050^{o} C followed by air cooling and then a 2 hours and 35 minutes treatment at 770^{o} C, again followed by air cooling. The original rolling direction was preserved in all processing and was so identified on the piece that was treated.

Table V-1 shows the chemical composition of various commercial 12Cr-1MoVW ferritic steels. All of these materials are claimed to be HT-9 which was first produced by the Swedish Sandvik Steel Company. The nominal HT-9 composition is shown in the table. The material, HT-9, is a commercial ferritic/martensitic steel and has been used in various areas for about 20 years. It has a chemical composition corresponds with the AISI 422 steel. From the continuous cooling curve of a material that has a chemical composition very close to HT-9,[4] the equilibrium phase of HT-9 after the heat treatment should be tempered martensite. A more detailed discussion of the

microstructure of as-received HT-9 will be presented in Chapter VI.

Although all these materials have roughly similar chemical composition, the minor differences in alloy components could play a significant role in the precipitate evolution of this material during thermal annealing and irradiation. The details of the microstructural evolution of the HT-9 alloy following thermal annealing and irradiation will be discussed in Chapter VI and VII.

B. Heavy Ion Irradiation Facility

The heavy ion irradiations of the HT-9 ferritic steel study were conducted at the University of Wisconsin Heavy-Ion Irradiation Facility which uses a tandem Van de Graff Accelerator (High Voltage Engineering Corporation, Model EN). A schematic of the irradiation facility is shown in Fig.V-1 and it has been described in detail elsewhere.[5]

To produce a high enough intensity of heavy ion beams in the accelerator requires a bright and reliable source of negative ions. This facility uses a SNICS (source of negative ions by cesium sputtering) type negative ion

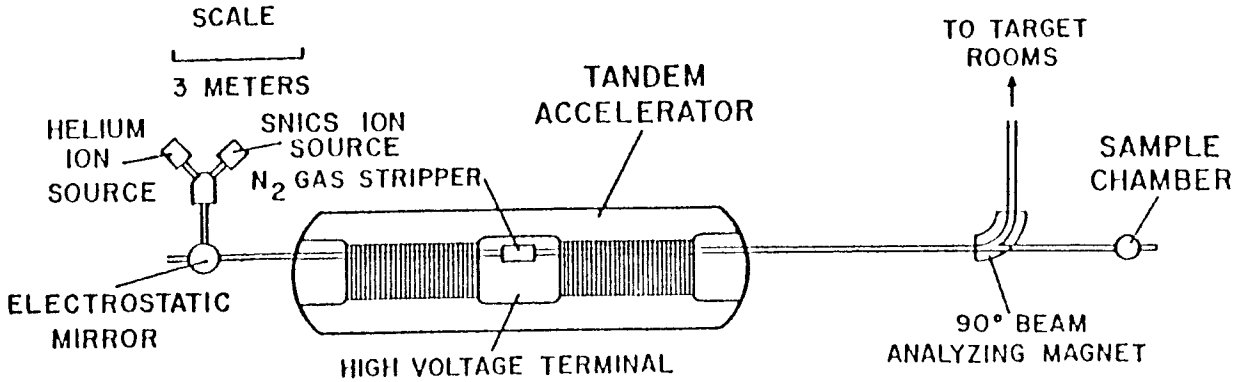

Fig.V-1 Schematic of heavy-ion irradiation facility. (5)

source developed by Billen and Richards[6,7] to produce negative heavy ion beams, such as Ni, Cu, Al ions etc. The basic components of the SNICS source include a negatively biased cylindrical cathode (e.g., nickel cathode for Ni ion beam), a helical tungsten ionizing filament, and a cesium reservoir. The cesium atoms are vaporized from the reservoir and ionized on the hot tungsten filament. The positive cesium ions will be attracted by the cathode and bombard the surface of the cathode sputtering nickel ions. The negative nickel ions (Ni^-) are formed from the charge exchange with Cs atoms and extracted through an exit aperature with an energy equal to the sputter cathode potential (2-4 KV).

These negative nickel ions then pass through a selecting magnet, are deflected 90 degree by an electronstatic mirror, are focussed by a quadrupole triplet, and injected into the low energy end of the accelerator. The negative ions are accelerated by the high positive potential V of the high voltage terminal and collide with nitrogen gas molecules in the gas stripper located in the high voltage terminal. The collision stage converts the energetic negative ions into

positive ions with different charges (e.g., +1, +2, +3, etc.) These positive ions are then accelerated through the high energy end of the accelerator and go into the target chamber.

Because of the random collision processes between negative heavy ions and nitrogen gas molecules, the beam of positive ions coming out of the accelerator has variant charge states. The energy of each state is given by:

$$E_n = eV(1+n), \quad n=1,2,3, \ldots . \qquad (V-1)$$

In this study, by using the Ni^{+3} charge state and a dome voltage of 3.5 MV, a 14 MeV Ni^{+3} ion beam can be obtained. The charge state is selected by using a quadrupole lens situated just outside of the high energy end of the accelerator.

The target chamber and its vacuum systems shown in Fig.V-2 is described by Smith and Lott.[5] As the figure shows, the heavy ion beams come into the target region from the tandem accelerator. The vacuum system for the target section is divided into three stages. The first pumping stage operated in the 10^{-4} Pa (1 Pa = 10^{-2} Torr)

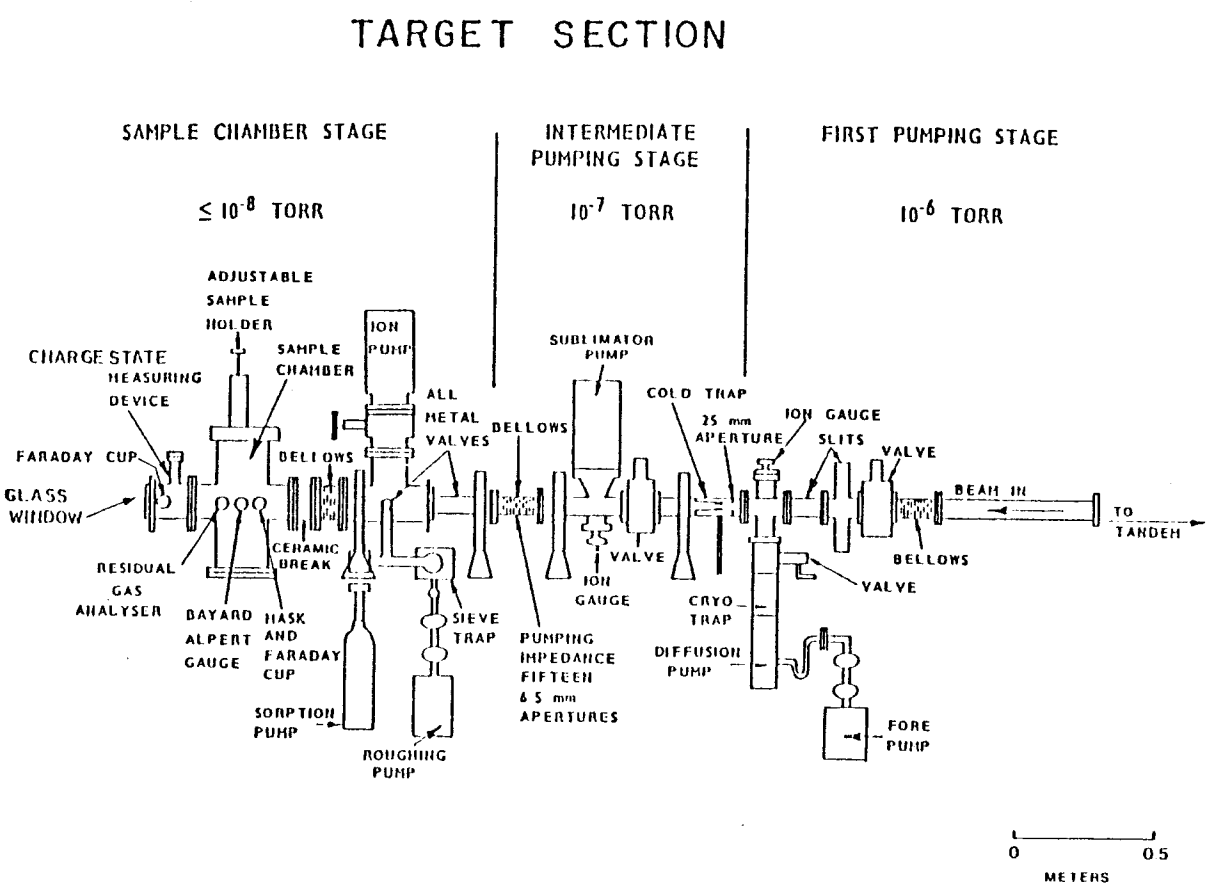

Fig.V-2 Schematic of the target section of the heavy-ion irradiation facility.

range which is provided by a 200 liter/sec diffusion pump. The intermediate stage can achieve 10^{-5} Pa by using a 400 liter/sec titanium sublimator pump. The third stage, the sample chamber stage, can reach a vacuum of 10^{-7} Pa and it is pumped by a large orbitron pump. The sample chamber is equipped with a Varian Model VGA-100 residual gas analyzer to allow the composition of residual gases in the sample chamber to be obtained. The whole target section lies about 1/2 degree off the axis of the tandem accelerator to prevent low Z ions and neutral atoms from hitting the specimen. Deflection of the heavy ion beam into the target section is accomplished by using the large analyzing magnet.

The Faraday cups used for detecting beam current are located at the entrance to the first pumping stage (entrance cup), directly before the specimen (mask cup), and directly behind the charge stage measuring device (exit cup), respectively. A 3 mm mask aperture is mounted in conjunction with the mask cup to precisely define the beam hitting the specimen during irradiation and prevent incorrect beam current readings. During irradiation, the beam currents are typically from 100 to 200 nA of charge.

A gold foil is inserted into the beam line, scattering the charge particles 90 degree from the beam axis into a solid state detector, which allows us to do the charge state analysis. The energy spectra of the heavy ion beam can be produced to insure that over 95% of the total charge particles are in the +3 charge state.

The specimen holder assembly, which was originally designed by Knoll[8], consists of a carousel with eight individual sample holders. This design allows individual heating of each specimen during irradiation by thermal radiation from ohmic-heated tantalum sheets. The individual thermocouple of each specimen holder allows continuous monitoring the temperature of all eight specimens during irradiation. The range of operating temperatures for this sample holder assembly is about 100 to 700^{o} C. The temperature of specimens immediately adjacent to the irradiating sample is about 200^{o} C lower than the irradiating temperature (e.g., for a irradiation at 500^{o} C, the adjacent specimen will be heated to 300^{o} C).

C. Light Ion Irradiation Facility

Helium has major effects on the microstructural evolution of ferritic steels during high temperature irradiation.[9,10] Therefore, a part of this study will be the examination of the effect of preimplanting helium into HT-9 specimens to the microstructural evolution under irradiation.

The experiments of helium effect studies will be conducted at the University of Wisconsin Light Ion Accelerator. This facility, which was described in detail by Bullen[11], is shown in Fig.V-3. The AN-700 accelerator, which is manufactured by the High Voltage Engineering Corporation, operates at an accelerating potential range from 200 to 700 KV.

The helium beam is supplied by the He gas supply cylinder and flows into the ion source which is controlled by a gas valve. Helium ions are accelerated through the dome and go into the target region. There are three major beam handling components situated along the beam line, including up-down, left-right steerers, a magnetic quadrupole doublet and a 90 degree analyzing magnet.

The specimen holder consists of a stainless steel

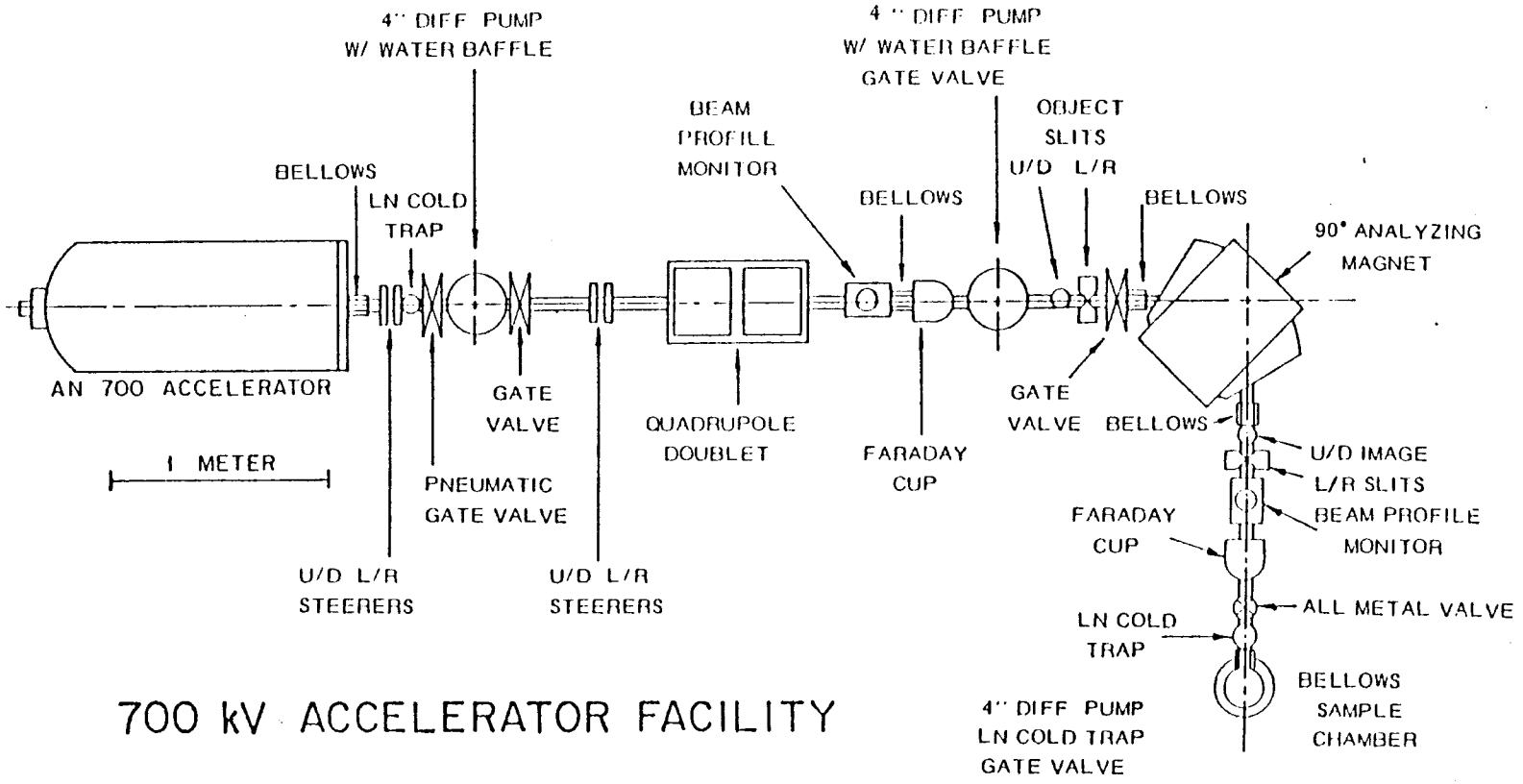

Fig.V-3 Schematic of light-ion irradiation facility. (11)

holder on which is mounted a specimen holder capable of accommodating three 5mmX10mm foils and/or three 3 mm discs. The holder is heated by electron bombardment from a biased filament. The isolated sample is radiatively heated with the temperature measured by thermocouples attached behind each sample position. The temperature range during the helium preimplantation was between 20 and 50^{o} C due to the beam heating.

D. Specimen Preparation

In this section, the methods that were used to prepare and to analyze specimens before and after thermal annealing and irradiation are discussed. The cross-section technique that used for preparing irradiated specimens was described in detail elsewhere.[12]

D.1 Thermal Anneal Study

A substantial portion of this thesis research was devoted to an investigation of the microstructures of HT-9 following thermal annealing. Two forms of specimens were prepared for this study. Foils of dimensions about 5mmX10mm were used for preparing carbon replicas, optical

micrographs and for microhardness tests and 3 mm discs were used for examing the microstructures in the transmission electron microscope (TEM). Prior to thermal treatment, the specimens were mounted on a epoxy polishing block and mechanically polished by a series of sandpapers (ending at 600 grit). The specimen block was then finished on a rotating wheel with 0.3 um alumina powder (Al_2O_3). After these steps, the surface of the specimen was bright and smooth. The same technique was used for the other side surface of the specimens. For the purpose of studying under TEM, the thickness of the discs was ground down to less than 0.25 mm.

Thermal annealing was performed in a high vacuum furnace with a background pressure of 10^{-7} torr or lower. The specimens were annealed in the temperature range between 300 and 900^{o} C in 100^{o} C increments, for the time intervals of 2 hours and 24 hours. After thermal annealing, the specimens were cooled in the furnace. The specimen temperature was measured by calibrated chromel-alumel thermocouples attached to the specimen container and was maintained to within $\pm 10^{o}$ C.

The 3mm TEM specimens were electrothinned by

ultilizing a commercial twin-jet electropolisher with a solution of 10% $HClO_4$ and 90% ethanol at -20^{o} C and 20 mA. The opitical micrographes were produced from the 5mmX10mm foils by etching in a picral solution (1 gram picric acid, 5 ml hydrochloric acid and 100 ml ethanol) for about 45 seconds. The carbon extraction replicas were generated from coating a thin layer of carbon film to the etched surface of the foils by using a carbon evaporator and re-etched in the same solution for about 10 minutes to loosen the carbides on the foil surface. Fig.V-4 illustrates the procedures of making carbon extraction replica.

Room temperature Vickers microhardness tests were performed on the as-received and thermal annealed foils using a Buehler Micromet microhardness tester. Each specimen was tested at 20 different points and optically measured twice for each point. The Vicker hardness number was obtained by measuring the average diagonal length of the diamond-shape indented spots.

D.2 Ion Irradiation Study

There are two sets of HT-9 specimens which were irradiated with heavy ions for this study. One set of

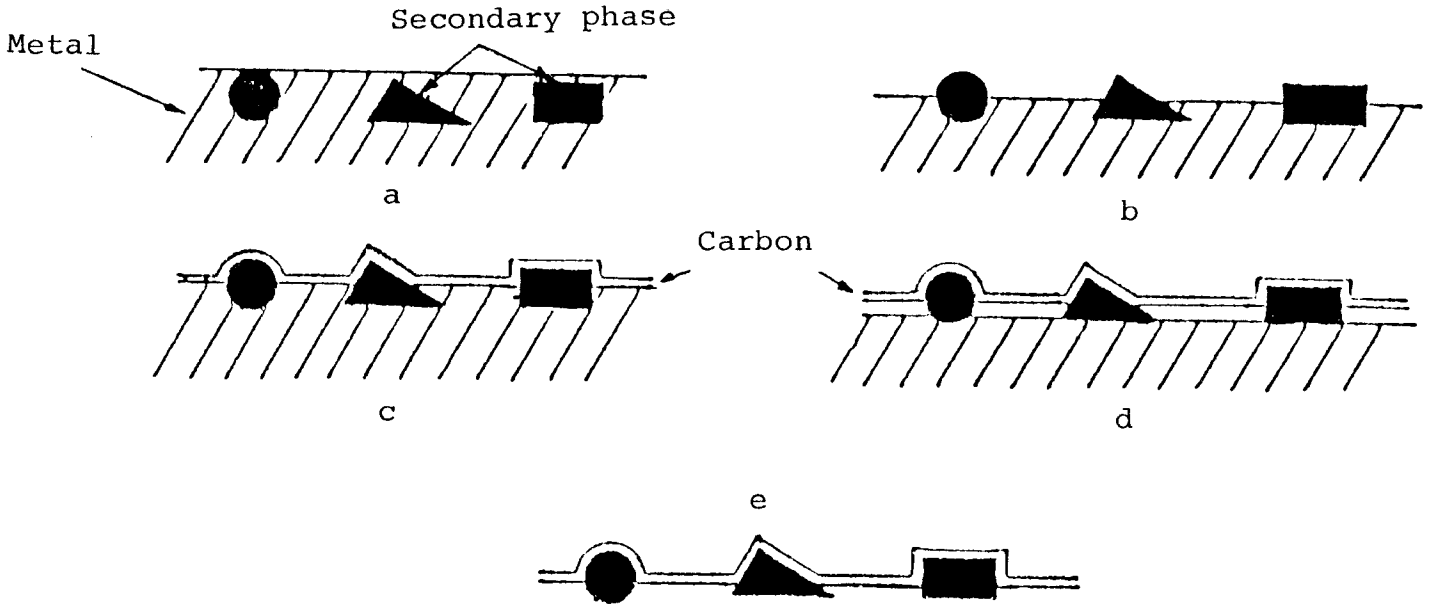

Fig.V-4 The carbon extraction replica method.

(a) Metal specimen.
(b) Metal surface after first etch.
(c) Carbon layer on the surface.
(d) After the second etch, showing how inclusions are released.
(e) Final replica with inclusions attached.

specimens was irradiated with 14 MeV Ni^{+3} ions alone and the other set of specimens was irradiated with 14 MeV Ni^{+3} ions after being implanted with 100 appm helium. All the irradiated specimens were examined using the cross-section technique.[12] Table V-2 shows the irradiation parameters for all the specimens in this study.

Before irradiation, the 5mmX10mm foils were mechanically polished as described in previous section. After irradiation, the specimens were removed from the accelerator and marked, and then stored in plastic vials filled with methanol and kept in a freezer (-20^{o} C) until electroplating. Fig.V-5 shows the schematic of the cross-section technique. The critical procedures are the steps 2 and 4, where the irradiated specimen is electroplated and thinned, respectively. Special care prior to and during the electroplating step is important in order to obtain a good adhersive interface.

The detail of the cross-section technique was described elsewhere.[12] The following summarizes the basic procedures and the experimental conditions. The electroplating solution consists of 200 gm ferrous chloride ($FeCl_2.4H_2O$), 75 gm pure salt (NaCl), 75 gm

Table V-2. Temperature and Dose Matrix for Ion Irradiation Study

Temp. (°C)	No Helium Dose (dpa) at 1.3 um			100 appm He Preimplanted Dose (dpa) at 1.3 um		
300	10 (40)	30 (100)*	---	---	---	---
400	10 (40)	30 (100)	---	10	30	---
500	10 (40)	30 (100)	60 (200)	10	30	60
600	10 (40)	30 (100)	---	10	30	---

* Numbers in the () indicate the doses at the peak damage region (2.2 um).

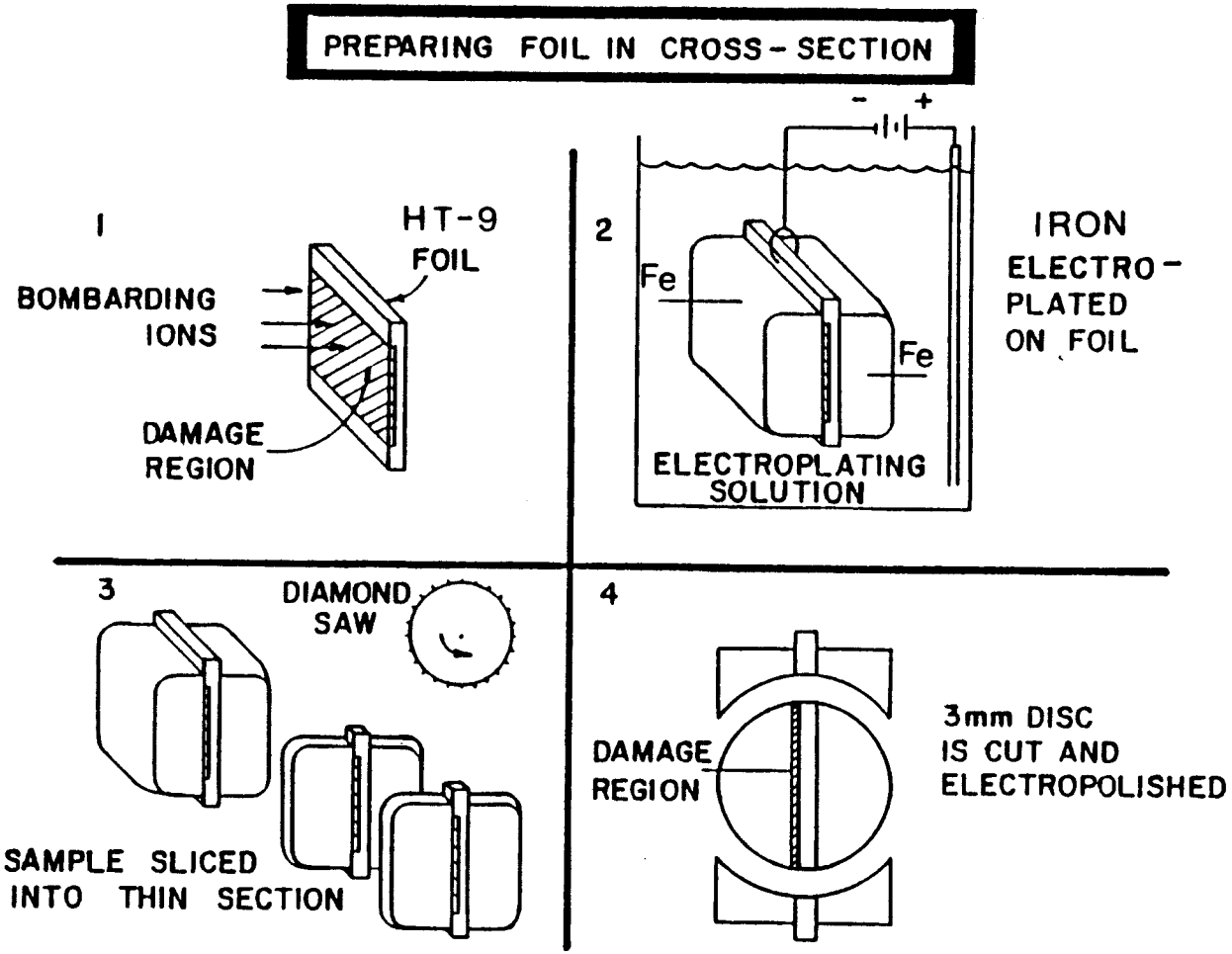

Fig.V-5 Schematic of the cross-section technique to prepare a TEM specimen.

calcium chloride ($CaCl_2$) and 850 ml distilled water. The electroplating is performed at about 88° C, and the temperature is controlled by an automatic feedback circuit. Prior to the start of the plating, the irradiated foil was dipped into a pickling solution to loosen the surface oxide and then quickly washed with distilled water spray and immediately transfered into the electroplating solution and struck for 7 seconds at 94° C and 100 mA to remove the surface oxide layer. The pickling solution consists of 2 gm thouriea, 15 ml sulfuric acid (H_2SO_4) and 80 ml distilled water. After the surface oxide was removed, the current is then reversed to allow the electroplating to begin. The temperature is set at 88° C during the whole plating period and the current is 70 mA. It usually takes about 24 hours to plate a thickness of 3 mm. During the plating period, the solution is constantly agitated by a nitrogen gas bubbler. Fig.V-6[13] shows the schematic of the sample holder and the gas bubbler used for the plating. Fig.V-7 shows the specimen position in the whole plating assembly.

After electroplating, the specimen is mounted in a

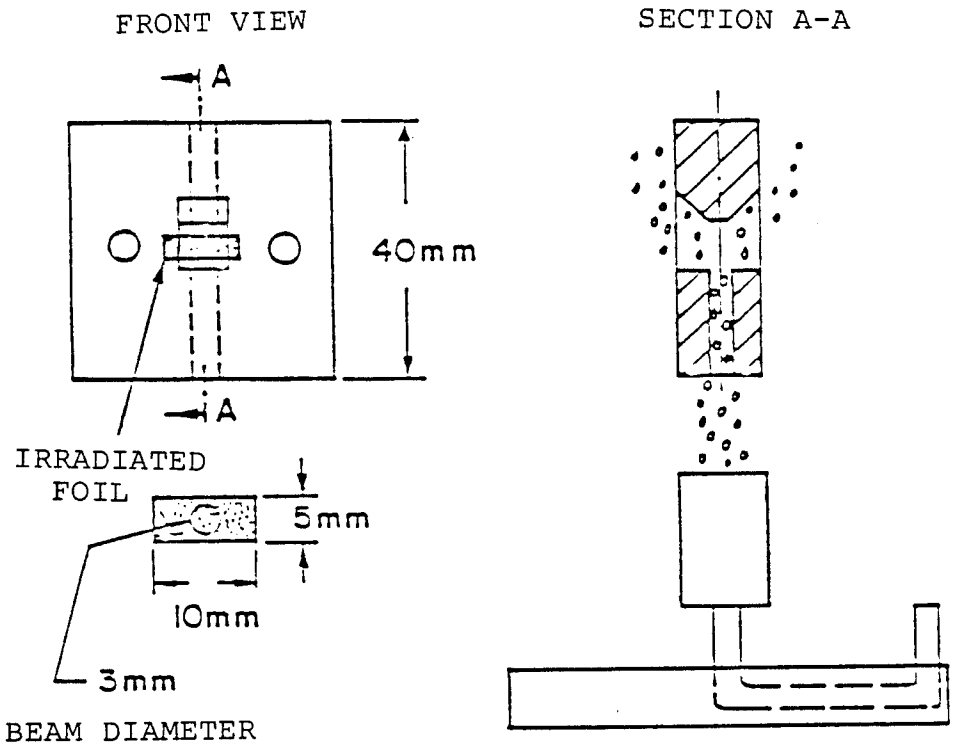

Fig.V-6 Schematic of sample holder and gas bubbler. (13)

SCHEMATIC OF THE WHOLE PLATING ASSEMBLY

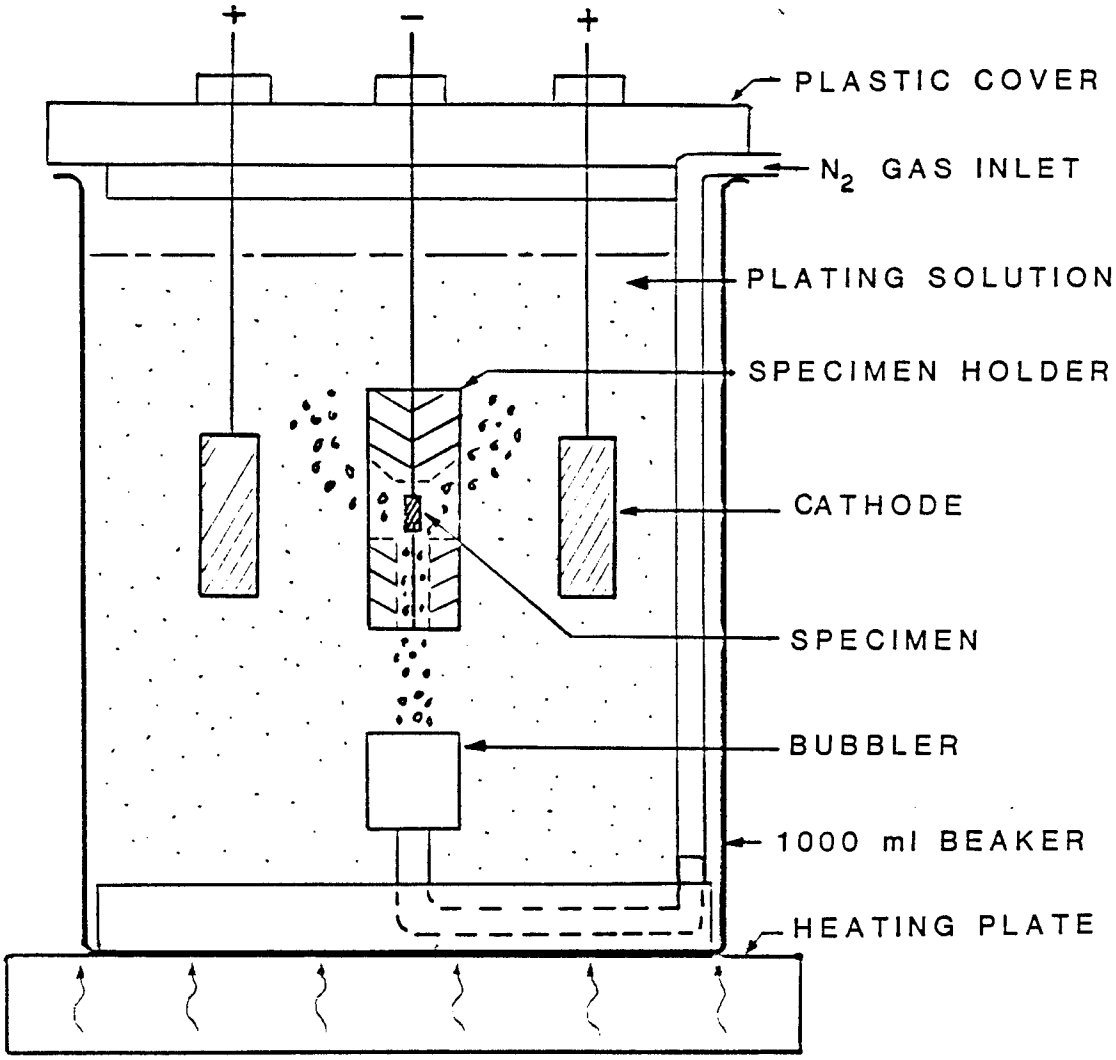

Fig.V-7 Schematic of the whole plating assembly.

box filled with epoxy agent to form a hard epoxy block. The block is then sliced by a diamond saw with the direction vertical to the irradiated surface of the specimen. The thickness of each slice is normally around 10 mils and generally about 6 slices can be cut from the irradiated zone. A 3 mm disc is punched from the center of each slice. The discs need to be cleaned very carefully to remove surface contamination. A commercial twin jet polisher is used to polish the discs until perforation. The polishing solution, which is used in this study , consists of 10% $HClO_4$ and 90% ethanol at the condition of -20^{o} C and 80 mA.

Since HT-9 has much higher chromium content than plated iron, it has relatively a lower polishing rate. This can cause the perforation to always occur in the plated iron region which is, of course, not the objective for the study. Another problem is that the irradiated region is only about 3 um wide. The probability of the perforation forming right on the interface or very close to the interface is relatively low. A technique that was developed by Zinkle[14] which has greatly improved the success rate of perforating at right place. Both sides of

the TEM disc are covered with a protective lacquer with the exception of a 50 um wide strip along the irradiated interface. The specimen is then electropolished for a period of time to form a dish along the interface which will insure that the final perforation will form along the irradiated interface. The lacquer is then removed and the specimen is polished until perforation occurs. In case that the perforation was not formed at the interface, the hole is then extended by an ion mill toward the interface. The successful rate of preparing a good TEM sample is very high in considering that there are 6 slices of specimen can be obtained from one irradiated specimen.

E. Analysis Procedures

The microstructure of both thermal annealed and ion irradiated specimens was examined in two ways: (a) conventional transmission electron microscopy (CTEM) and (b) X-ray energy dispersive spectroscopy (EDS) in STEM (scattering TEM) mode. The CTEM analyses were conducted in a JEOL-200CX II TEM/SCAN electron microscope operated at 200 KV. The main purpose for the CTEM analysis was to image microstructures (e.g., dislocations, loops,

precipitates, voids, etc.) and the diffraction patterns of various phases. The EDS system, which is mounted on the 200CX electron microscope, was used for detecting the chemical composition of the various phases. Combining the EDS analysis and the diffraction pattern of a precipitate with the carbon extraction replica method allows the precipitate evolution during thermal annealing and irradiation to be readily analyzed.

According to Goldstein[15], in the thin film approximation, the relative concentration ratio of any two elements under observation is directly proportional to their integrated X-ray intensity ratio, independent of the foil thickness and composition.

$$\frac{C_A}{C_B} = R_{AB} \frac{I_A^{K_\alpha}}{I_B^{K_\alpha}} \qquad \text{(V-2)}$$

This equation is known as Cliff-Lorimer equation,[16] where C refers to concentration, I is relative intensity of the K_α line, and R_{AB} is a material and machine constant. The constant used in this study was determined from the experimental measurement of relative X-ray intensity ratios from specimens of known composition.[17]

The thin film approximation can only be used when the thin film criterion is held. Tixier and Philibert[18] described the criterion which is for each element measured in the thin film,

$$\chi_A \rho t < 0.1 \qquad \text{(V-3)}$$

otherwise an absorption correction is necessary. The term χ_A is equal to $(u/\rho)\csc(\alpha)$, where (u/ρ) is the mass absorption coefficient for the charateristic X-ray of element A in the specimen and α is the take-off angle. The term t is the foil thickness and ρ is the density of the specimen.

There were a few specimens which contained very small precipitates (e.g., diameter less than 20 nm) that were beyond the resolution ability of JEOL-200CX electron microscope. These precipitates were then examined using a VG-HB501 STEM equipped with both X-ray EDS and electron energy loss spectroscopy (EELS) systems. The HB501 uses a field emission gun so that the electron probe size is about 0.5 nm which is quite suitable for small precipitate analysis. The EELS system was used for identifying light

elements (e.g., nitrogen, carbon, etc.) in precipitates. This system allows a distinction between carbides and nitrides to be made.

REFERENCES FOR CHAPTER V

1. R. D. Stevenson, B. E. Thurgood, and S. N. Rosennasser, in ADIP Progress Report DOE/ER-0045/3 (1980) 192-200.

2. T. A. Lechtenberg, ADIP DOE/ER-0045/8 (1982) 363-370.

3. R. F. Bomagala, Sr., private communication (Material Science Division, Argone Natl. Lab.)

4. E. Kauhausen and P. Kaesmacher, "The Metallurgy of Welded Heat-Resistant 12%Cr Steels + Mo-V-W", Schweissen and Schneiden 9 (1957) 414-419.

5. H. V. Smith ans R. G. Lott, Nucl. Instr. Methods 143 (1977) 125-132.

6. J. H. Billen and H. T. Richards, Proc. of symp. of Northeastern Accelerator Personnel, Oak Ridge Natl. Lab. (1978) p.137.

7. J. H. Billen, in the Sixth Conf. on Application of Accelerators in Research and Industry, Nov. 1980, also UWFDM-368.

8. R. W. Knoll, "Effects of Heavy Ion Irradiation on the Phase Stability of Several Cu-based Alloys", Ph.D. thesis in Nuclear Engr. Dept. at the Univ. of Wisconsin-Madison (1981), also UWFDM-436.

9. P. J. Maziasz, R. L. Klueh, and J. M. Vitek, ADIP DOE/ER-0045/14 (1985) 81-86.

10. G. Ayrault, DAFS Progress Report DOE/ER-0046/8 (1982) 182-190.

11. D. B. Bullen, "The Effects of Implanted Hydrogen and Helium on Cavity Formation in Self-Ion Irradiated Nickel", Ph.D. thesis in Nuclear Engr. Dept. at Univ. of Wisconsin-Madison (1984).

12. J. J. Kai and G. L. Kulcinski, "The Cross-Section Technique for Preparing TEM specimens of Heavy Ion Irradiated Ferritic Steels", UWFDM-643 (1985).

13. S. J. Zinkle and R. L. Sindelar, DAFS Report DOE/ER-0046/18 (1984) 133-141.

14. S. J. Zinkle, "Effects of Thermal Annealing and Ion Irradiation on the Properties and Microstructures of Copper Alloys", Ph.D. thesis in Nuclear Engr. Dept. at the Univ. of Wisconsin-Madison (1985), also UWFDM-642.

15. J. I. Goldstein, in Introduction to Analytical Electron Microscopy, Chapter 3, J. J. Hren, J. I. Goldstein, and D. C. Joy (Eds.), Plenum Press., New York (1979).

16. G. Cliff and G. W. Lorimer, in the Proc. of 5th European Congress on Electron Microscopy, Institute of Phys., Bristal (1972) p.140.

17. N. J. Zaluzec, in Phase Stability during Irradiation, AIME (1981) 141-164.

18. R. Tixier and J. Philibert, in the Proc. of 5th Intl. Cong. on X-ray Optics and Microanalysis, G. Mollenstedt and K. H. Gaukler (Eds.), Berlin (1969) p.180.

CHAPTER VI

MICROSTRUCTURAL CHARACTERISTICS OF AS-RECEIVED AND THERMAL ANNEALED HT-9

A. Microstructures of As-Received HT-9 Ferritic Steel

The as-received HT-9 ferritic steel that was used in this study has been described in Section V.A of this thesis. Fig. VI-1(a) shows the optical micrographs of an as-received HT-9 specimen after mechanical polishing and etching. It is clearly seen that the tempered lath martensite is the major structure of this alloy. A very small amount (<1%) of δ-ferrite is also found in the microstructure. The material is filled with large carbides, especially, along the residual austenite grain boundaries. The typical average size of austenite grain is about 40 um in diameter and the average width of martensite lath is only about 1 um. Fig.VI-1(b) shows an as-received HT-9 foil that has been electroplated with iron and cross-sectioned. The interface between HT-9 and plated iron is clearly seen. It is noticed that in the region near interface, the HT-9 material has a relatively

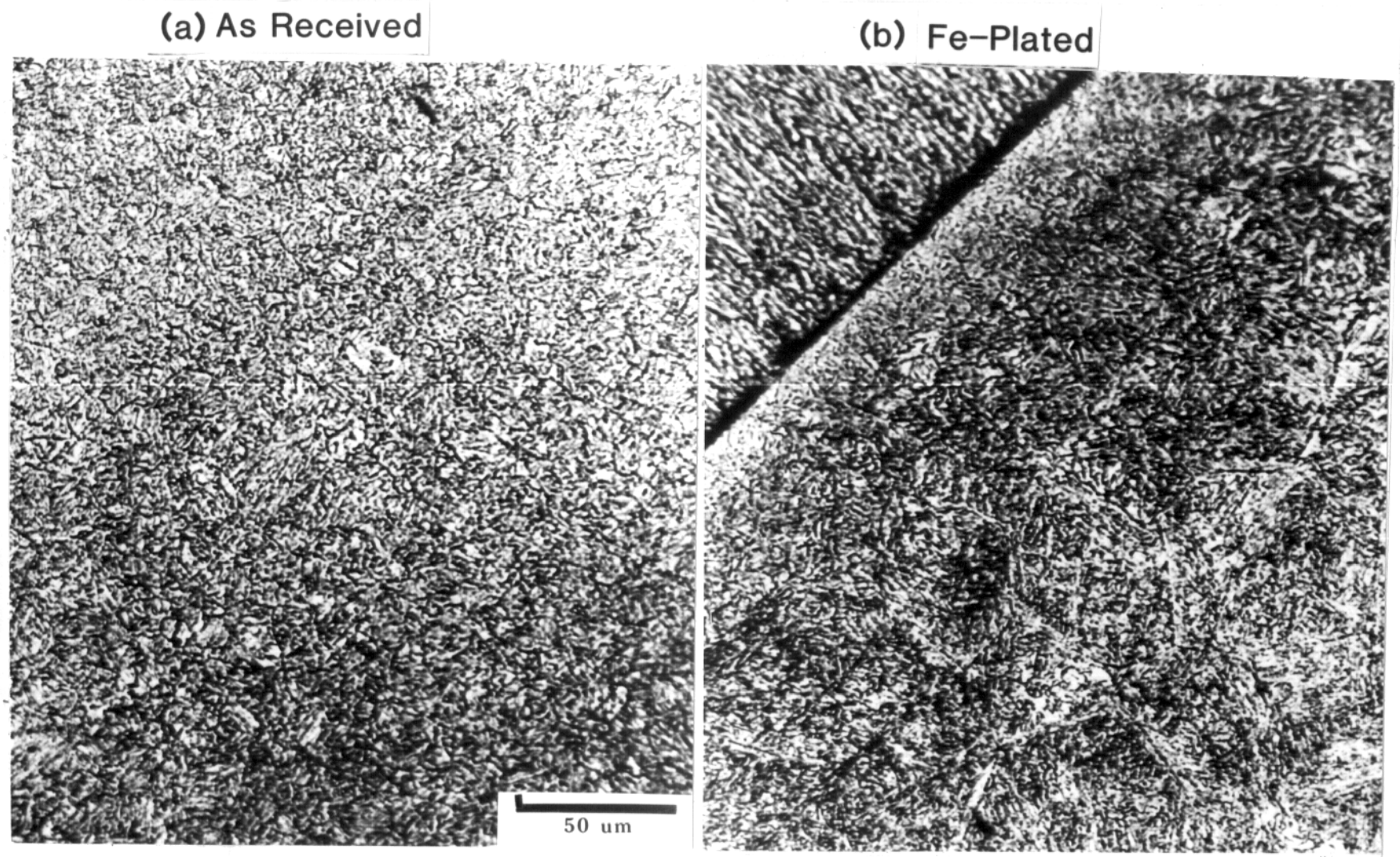

Fig.VI-1 Optical micrographes of as-received and Fe-plated HT-9 alloy.

less etching effect and therefore, the microstructure is not as clear as in other areas away from the interface. This is due to the passive protection effect of plated iron on the high chromium alloy (HT-9).

The general TEM microstructure of as-received HT-9 is given in Fig.VI-2. A low magnification picture is shown in Fig.VI-2(a) which gives a rough idea of how complicated this material is in its original form. Fig.VI-2(b), (c) and (d) are at three times higher magnification of certain specific regions in Fig.VI-2(a) and show the three regions of tempered martensite, ferrite, and heavily tempered carbides region, respectively. The tempered martensite region contains tempered martensite laths with some precipitates (mainly $M_{23}C_6$) along the lath boundaries. It is the predominant microstructure in the HT-9 ferritic steel and occupies more than 90% of the total volume of the material. The heavily tempered carbide region contains a high number density (about $1X10^{14}$ cm^{-3}) of carbides including the $M_{23}C_6$ and MX phases. The ferrite region is the relatively clean area and contains some needle-like precipitates which are identified as M_2X phase (Cr-enriched). All regions have a very high dislocation

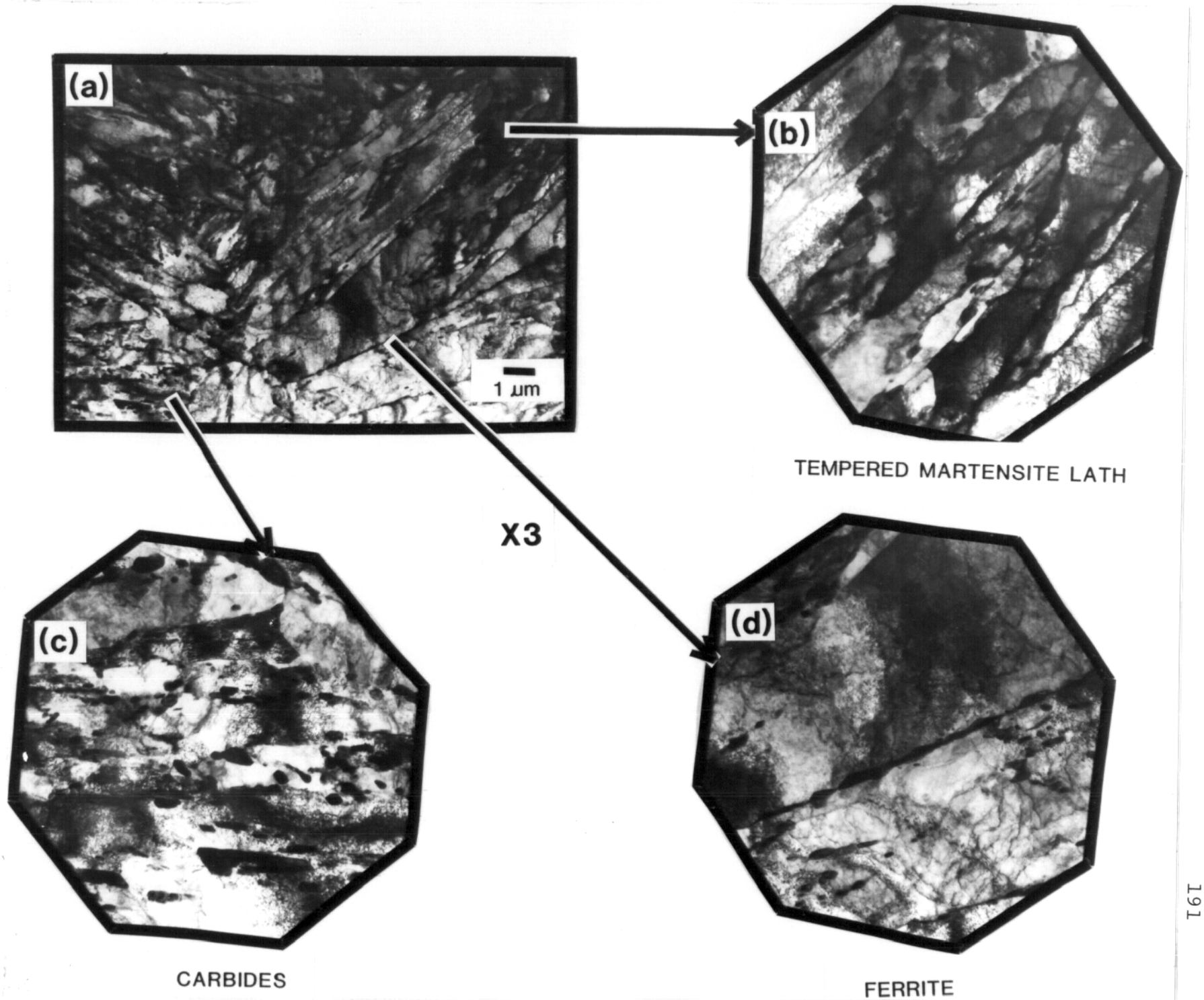

Fig.VI-2 TEM microstructures of as-received HT-9 alloy.

density. Fig.VI-3 shows the typical dislocation microstructure in HT-9 in bright field, dark field, and weak beam dark field images. The average dislocation density in the as-received HT-9 is about $2X10^{11}$ cm^{-2}. The dislocation density measurement is accomplished by using the ($\vec{g}$, $3\vec{g}$) weak beam dark field (WBDF) technique.[15] The specimen thickness is determined by examining an inclined dislocation running through the specimen from top to bottom and counting the number of segments of the dislocation in matrix. This is also double checked by focusing the electron beam to produce a pair of contamination spots and measuring the distance between the two spots after tilting a large angle.

Fig.VI-4 shows a carbon extraction replica which is another way to further examine the various precipitates and related regions in as-received HT-9. Fig.VI-4(a) is a low magnification microstructure at a triple point of residual austenite grain boundaries. Fig.VI-4(b), (c) and (d) are three times enlarged view of each individual region of precipitates in tempered martensite lath, ferrite, and residual austenite grain boundary, respectively. In all, four types of precipitates were

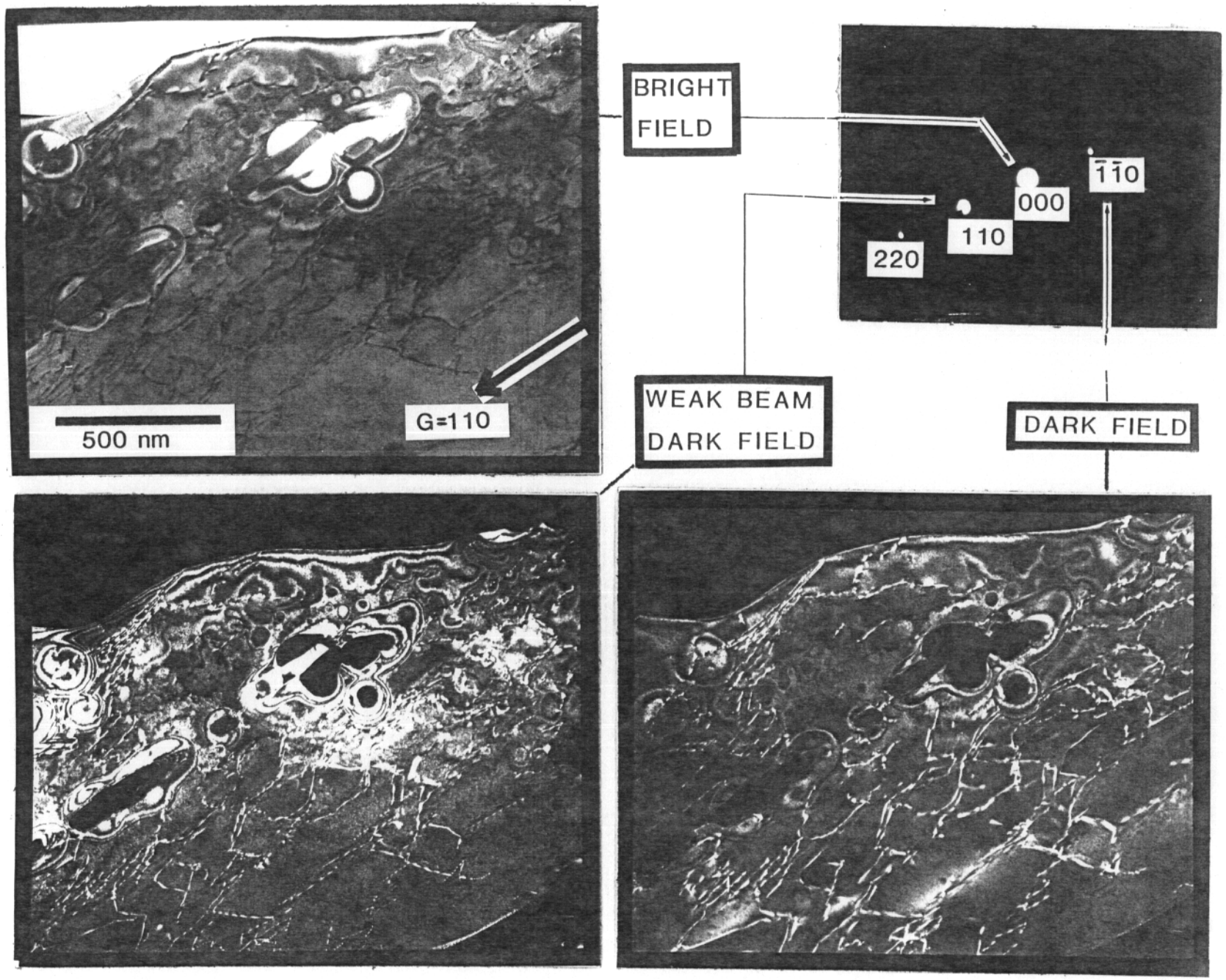

Fig.VI-3 Dislocation density measurements in HT-9 alloy.

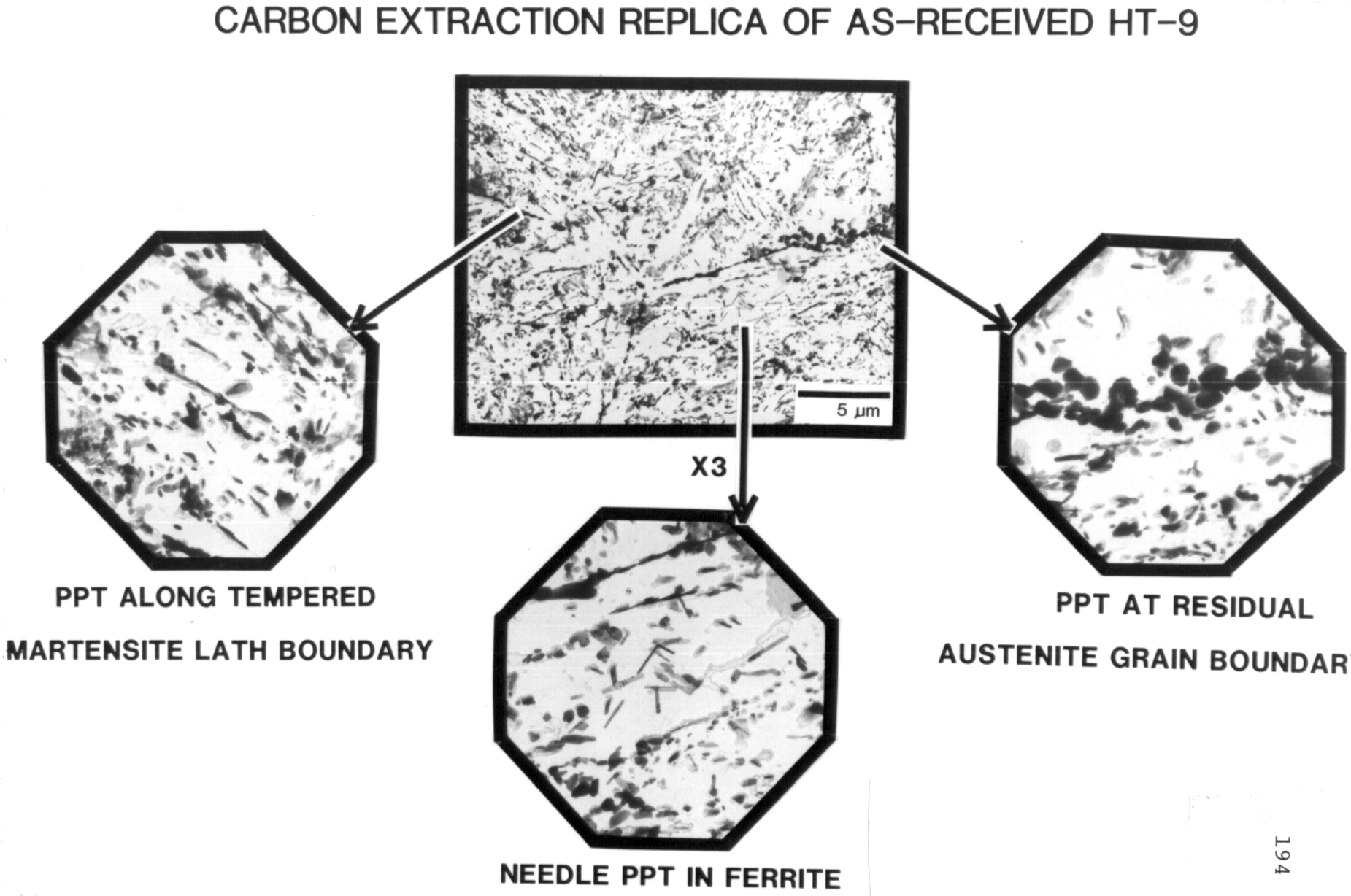

Fig.VI-4 Carbon extraction replica of as-received HT-9 alloy.

identified by the individual precipitate electron diffraction pattern and the X-ray EDS microanalysis. They are equiaxed $M_{23}C_6$, elongated $M_{23}C_6$, platlet shaped MX, and needle-like M_2X phases.

The most predominant precipitate phase in HT-9 is the equiaxed $M_{23}C_6$ carbides which are distributed along the resicual austenite grain boundaries and in the matrix of the heavily tempered carbides region. The size of this type precipitate varies from 0.1 um to about 1 um in diameter. The $M_{23}C_6$ phase has a complex fcc crystal structure with a lattice parameter of 1.062 nm. An example of an $M_{23}C_6$ particle in a carbon replica is shown in Fig.VI-5. Both the bright and dark field images and the diffraction pattern are shown as well as the quantitative EDS result. It is clearly shown that the $M_{23}C_6$ is Cr-riched and the chemical composition is 62Cr-25Fe-8Mo-5W. It was found previously[1] that the matrix has a significant effect on the EDS results. Therefore, for an accurate quantitative chemical composition study, the carbon extraction replica technique is essential. Fig.VI-6 shows the lattice interference fringes of the {111} planes in an $M_{23}C_6$ particle that was protruding from

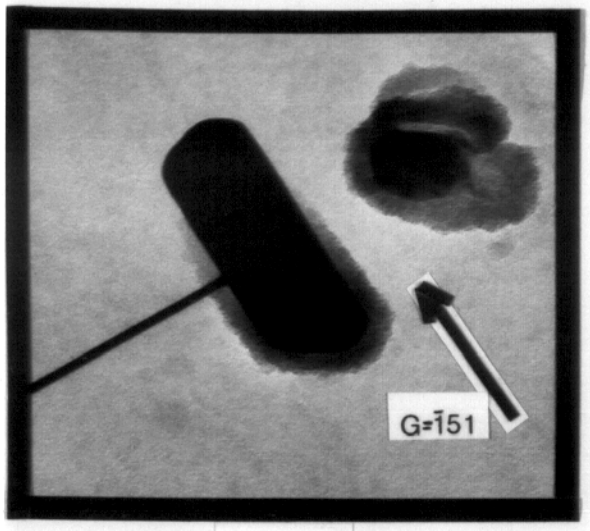

BF

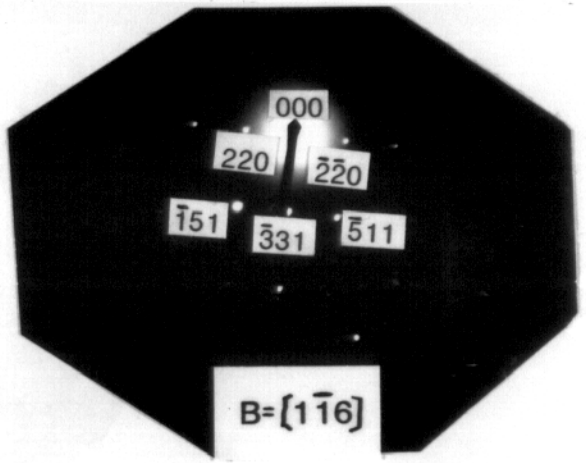

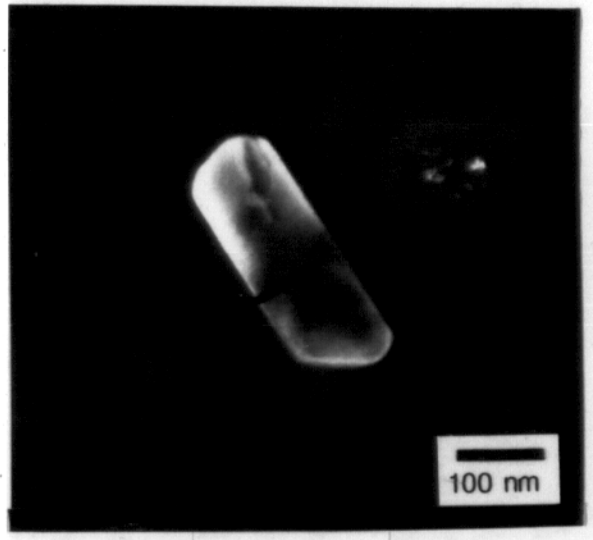

CDF

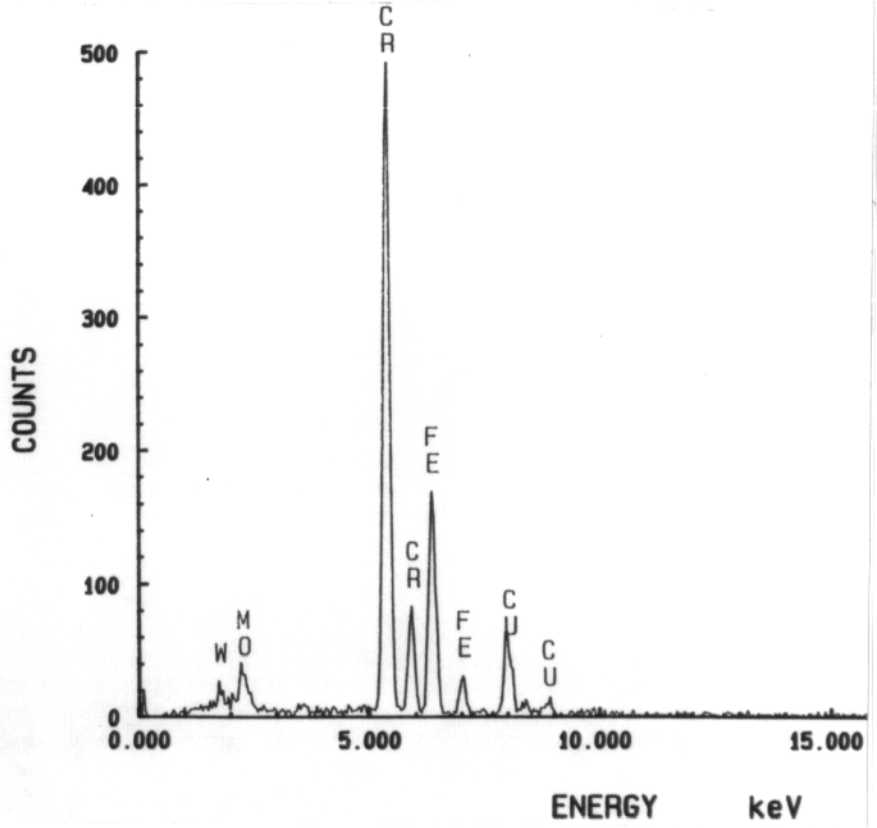

Fig.VI-5 $M_{23}C_6$ precipitates in carbon replica of as-received HT-9 alloy.

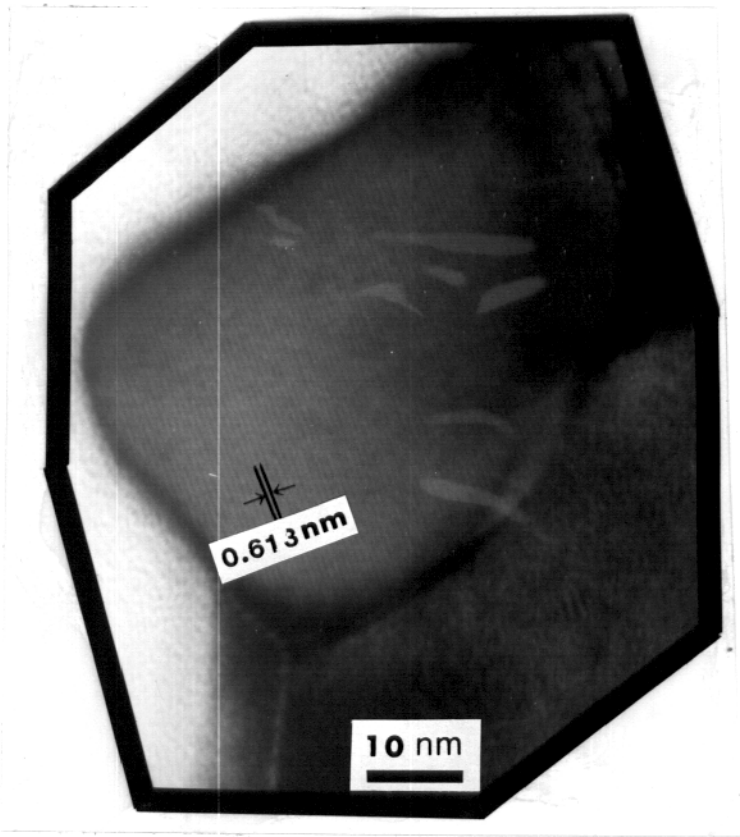

Fig.VI-6 The lattice interference fringes of the ‹111› plances of an $M_{23}C_6$ particle in HT-9 alloy.

the matrix at the edge of the hole in an HT-9 specimen. The comparison between the measurement of the fringe space and the tabulated value shows that the calibration of magnification of the JEOL 200CX TEM used in this study is accurate to ± 2%.

The precipitates along the tempered martensite lath boundary, which had irregular elongated morphology, were also identified as $M_{23}C_6$. Although these precipitates have a rather different morphology and chemical composition with respect to the equiaxed $M_{23}C_6$ phase, the individual precipitate diffraction pattern shows that they are indeed the $M_{23}C_6$ phase. Fig.VI-7 shows the phase both in the matrix and in a carbon replica. The quantitative EDS results show that this phase is highly enriched in Cr and also contains a small amount vanadium and iron. The chemical composition is 77Cr-3Fe-10V-8Mo-2W.

The third type of precipitate, which can be easily distinguished from others, is the needle-like particles appearing in the ferrite region. These particles were evenly distributed within the ferrite grains although sometimes a high density of the particles was found in areas close to residual austenite grain boundaries (see

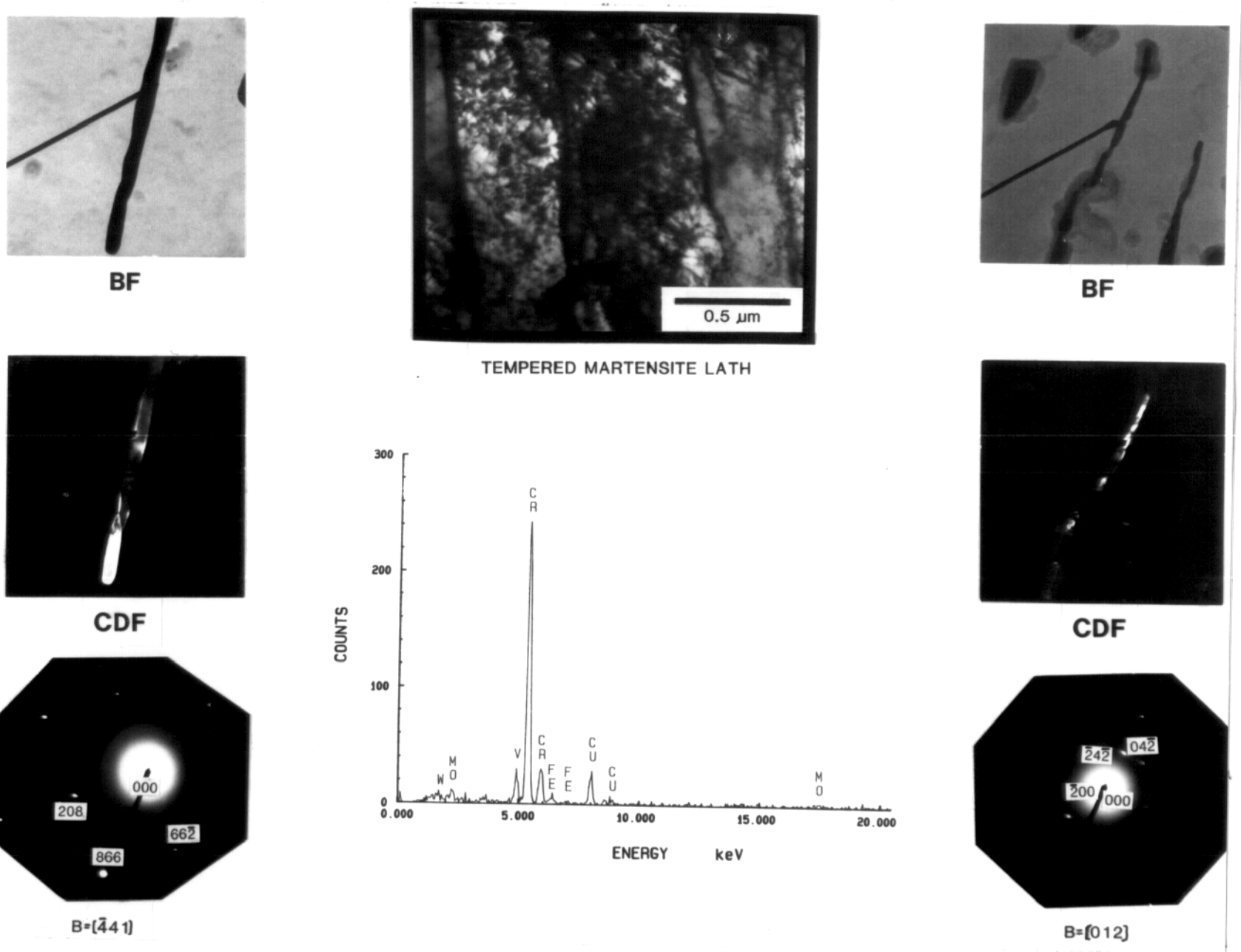

Fig.VI-7 Elongated $M_{23}C_6$ precipitates along tempered martensite lath boundaries in as-received HT-9 alloy.

Fig.VI-4). The diffraction pattern shows that this phase is M_2X and has an hcp crystal structure with lattice parameters of a_o=0.27nm, c_o=0.44nm. Fig.VI-8 illustrates the morphology, the diffraction pattern, and the EDS result. This phase is highly enriched in Cr and the quantitative chemical composition is 73Cr-3Fe-10V-11Mo-3W. The size of this type precipitate is about 0.2 um to 2 um long and 20 to 50 nm wide. It is noted that this phase is either the Cr_2C[2] or Cr_2N[3] phases that have been reported previously.

The fourth type precipitate is identified as MX phase with fcc crystal structure and lattice parameter of 0.42 nm. This type precipitate is characterized by thin plates and laths with edge dimensions from 50 to 300 nm. Gelles and Thomas[4] have reported an MX phase as a nitride in their neutron irradiation study. By using an electron energy loss spectrometry (EELS), they found that this phase is (V,Cr)N with no carbon, oxygen or boron. However, in earlier thermal tempering study by Smith[5], the V_4C_3 phase was identified as a transient phase in a material that has a chemical composition quite similar to HT-9. Therefore, at the present time without an EELS

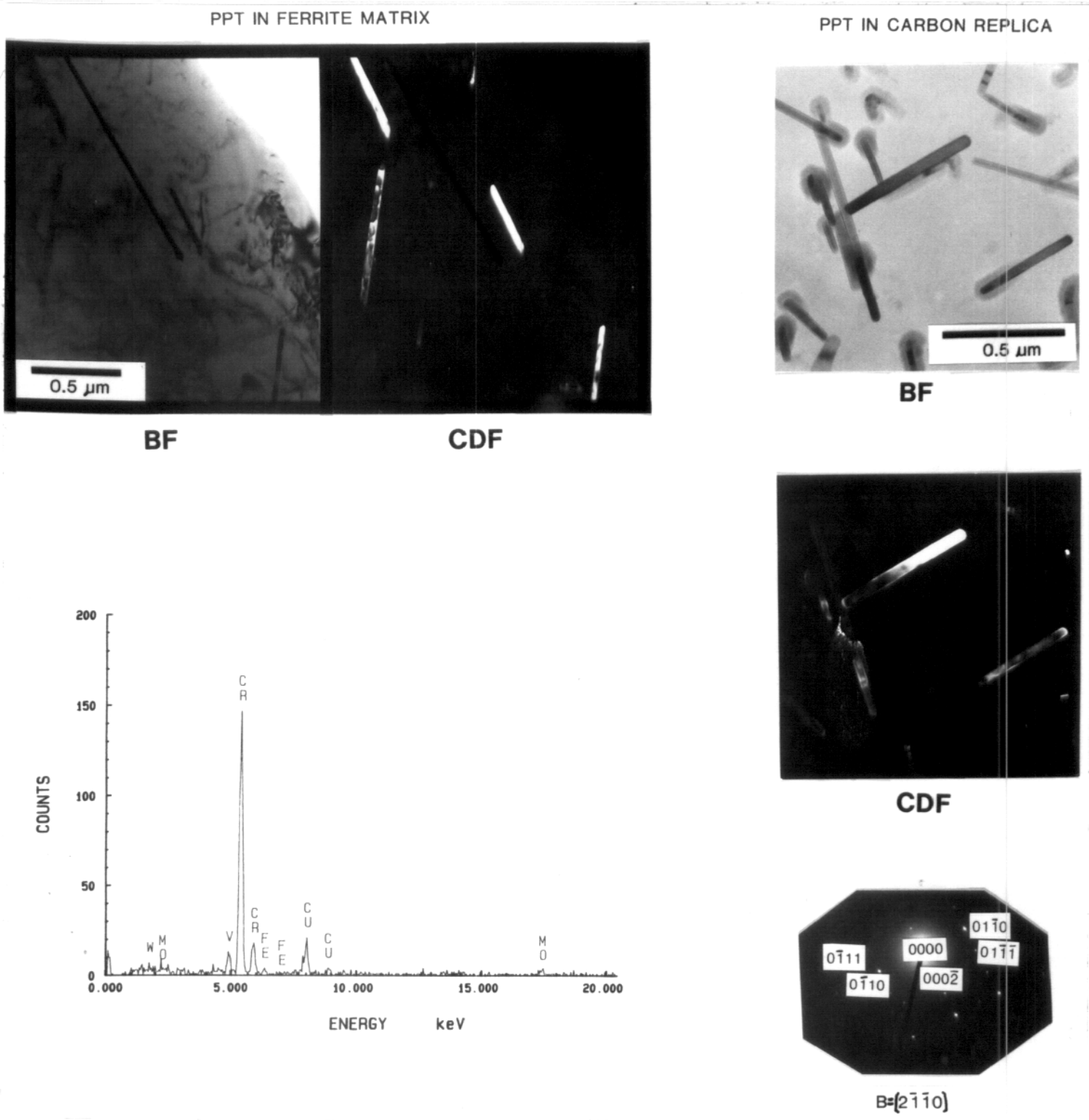

Fig.VI-8 M_2X needle-like precipitates in ferrite region of as-received HT-9 alloy.

analysis, this phase could be either carbide or nitride or a mixture of these two.[6] Fig.VI-9 shows the phase and EDS results.

Table VI-1 illustrates the quantitative analysis of these precipitates in as-received HT-9.

B. Thermal Annealing Effects

A thermal annealing study was initiated in order to investigate the microstructural stability of the as-received HT-9 ferritic steel under thermal effect alone. Since the irradiation experiments in this thesis were conducted over the temperature range of 300 to 600^{o} C for a time period between 2 to 24 hours, the thermal annealing study was also designed in these conditions. The thermal annealed specimens were held at a temperature between 300 and 900^{o} C (in 100^{o} C increment) for 2 h and 24 h time periods.

A sequence of optical micrographs that were taken from the various thermal annealed specimens are shown in Fig.VI-10 and VI-11. The microstructure did not change in the specimens annealed up to 600^{o} C. However, after annealing at 700^{o} C and higher temperatures, the tempered

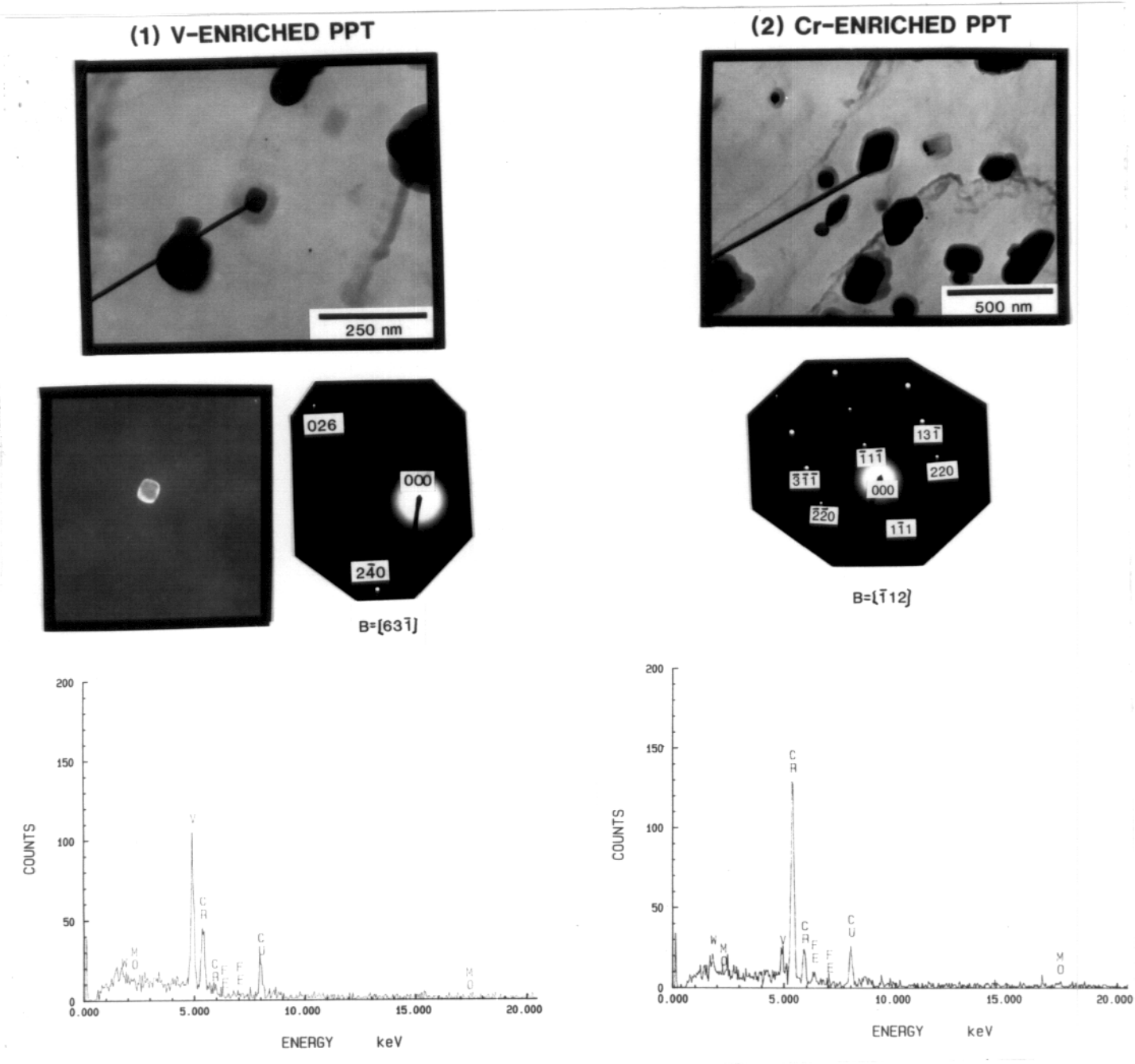

Fig.VI-9 MX platelet precipitates in carbon replica of as-received HT-9 alloy.

Table VI-1 Precipitation Phases in As-received HT-9

precipitate type	number density ($\#/cm^3$)	average dimension (nm)	morphology	quantitative EDS results (wt.%)	regions
$M_{23}C_6$ +	$6x10^{13}$	150	equiaxed	62Cr-23Fe-8Mo-5W-2V	tempered martensite
MX	$1x10^{13}$	50	platelet	81V-19Cr $ or 72Cr-28V	tempered martensite
M_2X	$5x10^{13}$ * $2x10^{12}$	20x400	needle-like	73Cr-3Fe-10V-11Mo-3W	ferrite
$M_{23}C_6$ +	$3x10^{13}$	30x200	elongated	77Cr-10V-3Fe-8Mo-2W	martensite lath boundary

* local density of small ferrite regions
+ same diffraction pattern but different morphology and composition
$ two kinds of chemical compositions of the same type precipitate

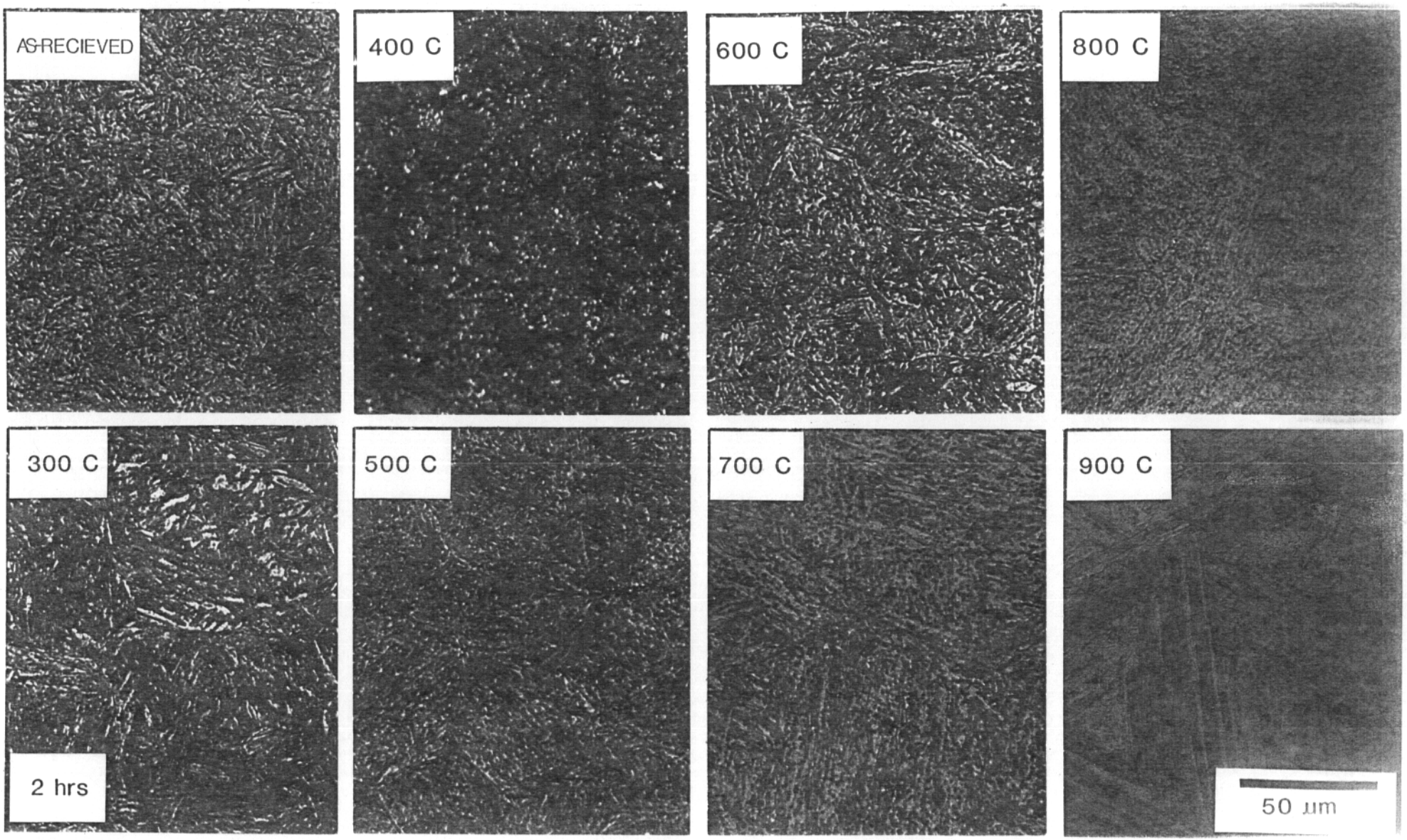

Fig. VI-10 Optical micrographs of HT-9 following thermal annealing for 2 hou

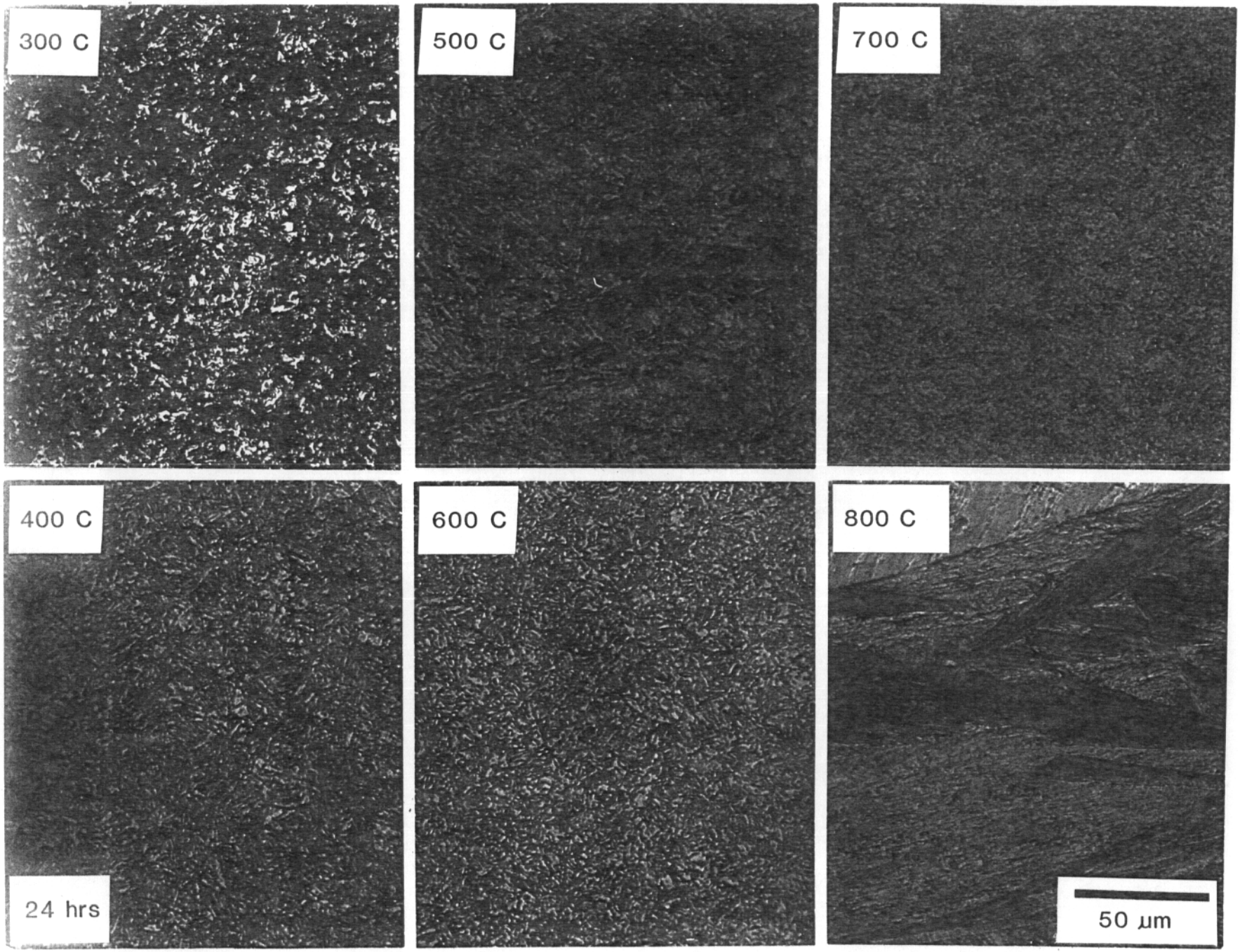

Fig. VI-11 Optical micrographes of HT-9 following thermal annealing for 24 hours

martensite lath started to recrystalize and eventually transfered totally back to martensite due to re-austenitization and the austenite to martensite transformation.

The transformation from tempered martensite to austenite and to martensite again was also showed in the microhardness test results. Fig.VI-12 shows the curves of Vicker hardness number (VHN) versus annealing temperature. It is clearly shown that VHN value graduately decreases with increasing annealing temperatures up to 600^{o} C and increases sharply after annealing at 700^{o} C and above. This indicates that the re-austenitization has occured and the austenite to martensite transformation produces the increase of VHN. Fig.VI-13 shows the VHN versus the universal parameter (Larson-Miller parameter)[7] $P=T(20+\log t)10^{-3}$, where T is the annealing temperature in ^{o}K and t is time in hour. The VHN value continuously decreases to a certain point and then increases sharply to about 450 and saturated, which is the VHN value for martensite structure.

A group of TEM micrographs that were obtained from these thermal annealed HT-9 specimens are shown in Fig.VI-

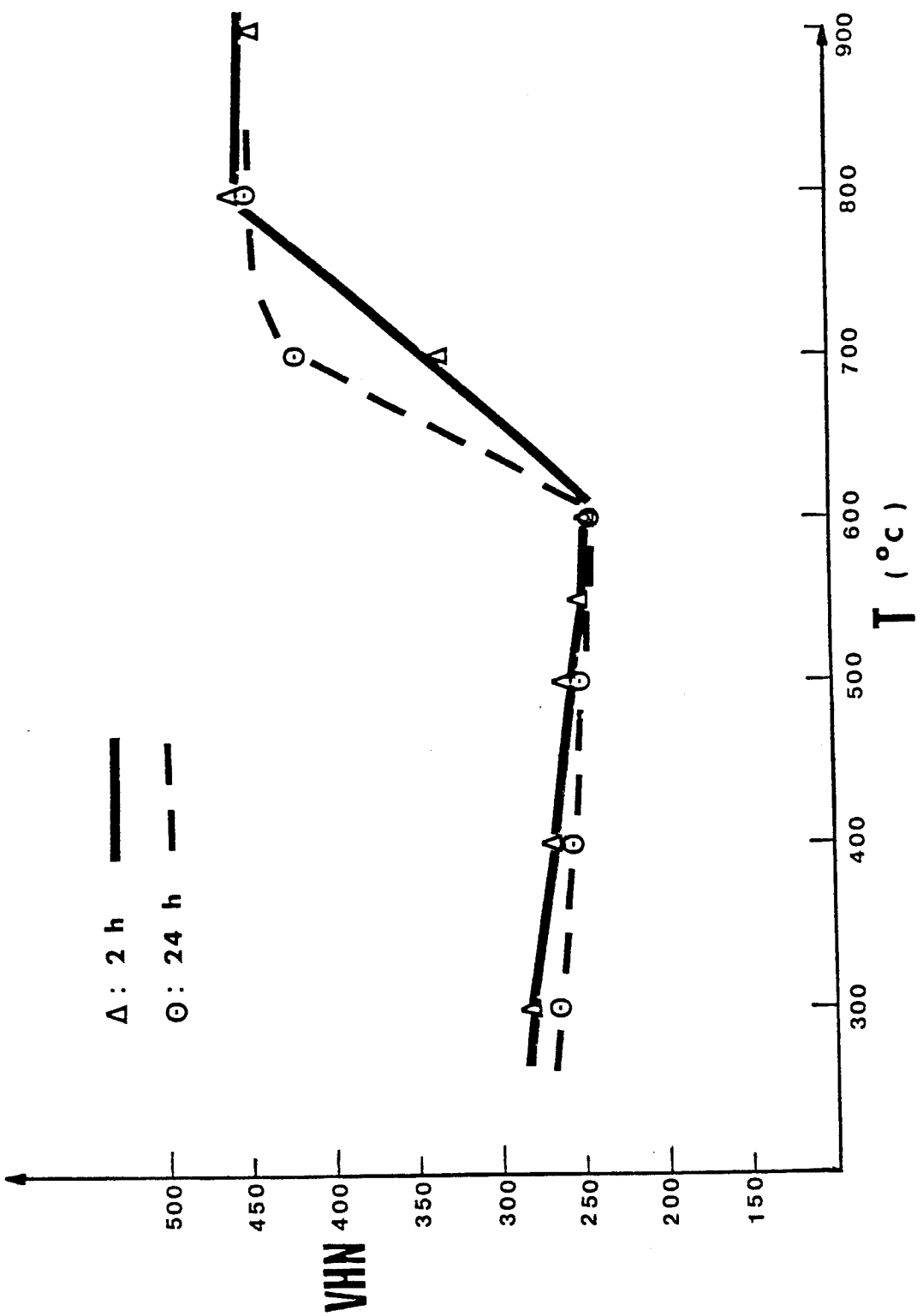

Fig.VI-12 Vickers microhardness of thermal annealed HT-9 alloy.

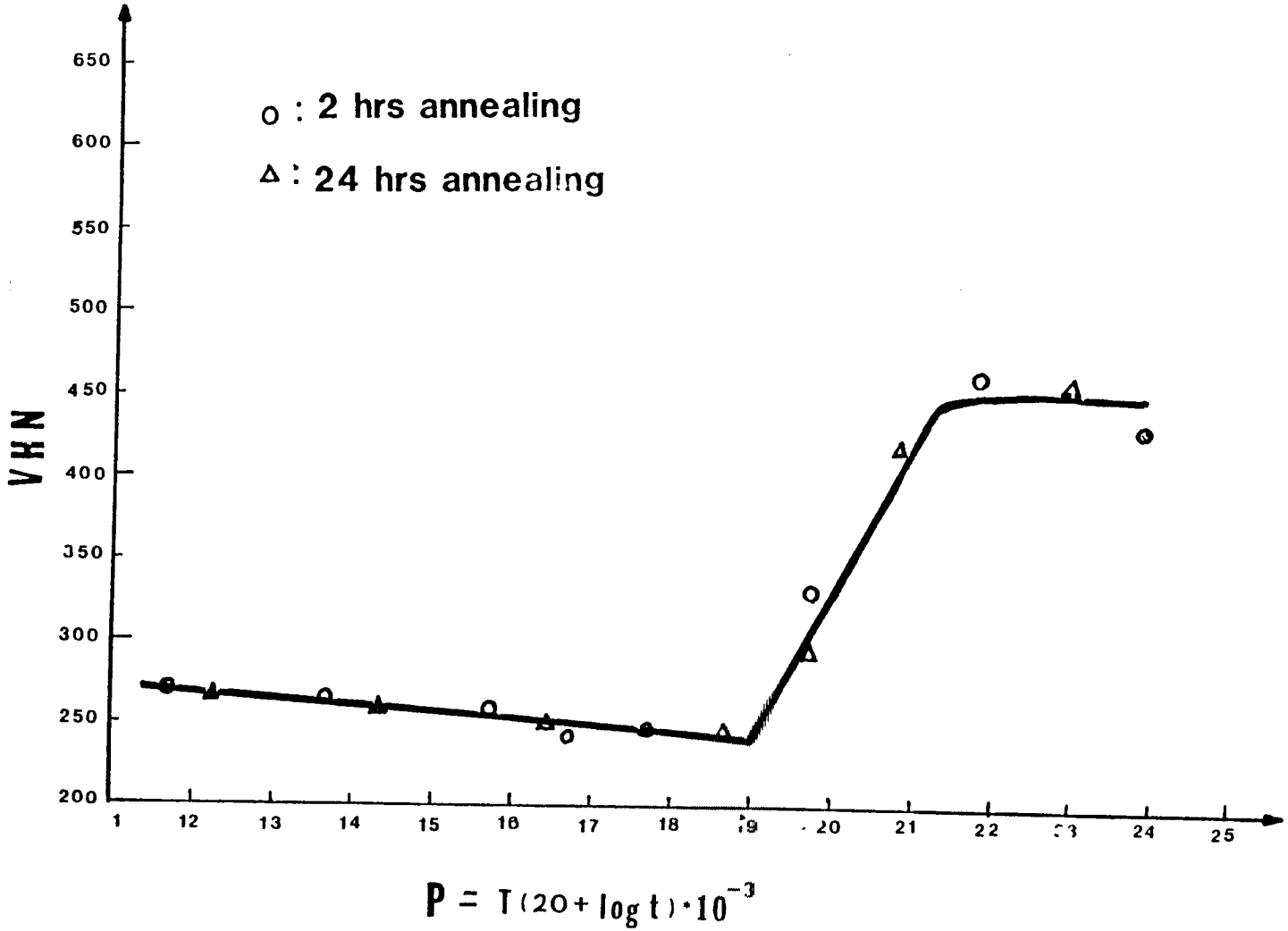

Fig.VI-13 Vickers microhardness of thermal annealed HT-9.

14 to VI-17. From the Larson-Miller parameter equation, it is clearly seen that the temperature has much greater effect than the time of thermal annealing. In the following descriptions of the results, the thermal annealing effect is increased in the following order:

(1) 300^{o} C, 2 h (P=11.6); (2) 300^{o} C, 24 h (P=12.3); (3) 400^{o} C, 2 h (P=13.7); (4) 400^{o} C, 24 h (P=14.4); (5) 500^{o} C, 2 h (P=15.7); (6) 500^{o} C, 24 h (P=16.5); (7) 600^{o} C, 2 h (P=17.7); (8) 600^{o} C, 24 h (P=18.7); (9) 700^{o} C, 2 h (P=19.8); (10) 700^{o} C, 24 h (P=20.8); (11) 800^{o} C, 2 h (P=21.8); (12) 800^{o} C, 24 h (P=22.9); (13) 900^{o} C, 2 h (P=23.8).

Because the tempered martensite lath is the predominant phase in as-received HT-9, it is used for the comparison of the thermal annealing effect on microstructure. Fig.VI-14 and VI-15 show the TEM microstructure of the tempered martensite lath in thermal annealed specimens. There is no major microstructural change up to 600^{o} C for 2 h annealing except for a small amount of dislocation recovery in certain lath. After annealed at 700^{o} C for 2 h, the subgrain of the tempered martensite lath started to recrystalize and the

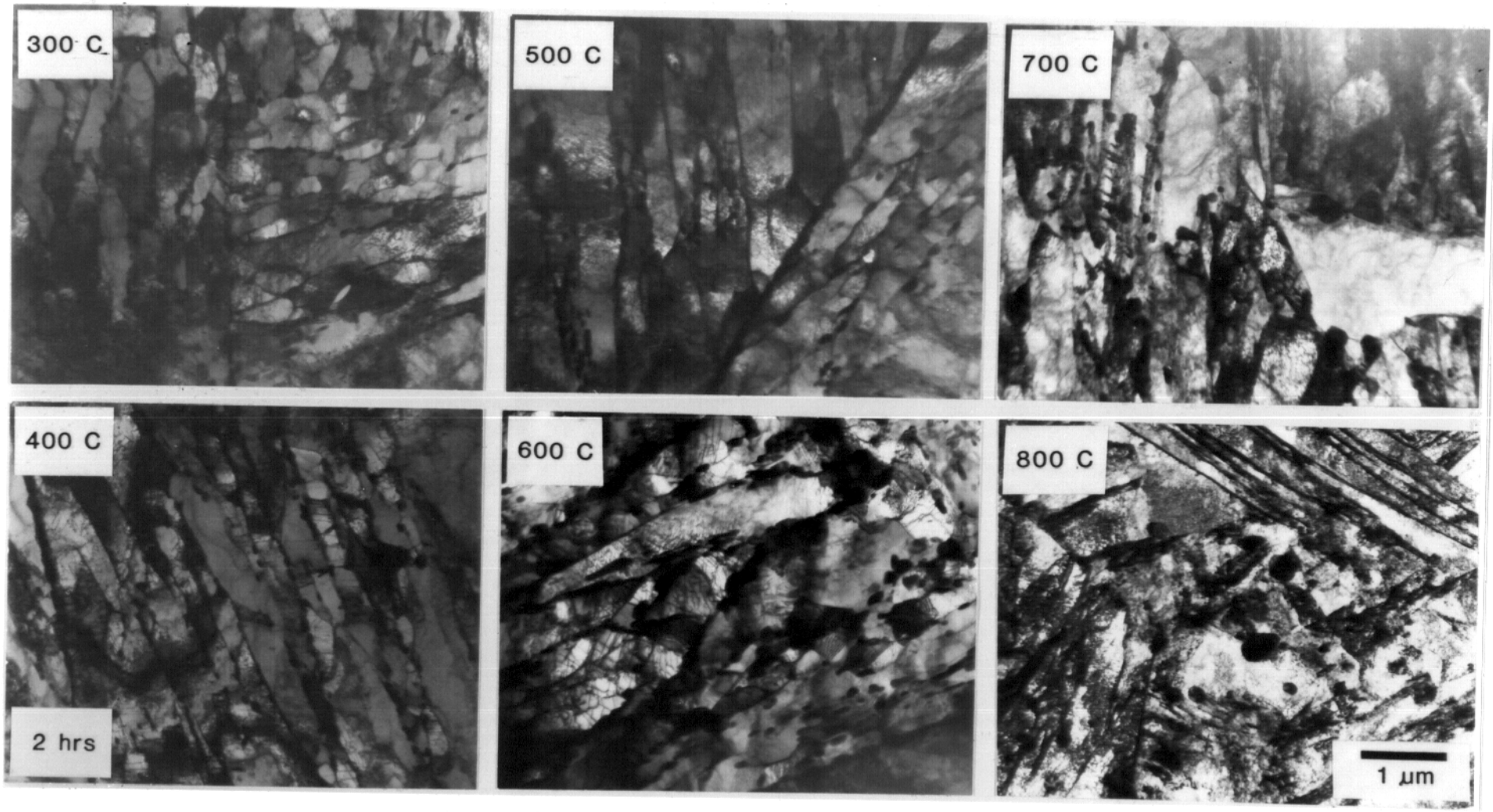

Fig.VI-14 TEM microstructures of HT-9 following thermal annealing for 2 h.

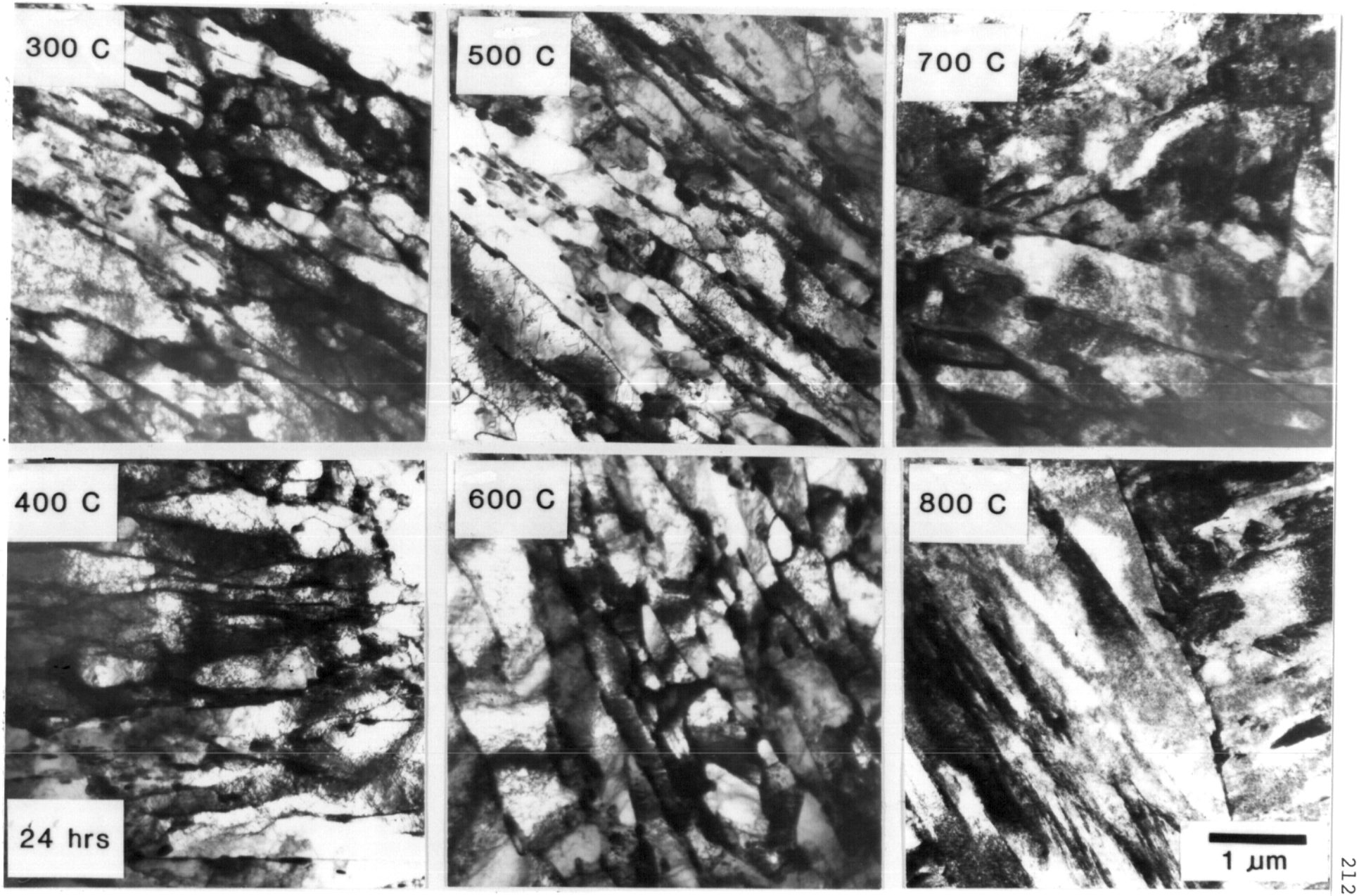

Fig.VI-15 TEM microstructures of HT-9 following thermal annealing for 24 h.

precipitate number density was gradually decreased. After 800^{o} C for 24 h annealing, the microstructure was changed to martensite on cooling without any blocky precipitate in the matrix or on the grain boundary. This result furtherly demonstrates that the re-austenitization and the austenite to martensite transformation that was found in optical micrographs and in the microhardness test has indeed occured.

The precipitate evolution under thermal annealing was studied by using the carbon extraction replica technique. Fig.VI-16 and VI-17 show the micrographs that were taken from the carbon replica of these thermal annealed specimens. The morphology and the chemical composition of each type of precipitate remained mostly unchanged which were compared to the precipitates in the as-received material. However, the number density and average size of each phase did change with temperature and time at high temperature annealings (T$>$600^{o} C).

The distribution and the structure of each type of precipitate was roughly unchanged during thermal annealings up to 600^{o} C for 2 h (P=17.7). The M_2X needle-like phase disappeared after annealing at 600^{o} C for 24 h

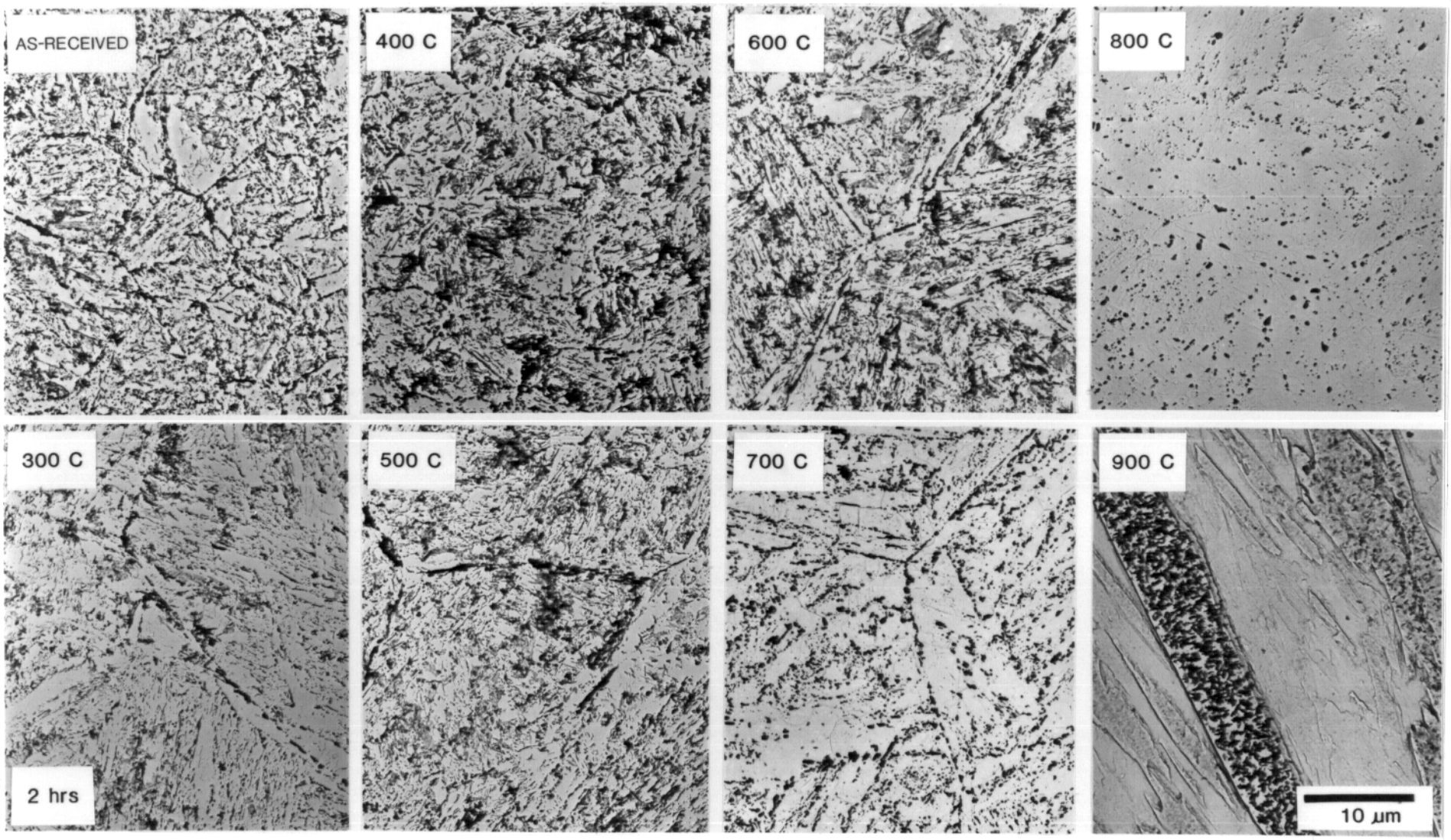

Fig.VI-16 Carbon extraction replica of HT-9 after thermal annealing for 2 h.

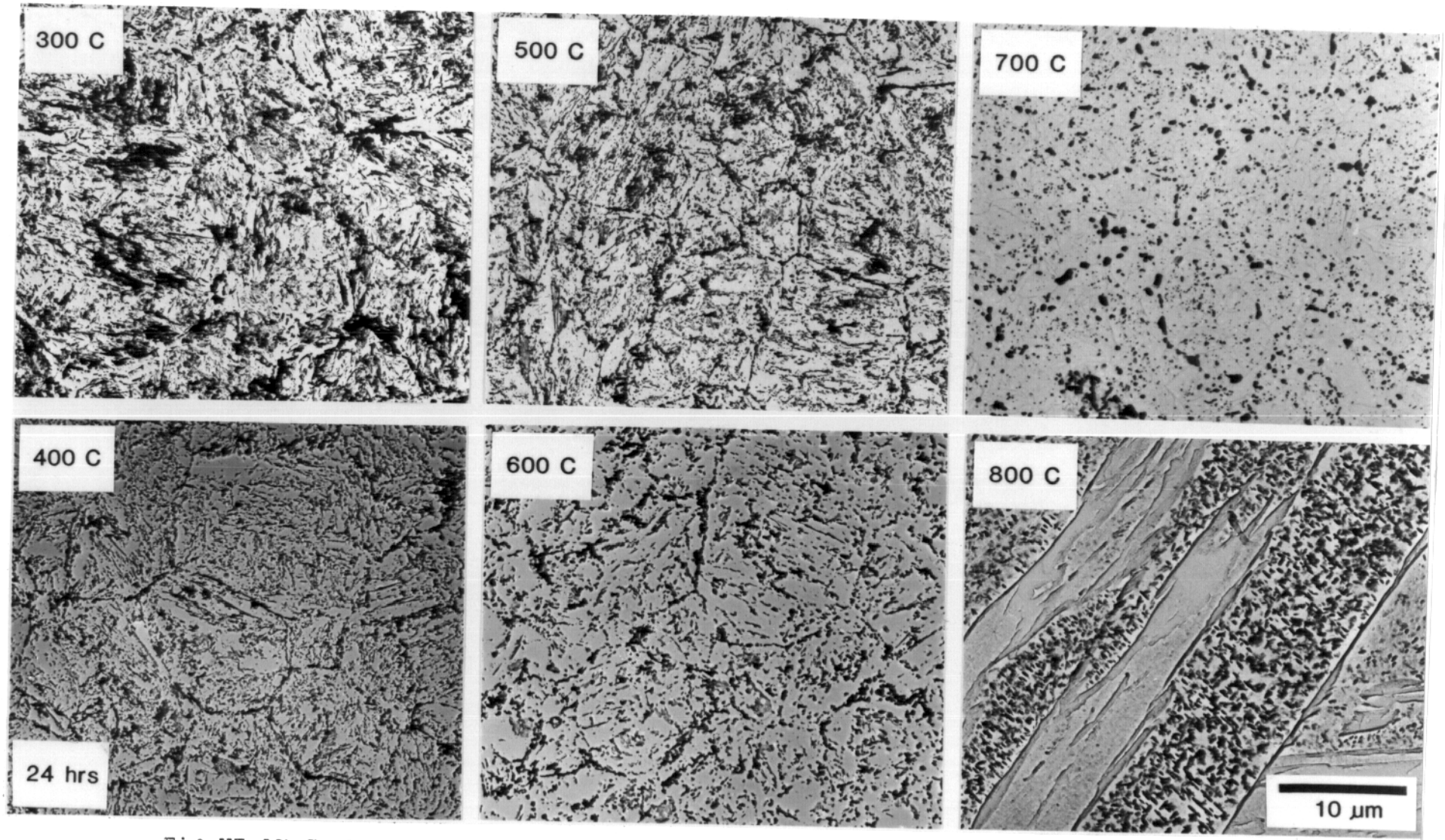

Fig.VI-17 Carbon extraction replica of HT-9 after thermal annealing for 24 h.

(P=18.7). The irregular elongated $M_{23}C_6$ phase along the tempered martensite lath boundaries started to dissolve after 700° C for 2 h (P=19.8) and disappeared after 700° C for 24 h (P=20.8). After 800° C for 2 h (P=21.8), the MX phase was dissolved and some M_3C carbides formed due to autotempering. The most stable precipitate phase in thermal annealed HT-9 is the equiaxed $M_{23}C_6$ particles which are the only precipitate phase still remaining in the material after 800° C for 2 h annealing. After annealing at 800° C for 24 h (P=22.9) and 900° for 2 h (P=23.9), the original precipitates all disappeared and a new generation of M_3C phase was formed. This is consistent with the microstructural evolution showed in TEM micrographs.

The X-ray EDS quantitative analyses showed that the chemical composition of each type of precipitate was roughly unchanged and the new M_3C phase had a high Fe peak along with some Cr. However, in the higher temperature anneals (700° C for 24 h and 800° C for 2 h), the $M_{23}C_6$ phase had a V-peak which was about 3 wt.%. This is probably due to the dissolution of other phases and the incorporation of the vanadium into the $M_{23}C_6$ phase.

C. Discussion

C.1 As-Received Microstructures

The four different types of precipitates that found in the as-received HT-9 ferritic alloy are unique in this study. Several other studies[2-5,8,9] also examined the microstructure of HT-9 ferritic steels and found only some of the phases. For example, Klueh and Vitek[8] reported $M_{23}C_6$ and Nb-riched MC phases. Gelles[4] found only $M_{23}C_6$ phase in as-received HT-9. The discrepancy between studies may be explained by the minor elements difference among various HT-9 alloys. Table V-1 has showed the chemical composition of various HT-9 ferritic steels that have currently been studied. Another possible explaination is the difference between the heat treatments that have been employed.[10-12]

From earlier work by Smith[5], it is clearly seen that all the phases found in this study are in the phase diagram (see Fig.IV-5). As stated by Smith[5], during tempering, all the phases that occured between the origin and the composition of the material in the equilibrium phase diagram could possibly form. The equilibrium

precipitate phase in the HT-9 ferritic steel annealed for a long period of time would be $M_{23}C_6$ only. Therefore, the four phases discovered in this study indicate that the as-received HT-9 alloy used in this study had not reached the equilibrium condition and the precipitate evolution will proceed further during thermal annealing. This is exactly what was found in the thermal annealing study.

The strengthing mechanisms that could be applied to this material include precipitate and dispersion hardening (high density of precipitates), grain-size hardening (very small subgrain size, width ‹1 um), martensite hardening (tempered martensite lath), and solution hardening (carbon and nitrogen interstitials in matrix). Therefore, the mechanical strength evolution in this material is complicated due to the interaction among these mechanisms. It is believed that none of these mechanisms can play a dominant role by itself. Therefore, it is important to carefully study the microstructural evolution in order to correlate the microstructure to the mechanical strength of the material.

C.2 Thermal Annealing Effects

The dislocation density in as-received HT-9 is very high and it is also high in thermal annealed HT-9. This is due to the special heat treatment response of this type material. At lower temperature anneals ($T \leq 500^{\circ}$ C), the thermal diffusion rate is low and the small subgrain size along with the original high number density of precipitates slow down the recovery process. During higher temperature anneals ($T \geq 700^{\circ}$ C), certain portions of the material are re-austenitized and the austenite to martensite transformation occurs during the cooling process, producing the high dislocation density. The only possible annealing temperature that could anneal out the high dislocation density is 600° C. However, due to the complicated structure of this material, the annealing time periods (2 h and 24 h) in this study are not long enough to show any significant effect.

The thermal effect on the TEM microstructure and the microhardness results can also be explained by the re-austenitization and the austenite to martensite transformation. Irvine et al.[2] have pointed out that the Ac_1 (re-austenitizing) and M_s (martensite starting)

temperatures are both affected by the minor alloy elements. According to the information offered by Irvine et al.[2], the calculated Ac_1 and M_s temperatures of the HT-9 ferritic steel used in this study are 756° C and 255° C, respectively.

It seems that the re-austenitization should not occur during the 700° C anneals. However, it is found that the re-austenitization that occurs during tempering is a function of the time of tempering. It therefore becomes very difficult to determine the Ac_1 and it has been found that the tempering curve itself is probably the best indication of the re-austenitization temperature, i.e., the hardness increases suddenly when austenite is reformed. The possible explaination is that local chemical composition variations could reduce the local re-austenitization temperature to below 700° C.

The TTT diagram shown in Fig.VI-18 comes from a material very similar to HT-9.[13] It is clearly seen that the nose of the C-curve is pushed farther back so that the cooling rate is not crucial to the transformation from austenite to martenite. All the thermal annealed specimens were cooled down below 250° C in less 5 minutes,

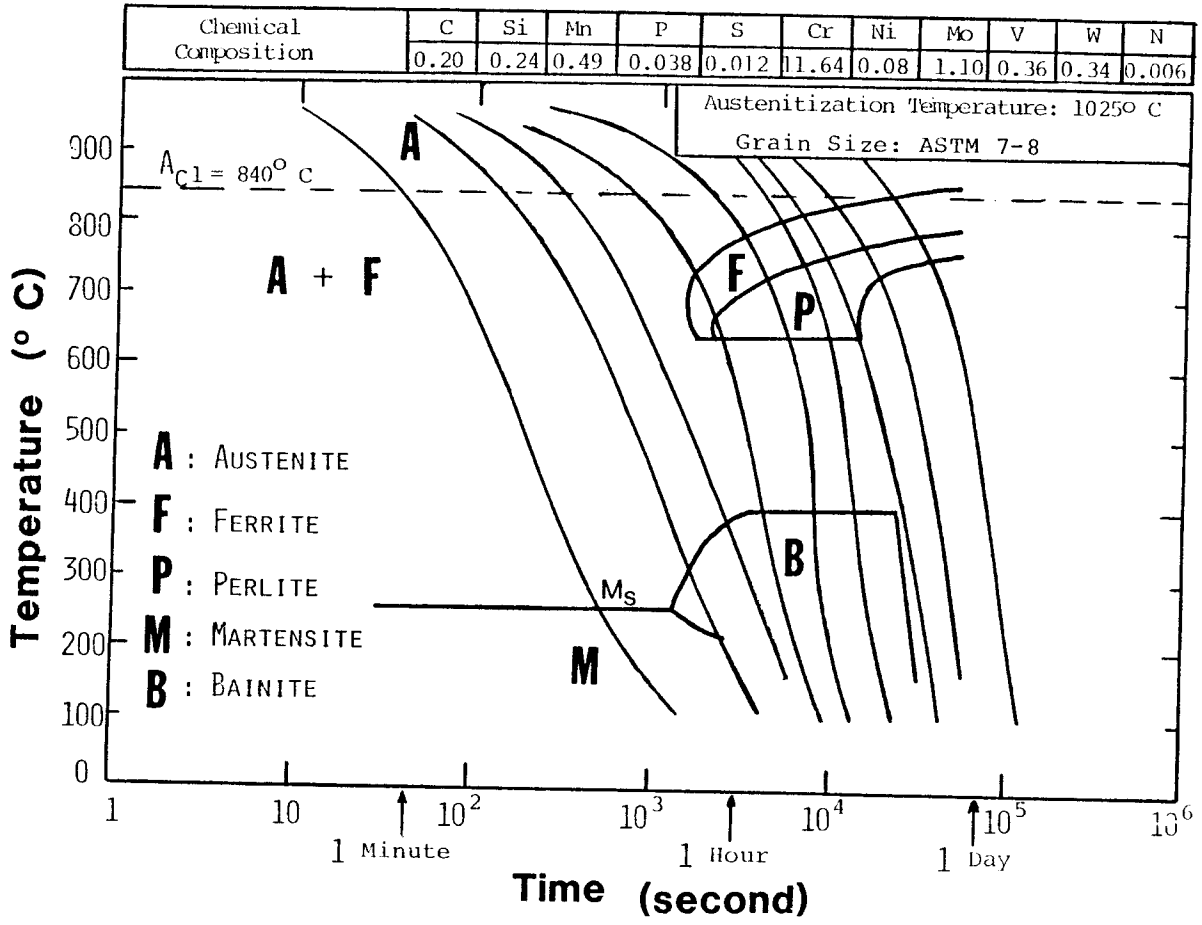

Fig.VI-18 The continuous cooling temperature (CCT) diagram of a material that has a chemical composition very similar to HT-9. (13)

therefore, all the reformed austenite should transform to martensite during the cooling process.

The precipitate evolution results are explained as follows. For lower temperature anneals ($T \leq 500^{\circ}$ C), the precipitate structure remained unchanged due to the slow diffusion rate of the alloy elements in the material. For higher temperature anneals ($T \geq 600^{\circ}$ C), the non-equilibrium phases start to become unstable and eventually are dissolved. Another reason is that a portion of the matrix is re-austenitized during higher temperature anneals ($T \geq 700^{\circ}$ C) and the austenite usually has much higher carbon and nitrogen solubility than does ferrite. Therefore, the smaller precipitates and the unstable phases start to dissolve due to lose carbon or nitrogen to the matrix.

The M_2X phase has a relatively higher formation enthalpy[14] and also smaller size so that it disappeared first during thermal annealing. The elongated $M_{23}C_6$ phase disappeared during annealing studies due to the tempered martensite laths which no longer existed after high temperature ($T \geq 700^{\circ}$ C) annealing. The equiaxed $M_{23}C_6$ phase is the equilibrium phase in a material very similar

to HT-9[5], therefore, it is the precipitate second phase dissolved after thermal annealing.

The quantitative EDS results showed that most of the precipitates were Cr-enriched. It is understandable because the material contains about 12 wt.% Cr and only 3 wt.% of other alloying elements. From earlier studies[6], it is understood that the general formulae of the precipitate phases (such as $M_{23}C_6$, MX, M_2X) represent certain structural types rather than specific chemical species. It was also reported[6] that sometimes appreciable solubility of nitrogen could be present in carbide precipitate; this is particularly true of MX and M_2X phases. Since the X-ray EDS system in the JEOL 200CX TEM used in this study has difficulty in detecting any element lighter than sodium, it is not suitable to distingush whether the precipitate phase is a carbide or a nitride, or a mixture of both. The best way to solve this problem is to use a EELS system, however, at present time this system is not available for this study.

The new generation M_3C phase formed during anneals at 800^{o} C and above is due to the autotempering during the relatively slow cooling process in high vacuum furnace.

The formation of the M_3C phase is also an indication of re-austenitization and the austenite to martensite transformation.

D. Summary

The results of the as-received microstructure and the thermal annealing effect studies can be briefly summarized as follows:

1. There are four types of precipitates identified in as-received HT-9. Most of these precipitates were Cr-enriched.
2. The dislocation density is always relatively high ($>1X10^{11}$ cm^{-2}) in this material.
3. Thermal annealing studies showed that some major microstructural changes occured after annealing above 600° C which indicates that it is not practical to use this material at 600° C or above.
4. Annealing at 800° C and above produced re-austenitization and the austenite to martenite transformation would form untempered martensite in the matrix.
5. The M_3C phase formed after annealed at 800° C and above is due to the autotempering.

6. The quantitative EDS results did not change for most cases except for the $M_{23}C_6$ particles in the specimens annealed at 700° C for 24 h and 800° C for 2 h. These precipitates have a vanadium content of about 3 wt.%.

REFERENCES FOR CHAPTER VI

1. N. J. Zaluzec, in Introduction to Analytical Electron Microscopy: Chapter 4, J. J. Hren, J. I. Goldstein, and D. C. Joy (Eds.) Plenum Press. NY (1979).

2. K. J. Irvine, D. J. Crowe, and F. B. Pickering, JISI 195 (1960) 386-405.

3. A. Hede and B. A. Aronsson, JISI 207 (1969) p.1241.

4. D. S. Gelles and L. E. Thomas, ADIP DOE/ER-0045/9 (1982) p.162.

5. R. Smith, ISI Special Report No.64 (1959) 307-311.

6. J. H. Woodhead and A. G. Quarrell, JISI 203 (1965) 605-620.

7. F. R. Larson and J. Miller, Trans. of ASME, July 1952, pp.765-775.

8. J. M. Vitek and R. L. Klueh, Metall. Trans. 14A (1983) p.1047.

9. F. A. Smidt, Jr., P. R. Malmberg, J. A. Sprague, and J. E. Westmoreland, in Irradiation Effects on the Microstructure and Properties of Metals, ASTM-STP-611 (1976) p.227.

10. D. S. Gelles and L. E. Thomas, ADIP DOE/ER-0045/8 (1982) p.343.

11. J. M. Vitek and R. L. Klueh, ADIP DOE/ER-0045/11 (1983) p.108.

12. Section V.A in this dissertation.

13. E. Kauhausen and P. Kaesmacher, Schweissen and Schneiden 9 (1957) 414-419.

14. H. L. Schick, Thermodynamics of Certain Refractory Compounds, Academic Press. NY (1966).

CHAPTER VII

MICROSTRUCTURAL EVOLUTION OF HEAVY-ION IRRADIATED HT-9 FERRITIC STEEL

A. HT-9 Irradiated with 14 MeV Ni Ions

A set of HT-9 foil specimens were irradiated at temperatures of 300, 400, 500 and 600^{o} C (about 0.3 to 0.5 T_m) to total dose levels of 3X10^{20}, 8X10^{20}, and 15X10^{20} ions/m^2 (the highest dose only at 500^{o} C). These doses are equivalent to about 40 dpa, 100 dpa, and 200 dpa respectively at the damage peak and about 10 dpa, 25 dpa, and 50 dpa respectively at the 1 um depth. The calculated dpa and ion deposition distribution versus depth curves of 14 MeV Ni ions injected into HT-9 are shown in Fig.II-2.

A rather surprising result of this study was the complete lack of void formation in all the specimens that were investigated. This result confirms the superior swelling resistance that has been demonstrated by HT-9. The microstructural evolution of HT-9 following heavy ion irradiation consisted of dislocation loop formation, radiation-induced new precipitates, and radiation-enhanced

precipitate dissolution.

A.1 Dislocation Loop Evolution

Figure VII-1 shows the cross-section TEM microstructure of a group of HT-9 specimens irradiated to a peak damage level of 40 dpa at temperatures of 300, 400, 500 and 600^{o} C. This type of presentation allows both the damage and unirradiated regions of the specimen to be simultaneously examined. Figure VII-2 shows the enlarged view of the peak damage area of each specimen shown in Fig.VII-1.

At 300^{o} C there are many small black spots evenly distributed in the irradiated region. It turns out, in the enlarged view, that these black spots are actually small dislocation loops. The microstructure of the unirradiated region showed no evidence of dislocation loops. It is hard to identify any other difference, besides the dislocation loops, between the damage and unirradiated regions due to the high contrast of the high density loops. At 400^{o} C the microstructure of the damage region is very similar to that of the specimen irradiated at 300^{o} C, although the average diameter of the

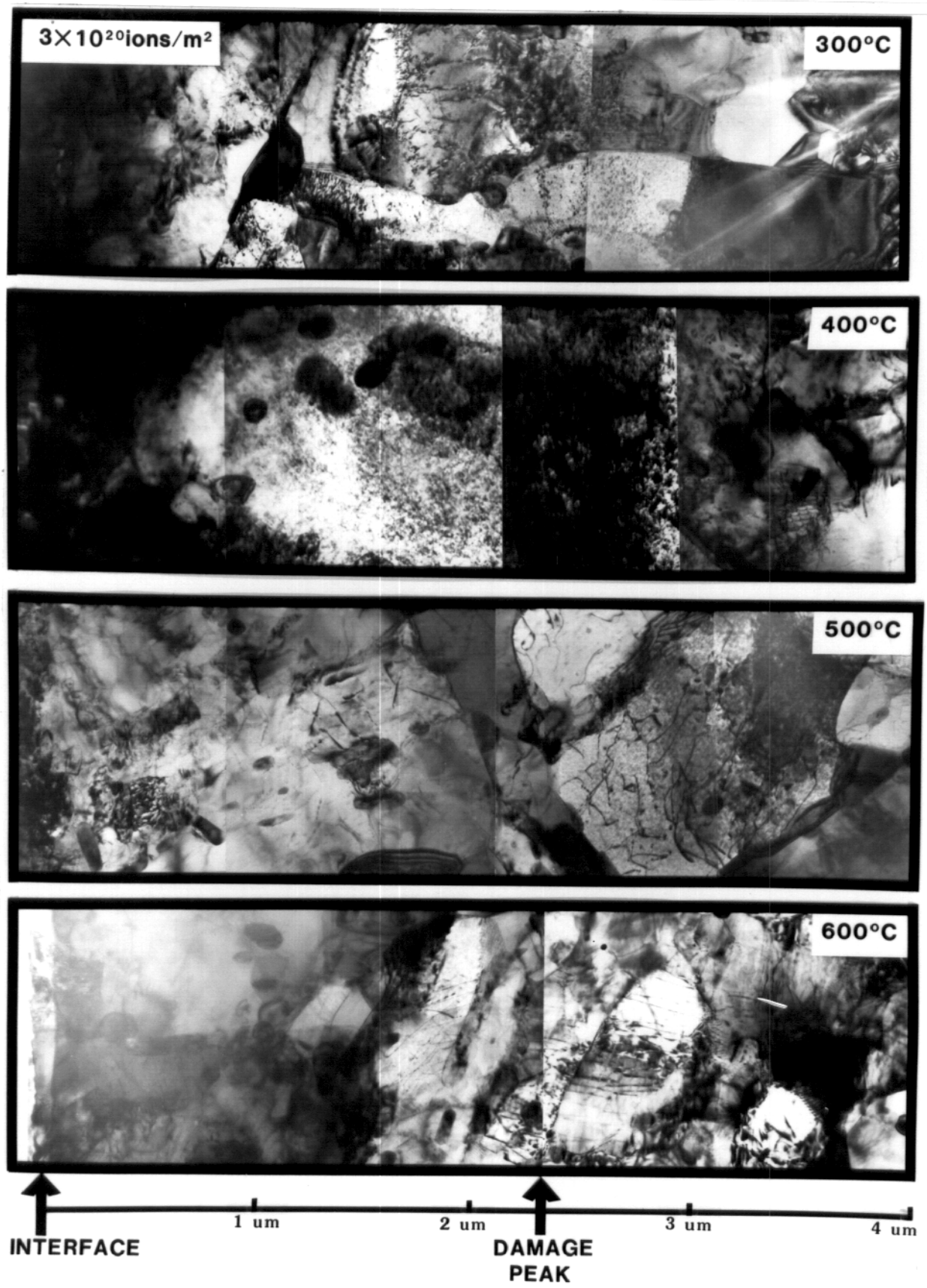

Fig.VII-1 TEM cross-section microstructure of HT-9 following ion irradiation to a peak damage level of 40 dpa.

dislocation loops is larger. There is again very little difference between the damage and the unirradiated regions, other than the dislocation loops.

At 500° C the dislocation loops grew to a significantly larger size. In addition, a relatively low density of dislocation segments ($<10^{10}$ cm^{-2}) was also observed in the damage region. These dislocation segments are believed to be formed by the overgrown loops intercepting the surfaces of the TEM specimen. Another special feature of the microstructure of the 500° C specimen is the small precipitates which show a strong Moire fringe contrast in Fig.VII-2. These precipitates were identified as chi phase,[1] and will be discussed in the next section. At 600° C there is virtually no difference in the microstructure of the irradiated and the unirradiated regions, which indicates that thermal effects dominate the microstructural evolution at this temperature or above.

Figure VII-3 shows the low angle tilt series of micrographes of the dislocation loops and subgrains coming in and out of contrast in an HT-9 specimen irradiated at 400° C to 30 dpa. This result illustrates the complexity

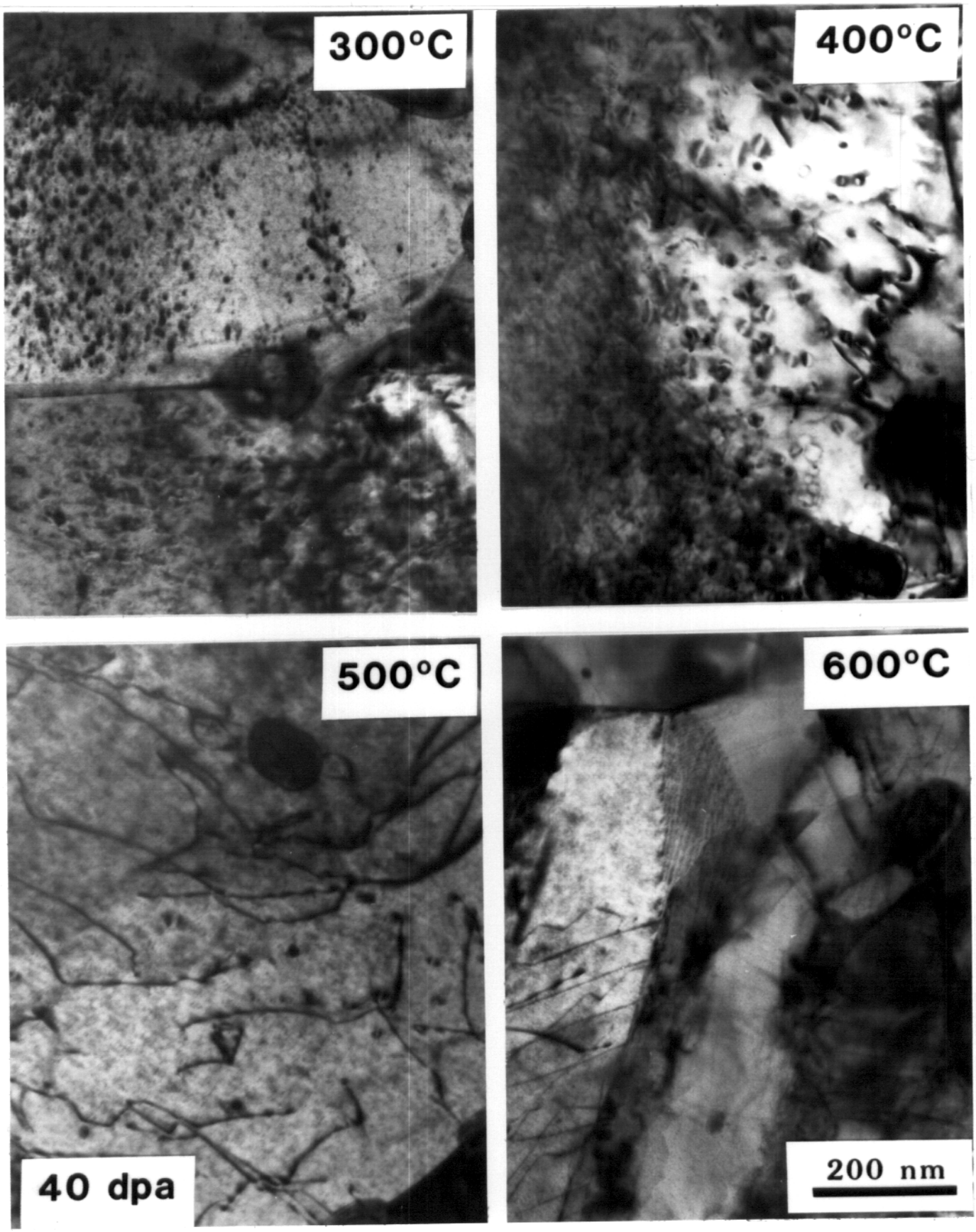

Fig.VII-2 TEM microstructures in the peak damage regions of HT-9 following ion irradiation to 40 dpa.

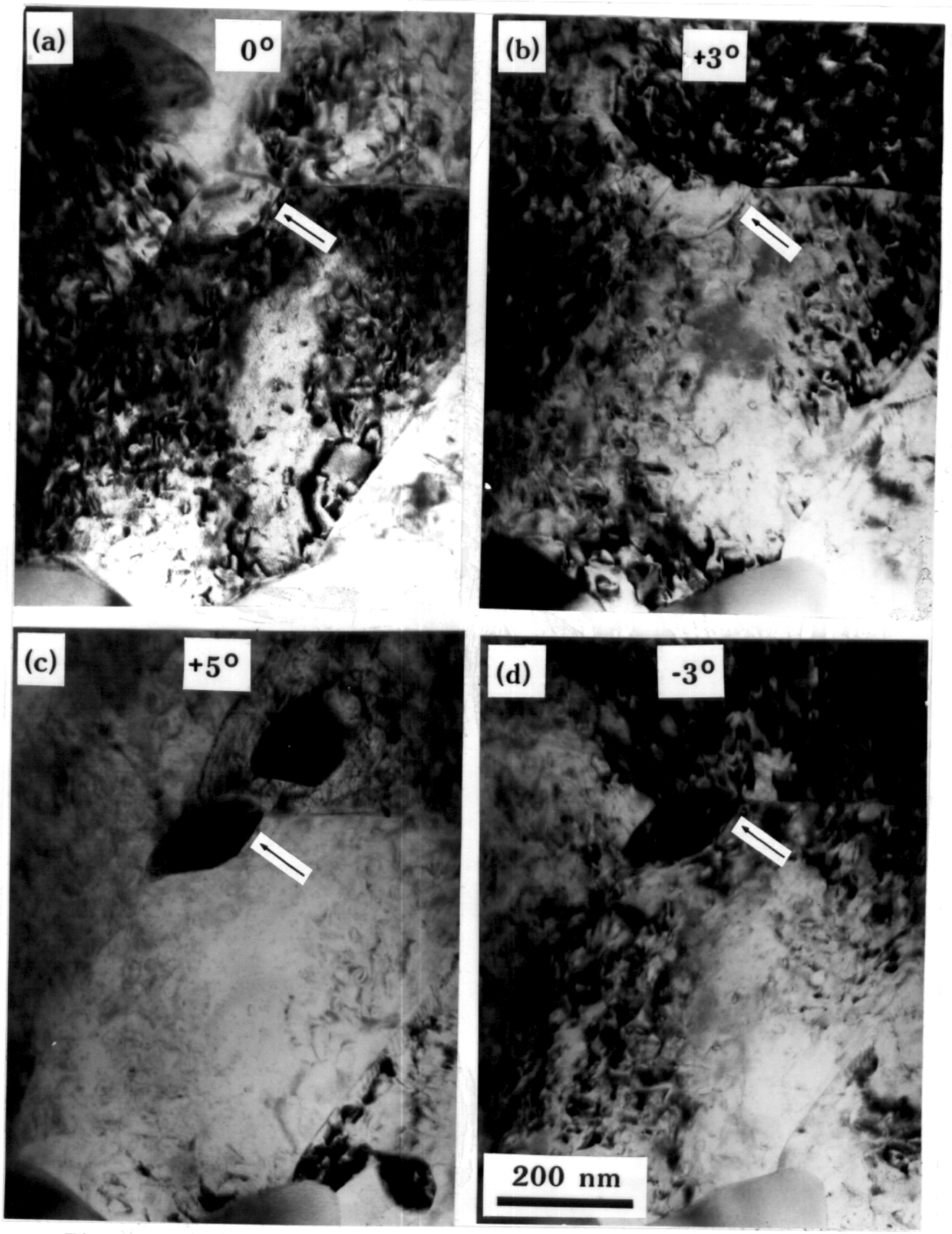

Fig.VII-3 Low angle tilt series showing loops and subgrains coming and out of contrast in HT-9 irradiated at 400° C to 30 dpa.

of analyzing the microstructures in the HT-9 alloy following ion irradiation.

Figure VII-4 shows the cross-section microstructure of another set of HT-9 specimens which were irradiated to a higher peak damage level of 100 dpa at temperatures of 300, 400, 500 and 600^{o} C. The general characteristics of the microstructural evolution in these specimens are very similar to those irradiated to lower doses. However, the saturation effect of the loop density can be clearly seen in the micrographs. Figure VII-5 shows the peak damage areas from Fig.VII-4, but at a higher magnification.

The dislocation loops were mostly interstitial in nature with b=a‹100› Burgers vector. In the tempered martensite laths, the high pre-irradiation dislocation density was eliminated and replaced with the dislocation loops. Figure VII-6 shows the saturation density and the average diameter of dislocation loops versus irradiation temperature.

A.2 Precipitation Response

The effect of ion-irradiation on precipitate evolution in the HT-9 alloy may be separated into two

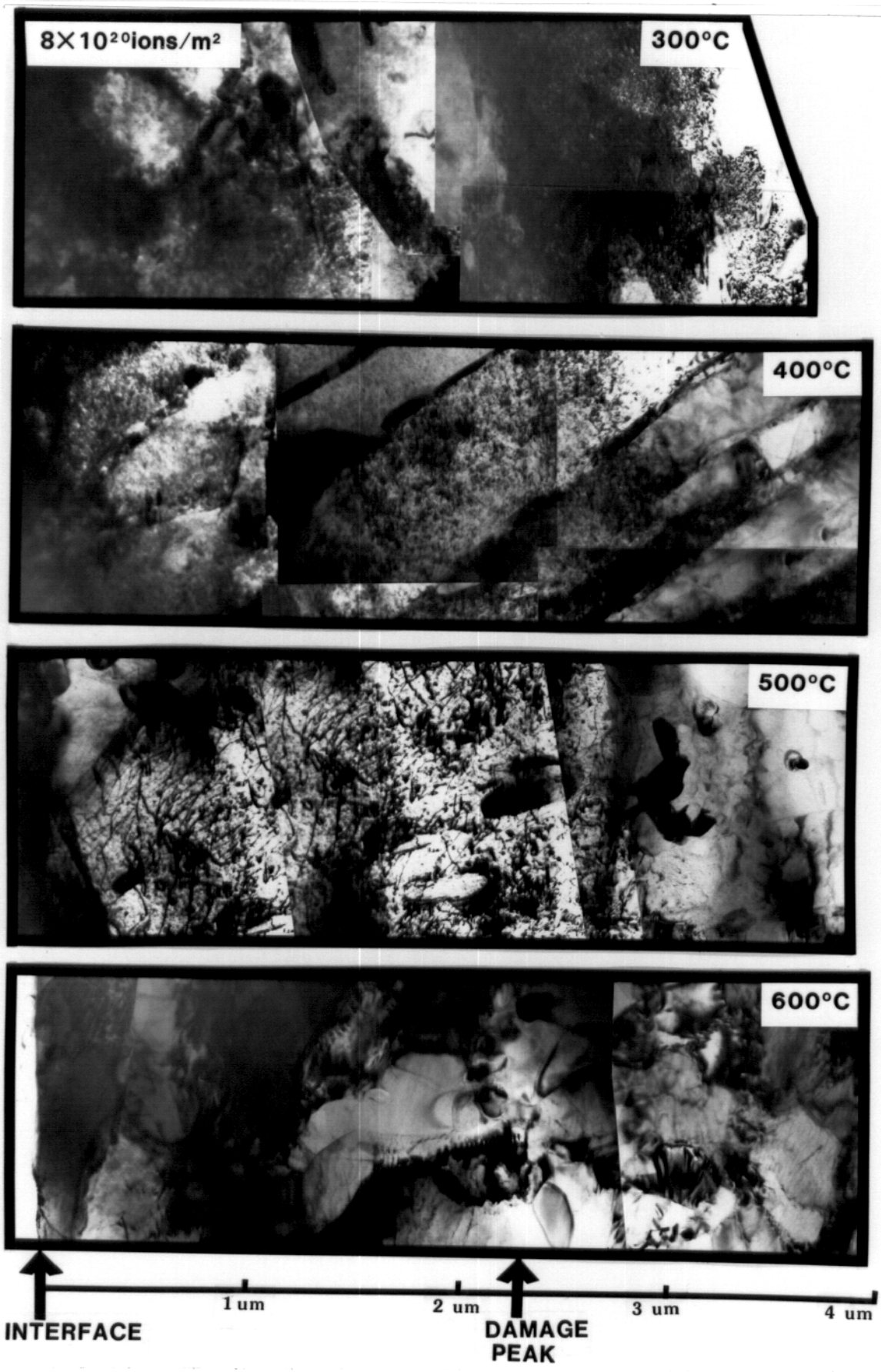

Fig.VII-4 TEM cross-section microstructure of HT-9 following ion irradiation to a peak damage level of 100 dpa.

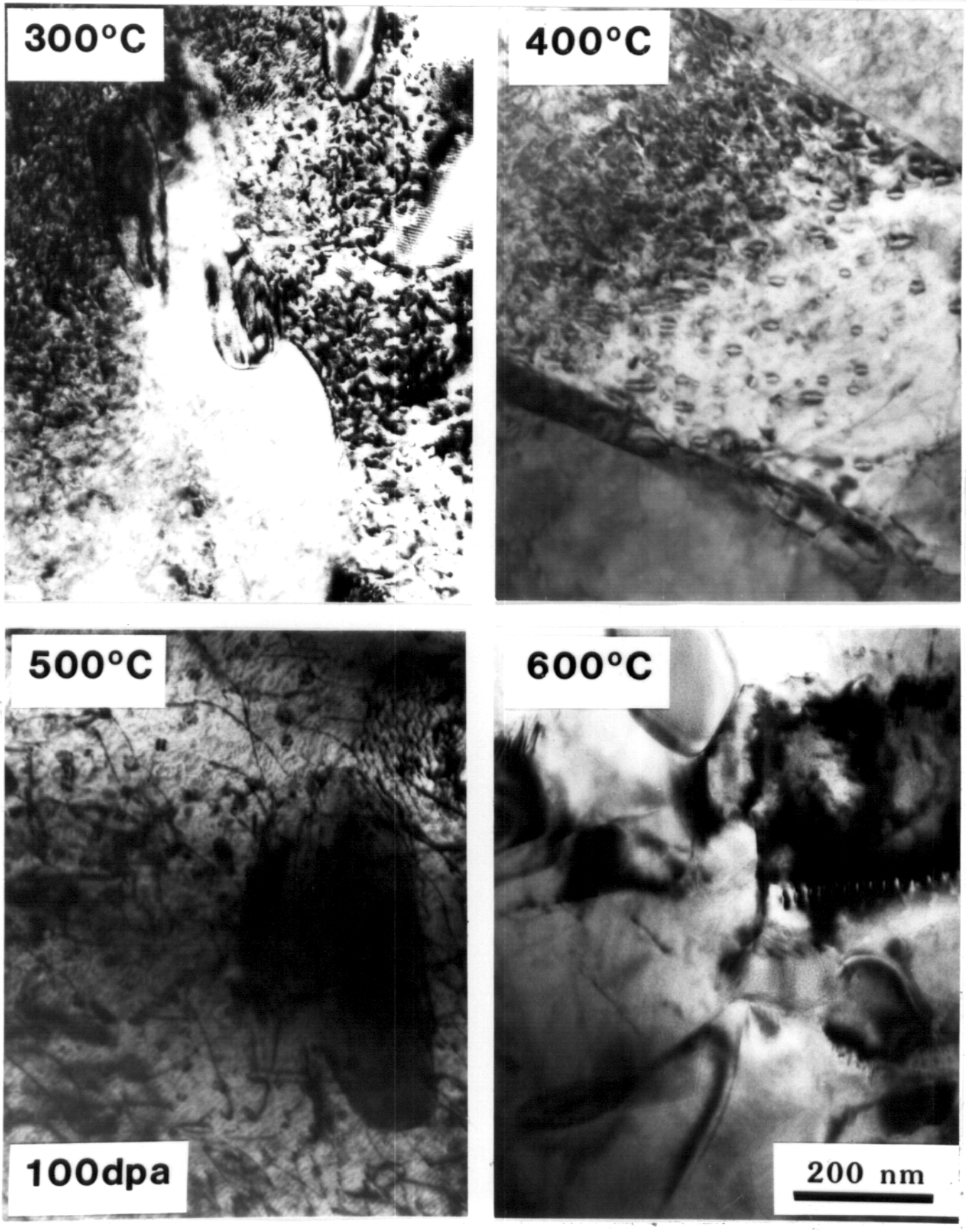

Fig.VII-5 TEM microstructures in the peak damage regions of HT-9 following ion irradiation to 100 dpa.

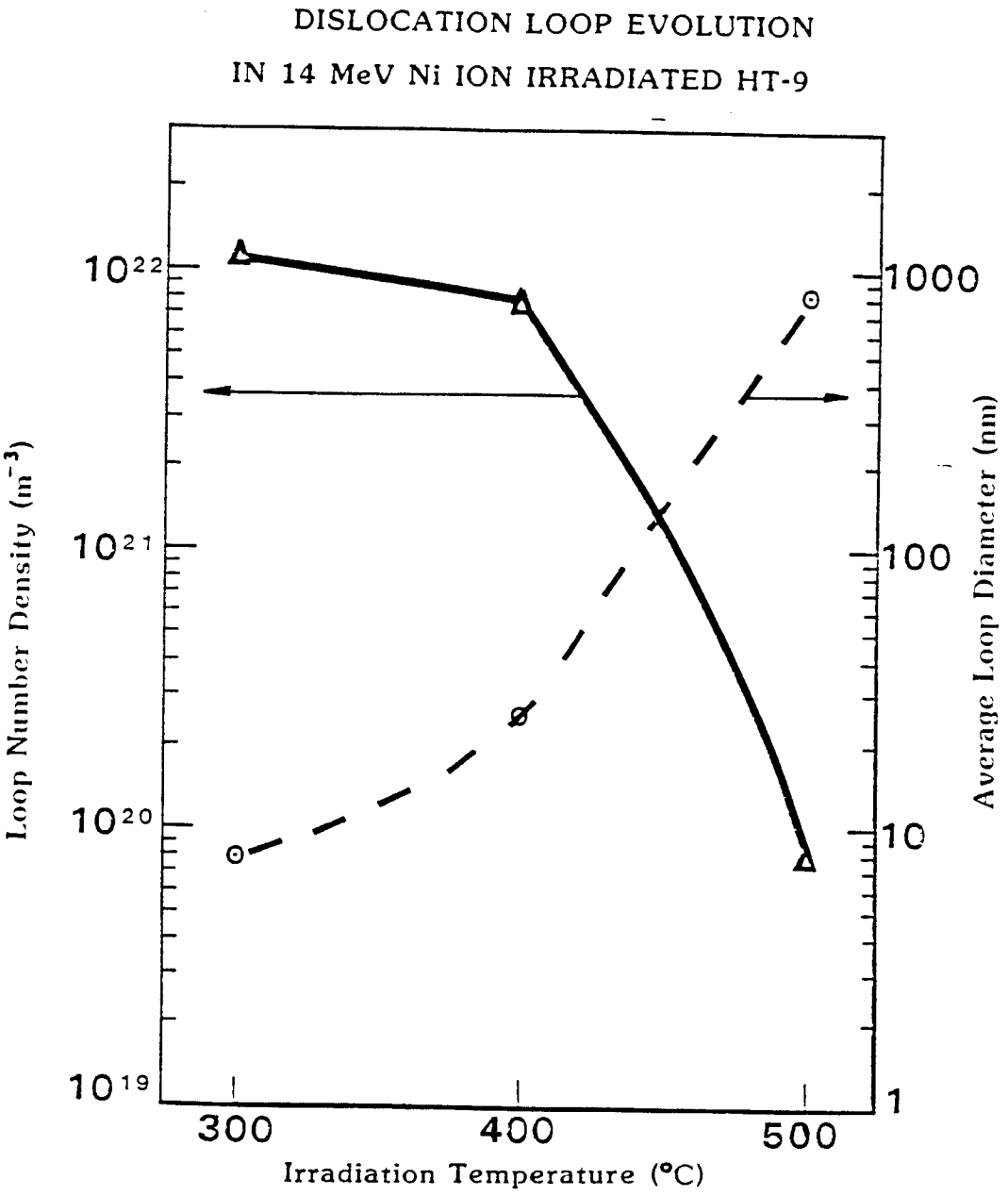

Fig.VII-6 Plot of dislocation loop density and average diameter vs. irradiation temperature in ion-irradiated HT-9 alloy.

categories: (a) modification of existing precipitates, and (b) formation of new precipitates. The microstructure of the as-received HT-9 alloy and the thermal annealing effects on the microstructural evolution of the alloy have been described in detail in Chapter VI of this thesis.

From Chapter VI, there are four types of precipitate phases existing in the as-received HT-9 ferritic steel, namely the equiaxed $M_{23}C_6$, the platelet MX, the elongated $M_{23}C_6$ and the needle-like M_2X phases. During irradiation the equiaxed $M_{23}C_6$ and the platelet MX phases were roughly unchanged. The needle-like M_2X phase was completely dissolved at all irradiation temperatures, and some dissolution of the elongated $M_{23}C_6$ phase also occured, especially at higher irradiation temperatures. Figure VII-7 shows a carbide extraction replica taken from the specimen irradiated at 500^{o} C to a peak damage level of 40 dpa. The EDS analysis showed that there is no significant changes in the chemical composition of the stable $M_{23}C_6$ and MX phases. By comparing the micrographs between the damage region and the thermal control region, it is clearly seen that M_2X precipitates have dissolved in the damage region but not in the unirradiated region.

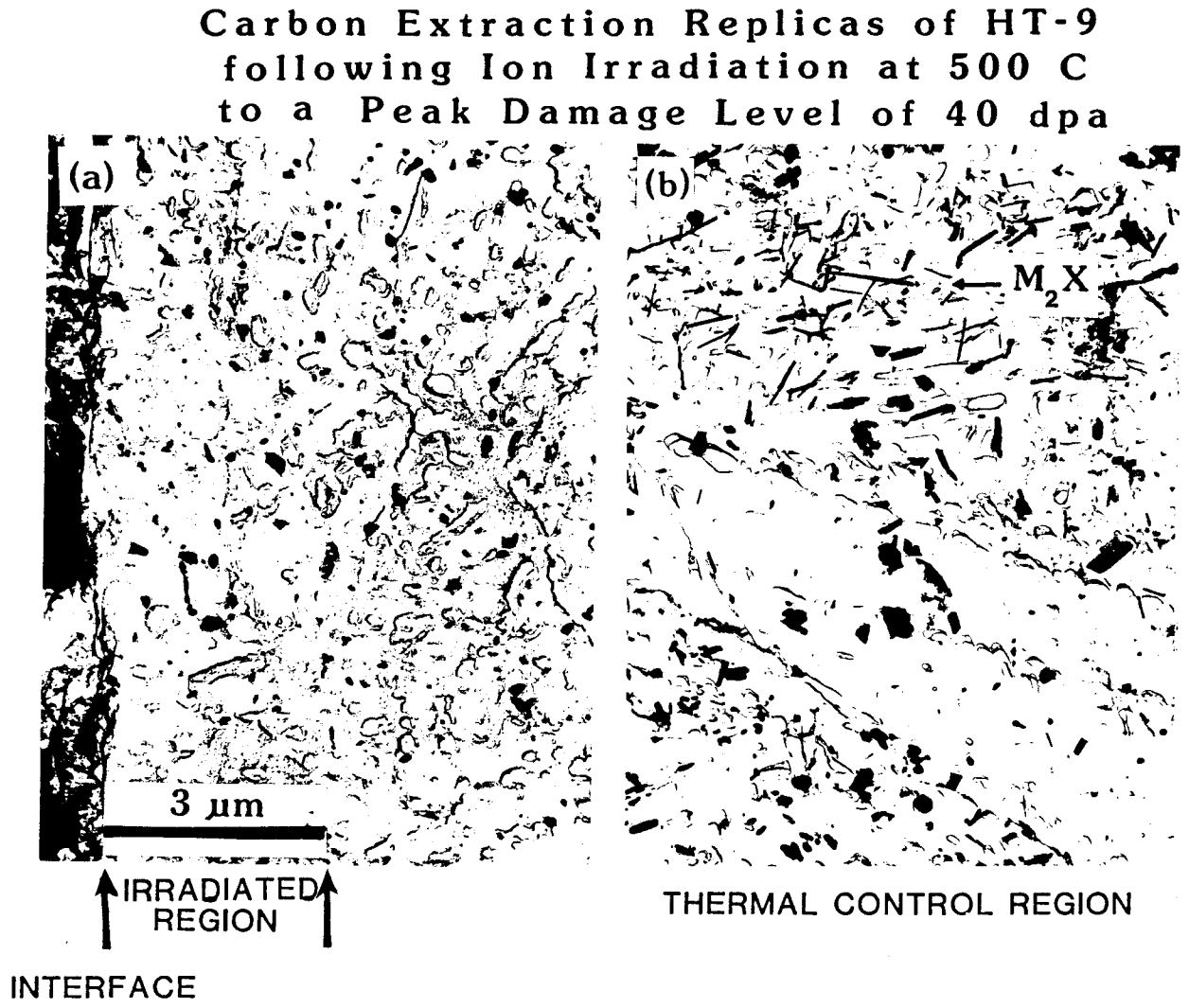

Fig.VII-7 Carbon extraction replica of HT-9 following ion irradiation at 500° C to a peak damage dose of 40 dpa. (a) the irradiated region shows no M_2X needles; (b) the thermal control region contains M_2X needles.

Figure VII-8 shows the cross-section microstructure of a HT-9 specimen irradiated at 500° C to a peak damage level of 200 dpa. Figure VII-9 shows the microstructures of the new phase induced by ion-irradiation at 500° C to peak damage levels of 40 dpa, 100 dpa, and 200 dpa, respectively. This phase was identified as chi phase,[1] which has a bcc crystal structure with a lattice parameter of 0.889 nm. The chi phase particles have a cube-on-cube orientation relationship with the bcc ferrite matrix. Figure VII-10 shows the chi phase particles in Moire fringe contrast in the peak damage regions of the HT-9 specimens irradiated at 500° C to 40, 100 and 200 dpa, respectively. Figure VII-11 illustrates the relationship of the density and the average diameter of this phase versus the dose level. It is noticed that the chi phase particles are relatively homogeneously distributed in the matrix and grow to a larger size (but smaller number densities) with increasing doses.

Another possible new phase induced by ion-irradiation is the new phase found in the specimens irradiated at 400° C. This phase has a very small average diameter (about 5 nm). Figure VII-12 shows the bright and dark field images

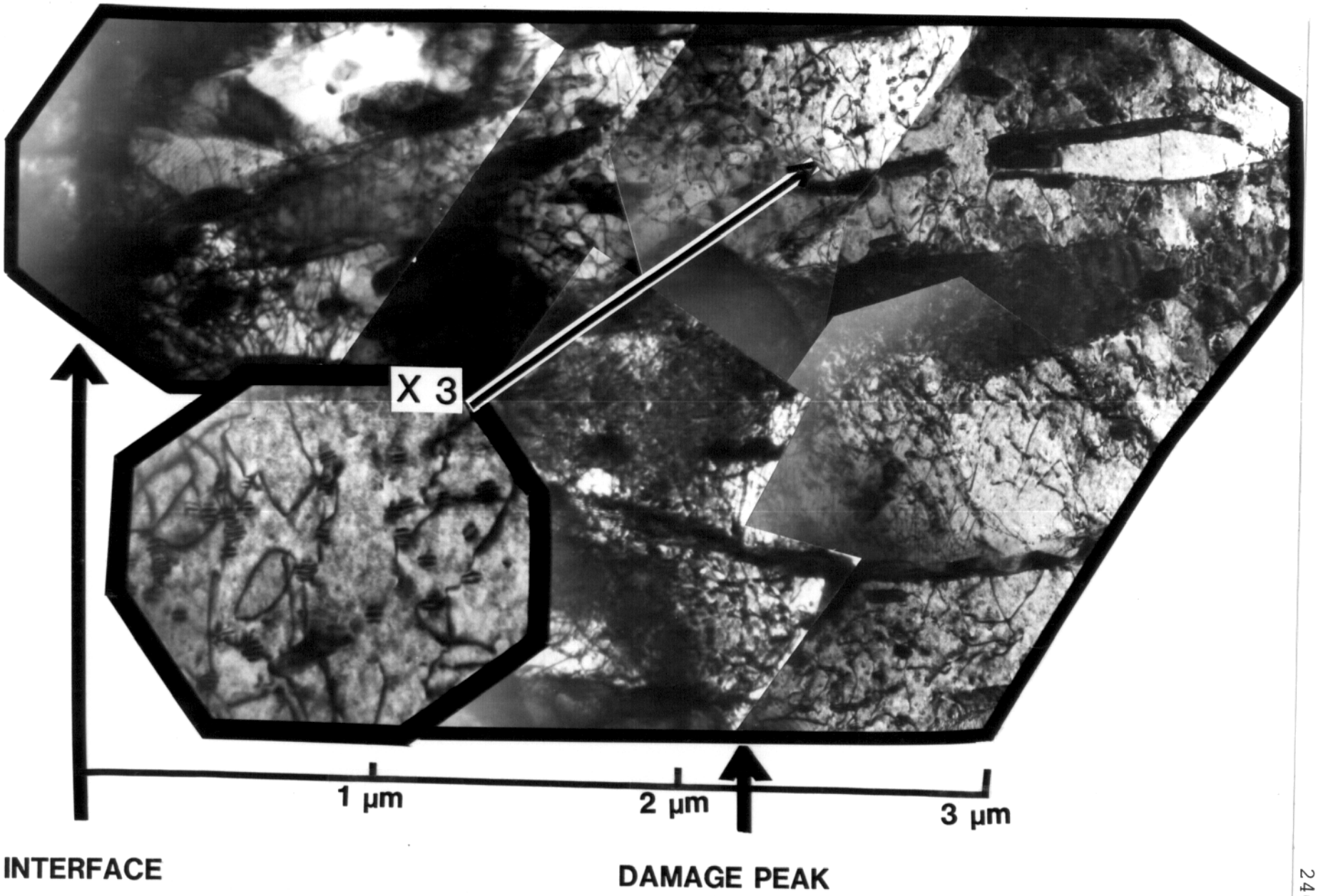

Fig.VII-8 TEM cross-section of HT-9 irradiated at 500° C to a peak damage level of 200 dpa.

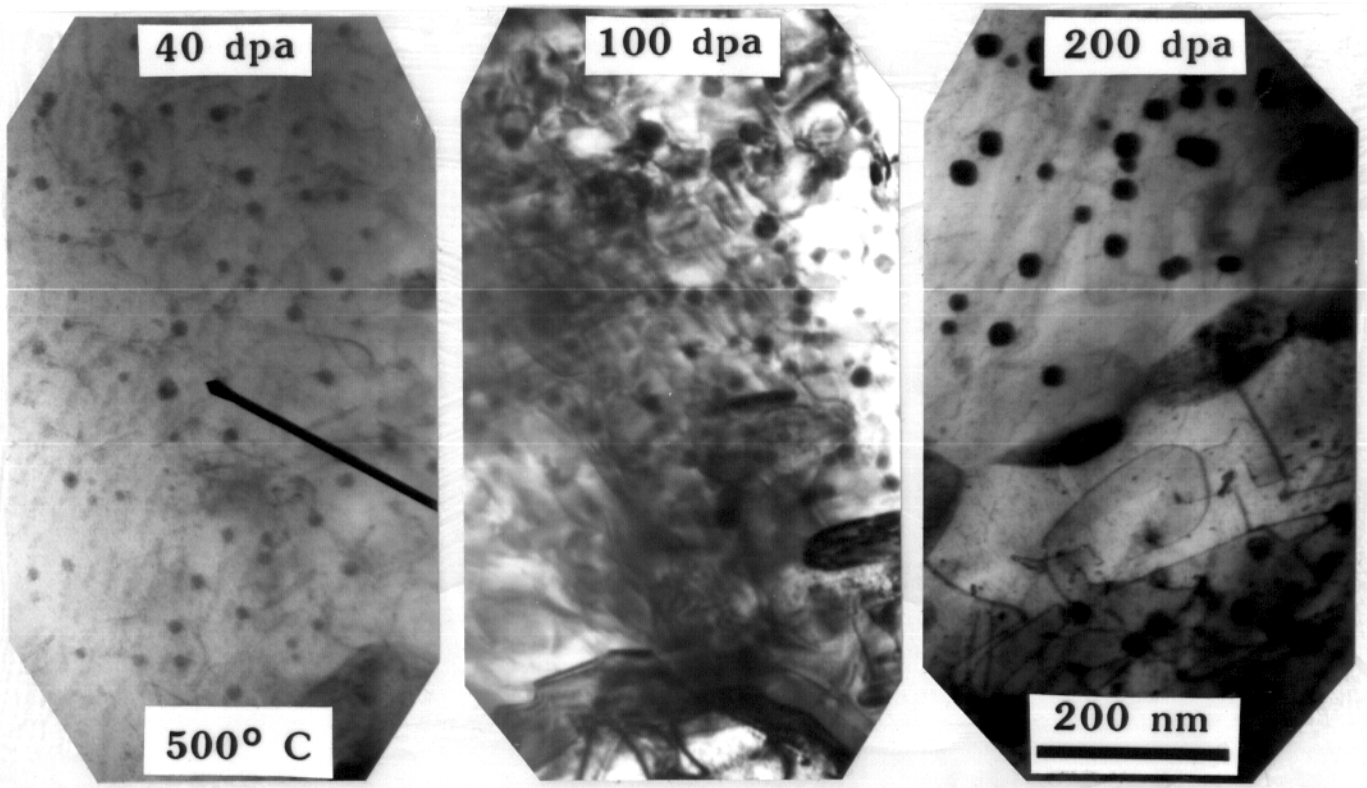

Fig.VII-9 The chi phase particles in HT-9 following ion irradiation at 500° C.

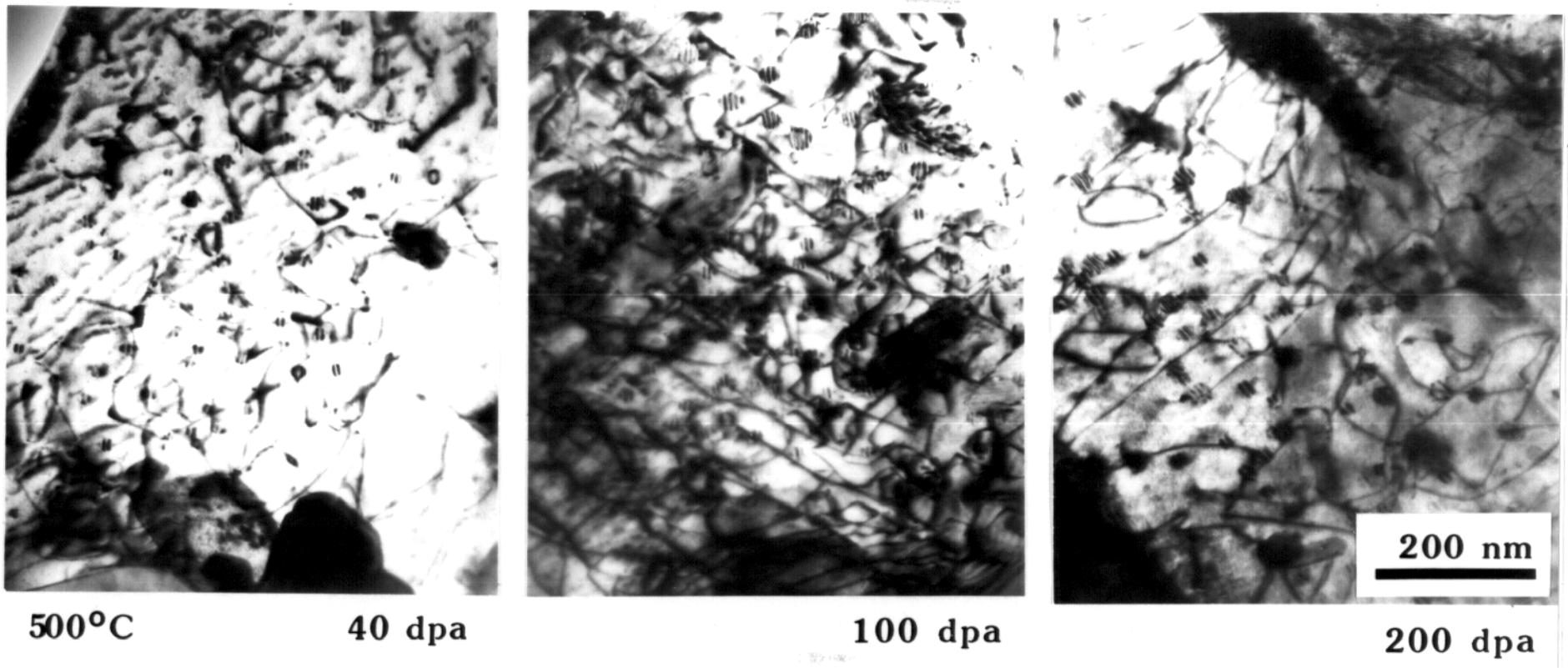

Fig.VII-10 The chi phase precipitates in Moire fringe contrast in HT-9 following ion irradiation at 500° C.

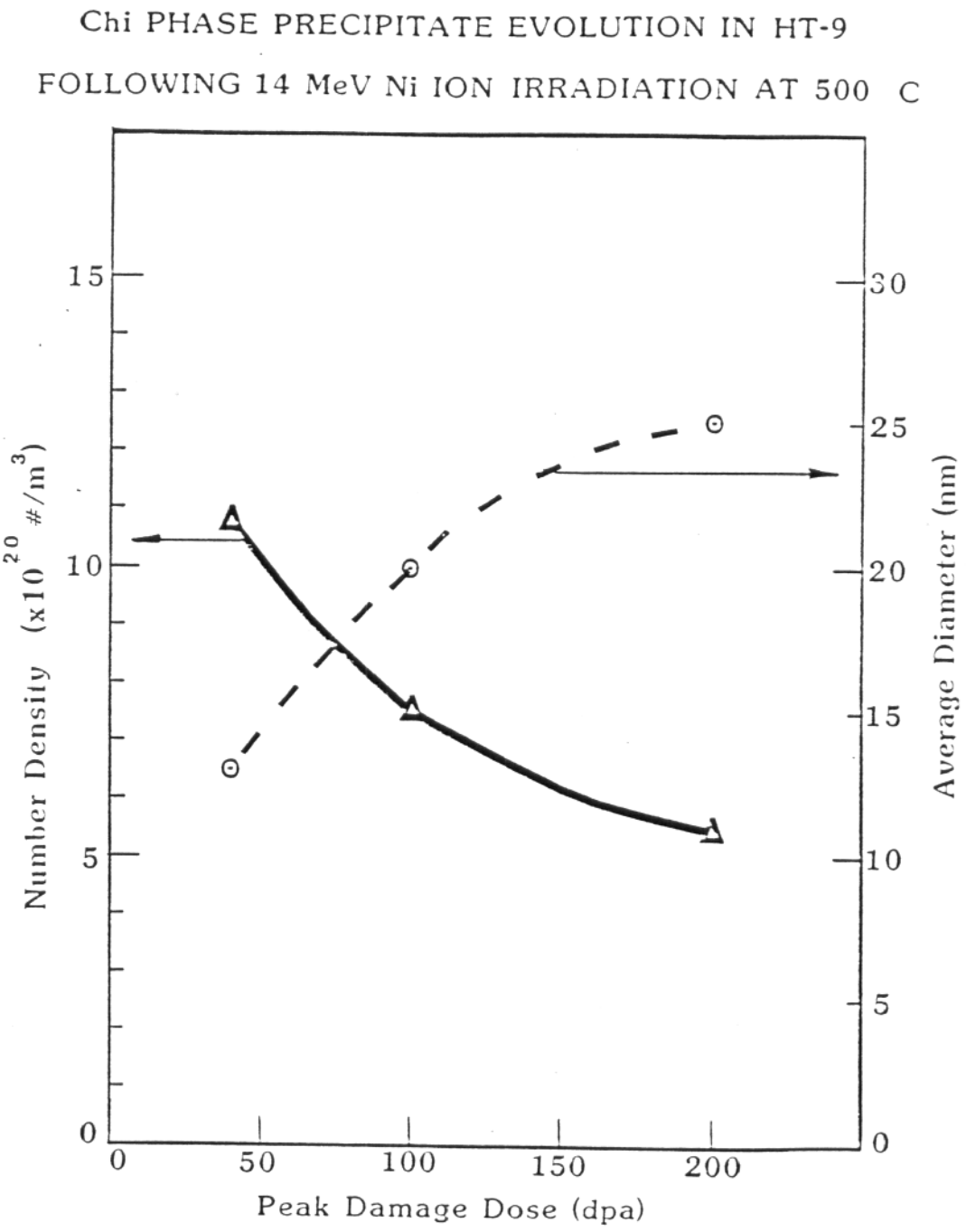

Fig.VII-11 Plot of the number density and average diameter of the chi phase particles versus dose level.

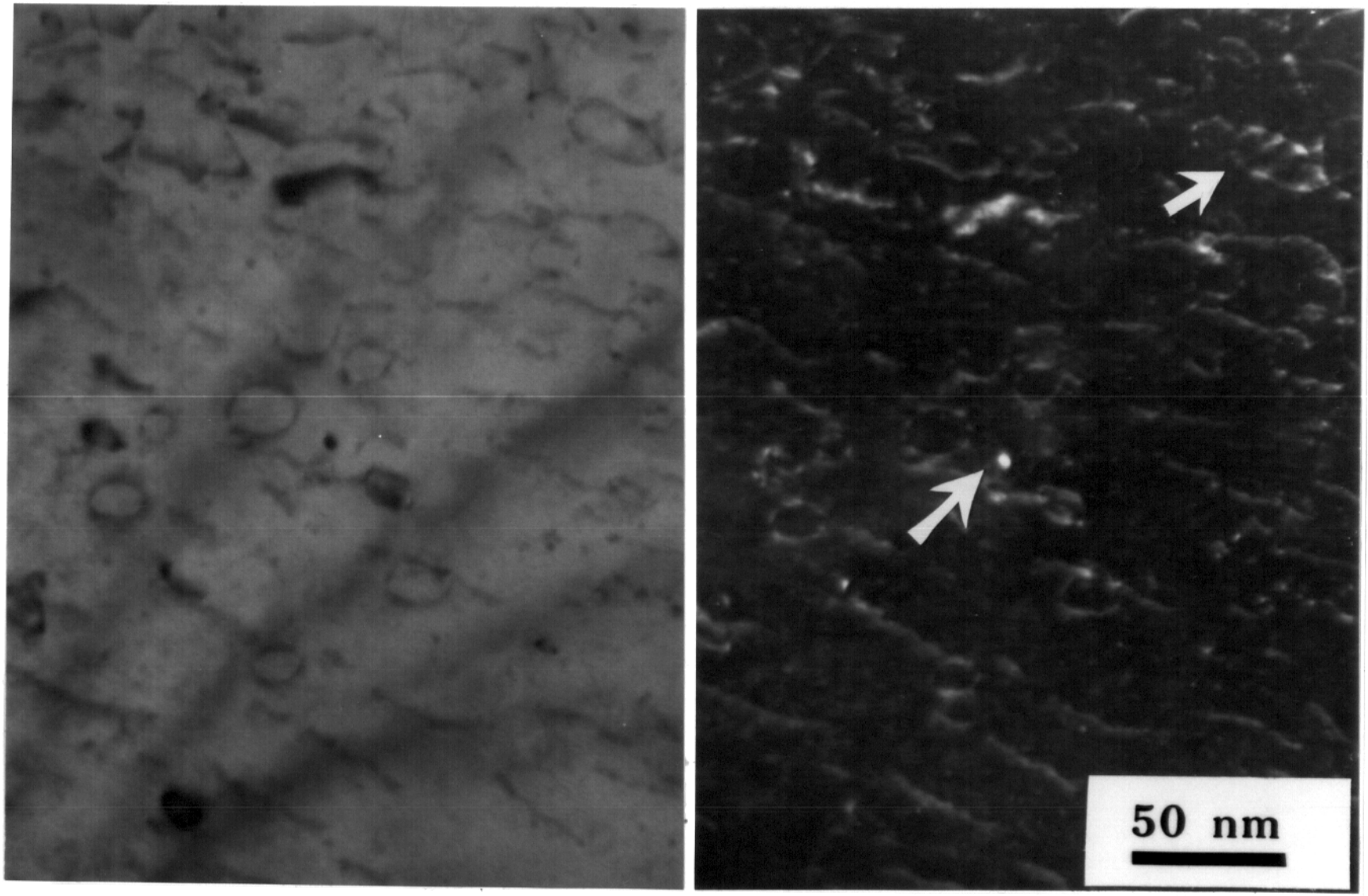

Fig.VII-12 Small α′ precipitates associated with dislocation loops in HT-9 following ion irradiation at 400° C to 40 dpa.

of the correlation between this phase and the perfect dislocation loops. Because of the small size, it was not possible to identify this new phase. However, it seems similar to the α' phase (Cr-riched) reported by Little and Stow[4] in neutron irradiated Fe-Cr alloys containing greater than 10 wt.% chromium. In addition, both Gelles and Thomas[5] and Little and Stoter[6] found the α' phase in their studies of neutron irradiated 12Cr-1MoV ferritic steels. Therefore, it is possible that this phase is the α' phase.

B. Irradiation Effects of HT-9 Specimens Preimplanted with 100 appm Helium

Figure VII-13 shows the dpa and ion deposition versus depth curves of 14 MeV Ni ions injected into HT-9 specimens preimplanted with 100 appm helium. Because the maximum energy of helium ion is 700 KeV, the maximum penetration depth of helium ion is about 1.3 um. The shaded area in Fig.VII-13 is the region with 100 appm helium evenly preimplanted.

One significant effect of preimplanting helium into HT-9 specimens followed by ion irradiation is the

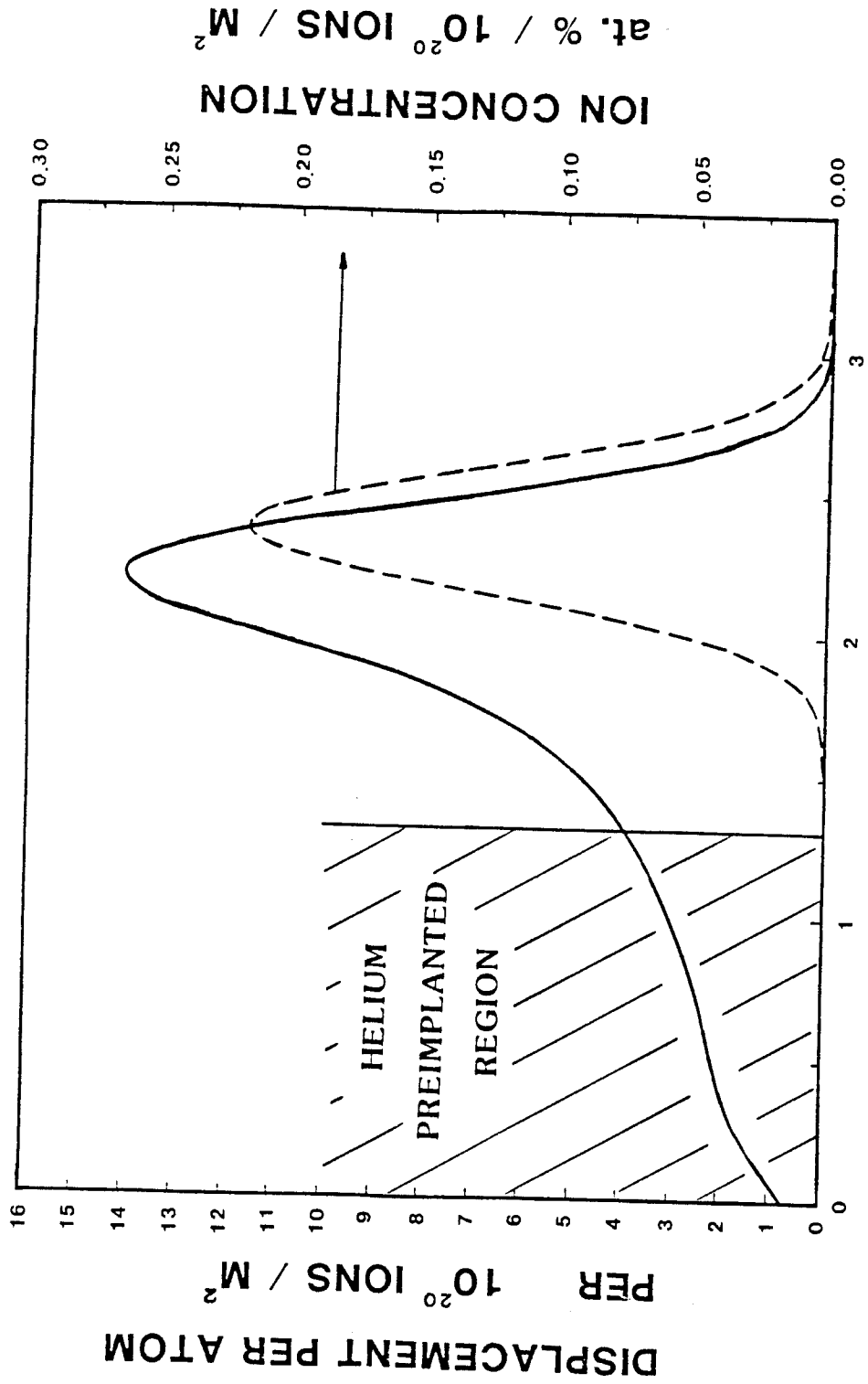

Fig.VII-13 Relationship between the calculated 14 MeV Ni ion damage profile and the helium implantation region in HT-9 alloy.

formation of cavities in the helium preimplanted region. At damage levels as low as 10 dpa, there were observable small cavities in the specimen irradiated at 600^{o} C which were determined to be helium bubbles. Figure VII-14 shows these helium bubbles in under focus, exact focus, and over focus situations. It is clearly seen that at this temperature most bubbles were formed along the subgrain boundaries.

Figure VII-15 shows the voids observed in the specimens irradiated at 500^{o} C to dose levels of 30 dpa and 60 dpa. In the 30 dpa specimen, voids were heterogeneously distributed in various regions. The number density is very low ($\leq$ 1X10^{11} cm^{-3}) and the total swelling is negligible. In the 60 dpa specimen, voids were also heterogeneously distributed in various regions although the number density and average diameter are larger. The total swelling, however, is still low. Table VII-1 summarizes the quantative data of cavities observed in this study. Figure VII-16 illustrates the swelling versus dose level relationship in the specimens irradiated at 500^{o} C. It is noticed that even the highest local swelling rate is less than 0.01%/dpa.

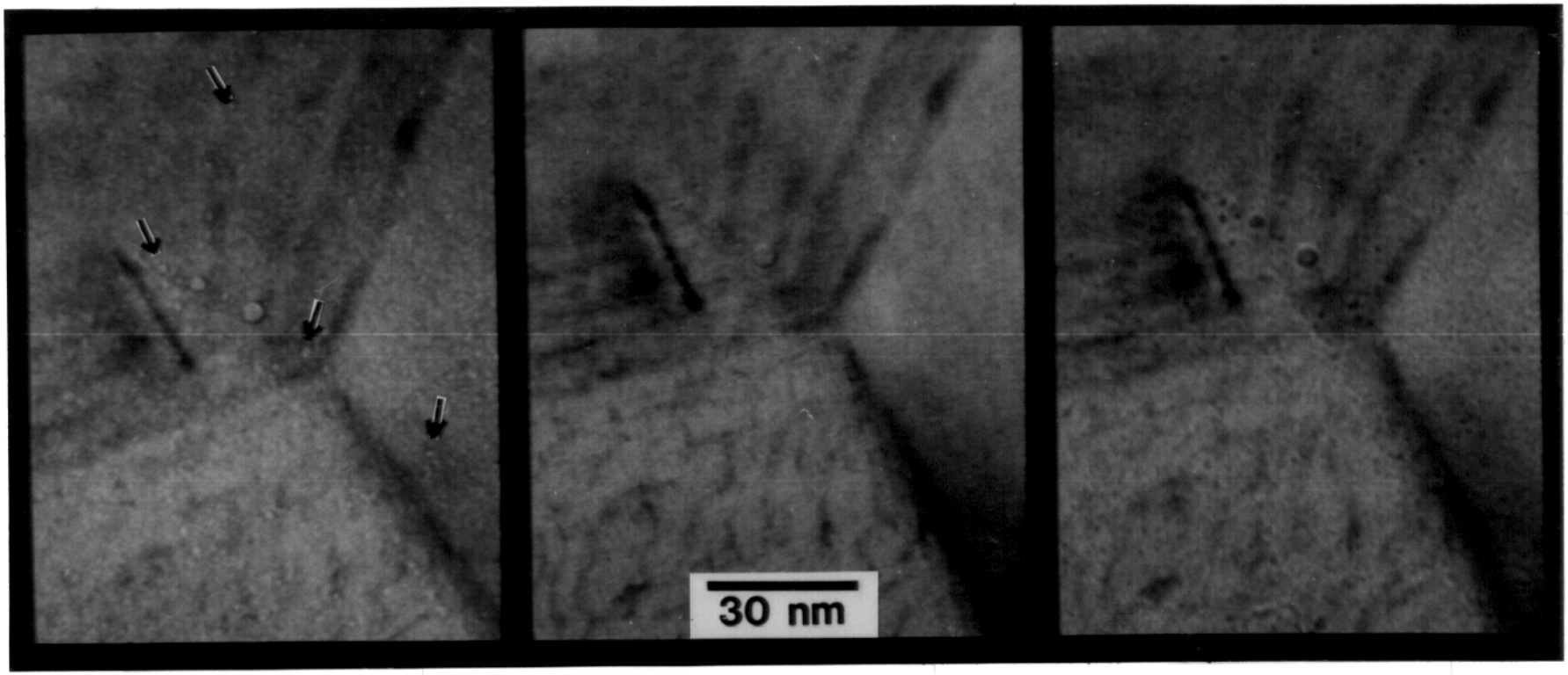

Fig.VII-14 Helium bubbles in helium doped HT-9 irradiated at 600^{o} C to 10 dpa.

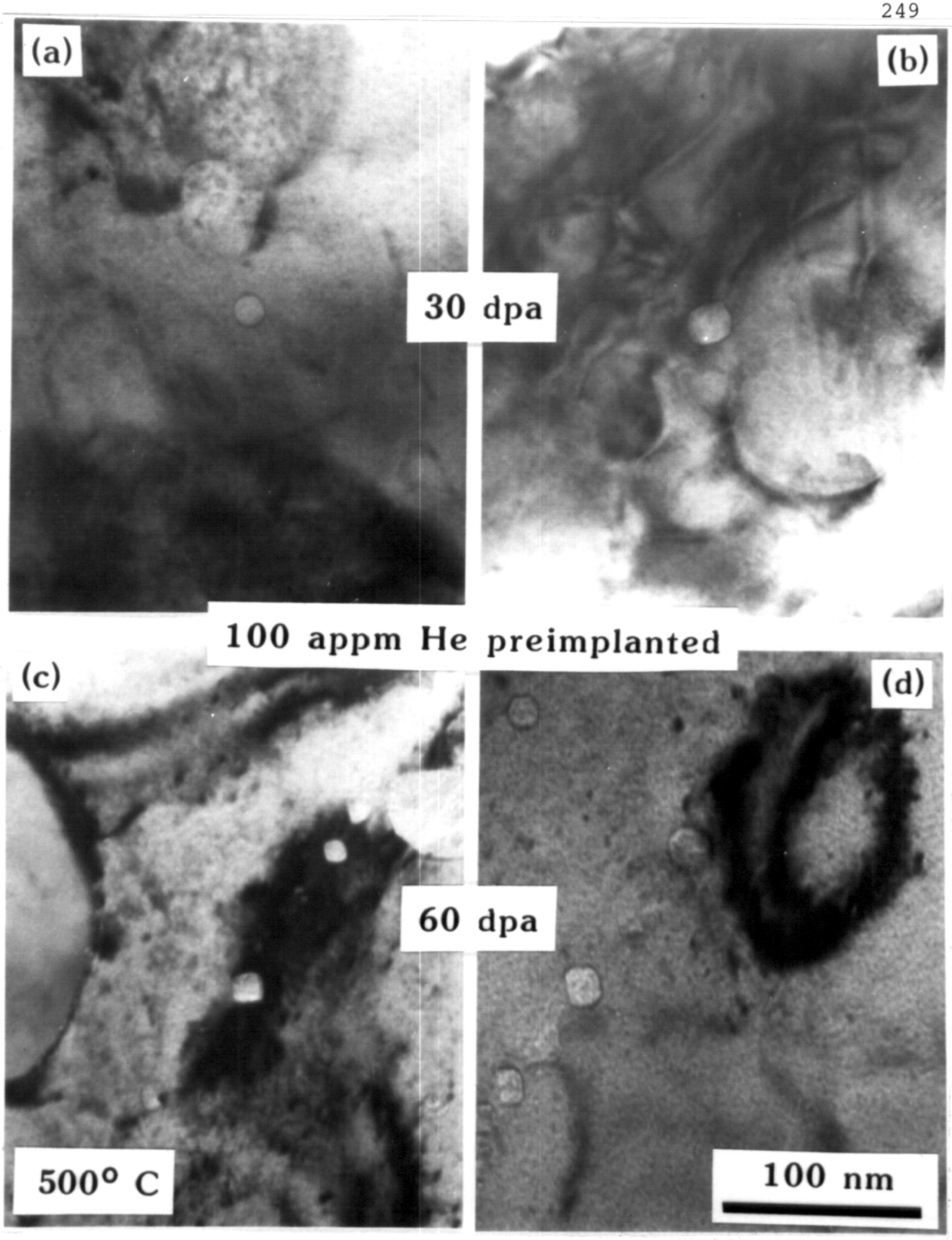

Fig.VII-15 Voids observed in HT-9 following ion irradiation with 100 appm He preimplantation. (a) and (b): 30 dpa; (c) and (d): 60 dpa.

Table VII-1 Cavity Characteristics of HT-9 Bombarded with 14 MeV Ni Ions After Preimplantation with 100 appm Helium.

Irradiation Temp.(^{o}C)	Fluence (dpa)	Voids d_v (nm)	Voids n_v (cm^{-3})	$\Delta V/V$ (%)	Helium Bubbles d_b (nm)	Helium Bubbles n_b (cm^{-3})
400	10	---	---	---	---	---
400	30	---	---	---	---	---
500	10	---	---	---	---	---
500	30	19	$\leq 1x10^{11}$	$<<0.01$	1.5	$2x10^{16}$
500	60	27	$1x10^{14}$	0.1 (locally)*	---	---
			$2x10^{13}$	0.02(average)*	---	---
600	10	---	---	---	2.2	$8x10^{15}$
600	30	---	---	---	2.3	$1x10^{16}$

* Voids distributed heterogeneously so that the local swelling is much higher than the average total swelling.

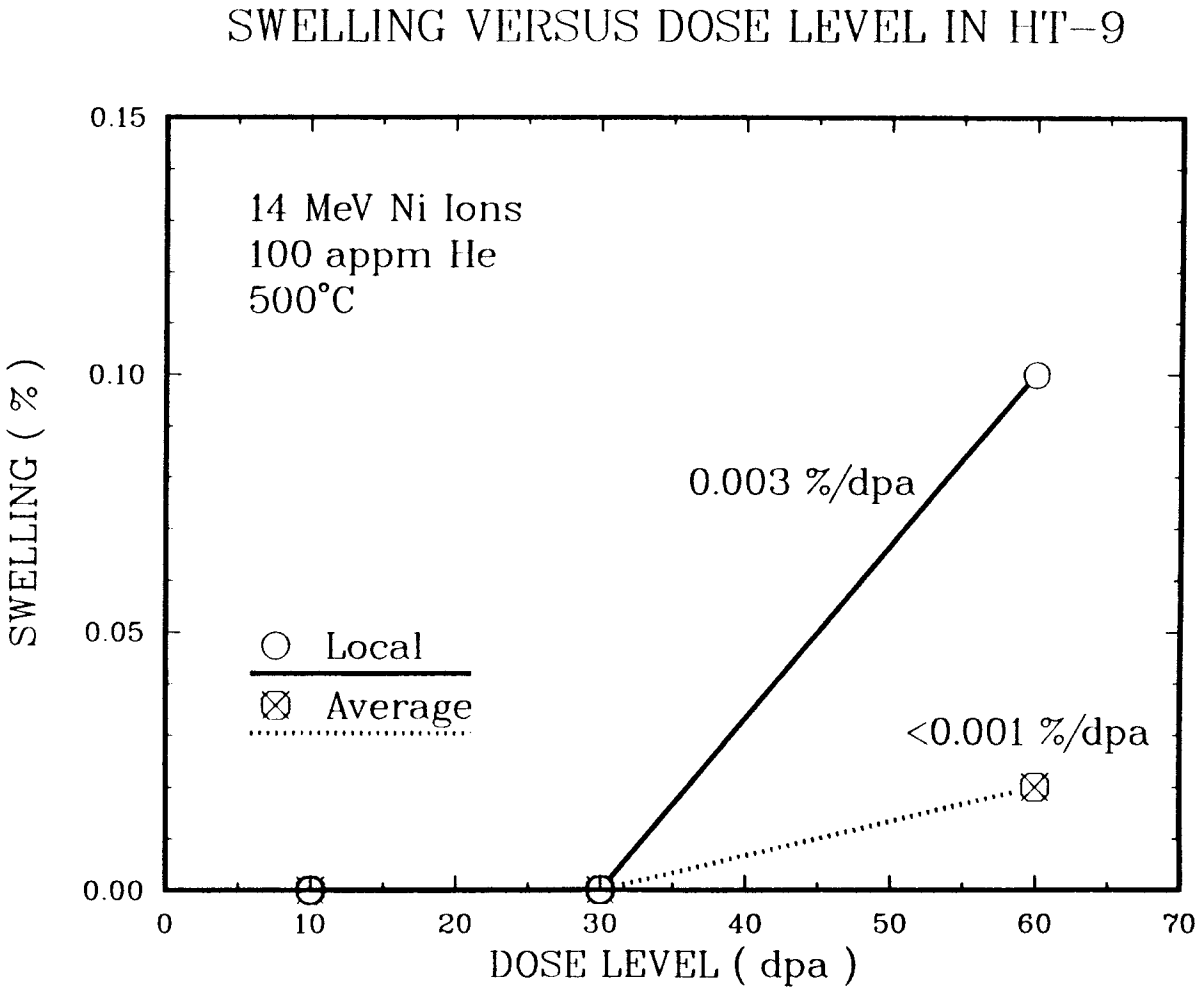

Fig.VII-16 Swelling vs. dose level in helium doped HT-9 irradiated at 500° C.

Helium preimplantation showed no effect, or very little effect, on other microstructures; namely, dislocation loops and precipitates. Figures VII-17 and 18 show the TEM microstructures in the helium preimplanted region of the HT-9 specimens irradiated to 10 dpa and 30 dpa, respectively. At 400^{o} C the major microstructure in the entire damage region is a high number density of small dislocation loops and there is virtually no difference when these specimens are compared to the microstructure of the specimens irradiated without helium under the same conditions. No observable cavities were found in the specimens irradiated at 400^{o} C. AT 500^{o} C, the microstructure of the specimen irradiated to 10 dpa showed no observable cavities or new precipitates which is the same as found in specimen which contained no helium. However, in the specimen irradiated to 30 dpa, there were cavities formed (see Fig.VII-15 (a) and (b)) and some of the voids existed simultaneously with a high number density of small helium bubbles (see Fig.VII-19 (a) and (b)). These small bubbles exist simultaneously with the void which indicates that the critical cavity size model suggested by Mansur and Coghlan[7] is valuable. The

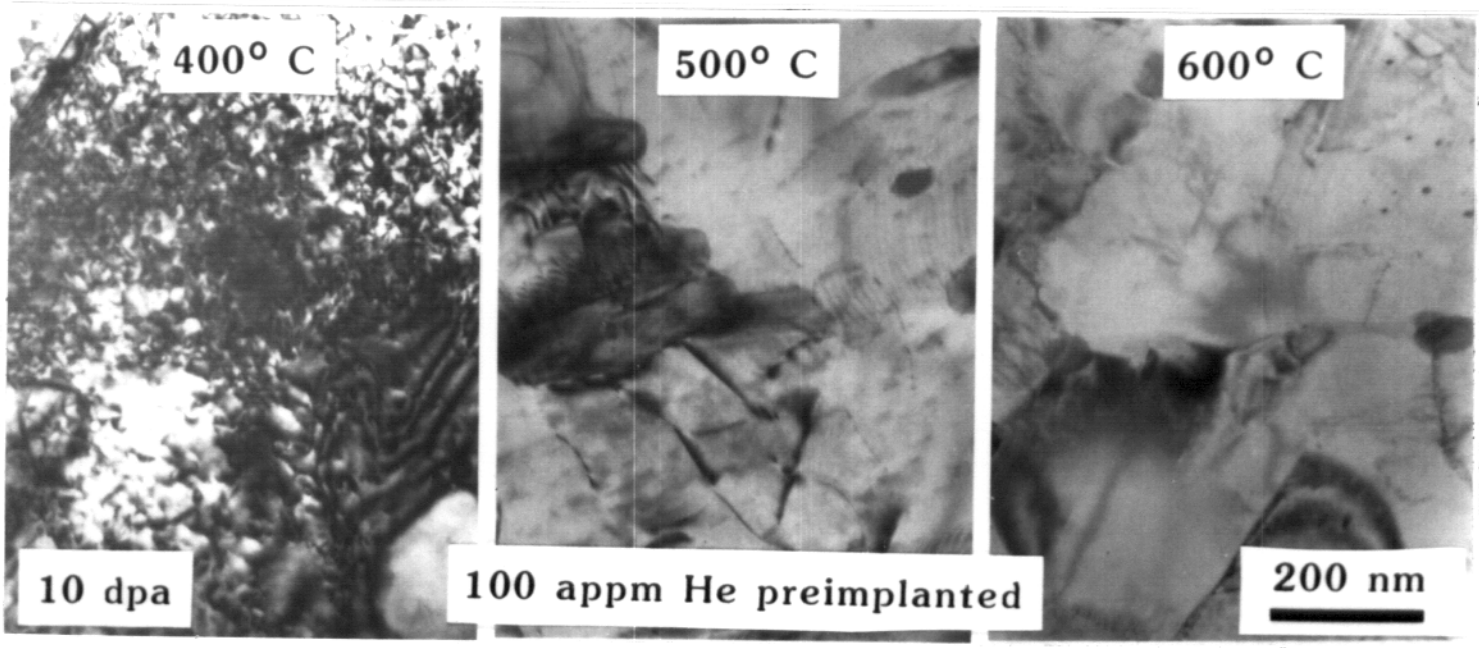

Fig.VII-17 TEM microstructures of HT-9 following ion irradiation to 10 dpa with 100 appm He preimplantation.

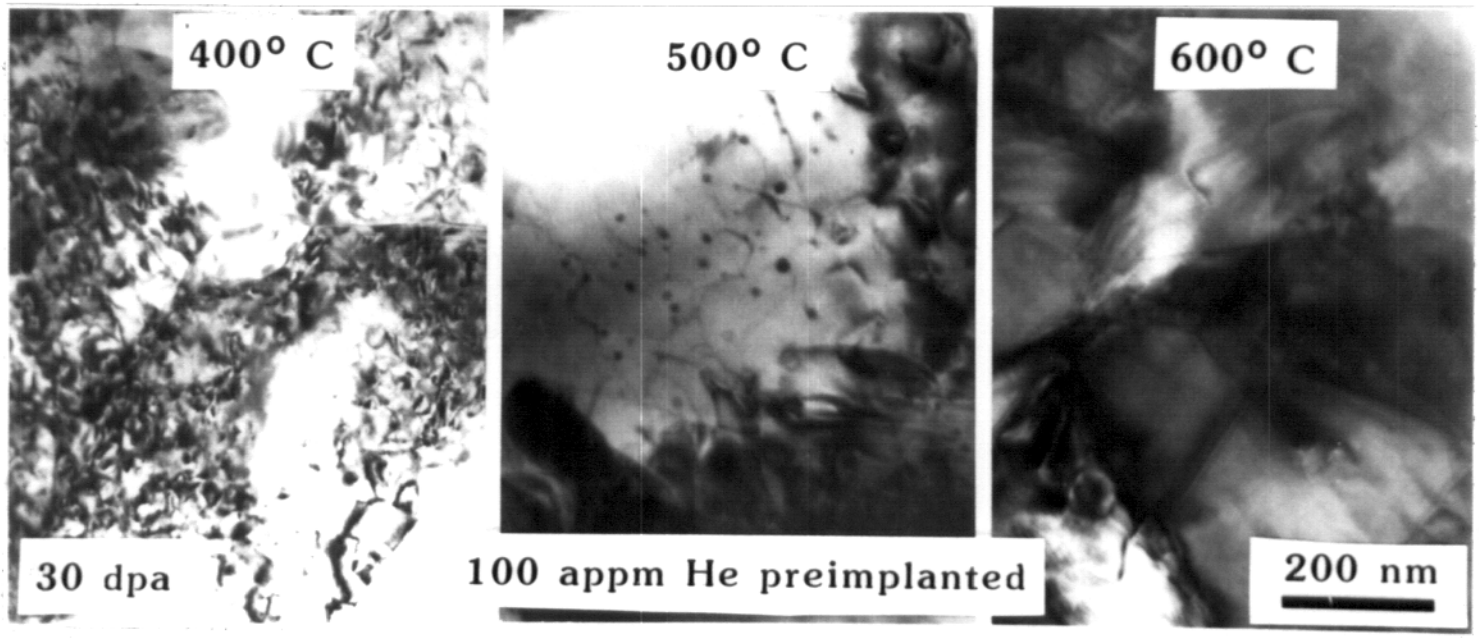

Fig.VII-18 TEM microstructures of HT-9 following ion irradiation to 30 dpa with 100 appm He preimplantation.

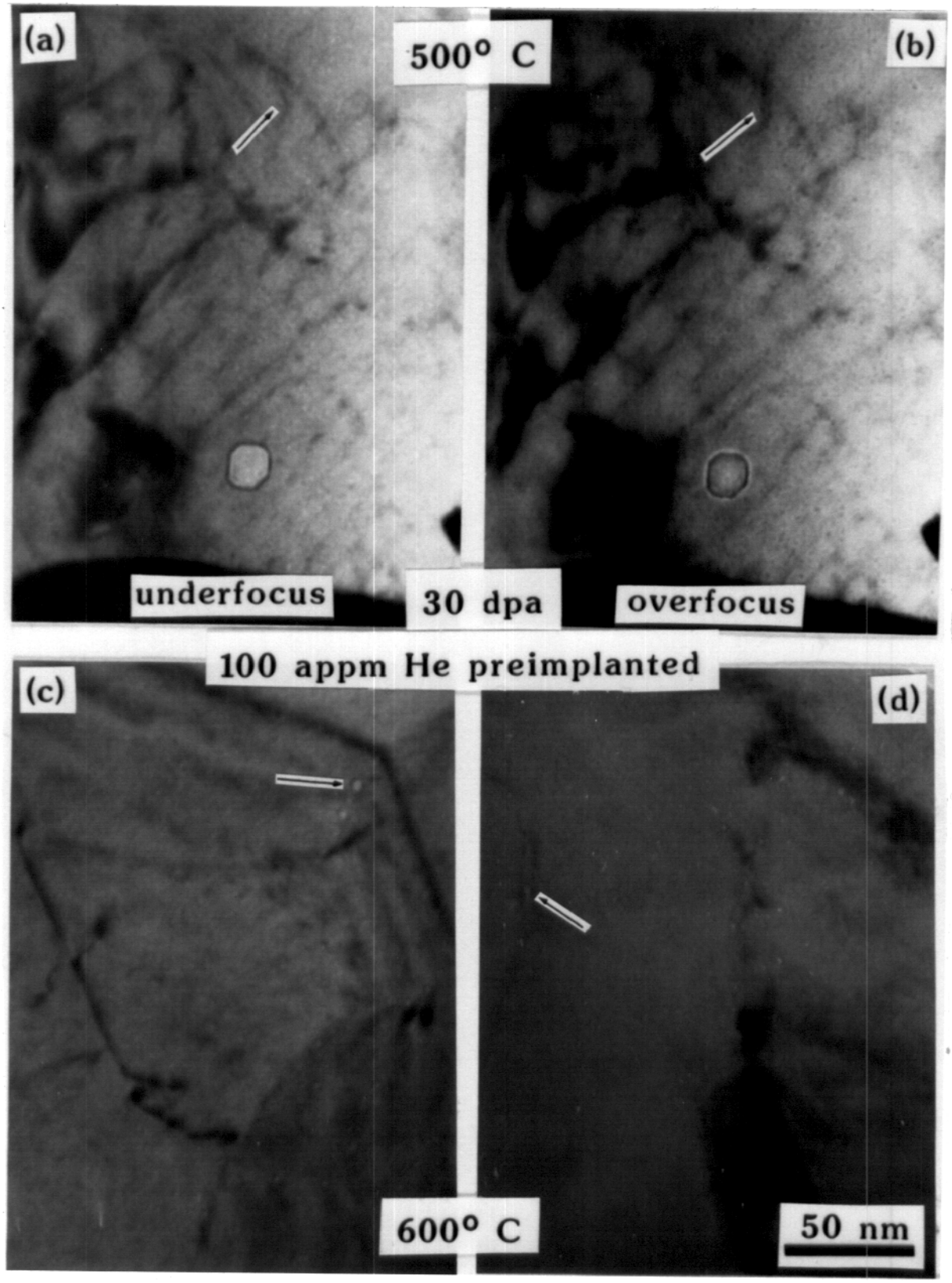

Fig.VII-19 Cavities observed in HT-9 following ion irradiation to 30 dpa with 100 appm He preimplantation. (a) and (b): 500° C; (c) and (d): 600° C.

average diameter and number density of these bubbles are about 1.5 nm and $2x10^{16}$ #/cm^3, respectively. At 600^{o} C the only distinguishable difference between irradiated and unirradiated regions is the small helium bubbles that were found in the helium preimplanted region. It is noted that most bubbles were formed along the subgrain boundaries and the interfaces between precipitates and matrix (see Fig.VII-14 and Fig.VII-19 (c) and (d)).

The critical cavity size of the HT-9 alloy following heavy ion irradiation can be roughly determined by using the similar precedures reported by Horton and Mansur.[46] Following their procedures, the critical cavity radius of HT-9 irradiated at 500^{o} C is greater or equal to 1.3 nm and at 600^{o} C it is greater than 2.6 nm.

C. Discussion

The discussion of the microstructural evolution of the HT-9 ferritic steel following ion irradiation with and without helium preimplantation will include three subsections, namely cavity formation and growth, dislocation loop evolution, and precipitation reponse during irradiation.

C.1 Cavity Formation and Growth

The complete lack of void swelling in all specimens without helium preimplantation after heavy ion irradiation up to a peak damage level of 200 dpa indicates that HT-9 is a highly swelling resistant material. Similar results have also been found in other ion-irradiated ferritic steel studies.[8,9] Several mechanisms have been presented to explain the low swelling behavior exhibited by ferritic alloys.[10-14] Sniegowski and Wolfer[10] suggested that the net bias difference between fcc and bcc structures initiated the inherent difference of the swelling resistance between austenitic steels and ferritic steels. Little[11] suggested that the existance of strong point defect trapping with solutes will increase recombination rate, which together with dislocation-solute interactions decreasing the bias of dislocation for interstitials will result in low swelling in ferritic steels. Hayns and Williams[12] presented a model based on incorporating point defect trapping into a rate theory model and found a low swelling in ferritic alloys. Little and

co-workers[13,14] also presented another possible explanation involving two types of dislocation loops (b=a‹100› and b=a/2‹111›) with different bias formed during irradiation which might also result in suppression of void nucleation. Other explanations include the effect of fine grain size on void formation,[15] and the initial high dislocation density and precipitate density in the matrix which increases the point defect recombination rate also resulting lower the void swelling.

One dramatic effect of preimplanting helium into HT-9 specimens following heavy ion irradiation is the formation of cavities in the helium preimplanted region. For a damage level as low as 10 dpa, there were helium bubbles in the specimen irradiated at 600° C. Void swelling was shown in the specimens irradiated at 500° C to dose levels of 30 and 60 dpa.

It was also found in other experimental studies that with co-implantation of helium,[8] or with as little as 1 appm helium preimplantation,[16] cavities formed in the HT-9 alloy following ion irradiation to a dose level of 10 dpa and above. These results indicate that free gas atoms in HT-9 play a major role in cavity formation and growth.

Therefore, the complete lack of void swelling in the specimens irradiated without helium preimplantation might partially be due to the lack of free gas atoms.

Farrell[18] has recently reviewed the helium effects on void swelling and concluded that helium is the most important inert gas in nuclear structural materials and is primarily active as a cavity nucleant. Wolfer[19] has also pointed out that some reactive gases such as oxygen and hydrogen can be absorbed on subcritical size cavity surfaces, thereby reducing the surface energy and the activation barrier for cavity nucleation. Both of these elements are presented in the HT-9.

The low swelling rate found in this study is also consistent with the results from other experiments.[5,8,16,21,22] The 0.01%/dpa local swelling rate shows the superior swelling resistance of this alloy. It is noted, however, that the dose level (60 dpa) is probably not sufficient to establish the steady state[23] swelling rate. It is recognized that helium affects mainly the incubation dose for swelling but not the final rate of steady-state swelling.[24] As the He/dpa ratio is increased, void nucleation is enhanced.

For moderately large values of the He/dpa ratio, over nucleation may occur. During subsequent irradiation, however, the void number density may drop and eventually reach a value independent of the He/dpa ratio.

The present results of over nucleation in specimens irradiated at 500^{o} C with 100 appm helium preimplantated suggest that cold preimplantation of helium produces much more nucleation sites than does normal neutron irradiation.

Farrell et al.[20] summarized the use of helium implantation in ion irradiation studies. They found that the nucleation rate due to helium implantation increases in the following order: co-implantation, hot preimplantation, and cold preimplantation. This suggests that the proper way to simulate the neutron irradiation is lower the amount of helium introduced by cold preimplantation (e.g., 10 appm), or by using co-implantation or hot preimplantation.

The origin of the critical size concept lies in the recognition that a pressure of gas in a cavity will retard thermal shrinkage of the cavity.[7,20] Thus, in a radiation-induced cavity the gas will affect the

competition between the net flux of vacancies causing cavity growth and the thermal emission of vacancies causing cavity shrinkage. The critical cavity radius, r_c, is the radius of a cavity that must be achieved for bias-driven growth. The r_c is strongly dependent on irradiation conditions (e.g., dose rate[43], irradiation temperature[43,44]) and material pamameters (e.g., dislocation density[45]). Horton and Mansur[46] have determined the critical cavity radius (about 2.5 nm at 575^{o} C) for Fe-10Cr ferritic alloy under ion irradiation. Other experiments[47,48] have also been conducted to determine the r_c in austenitic alloys. Following the same procedures, it was found in this thesis work that the critical cavity radius of HT-9 following irradiation at 500^{o} C is about 1.3 nm and at 600^{o} C is greater than 2.6 nm which is in good agreement with other experiments.[46]

The overall low swelling characteristics of the HT-9 ferritic alloy observed in this study is in consistent with other studies. However, as described before, there is no general agreement upon explanation for the superior swelling resistance of ferritic steels. More studies are needed in order to understand this superior swelling

resistance.

C.2 Dislocation Loop Evolution

The dislocation loop evolution versus irradiation temperature in this study followed normal patterns. The number density decreases with increasing irradiation temperature, and the average diameter behaves just the opposite way. At lower temperatures (300 and 400° C) the high density of small loops may affect the mechanical strength of the material. Little[25] pointed out that the magnitude of irradiation hardening at low temperatures ($T<0.4\ T_m$) correlated with the size distributions of resolvable dislocation loops, which were the localized obstacles to dislocation slip. Theoretical considerations demonstrate that the shear stress increase, $\Delta\tau$, resulting from interactions of glide dislocations with an array of dislocation loops is a function of loop density, n_L, and diameter, d_L, and can be expressed as: $\Delta\tau = \alpha\mu b f(n_L, d_L)$. The form of the function f is either $(d_L n_L)^{1/2}$ [26] or $(d_L n_L)^{2/3}$ [27] where α is a factor proportional to the obstacle length and μ and b are the shear modulus and Burgers vector, respectively.

Several research groups[13,22,28,29] have found dislocation loops in irradiated 12Cr-1MoV ferritic steels. Unfortunately, only one[13] of them provided detailed quantitative data. Little et al.[13] reported the dislocation loop evolution of the FV448 ferritic steel following neutron irradiation. In their results, the behavior of the loop evolution versus irradiation temperature was rather unusual. At 420° C they found a higher density and smaller average diameter of dislocation loops than at 380° C and 460° C. The reason for the discrepancy between their results and the results of this study is not clear. However, other studies in iron and simple ferritic alloys[30-32] showed that the behavior of the dislocation loop evolution was very similar to that presently reported.

Due to the magnetic characteristics of the HT-9 alloy, it is difficult to use normal loop analysis procedures. However, by using the 2 1/2 D TEM technique described by Bell and Mitchell,[2,3] it was found that most of the loops were interstitial in nature. The loops were mostly perfect with b=a‹100› Burgers vector and distributed homogeneously in the matrix.

There is no significant effect of preimplanted helium in the ion irradiated microstructure other than cavity formation in the specimens of this study. The result is consistent with other experiments in HT-9.[33] Although Farrell et al.[20] have reported that preimplanted helium increases the concentrations of dislocation loops, it is noticed that the maximum effects of helium on dislocation densities should be found at the loop formation stage, i.e., at doses much less than 1 dpa for pure metals and about 1 dpa for swelling-resistant alloys. The lowest dose level of ion irradiated specimens in this study is 10 dpa which is too high to easily distinguish effects of helium on dislocation loops. This is due to the dislocation loop density tends toward saturation values (which is exactly the situation found in this study), and any differences in dislocation loop density originally due to helium are obscured.

C.3 Phase Stability during Irradiation

The modification of existing phases by irradiation resulted in a precipitate evolution very similar to the thermal annealing study of the same material.[34] This

phenomenon indicates that for the existing precipitate phases, irradiation will enhance the thermal diffusion process and in turn accelerate the thermal annealing effect. The mechanism involved has been described as radiation-enhanced diffusion.[35]

The observation of radiation-induced chi phase in HT-9 following heavy ion irradiation at 500° C is unique to this study, although this phase has been reported in similar neutron irradiated materials in the temperature range between 420 and 540° C. The reason for the formation of this intermetallic phase in HT-9 during irradiation is not clear. However, in the Fe-Cr-Mo ternary phase diagram,[36] the chi phase exists as a stable phase with a composition of Fe_3CrMo. Since the major components of HT-9 are iron, chromium (12 wt.%), and molybdenum (1 wt.%), the free energy of the chi phase must decrease during irradiation to a level such that it becomes a stable phase.[37] One other possibility is the decomposition of $M_{23}C_6$ phase during irradiation due to the loss of carbon atoms into the matrix. This explanation has been used for the formation of chi phase in AISI 316 austenitic steel.[38]

The chi phase has been proved to be an irradiation-induced phase via an experiment involving a 100 h, 500° C post-irradiation annealing of a specimen irradiated at 500° C to 200 dpa peak damage level. The TEM microstructural analysis showed that after the thermal annealing, all the chi phase particles disappeared along with the dislocation loops.

The small particles of an additional phase that were observed in the HT-9 specimens irradiated at 400° C were too small to permit identification. However, if it is the α' phase as believed, then there is a potential irradiation embrittlement problem in using HT-9 material in reactor systems around 400° C. This phase, when produced in high chromium ferritic stainless steels during thermal aging, is responsible for the so-called "475° C embrittlement".[39,40] The homogeneously distributed chi phase particles that were found in the specimens irradiated at 500° C might also introduce some irradiation embrittlement; however, in general, it is not as serious as the α' phase.[41]

Helium preimplantation showed no significant effect on the precipitate evolution of this study. Although some

studies[18,20] have shown that helium can retard irradiation-induced phase formation in austenitic stainless steels, there is, unfortunately, no other ferritic steel study that can be used as a comparison. Recently, Maziasz[42] has found a helium promoted chi phase formation in HT-9 + 2Ni irradiated in HFIR. That phase is also associated with cavity formation. The discrepancy between Maziasz's study and the present results is not clear. More efforts are needed in this area.

Comparing the current study with other experimental results of similar materials [5,6,21,42] it seems that the HT-9 alloy has a microstructure so complicated that it is difficult to thoroughly understand the precipitate evolution during irradiation. However, because many types of precipitates can form in 12Cr-1MoV ferritic steels, minor changes in heat treatment or alloying composition may eliminate the undesirable phases, resulting in improved properties.

D. Summary

The results of this study can be briefly summarized as follows:

(a) Without a helium preimplantation or coimplantation, there is virtually no void swelling in all the HT-9 specimens following ion irradiation to a peak damage level of 200 dpa in the temperature range between 300 and 600^{o} C.

(b) With 100 appm helium preimplantation, there were cavities formed in the specimens irradiated at higher temperatures (500 and 600^{o} C). The total swelling in all specimens were low (<0.1%) and the swelling rate was also low (<0.01%/dpa).

(c) At lower temperature irradiations (300 and 400^{o} C), the formation of a high density of small dislocation loops is the major microstructural change. These loops may introduce irradiation hardening into the HT-9 alloy irradiated at these temperatures.

(d) At 500^{o} C the irradiation-induced chi phase was observed in the matrix. The average diameter of the chi phase particles increases with increasing doses and the number density decreases concomitantly.

(e) At 600^{o} C the microstructure shows no difference between irradiated and unirradiated regions which indicates that thermal diffusion processes dominate at this temperature and above. It is also suggested from the thermal annealing study that it is not practical to apply HT-9 in reactor systems at 600^{o} C or above.

(f) The equiaxed $M_{23}C_6$ and the platelet MX phases are relatively stable during ion irradiation in this study.

(g) Helium showed no significant effects in the dislocation loop evolution or the precipitation reponse following ion irradiation.

(h) A new phase was observed in the specimens irradiated at 400^{o} C. It was temperarily identified as α' phase which might introduce irradiation embrittlement into this alloy.

REFERENCES FOR CHAPTER VII

1. J. J. Kai, G. L. Kulcinski, and R. A. Dodd, DAFS Progress Report DOE/ER-0046/21 (1985) 68-72.

2. W. L. Bell, J. of Appl. Phys. 47, No.4 (1976) 1676.

3. J. B. Mitchell and W. L. Bell, Acta. Metall. 24 (1976) 147-152.

4. E. A. Little and D. A. Stow, Metal Sci. 14 (1980) 89-94.

5. D. S. Gelles and L. E. Thomas, in the Proceedings of Topical Conf. on Ferritic Alloys for Use in Nuclear Energy Technologies, J. W. Davis and D. J. Michel (Eds.), (1983) p.559.

6. E. A. Little and L. P. Stoter, in Effects of Radiation on Materials: 11th Conf., ASTM-STP-782, H. R. Brager and J. S. Perrin (Eds.), (1982) 207-233.

7. L. K. Mansur and W. A. Coghlan, J. of Nucl. Mater. 119 (1983) 1-25.

8. G. Ayrault, DAFS Report DOE/ER-0046/8 (1981) p.182.

9. R. L. Sindelar, J. J. Kai, D. L. Plumton, R. A. Dodd, and G. L. Kulcinski, "Microstructural Modification of 2 1/4 Cr-1 Mo Steel by Irradiation with 14 MeV Nickel Ions" presented at the 1985 TMS-AIME Fall Meeting, Irradiation Effects Associated with Ion Implantation, Toronto, Canada, 1985.

10. J. J. Sniegowski and W. G. Wolfer, in Ref. 5 (1983) p.579.

11. E. A. Little, J. of Nucl. Mater. 87 (1979) 11-24.

12. M. R. Hayns and T. M. Williams, J. of Nucl. Mater. 74 (1978) 151-162.

13. E. A. Little, R. Bullough, and M. H. Wood, Proc. of the Roy. Soc. Lon. A372 (1980) 565-579.

14. R. Bullough, M. H. Wood, and E. A. Little, in Effects of Radiation on Materials: 10th Conf., ASTM-STP-725, D. Kramer, H. R. Brager, and J. S. Perrin (Eds.), (1981) 593-609.

15. B. N. Singh, Phil. Mag. 29 (1974) 25-42.

16. F. A. Smidt, Jr., P. R. Malmberg, J. A. Sprauge, and J. E. Westmoreland, in Irradiation Effects on the Microstructure and Properties of Metals, ASTM-STP-611 (1976) 227-241.

17. H. Ullmaier, Nucl. Fusion 24, No.8 (1984)1039-1083.

18. K. Farrell, Rad. Effects 53 (1980) 175-194.

19. W. G. Wolfer, J. of Nucl. Mater. 122&123 (1984)367.

20. K. Farrell, P. J. Maziasz, E. H. Lee, and L. K. Mansur, Rad. Effects 78 (1983) 277-295.

21. J. M. Vitek and R. L. Klueh, in Ref. 5 (1983) 551.

22. P. Dauben, R. P. Wahi, and H. Wollenberger, J. of Nucl. Mater. 133&134 (1985) 619-622.

23. F. A. Garner, J. of Nucl. Mater. 122&123 (1984)472.

24. W. G. Wolfer and F. A. Garner, Rad. Effects 78 (1983) p.275.

25. E. A. Little, Intern. Metals Reviews 21 (1976) 25.

26. J. Friedel, Dislocations, Addison-Wesley, NY 1964.

27. F. Kroupa and P. B. Hirsch, Discussions of the Faraday Society 38 (1964) p.49.

28. D. S. Gelles and L. E. Thomas, ADIP Progress Report DOE/ER-0045/9 (1982) 162-177.

29. D. S. Gelles, J. of Nucl. Mater. 108&109 (1982)515.

30. L. L. Horton, J. Bentley, and K. Farrell, J. of Nucl. Mater. 108&109 (1982) 222-233.

31. L. L. Horton, J. Bentley, and W. A. Jesser, J. of Nucl. Mater. 103&104 (1981) 1085-1090.

32. K. Suganuma and H. Kayano, Rad. Effects 54 (1981) 81-86.

33. D. S. Gelles, ADIP Report DOE/ER-0045/14 (1985)129.

34. J. J. Kai, G. L. Kulcinski, and R. A. Dodd, DAFS Report DOE/ER-0046/21 (1985) 56-67.

35. Y. Adda, M. Beyeler, and G. Brebec, Thin Solid Films 25 (1975) 107-156.

36. T. Wada, "Constitution of Ternary Alloys: Cr-Fe-Mo" in Metals Handbook, 9th Ed., ASM.

37. P. Wilkes, K. Y. Liou, and R. G. Lott, Rad. Effects 29 (1976) p.249.

38. J. K. Lai and J. R. Haigh, Welding J. Res. Suppl. 58 (1979) p.1-s.

39. P. J. Grobner, Metall. Trans. 4 (1973) 251-260.

40. P. Jacobsson, Y. Bergstrom, and B. Aronsson, Metall. Trans. 6A (1975) 1577-1580.

41. M. Snykers and J. J. Huet, in the Proceedings of Intern. Conf. in Creep Strength in Steel and High Temperature Alloys, The Metals Soc., London (1974) 237-241.

42. P. J. Maziasz, private communications.

43. J. R. Townsend, J. of Nucl. Mater. 108&109 (1982) 544-549.

44. W. A. Coghlan and L. K. Mansur, J. of Nucl. Mater. 122&123 (1984) p.495.

45. W. A. Coghlan and L. K. Mansur, in Effects of Radiation on Materials: 12th Intern. Symp., ASTM-STP-870, F. A. Garner and J. S. Perrin (Eds.), (1985) 481-492.

46. L. L. Horton and L. K. Mansur, ibid., 344-362.

47. D. J. Mazey and R. S. Nelson, J. of Nucl. Mater. 85&86 (1979) 1127.

48. E. H. Lee and L. K. Mansur, Phil. Mag. in press.

CHAPTER VIII

CONCLUSIONS

The main conclusions resulting from this thesis research are listed below. Suggested topics that need further study are given at the end of this chapter.

A. As-Received and Thermal Annealed HT-9 Ferritic Steel

1. There are three different microstructures in the as-received HT-9 ferritic steel. The tempered lath martensite is the major phase and occupies more than 90% of the total volume. The heavily tempered carbide region and the ferrite region both exist in the microstructure but at relatively small fraction.

2. There are four types of precipitate phases identified in as-received HT-9, namely, equiaxed $M_{23}C_6$, platelet MX, elongated $M_{23}C_6$ and needle-like M_2X. Most of these precipitates are chromium-enriched.

3. Thermal annealing studies showed that some major microstructural changes occured after annealing at 600^{o} C and above. This result indicates that it is not practical

to use this alloy in reactor systems at 600° C or above.

4. The quantitative EDS results showed that thermal annealing did not alter the chemical composition of each phase except for the equiaxed $M_{23}C_6$ particles at higher temperatures (i.e., 700 and 800° C). These $M_{23}C_6$ particles contain vanadium at about 3 wt.% which is due to the dissolution of other phases and the vanadium must be incorporated into the only phase left in the matrix.

B. Ion-Irradiated HT-9 Ferritic Steel

1. There is virtually no void swelling in the HT-9 specimens following ion irradiation to a peak damage level of 200 dpa without helium preimplantation or coimplantation. This result is consistent with other ferritic steel studies. It also demonstrates the superior swelling resistance of this alloy.

2. However, with 100 appm helium preimplantation, there are cavities formed in the helium implanted region following ion irradiation. This result indicates that helium atoms are essential in cavity formation and growth in ion-irradiated HT-9. There is some evidence of the over-nucleation of helium bubbles which indicates that the

cold preimplantation of 100 appm helium might be too high to simulate neutron damage in this alloy.

3. Radiation-induced phases are observed in the ion-irradiated specimens. At 500° C the chi phase was identified. At 400° C the new phase which was found in the irradiated region may be the α' phase. These small size particles may cause embrittlement of HT-9 during irradiation.

4. The major microstructural changes in the HT-9 specimens following ion irradiation at 300 and 400° C are the formation of a high number density of dislocation loops. These loops were mostly interstitial in nature with b=a‹100› Burgers vector and homogeneously distributed in the matrix. It is believed that the high density of small loops is the major cause of the irradiation hardening in HT-9 irradiated at these temperatures.

5. Radiation-enhanced precipitate dissolution was observed in the specimens following ion-irradiation, also. The result of the precipitate dissolution is very similar to that of thermal annealing study.

6. Void swelling will not be a major concern, below 200 dpa, for the use of the HT-9 alloy in the first walls

and blankets of fusion reactors or the structural materials for fast breeder reactors because of the superior swelling resistance of this alloy. In contrast, the irradiation embrittlement produced by the radiation-induced second phases and the high density of small dislocation loops might be a critical factor and needs further study.

C. Suggestions for Future Work

1. The superior swelling resistance of HT-9 needs to be demonstrated at even higher dose levels (e.g., up to 500 dpa in the peak damage region with helium implantation). A thorough experimental investigation should be initiated on helium implantation effects in ion-irradiated HT-9 in order to understand the role of free gas atoms on cavity nucleation and growth in this alloy. Such study should also be directed toward experimentally determining the critical cavity radius of HT-9 under various irradiation conditions.

2. Theoretical work on the mechanism of formation of radiation induced new phases is needed to further understand the basic mechanisms which promote the

microstructural evolution of materials during irradiation.

3. Future studies in the microstructural changes of low activation ferritic alloys are required. The correlation between microstructure and mechanical properties in the low activation alloys is important to investigate in order to substitute for the existed ferritic alloys.

4. Ion irradiation experiments with finer temperature increments is prefered in order to thoroughly understand the dislocation loop evolution. In addition, low dose ion irradiation experiments should be designed to investigate the dose effects and the preimplanted helium effects on the dislocation loops.

5. The potential application of a ultrasensitive microhardness tester to measure the irradiation hardening or softening in ion-irradiated cross-section specimens and to correlate with the microstructure examinations is needed. It is a non-destructive technique in a macro sense, therefore it will allow other experimental data (e.g., TEM) to be subsequently extracted from the same specimen.